SHEAR STRENGTH AND DISPLACEMENT CAPACITY OF SQUAT REINFORCED CONCRETE SHEAR WALLS

by

Carlos M. Adorno-Bonilla

Dissertation submitted in partial fulfillment
of the requirements for the degree of

DOCTOR OF PHILOSOPHY
in
CIVIL ENGINEERING

UNIVERSITY OF PUERTO RICO
MAYAGÜEZ CAMPUS
2016

Approved by:

_____	_____
Daniel A. Wendichansky-Bard, Ph.D. Member, Graduate Committee	Date
_____	_____
Luis A. Montejo-Valencia, Ph.D. Member, Graduate Committee	Date
_____	_____
Ricardo R. López-Rodríguez, Ph.D. Member, Graduate Committee	Date
_____	_____
Aidcer L. Vidot-Vega, Ph.D. President, Graduate Committee	Date
_____	_____
Ismael Pagán-Trinidad, M.S.C.E. Chairperson of the Department	Date
_____	_____
Elsie I. Parés-Matos, Ph.D. Representative of Graduate School	Date

ABSTRACT

Squat reinforced concrete (RC) walls are essential structural components in nuclear power facilities (NPP) and in many civil structures. An adequate prediction of the shear strength and displacement capacity of these elements are important for the seismic design and performance assessment of structures whose primary lateral force resisting system is comprised by squat walls. These walls have aspect ratios less than or equal to 2. Due to their geometry, squat shear walls tend to have shear-dominated behavior while exhibiting strong coupling between flexural and shear responses. This dissertation presents an evaluation of current expressions for the prediction of peak shear strength and displacement capacity of squat RC walls available in US design codes and in the literature. An updated database was assembled with the results of moderate to large-scale experimental tests walls with shear-dominated failures and subjected to cyclic loads found in the literature. Key parameters influencing the peak shear strength and displacement capacity were identified and improved predictive equations were developed by calibration against the available data. Multiple-linear regression analyses were used to develop the predictive equations. It was found that the peak shear strength of such walls has not been adequately addressed by current US code equations in ASCE 43-05 and ACI 349-13 / ACI 318-14 since there is significant scatter on the predictions. It was also found that the peak shear strength equations in current US codes and standards tend to over-estimate the strength of squat RC walls with rectangular cross section, as well as to considerably under-estimate the peak shear strength of the squat RC walls with enlarged boundary elements considered in the assembled database. Experimental data suggested that allowable drift limits requred by ASCE 7-10 design code provisions for damage control are unconservative for the case of squat walls. Finally, two simplified analytical modeling approaches were presented. A Fiber-Based Model with flexure-shear interaction and a Macro-Hysteretic model were studied. A tri-linear backbone, calculated with the developed strength and displacement capacity expressions, was proposed to use in conjunction with the Macro-Hysteretic model for the nonlinear-cyclic analysis of squat RC walls.

RESUMEN

Los muros robustos de hormigón armado son componentes estructurales esenciales en plantas de energía nuclear y en muchas otras estructuras civiles. Una predicción adecuada de su resistencia a cortante y capacidad de desplazamiento es importante para el diseño y evaluación de desempeño de estructuras cuyo sistema de resistencia a carga lateral consiste de muros robustos. Estos muros tienen una relación de aspecto igual o menor a 2. Debido a su geometría, los muros de corte robustos tienden a mostrar un comportamiento dominado por cortante y un fuerte acoplamiento entre las respuestas a flexión y a cortante. Esta disertación presenta una evaluación de algunas expresiones existentes para la predicción de la capacidad a cortante y la capacidad de desplazamiento, encontradas en los reglamentos de diseño de EEUU y en la literatura. Se ensambló una base de datos actualizada, con los resultados experimentales de muros robustos de escala moderada a grande, con falla dominada por cortante y sujetos a carga lateral cíclica, hallados en la literatura. Se identificaron los parámeteros influyentes en la resistencia a cortante y en la capacidad de desplazamiento, y se desarrollaron ecuaciones para la predicción de ambos, mediante la calibración con los datos experimentales disponibles. Se usó el análisis de regresión lineal multi-variable para el desarrollo de las ecuaciones. Se encontró que en los tres reglamentos de construcción de EEUU, ASCE 43-05, ACI 349-13 y ACI 318-14, no se estima adecuadamente la resistencia a cortante de los muros robustos de hormigón armado ya que estos producen gran dispersión en los estimados de capacidad. Además se encontró que las provisiones de los reglamentos de diseño de EEUU tienden a sobre-estimar la resistencia de muros robustos con sección rectangular y a sub-estimar considerablemente la resistencia de muros robustos con elementos de borde agrandados. El código ASCE 7-10 recomienda límites de distorción de entrepiso permisibles que resultan no-conservadores para el caso de los muros robustos de hormigón armado. Finalmente, se evaluaron dos metodologías existentes para la modelación de muros robustos: un modelo basado en fibras con interacción flexión-cortante y un modelo Macro-Histerético. Se propuso una curva tri-linear para estimar la envolvente de carga-desplazamiento, calculada con las ecuaciones desarrolladas para la predicción de resistencia máxima a cortante y la capacidad de desplazamiento. Se propuso utilizar el modelo de envolvente tri-lineal en conjunto con el modelo Macro-Histerético estudiado para el análisis cíclico no-lineal de muros robustos de hormigón armado.

© Carlos M. Adorno-Bonilla 2016

This dissertation is dedicated to my parents, Eng. Ángel M. Adorno-Castro and Mrs. Carmen L. Bonilla-Maldonado, for their patience and unconditional support during my academic career.

ACKNOWLEDGEMENTS

I would like to thank my research advisor, Dr. Aidcer L. Vidot, for her continuous guidance and support throughout the course of this research work. Her patience, dedication, willingness to discuss ideas and findings, and disposition to clarify doubts during the whole research work has been key for the completion of this dissertation.

I would also like to thank Professor Ismael Pagán-Trinidad, and Dr. Luis A. Montejo for their availability to review this manuscript.

The help and technical support of Dr. Luis A. Montejo and Dr. Aidcer L. Vidot on the use of the OpenSees analysis platform is greatly valued.

I would like to express my gratitude to Dr. Daniel A. Wendichansky and Dr. Ricardo R. López for their review and insightful comments on this manuscript. Also, their encouragement and helpful advices provided during my graduate student career is gratefully appreciated.

Special thanks are given to my family for their trust and unconditional support during every step of my academic career, which has always allowed me to pursue my goals.

This research work was supported by awards NRC-HQ-12-G-38-0018 and NRC-HQ-84-14-G-0057 from the US Nuclear Regulatory Commission. The statements, findings, conclusions, and recommendations are those of the author and do not necessarily reflect the view of the US Nuclear Regulatory Commission. Additional financial support was provided by Intelligent Diagnostics for Aging Civil Infrastructure, under the IGERT Fellowship Program of the National Science Foundation (Award Number DGE-0654176).

TABLE OF CONTENTS

CHAPTER 1. INTRODUCTION 1
1.1 Research Significance and Motivation 1
1.2 Scope and Research Objectives 3
1.3 Methodology 4
1.4 Squat Wall Behavior 5
1.5 Failure Modes of Squat Reinforced Concrete Walls 8
1.5.1 Diagonal Tension Failure 8
1.5.2 Diagonal Compression Failure 9
1.5.3 Sliding Shear Failure 10
1.5.4 Flexural Failure 11
1.6 Review of Experimental Studies 12
1.7 Organization of Dissertation 30
CHAPTER 2. SQUAT WALLS DATABASE 32
2.1 Introduction 32
2.2 Walls with Rectangular Cross Section 36
2.3 Walls with Boundary Elements 39
CHAPTER 3. SHEAR STRENGTH OF SQUAT WALLS WITH RECTANGULAR CROSS SECTION 42
3.1 Introduction 42
3.2 Current Expressions for Peak Shear Strength 43
3.2.1 ACI 318-14 43
3.2.2 ASCE 43-05 48
3.2.3 Barda et al. (1977) 49
3.2.4 Wood (1990) 50
3.3 Development of New Peak Shear Strength Predictive Equation 50
3.4 Evaluation of Selected Peak Shear Strength Equations 56
CHAPTER 4. DISPLACEMENT CAPACITY OF SQUAT WALLS WITH RECTANGULAR CROSS SECTION 61
4.1 Introduction 61
4.2 Current Expressions for Estimation of Displacement Capacity 62
4.2.1 Hidalgo et al. (2000) 62
4.2.2 Carrillo (2010) 64

4.2.3 Sánchez (2013) 65
4.2.4 Gérin and Adebar (2004) 67
4.2.5 ASCE 41-13 69
4.2.6 Duffey et al. (1994a, 1994b) 71
4.3 Development of New Displacement Capacity Predictive Equations 71
4.3.1 Drift Ratio at Diagonal Cracking 74
4.3.2 Drift Ratio at Peak Strength 75
4.3.3 Drift Ratio at Ultimate Damage State 76
4.4 Evaluation of Selected Displacement Capacity Equations 78
4.4.1 Drift Ratio at Diagonal Cracking 78
4.4.2 Drift Ratio at Peak Strength 80
4.4.3 Drift Ratio at Ultimate Damage State 84
CHAPTER 5. SHEAR STRENGTH OF SQUAT WALLS WITH BOUNDARY ELEMENTS 88
5.1 Introduction 88
5.2 Current Expressions for Peak Shear Strength 88
5.3 Development of New Peak Shear Strength Predictive Equation 89
5.4 Evaluation of Selected Peak Shear Strength Equations 95
CHAPTER 6. DISPLACEMENT CAPACITY OF SQUAT WALLS WITH BOUNDARY ELEMENTS 101
6.1 Introduction 101
6.2 Current Expressions for Estimation of Displacement Capacity 101
6.3 Development of New Displacement Capacity Predictive Equations 104
6.3.1 Drift Ratio at Diagonal Cracking 105
6.3.2 Drift Ratio at Peak Strength 107
6.3.3 Drift Ratio at Ultimate Damage State 107
6.4 Evaluation of Selected Displacement Capacity Equations 109
6.4.1 Drift Ratio at Diagonal Cracking 109
6.4.2 Drift Ratio at Peak Strength 111
6.4.3 Drift Ratio at Ultimate Damage State 115
CHAPTER 7. ANALYTICAL MODELING OF SQUAT WALLS 120
7.1 Introduction 120
7.2 Fiber-Based Flexure-Shear Interaction Model 121
7.3 Macro-Hysteretic Model 131

7.3.1 Basic Parameters Calibration 132
7.3.2 Developed Backbone Model 137
7.3.3 Macro-Hysteretic Model using Developed Backbone Model 142
CHAPTER 8. SUMMARY AND CONCLUSIONS 146
8.1 Summary 146
8.2 Conclusions 147
8.3 Future Work 150
REFERENCES 152
Appendix A Squat RC Walls Database 161
A.1 Squat RC Walls with Rectangular Cross Sections 161
A.2 Squat RC Walls with Enlarged Boundary Elements 170
Appendix B Opensees Hysteretic Model Input File Example 186
Appendix C Opensees Flexure-shear Interaction Model Input File Example 192
Appendix D Opensees Moment-curvature Cross Section Analysis Input File Example 200

LIST OF FIGURES

Figure 1-1. Stable hysteretic behavior of a ductile wall structure (Paulay and Priestley, 1992). ... 6

Figure 1-2. Hysteretic response of a structural wall controlled by shear (Paulay and Priestley, 1992). ... 7

Figure 1-3. Typical wall cross sectional shapes: (a) rectangular cross section (adapted from Whyte and Stojadinovic, 2013); (b)barbell cross section (adapted from Matsui et al., 2004); (c) flanged cross section (adapted from Barda, 1972) ... 7

Figure 1-4. Diagonal tension failure modes (Paulay et al., 1982): (a) corner-to corner crack; (b) steep-angle crack. ... 9

Figure 1-5. Diagonal compression failure modes (Paulay et al., 1982): (a) crushing under monotonic loading; (b) crushing under cyclic loading. ... 10

Figure 1-6. Sliding shear failure mode (Paulay et al., 1982). ... 11

Figure 1-7. Typical flexural cracking pattern at a moderate stage of damage (ATC, 1998). ... 12

Figure 2-1. Histogram of cross section shape of specimens used in our assembled database. ... 33

Figure 2-2. Variation of normalized maximum average shear stress with shear span-to-length ratio for different cross sectional shapes. ... 33

Figure 2-3. Histogram of loading type for the walls population included in the assembled database. ... 34

Figure 2-4. Histograms of geometric and loading properties of wall specimens with rectangular cross section. ... 37

Figure 2-5. Histograms of reinforcement and material properties of wall specimens with rectangular cross section. ... 38

Figure 2-6. Histograms of geometric and loading properties of walls with flanged and barbell cross section. ... 40

Figure 2-7. Histograms of reinforcement and material properties of walls with flanged and barbell cross section. ... 41

Figure 3-1. Contribution to peak shear strength attributed to each of the equation 3-13 parameters for wall specimen MRN100C. ... 52

Figure 3-2. Variation of effective reinforcement constants with aspect ratio. ... 54

Figure 3-3. Correlation between calculated nominal shear stress and measured peak shear stress using various available equations: (a) to (e); and the new equation proposed in this study (f). ... 57

Figure 3-4. Distribution of the ratio of predicted-to-measured peak strength. 59

Figure 3-5. Variation of the predicted and measured normalized peak shear strength with wall aspect ratio compared to ACI 318 upper limit. 60

Figure 4-1. Tri-linear backbone model proposed by Hidalgo et al. (2000). 63

Figure 4-2. Backbone model proposed by Sánchez (2013). 66

Figure 4-3. Backbone model proposed by Gérin and Adebar (2004). 68

Figure 4-4. Backbone model proposed by Wallace (2007) and ASCE 41-13. 70

Figure 4-5. Representative experimental load-displacement envelope (adapted from Palermo and Vecchio, 2002). 73

Figure 4-6. Correlation between calculated drift ratio at 60% peak strength and measured drift ratio at 60% peak strength for walls with rectangular cross section included in the database. 79

Figure 4-7. Correlation between calculated drift ratio at peak strength and measured drift ratio at peak strength using various available equations: (a) to (e); and the new equation proposed in this study (f). 81

Figure 4-8. Distribution of the ratio of predicted-to-measured drift at peak strength. 83

Figure 4-9. Correlation between calculated ultimate drift ratio and measured ultimate drift ratio using various available equations: (a) to (e); and the new equation proposed in this study (f). 85

Figure 4-10. Distribution of the ratio of predicted-to-measured ultimate drift 86

Figure 5-1. Contribution to peak shear strength attributed to each of the equation 3-13 parameters for wall specimen U-1. 91

Figure 5-2. Effective flange width concept (adapted from Moehle et al., 2011). 94

Figure 5-3. Correlation between calculated nominal shear stress and measured peak shear stress using various available equations: (a) to (e); and the new equation proposed in this study (f). 97

Figure 5-4. Distribution of the ratio of predicted-to-measured peak strength. 99

Figure 5-5. Variation of the predicted and measured normalized peak shear strength with wall aspect ratio compared to ACI 318 and ASCE 43-05 upper limits 100

Figure 6-1. Correlation between calculated drift ratio at 60% peak strength and measured drift ratio at 60% peak strength for walls with boundary elements included in the database. 110

Figure 6-2. Correlation between calculated drift ratio at peak strength and measured drift ratio at peak strength using various available equations: (a) to (e); and the new equation proposed in this study (f). 112

Figure 6-3. Distribution of the ratio of predicted-to-measured drift at peak strength. 114

Figure 6-4. Correlation between calculated ultimate drift ratio and measured ultimate drift ratio using various available equations: (a) to (e); and the new equation proposed in this study (f). 116

Figure 6-5. Distribution of the ratio of predicted-to-measured ultimate drift..... 118

Figure 7-1. Wall model using Flexure-Shear Interaction Displacement-Based Beam-Column Element (Adapted from Massone, 2010a). 122

Figure 7-2. Flexure-Shear Interaction Displacement-Based Beam-Column Element: (a) model element (adapted from Orackal et al., 2006), and (b) element section modeling (Massone et al., 2012). 122

Figure 7-3. Constitutive models for concrete and steel: (a) *Concrete06* (adapted from Massone, 2010b) and (b) *Steel02* (adapted from Massone et al., 2004). 123

Figure 7-4. Cross section discretization model for the studied specimens SW1, SW3 and SW6. 126

Figure 7-5. Experimental and flexure-shear interaction model load-displacement results for wall SW1. 126

Figure 7-6. Experimental and flexure-shear interaction model load-displacement results for wall SW3. 127

Figure 7-7. Experimental and flexure-shear interaction model load-displacement results for wall SW6. 127

Figure 7-8. Sensitivity of the Fiber-Based Flexure-Shear Interaction Model to vertical wall discretization (No. vertical elements) on wall specimen SW3..... 128

Figure 7-9. Sensitivity of the Fiber-Based Flexure-Shear Interaction Model to concrete tension stiffening curve exponent (*b*) on wall specimen SW3. 129

Figure 7-10. Backbone curve definition parameters for the hysteretic material model (Scott and Filippou, 2013). 131

Figure 7-11. Effect of hysteretic parameters on the Hysteretic Material model: (a) pinching, (b) strength degradation, (c) and unloading stiffness degradation (Scott and Filippou, 2013). 132

Figure 7-12. Example backbone curve fitting for the Macro-Hysteretic Model (SW1)..... 133

Figure 7-13. Experimental and calibrated Macro-Hysteretic model results of the cyclic load- displacement behavior for walls SW1, SW3 and SW6. 135

Figure 7-14. Calculated backbone compared to experimental load-drift ratio envelope for squat RC walls with rectangular cross section. 138

Figure 7-15. Calculated backbone compared to experimental load-drift ratio envelope for squat RC walls with enlarged boundary elements. 140

Figure 7-16. Experimental and Macro-Hysteretic model results of the cyclic load-displacement behavior for walls SW7, SW9 and SW11 using calculated backbone and base hysteretic parameters. 144

LIST OF TABLES

Table 3-1. Summary of statistics of the ratio of predicted shear strength to the measured peak shear strength for walls included in the database. 58

Table 4-1. Summary of statistics of the ratio of predicted-to-measured drift at 60% peak strength for walls with rectangular cross section included in the database. 80

Table 4-2. Summary of statistics of the ratio of predicted-to-measured drift at peak strength for walls with rectangular cross section included in the database. 82

Table 4-3. Summary of statistics of the ratio of predicted-to-measured ultimate drift for walls with rectangular cross section included in the database. 86

Table 5-1. Trials for effective flange width determination. 94

Table 5-2. Summary of statistics of the ratio of predicted shear strength to the measured peak shear strength for walls included in the database. 98

Table 6-1. Summary of statistics of the ratio of predicted-to-measured drift at 60% peak strength for walls with boundary elements included in the database. 111

Table 6-2. Summary of statistics of the ratio of predicted-to-measured drift at peak strength for flanged/barbell walls included in the database. 113

Table 6-3. Summary of statistics of the ratio of predicted-to-measured ultimate drift for flanged/barbell walls included in the database. 117

Table 7-1. Properties of the studied specimens. 121

Table 7-2. *Concrete06* constitutive model calibrated parameters. 125

Table 7-3. *Steel02* constitutive model calibrated parameters. 125

Table 7-4. Experimental vs. Fiber-Based Model peak shear strength. 130

Table 7-5. Calibrated backbone control points parameters. 134

Table 7-6. Calibrated pinching and damage parameters. 134

Table 7-7. Calculated backbone control points parameters. 142

Table 7-8. Selected pinching and damage parameters. 143

Table A-1. Geometric properties of squat RC walls with rectangular cross section. 161

Table A-2. Reinforcement configuration of squat RC walls with rectangular cross section. 164

Table A-3. Materials properties of squat RC walls with rectangular cross section. 166

Table A-4. Loading, strength and drift ratio of squat RC walls with rectangular cross section. 168

Table A-5. Geometric properties of squat RC walls with enlarged boundary elements..... 170

Table A-6. Reinforcement configuration of squat RC walls with enlarged boundary elements. 174

Table A-7. Material properties of squat RC walls with enlarged boundary elements. 178

Table A-8. Loading, strength and drift ratio of squat RC walls with enlarged boundary elements. 182

GLOSSARY

A	efficiency factor for vertical reinforcement
A_{be}	gross area of each boundary element, mm^2
A_{cv}	gross area of concrete section bounded by web thickness and length of section in the direction of shear force considered, mm^2
A_{cw}	area of concrete section of an individual pier, horizontal wall segment, or coupling beam resisting shear, mm^2
A_g	gross area of wall cross section, mm^2
A_{sbe}	effective longitudinal boundary element reinforcement area in tension, mm^2
A_v	area of shear reinforcement within spacing $\boldsymbol{s}$, mm^2
A_{vf}	area of shear friction reinforcement (total area of vertical reinforcement in wall), mm^2
B	efficiency factor for horizontal reinforcement
b_{eff}	effective flange width to determine A_{sbe} for walls with flanged cross sections, mm
b_f	actual flange width for walls with flanged cross sections, mm
c_1	factor to include flexural cracking effects on stiffness (1.0 for uncracked)
c_2	factor to include shear cracking effects on stiffness (1.0 for uncracked)
d	distance from extreme compression fiber to centroid of longitudinal tension reinforcement, mm
E_c	modulus of elasticity of concrete
E_s	modulus of elasticity of reinforcement
f'_c	compressive strength of concrete, MPa
$\sqrt{f'_c}$	square root of compressive strength of concrete, MPa
f_{ybe}	yield strength of longitudinal boundary element reinforcement, MPa
f_{ube}	ultimate strength of longitudinal boundary element reinforcement, MPa
f_y	yield strength of reinforcement, MPa
f_{yh}	yield strength of horizontal reinforcement, MPa
f_{uh}	ultimate strength of horizontal reinforcement, MPa
f_{yse}	effective yield strength of shear reinforcement, MPa
f_{yv}	yield strength of vertical reinforcement, MPa

f_{uv} ultimate strength of vertical reinforcement, MPa

G_c shear modulus of concrete

h_w wall panel height, mm

h_L height of lateral load application, mm

h_w/l_w wall panel aspect ratio, mm

h_{be} length of boundary element (out of plane direction), mm

I_g moment of inertia of gross concrete section about centroidal axis

K_{cr} cracked initial stiffness including both shear and flexural deformations

K_e initial elastic stiffness considering flexural and shear deformations and uncracked properties ($c_1 = c_2 = 1.0$).

l_{be} length of boundary element (in-plane direction), mm

l_w total length of wall, mm

M moment at section, N•mm

M/Vl_w wall shear span-to-length ratio, mm

P axial load normal to cross section, taken as positive in compression, N

R_{cr} drift ratio at diagonal cracking

R_{peak} drift ratio at peak strength

R_u drift ratio at ultimate damage state

s center-to-center spacing of reinforcement bars, mm

s_h center-to-center spacing of horizontal reinforcement bars, mm

s_v center-to-center spacing of vertical reinforcement bars, mm

t_f flange thickness, mm

t_w wall web thickness, mm

V shear force at section, N

V_c nominal shear strength provided by concrete, N

v_{cr} shear stress at diagonal cracking

$V_{flexure}$ Calculated shear force associated to the development of flexural strength of the cross section at the maximum moment location (base of wall), N

V_n nominal shear strength of wall, N

v_n nominal shear stress strength of wall, N

V_{peak} measured peak shear strength as reported from experimental tests (average from positive and negative excursions), N

V_s nominal shear strength provided by shear reinforcement, N

v_y shear stress at yield (taken as the shear strength)

α_c coefficient defining the relative contribution of concrete strength to wall shear strength

γ_{cr} shear strain at diagonal cracking

γ_u shear strain at ultimate displacement

γ_y shear strain at yield

Δ_{cr} drift at diagonal cracking, mm

$\Delta_{cr\text{-}f}$ drift at flexural cracking, mm

Δ_f drift due to flexural deformations, mm

Δ_s drift due to shear deformations, mm

Δ_u drift at ultimate damage state, mm

$\Delta_{\rho h}$ horizontal reinforcement contribution to drift, mm

λ modification factor reflecting the reduced mechanical properties of lightweight concrete relative to normalweight concrete of the same compressive strength

ρ_{be} longitudinal boundary element reinforcement ratio, calculated as the ratio of effective longitudinal boundary element reinforcement area (A_{sbe}) to the effective shear area (A_{cv})

ρ_h reinforcement ratio of distributed horizontal web reinforcement in wall

ρ_{se} effective shear reinforcement ratio

ρ_v reinforcement ratio of distributed vertical web reinforcement in wall

φ design strength reduction factor

CHAPTER 1. INTRODUCTION

1.1 Research Significance and Motivation

Short or squat reinforced concrete walls are important structural components in nuclear power facilities and in many other civil structures. The seismic performance of these type of walls, with height to length ratio less than or equal to 2, is important to the structural safety since they are designed to provide most of the lateral stiffness and strength of the structure. Recent experimental research has shown that squat walls are prone to undesirable (non-ductile) shear failures characterized by sudden loss of strength and stiffness under lateral cyclic loading.

According to Li and Manoly (2012), the US Nuclear Regulatory Commission (NRC) determined that the estimates of seismic hazard for many operating nuclear power plants (NPP) in central and eastern United States have increased from earlier seismic hazard evaluations. It is important to note that the seismic hazard has not changed for a specific location but its estimation is continuously changing due to advances in the understanding of potential earthquake sources, ground motion propagation, site response and occurrence of seismic events. Also, the methodology for seismic hazard estimation used a few decades ago was based on a deterministic approach and has moved to a probabilistic approach which is the current state of practice.

Recently, nuclear power plants have experienced strong ground motions during earthquakes in Japan and the US. One of these cases is the North Anna nuclear power station which experienced ground motions at the site exceeding those of the design basis earthquake (DBE). This occurred during the magnitude 5.8 (Mw) Mineral, Virginia earthquake on August 23, 2011 and initiated the safety shutdown procedures. After extensive evaluation of the plant's structures, systems and components (SSCs), some minor damage was found but deemed not significant (Li and Manoly, 2012). According to Li and Manoly (2012), horizontal and inclined hairline cracks were found on interior walls of non-safety-related structures. The horizontal cracks were found to occur in pre-existing weaker interfaces such as in construction joints between concrete pour lifts.

Other documented events involving NPPs are the Kashiwazaki-Kariwa NPP in 2007 Niigata Earthquake and the Fukushima Daiichi NPP in the 2011 Tohoku earthquake. As reported by

Takada (2012), the Kashiwazaki-Kariwa NPP was struck by the Niigata earthquake on July 16, 2007 inducing recorded seismic input at the base of the reactor building exceeding twice its design level considerations. However, the plant behaved in a safe manner, with damage concentrated in non-safety related systems, and restarted operations in 2009 (Takada, 2012). The reason for the good performance of NPPs under unexpectedly large ground motions is thought to be due to the implicit conservatism in the seismic design procedures, requiring the structure to perform in the linear (elastic) range and thus, providing a considerable safety margin.

On the other hand, the March 11, 2011 Tohoku earthquake and tsunami generated a great disaster in Japan, and produced heavy damage to the Fukushima Daiichi NPP resulting in an environmental damage of unexpected proportions (Takada, 2012). In this case the major damage was caused by the tsunami flood, which damaged the emergency power supply subsequently interrupting the operation of the cooling system.

These issues along with the updated data from recent earthquakes have triggered a program that requires site seismic hazard re-evaluation and flood hazard for all US operating NPPs and that may require some plants to perform a seismic risk analysis to determine if the plant´s seismic design provides adequate seismic margin (Li and Manoly, 2012). Similarly, seismic and flood hazards re-evaluation are being carried out in Japan reflecting the lessons learned from the Niigata and Tohoku earthquakes (Takada, 2012).

An adequate understanding of the lateral loading behavior of squat walls is essential for the seismic design and performance assessment of NPP structures and other low rise shear wall civil structures. The key instruments for seismic design, evaluation and retrofitting of structures are the accuracy in the prediction of strength and stiffness of individual members and the ability to incorporate the behavior of such elements to model the global behavior of the structure. Depending on the required type of analysis, the estimation of the drift or displacement capacity and cyclic behavior may be necessary.

Many equations are found in current design codes (e.g., ACI 318, ACI 349, ASCE 43-05) and literature (e.g., Barda et al., 1977; Wood et al., 1990) for the prediction of the peak shear strength of reinforced concrete walls. However, recent studies (e.g., Orbovic et al., 2007; Gulec and Whittaker, 2009; Massone, 2010a) have shown that these equations yield significantly scattered

strength predictions. In general, it is agreed that the development of better equations to assess the peak shear strength of squat RC walls is necessary, since the lateral strength and performance of these walls depends mostly on its shear strength. Also, for performance-based design and assessment of structures, displacement or drift capacity becomes more important. Predictive equations for the drift capacity have not been widely addressed in literature.

Various nonlinear modeling approaches for RC squat walls have been proposed by different researchers. Detailed finite element models (Xu et al., 2007) have produced acceptable results against experimental data for both static cyclic analysis and dynamic simulation. However, such degree of refinement may not be feasible for a design environment due to the high modeling and computational efforts. For design and performance assessment, macro-level hysteretic models (Gulec and Whittaker, 2009) or extended fiber-based approaches (Orakcal et al., 2006) have been proposed. The research performed and related to this topic includes the evaluation of current strength design equations and simplified modeling approaches for further development and calibration as well as the development of new predictive equations for the strength and displacement capacity of RC squat walls.

1.2 Scope and Research Objectives

The scope of this work is limited to the analytical modeling, peak shear strength and force-displacement characteristics of shear-critical RC squat walls with conventional (vertical and horizontal) reinforcement which may have rectangular cross section or include boundary elements (flanges or barbells). Such walls investigated herein shall also have an aspect ratio (height-to-length ratio) less than or equal to 1.5, cross sectional shape be symmetric, be tested under cyclic loading in a cantilever setup, and have no web openings. A detailed description of the assembled database is found in Chapter 2.

The research objectives of this work can be summarized as follows:

- Comprehensive evaluation of currently available and most widely used equations for the prediction of peak shear strength of squat RC shear walls in the US.
- Given that the commonly used equations for strength prediction have been developed on a “best fit” basis of the limited data available at the corresponding time, and that current code provisions have remained unchanged in the last four decades (Gulec and Whittaker,

2009), development of improved equations for the prediction of peak strength using an updated database was presented.

- Since the seismic design and assessment of existing structures has been moving toward a performance-based philosophy, the development of predictive equations for the displacement capacity (in terms of drift ratio) at various performance stages of squat shear walls using experimental data available from literature was presented.
- Evaluation of simplified modeling approaches for further calibration and their feasibility to be used for performance-based design and assessment of existing structures was discussed.

1.3 Methodology

In order to achieve the aforementioned research objectives, the following tasks have been performed:

- A database including the latest experimental data of moderate to large scale shear-critical squat walls under cyclic lateral loading was assembled. Force-displacement data were recorded on the database when available from the reported information.
- Statistical analyses were used to evaluate the accuracy of the predictions of widely used peak shear strength equations. Each equation central tendency and dispersion measures of the ratio of predicted-to-measured strength were presented. Also, the level of confidence was assessed with the number of over-predictions.
- Walls with boundary elements usually achieved higher peak shear strength than similar walls of rectangular cross sections (ASCE 43-05). Therefore, the database was divided into two groups and all analyses were performed separately for each group.
- New empirical equations for the prediction of peak shear strength were developed by performing multivariable linear regression procedures based on the data of qualifying tests compiled into the database.
- Statistical analyses were used to evaluate the accuracy of the predictions of several displacement capacity equations found in the literature. Statistical analyses were carried out in a similar fashion as for peak strength equations.
- New empirical equations for the prediction of the displacement capacity of squat RC walls were developed by performing multivariable linear regression procedures based on

the data of qualifying tests compiled into the database. Empirical equations were developed for various performance levels resembling diagonal cracking point, peak strength, and at ultimate damage state.

- Two analytical modeling approaches were evaluated by simulation of experimental tests. One of the modeling approaches outlined in this work was an extended Fiber-Based Model capable of predicting the monotonic response (including internal stresses and strains) of a 2-D shear wall, called *Flexure-Shear Interaction Displacement-Based Beam-Column element*, which have been proposed by Massone et al. (2006) and introduced into the OpenSees analytical platform. Several walls were modeled using this analytical tool giving reasonable monotonic load-displacement results for walls of different aspect ratios. Also, analyses using a Macro-Hysteretic model called the *Hysteretic Material* available within OpenSees platform have been undertaken. This model is capable of reasonably simulating the hysteretic global response (shear force-displacement) of the selected squat RC shear walls including pinching and the deterioration of strength and stiffness under cyclic loading through the use of calibrated parameters.

1.4 Squat Wall Behavior

Reinforced concrete (RC) shear walls are commonly used in building systems and other structures such as nuclear facilities to resist most of the lateral loads due to wind and earthquake while also carrying vertical (gravity) loads transmitted by floor systems. As a result, these elements will be subjected to axial loads, bending moments and shear forces. Shear walls are typically categorized as two different types: tall (or slender) and squat (low rise, short) based on the aspect ratio h_w/l_w (height to length ratio). Walls with an aspect ratio less than or equal to 2 are considered as squat walls while walls with a higher aspect ratio are considered as slender walls.

Slender walls are more likely to have failure mechanisms controlled by flexural yielding near the base. These walls should be detailed to provide adequate load carrying capacity (axial-flexure) and ductility while brittle shear failures are prevented by providing the necessary strength to resist the maximum probable shear forces that may occur at the formation of the plastic hinge. The design of such slender walls is similar, in concepts, to the design of an axial-flexure (beam-column) element. These walls can typically be detailed to exhibit ductile behavior (Figure 1-1)

under cyclic lateral loading since they are typically designed to fail by flexure (Paulay and Priestley, 1992).

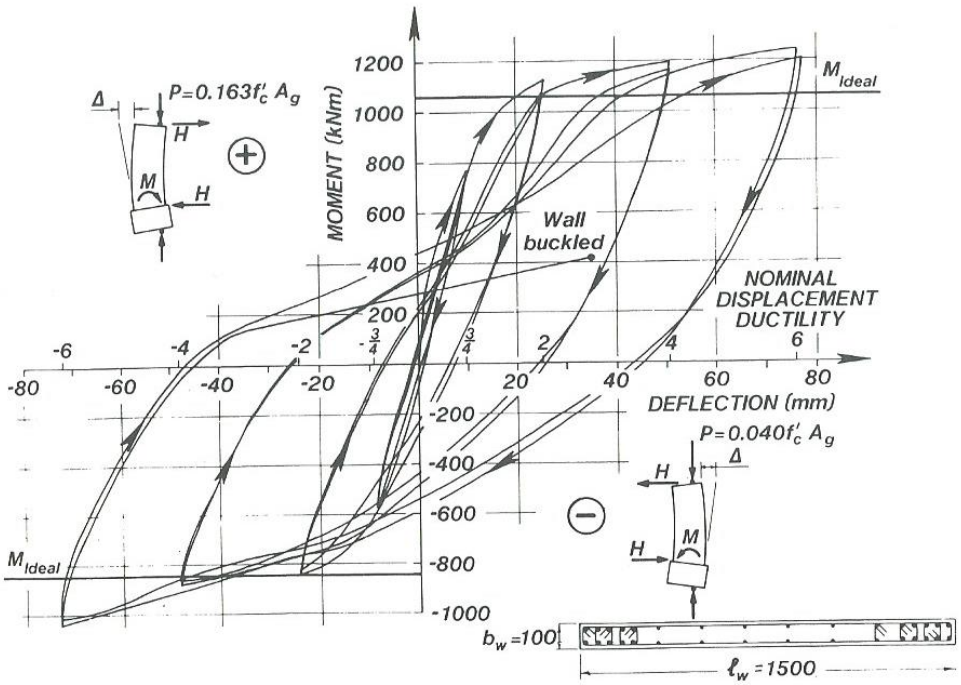

Figure 1-1. Stable hysteretic behavior of a ductile wall structure (Paulay and Priestley, 1992).

Due to their geometry, squat shear walls tend to have shear-dominant failure mechanisms. Generally, the flexural demand of such walls is relatively low when compared to the flexural capacity provided by the section. Therefore, it may be difficult or not economically feasible to prevent a shear failure by matching the shear resistance with the flexural strength as in the case of slender walls (Paulay and Priestley, 1992). Thus, typical squat walls are prone to undesirable (non-ductile) shear failures characterized by sudden loss of strength and stiffness under lateral cyclic loading (Figure 1-2). The main shear failure mechanisms associated with squat walls are diagonal tension, diagonal compression, sliding shear or a combination of the aforementioned (Paulay and Priestley, 1992; Gulec and Whittaker, 2009).

Typical cross section shapes found on experimental tests are shown in Figure 1-3. Squat walls with boundary elements (barbell or flanged) can usually achieve higher peak shear strength than

similar walls of rectangular cross sections (ASCE 43-05). This effect may be attributed to the additional reinforcement and wall web confinement provided by the boundary elements.

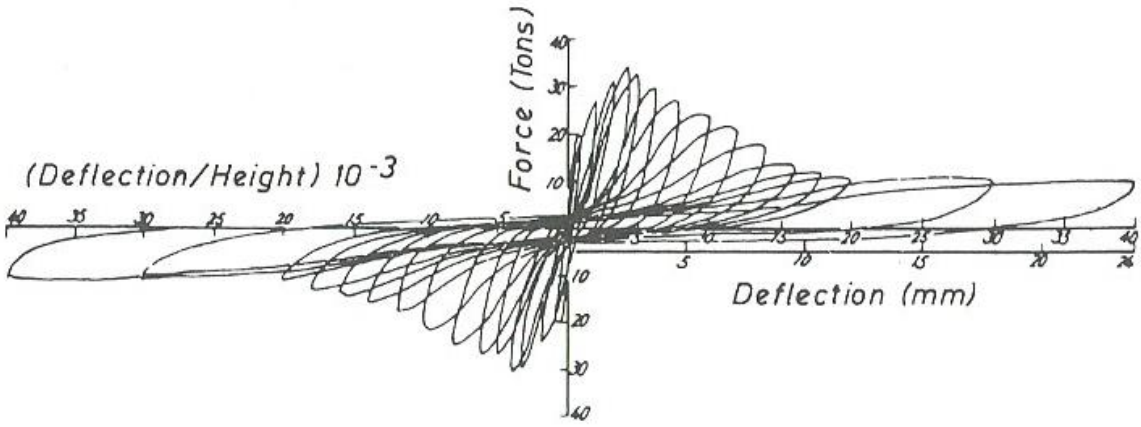

Figure 1-2. Hysteretic response of a structural wall controlled by shear (Paulay and Priestley, 1992).

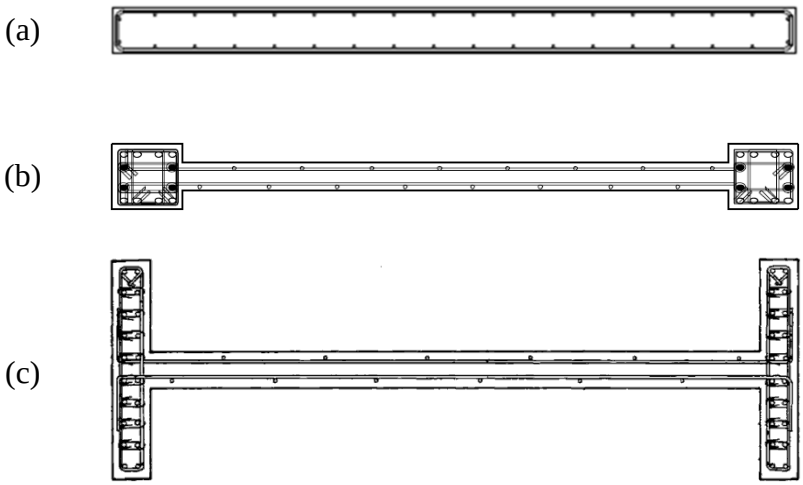

Figure 1-3. Typical wall cross sectional shapes: (a) rectangular cross section (adapted from Whyte and Stojadinovic, 2013); (b) barbell cross section (adapted from Matsui et al., 2004); (c) flanged cross section (adapted from Barda, 1972).

Walls with intermediate aspect ratios between 1.5 and 3.0 (often called medium-rise or moderate slenderness shear walls) tend to show a behavior influenced by both shear and flexure (ASCE

41-06). Thus, shear walls with aspect ratio higher than 3.0 can be considered as slender meanwhile walls with aspect ratio less than 1.5 can be considered as squat. Engineering judgment must be used when evaluating walls with intermediate aspect ratio since even when a shear capacity higher than the shear force corresponding to flexural yielding is provided, the wall can exhibit a shear failure when subjected to cyclic loading. This kind of failure can occur when the wall initially yields in flexure (denoted by horizontal cracking and reinforcement yielding initiated at the wall flexural tension zones or boundary elements) but then, the shear strength is degraded after various displacement cycles falling below the shear force associated with flexural yielding (Gulec and Whittaker, 2009). The shear failure leads to a sudden degradation of strength, stiffness and ductility, diminishing the wall energy dissipation capacity which is one of the main resources for earthquake resistance when the structure is designed to perform in the nonlinear (inelastic) range. This type of failure is often referred in the literature as to mixed flexure-shear failure.

1.5 Failure Modes of Squat Reinforced Concrete Walls

This work focuses in the behavior of squat shear walls with aspect ratio less than or equal to 1.5. For such walls, the mechanisms of shear resistance observed from extensive studies of reinforced concrete beams and slender walls are not entirely applicable due to the significant differences in relative dimensions, boundary conditions, and the shear load application mechanism (Paulay et al., 1982). Based on the studies of Barda (1977) and Paulay et al. (1982), among other researchers who studied the behavior of squat walls, it was found that besides the contribution of horizontal shear reinforcement, a large amount of the shear applied at the top of the wall is transmitted directly to the foundation by means of diagonal compression. This load transmission mechanism leads to the shear failure mechanisms mentioned before which will be briefly discussed in the following sections.

1.5.1 Diagonal Tension Failure

This failure mechanism is likely to occur when the wall has insufficient horizontal reinforcement and is characterized by one or more wide corner-to-corner crack as shown in Figure 1-4(a). This mechanism is initiated with the tension cracking of concrete in a principal state of stress; thereafter the steel yields significantly resulting in large crack widths and loss of the shear

friction resistance. The inclination of the crack is highly affected by wall geometry and the load distribution at the top of the wall. The presence of a stiff element such as a beam induces the formation of a corner-to-corner crack. The diagonal crack may also develop in a steeper angle (Figure 1-4b). This diagonal crack may result in failure if there is no way of redistributing the excess shear load to the rest of the wall top edge. A top slab or beam capable of redistributing the shear can suppress this premature failure after the crack formation. The damage associated with this failure mode is typically concentrated in one or few cracks which develop in both directions of loading (if loading is cycled) forming an X-pattern.

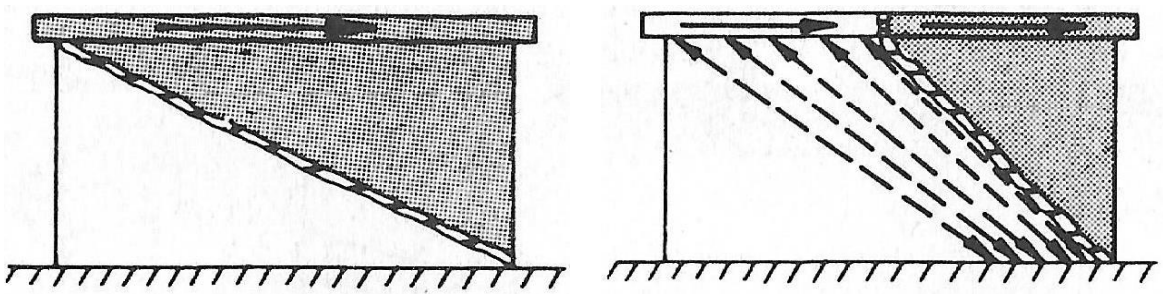

(a) (b)

Figure 1-4. Diagonal tension failure modes (Paulay et al., 1982): (a) corner-to corner crack; (b) steep-angle crack.

1.5.2 Diagonal Compression Failure

Diagonal compression failure could take place when a diagonal tension failure is prevented through an adequate horizontal reinforcement and large shear stresses are induced. The characteristic widespread crack pattern of this failure mode is shown in Figure 1-5a. Such mechanism is produced when stresses in diagonal compression struts become large enough as to exceed the concrete crushing strength. During cyclic loading interconnecting diagonal shear cracks develop in the two opposite directions and progressively degrade the concrete strength, which leads to concrete crushing at considerably lower shear load levels (Paulay et al., 1982). It has been observed (Figure 1-5b) that the crushing frequently extends through the length of the wall within few cycles of inelastic response (Paulay and Priestley, 1992). Walls with boundary elements are more prone to diagonal compression failure than walls with rectangular sections,

since they can produce higher flexural strength, thus increasing the shear demand on the web (Gulec and Whittaker, 2009).

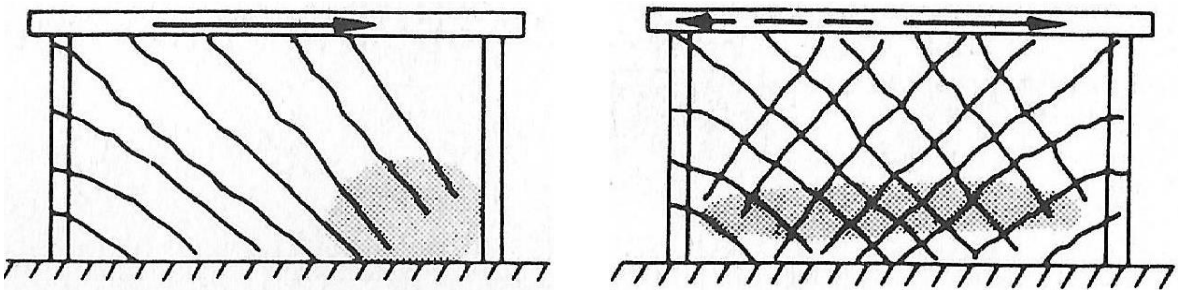

(a) (b)

Figure 1-5. Diagonal compression failure modes (Paulay et al., 1982): (a) crushing under monotonic loading; (b) crushing under cyclic loading.

This failure mode is more brittle than the diagonal tension because it is associated with concrete compressive crushing rather than tension yielding of steel. Thus, limiting the maximum shear stresses in the wall is enforced in design practice in order to avoid the diagonal compression failure.

1.5.3 Sliding Shear Failure

Sliding shear failure is characterized by concrete crushing and bar buckling over a narrow band along the base of the wall as shown in Figure 1-6. Even when both, diagonal tension and diagonal compression failures are suppressed, a sliding shear failure may be expected. Generally, prior to a sliding shear failure on squat walls, flexural and/or shear cracking of the wall have taken place. The development of this mechanism begins with the flexural steel yielding and cracking of concrete in one direction; then when loaded in the opposite direction both flexural cracks at the base intersect. With further cycling, and high residual strains in vertical reinforcement, the aggregate interlock (shear friction) resistance near or at the base decays progressively until the concrete crushes. Eventually, the shear transfer along the base will rely primarily in the dowel action of the vertical bars. This failure mode results in a significant loss of strength and stiffness as well as pronounced pinching in the hysteretic behavior. Squat walls typically carry low axial load levels which allow for easier crack opening and reduce the shear

friction resistance, making them more vulnerable to sliding shear failures than slender (high rise) walls which usually carry higher levels of axial load.

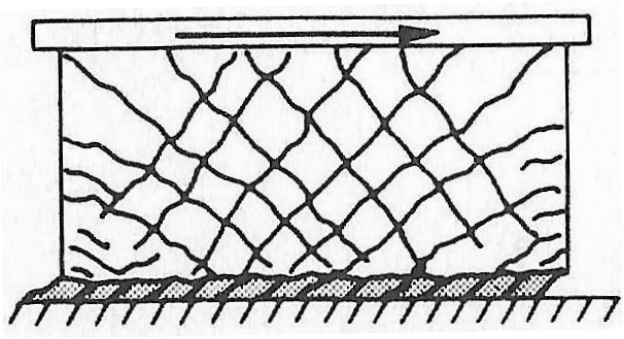

Figure 1-6. Sliding shear failure mode (Paulay et al., 1982).

1.5.4 Flexural Failure

Flexural failures are not commonly observed in squat RC shear walls, especially in those with very low aspect ratios (i.e. equal or less than one). While flexural failures are not common in walls of aspect ratios lower than 1.0, they can occur in such walls depending on the reinforcement configuration and may be observed in combination with any of the shear failures presented above. As suggested in FEMA 306 (ATC, 1998) ductile flexural failure typically occurs in well designed and relatively slender walls (with aspect ratios higher than 3.0) where shear failures are precluded by providing enough shear strength. Flexural failure in early stage begins with horizontal (flexural) cracking of the concrete in the extreme tension fibers near the base and propagating towards the neutral axis, followed by yielding of the flexural (vertical) reinforcement and spalling of the concrete cover in compression zones concentrated in the plastic hinge region. During cyclic loading, opposing flexural cracks join each other resulting in horizontal cracks through the length of the wall. Minor shear (inclined) cracking is often observed as the top displacement amplitude increases, which merges with the flexural cracks producing a crack pattern similar to the one as shown in Figure 1-7. In ultimate stages, bar buckling and crushing of the concrete in the boundary zone or tensile fracture of the flexural reinforcement may be observed.

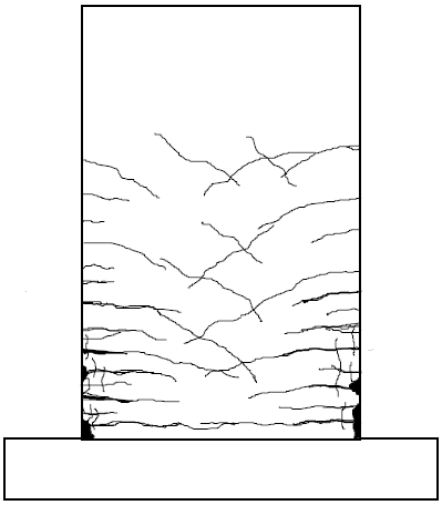

Figure 1-7. Typical flexural cracking pattern at a moderate stage of damage (ATC, 1998).

1.6 Review of Experimental Studies

In the past, the performance of squat walls has been compared to that of deep beams but their behavior is considerably different in terms of the load application and load resisting mechanism through arching action. Therefore, research findings from deep beam testing are not directly applicable to shear walls. Considerable experimental research on squat RC shear walls have been performed worldwide since 1950s yielding significant amount of experimental data. Most of these tests have been carried out at the component level, as isolated shear walls with a cantilever setup, where the load is applied to the wall panel through a rigid element at the top of the wall simulating a slab or beam of a structure and transferred through the wall panel to a stiff concrete foundation beam anchored to a strong floor. Other studies have tested specimens with fully restrained rotation at the top of the wall. These conditions may be representative of coupling beams and wall-piers where rotation is restricted at both ends instead of a cantilever shear wall within a structure, therefore they are not included in this study. In earlier times, most of the tests were conducted using monotonically increasing lateral load and using small scale specimens. Due to the size limitations, several of these small scaled specimens were constructed using cementitious mixes without coarse aggregates. Concrete containing a well distributed aggregate matrix, including coarse aggregates can behave differently to a mortar-like mix without coarse aggregates under the action of stresses. Therefore, these small scale specimens may not be representative of the actual construction practices and are not included in the present study.

Eventually, quasi-static cyclic loading and larger scale specimens were commonly used. Also, quasi-static hybrid-simulated earthquake loading and dynamic earthquake loading tests have been carried out in more recent research. The main characteristics of the specimens are the type of cross section (rectangular or flanged/barbell), aspect ratio (height to length ratio), reinforcement quantities, concrete and steel strength and presence of coexisting axial load. A summary of each experimental program included in the database have been considered within this section.

Barda (1972)

A total of eight walls with heavily reinforced flanges were tested without axial loading. All walls had the same cross sectional dimensions: 190 cm length, 10 cm thick web and flanges and 60 cm wide flanges. All walls were over-designed for flexure in a way that shear failure modes were expected. Two of the walls were tested under monotonic loading while other six were subject to reversed cyclic loading. Shear span-to-length ratios ranged between 0.25 and 1.0. Barda (1972) reported that load reversals produced around 10% peak shear strength reduction when compared to a companion specimen loaded monotonically. This study also concluded that both the horizontal and the vertical steel were effective providing shear strength and the proportion varies with aspect ratio. It was reported that horizontal reinforcement did not contribute to shear strength for walls with aspect ratios of 0.25 and 0.5 while vertical reinforcement was effective providing shear strength for those walls. Horizontal reinforcement improved wall behavior by inducing the formation of more distributed crack pattern and reducing crack widths on specimens with aspect ratios of 0.25 and 0.5. Effectiveness of vertical reinforcement in lateral strength decreased for the wall specimen with aspect ratio of 1.0. Therefore, recommendations were given on minimum reinforcement quantities in vertical as well as in horizontal direction. Decreasing wall aspect ratio (or shear span-to-length ratio) produced higher shear strengths. Well confined boundary elements helped in maintaining a gradual decrease in post-peak residual strength instead of sudden failure. Barda's design recommendations with slight modifications are still used on the design provisions for squat walls with flanged or barbell cross sections on the ASCE 43-05 standard.

Alexander et al. (1973)

Alexander's group tested a series of five walls at McMaster University at Ontario, Canada. The wall specimens had rectangular cross section, thickness of 10 cm, height of 137 cm and aspect ratios ranging between 0.5 and 1.5. Three of the walls had axial compressive load which ranged from 4.6% to 9.3% of the gross axial strength. Four of the panels included additional reinforcement at the foundation beam to panel interface (starter bars) which was reported to dramatically change the failure mechanisms and the force-displacement characteristics. The tests also aimed to evaluate the effects of axial load and wall aspect ratio. They found that axial loads increase the lateral load carrying capacity and improves stiffness degradation but reduces panel ductility. Also, higher panel aspect ratios produced lower maximum shear stresses.

Hirosawa (1975)

Hirosawa described a compilation of past experimental studies of RC shear walls under combined axial, shear and flexural loading carried out in Japan. Hirosawa's database included walls with rectangular, flanged and barbell cross sections. Experimental setup and main specimen properties along with experimental results have been listed on Hirosawa's report.

Cardenas et al. (1980)

Seven walls with rectangular cross-sections and aspect ratio of 1.0 (M/Vl_w =1.08) and without axial load were tested. Six of the walls were loaded monotonically and only one was subject to cyclic load. The main objective of this experimental program was to investigate the contribution of vertical and horizontal reinforcement on the shear strength. It was reported that both vertical and horizontal reinforcement contributed to the shear strength and effectively restrained crack widths of squat walls with aspect ratio of 1.0 under lateral loading. However, variation of effectiveness of vertical and horizontal reinforcement with aspect ratio was not investigated. It was also reported that the cyclically loaded specimen yielded lower shear strength than an identical specimen loaded monotonically.

Endo (1980)

Twenty wall specimens with barbell cross section were tested in Japan under this experimental program. Three specimens were tested under monotonic lateral load while reversed cyclic

loading was applied to the others. Main parameters were: aspect ratio of 0.78 and 1.22 (M/Vl_w of 0.83 and 1.28), wall thickness ranging from 5 cm to 10 cm, boundary element reinforcement ratio varying from 0.81% to 2.44%, wall web reinforcement ratio ranging from 0.23% to 0.71% and variations in boundary element confinement. Coexisting axial loads were applied to all walls which resulted in an axial load ratio ranging from 4.0% to 9.7%. One of the main findings from these tests was that the ductility of walls tested monotonically is different from the walls tested cyclically. By comparison of companion specimens tested under reversed-cyclic and monotonic loading, it was observed that monotonically loaded specimens can reach moderately higher strength and considerably higher drifts levels before failure. In concurrence the findings of other researchers, as the shear span-to-length ratio increases, the strength decreases but the displacement capacity (drift ratio) increases. The longitudinal boundary element reinforcement contributed significantly to the shear strength of the walls. Also, their tests reveal that the hoop reinforcement ratio of the boundary elements does not contribute significantly to the shear strength, but the higher confinement allows the walls to sustain the loads to higher drift ratios after peak strength as well as to minimize post-peak strength degradation.

Hernández (1980)

A total of twenty-two small scaled wall specimens including rectangular, flanged and barbell cross sections were tested in Mexico. All specimens had a coexisting axial load corresponding to 7% of $A_g f'_c$. While the scale of the specimens in this experimental program was very small (thickness of 2.5 cm), some important findings on general behavior were noted. Cyclic load reversals resulted in an average of 15% strength reduction when compared to similar monotonically loaded specimens. Lower aspect ratios resulted in increased shear strength, but reduced displacement capacities. Shear critical walls resulted in poor hysteretic behavior and progressive deterioration of strength under reversed cyclic loading.

Synge (1980)

Synge's group worked under the supervision of Dr. Thomas Paulay and Dr. Nigel Priestley at the University of Catenbury, New Zealand. Four walls of 300 cm long, 150 cm high and 10 cm thick were tested under reversed cyclic loading. Two of the specimens had rectangular cross section and other two had flanges. One wall of each cross section type included diagonal reinforcement

which was found to reduce sliding shear and improve hysteretic behavior. Synge's group reviewed failure mechanisms of squat walls with particular attention on sliding shear, as it was deemed that all squat walls with zero or very low axial load levels are prone to this failure mode.

Saatcioglu (1985-1994)

Dr. Murat Saatcioglu directed the work of Wiradinata (1985), Pilette (1987), Wasiewicz (1988) and Mohamaddi-Doostdar (1994) at the University of Toronto and the University of Ottawa, Canada. For a series of walls tested without axial load (wall 1 to wall 8), the concrete compressive strength ranged from 22 to 45 MPa, the aspect ratio varied from 0.25 to 1.0 (M/Vl_w between 0.33 and 1.09). Vertical reinforcement ratios ranged from 0.7 to 1.15, while horizontal reinforcement ratios ranged from 0.21 to 1.15. All walls had rectangular cross sections measuring 10 cm x 200 cm, except Wall 8 which length was 150 cm. Wasiewicz's group tested two specimens including additional reinforcement at the foundation to wall interface, intended to control sliding shear. These specimens with an additional interface reinforcement showed significantly different behavior to similar companion specimens tested by Wiradinata (1985). Their main findings, as described on their experimental program, have been summarized as follows:

- Wall aspect ratio is a key factor in wall strength and behavior.
- While all wall specimens showed sliding shear damage (with the exception of walls with additional joint reinforcement), walls with aspect ratios below 0.5 are more prone to sliding shear failure.
- Specially detailed additional reinforcement at construction joint effectively suppressed sliding shear failure.
- Walls with lower aspect ratios develop higher shear strength.
- Walls with aspect ratios of 0.5 and below showed predominant shear behavior.
- Walls with aspect ratios between 0.75 and 1.0 showed equally important deformation components for shear and flexure.

Chiba et al. (1985)

A series of 20 shear wall specimens without openings and 13 specimens with web openings were tested in Japan. The main parameters of the study were the reinforcement ratio of the wall

(ranging from 0 to 2.76%), the shear span-to-length ratio (M/Vl_w ranging from 0.35 to 0.70), the axial load ratio (ranging from 0 to 12.4%), and the presence and arrangement of openings. All wall specimens were tested under reversed cyclic loading and had thickness of 8 cm, boundary elements measuring 30 cm x 30 cm and total wall length of 230 cm. Gulec and Whittaker (2009) reported the results of these and several other wall experiments collected from Japanese literature which are part of a Japanese research program called "Load-Deflection Characteristics of Nuclear Reactor Building Structures". Experimental results for a total of 29 wall specimens without openings were collected from this program which are included in the database under the following researcher names: Chiba, Yagishita, Fukuzawa, Hatori and Taga. General findings were well in agreement with the reported tendencies from other researchers as the shear strength increased with increasing axial loads, increasing web reinforcement and decreasing shear span-to-length ratio (or conversely aspect ratio). It was also found that the specimens with higher web reinforcement ratios, which had closer bar spacing, showed more uniform and closely spaced diagonal cracks than those with lower reinforcement ratios. As reported by the authors, contribution of web reinforcement in shear strength was observed even on reinforcement ratios higher than 1.2% which was considered as maximum effective reinforcement in the Architectural Institute of Japan standards.

Hwang and Sheu (1988)

An experimental program on low-rise shear walls was conducted by M. S. Sheu at the National Cheng-Kung University at Taiwan, China. Gulec and Whittaker (2009) collected and reported the results of twenty-seven walls with rectangular cross section and seventeen walls with barbell cross section tested by Sheu. As reported by Gulec, shear span-to-length ratio (M/Vl_w) ranged between 0.65 and 1.90, four walls with rectangular cross sections were tested with a coexisting axial force of 0.12 $A_g f'_c$ and one wall with barbell cross-section was tested with a coexisting axial force of 0.063 $A_g f'_c$. Nineteen walls were tested under monotonic lateral load, 3 walls were subjected to repeated (one direction) loading, and 22 walls were tested under reversed cyclic loading. Analyzing the test results, it can be noted that: as aspect ratio decreases higher strengths are attained, the presence of axial loads produced a significant increment in shear strength, and both vertical and horizontal web reinforcement had a significant contribution in shear strength for the range of aspect ratios tested.

Saito et al. (1989)

Nine flanged specimens were tested with f'_c ranging from 23.5 MPa to 41.2 MPa, f_y of 369 MPa, equal horizontal and vertical reinforcement ratios ranging from 0.90% to 1.69%, shear span-to-length ratio M/Vl_w of 0.5 and 1.0, Axial load ratios $P/ A_g f'_c$ ranging from 2.38% to 8.33%. The main objective of the study was to evaluate the applicability of design practices used for walls with normal strength concrete of that time (around 24 MPa) to walls with higher strength (around 35 MPa). The effects of axial loads, reinforcement ratios and aspect ratio of the wall were similar to the observed tendencies from other researchers.

Sato et al. (1989)

Twenty-two flanged walls were tested. These walls have the following properties: f'_c ranging from 24.5 to 44.6 MPa, f_y from 296 to 528 MPa, equal horizontal and vertical reinforcement ratios ranging from 0.45% to 1.60%, shear span-to-length ratio ranging from 0.6 to 1.2, and axial load ratios ranging from 4.5% to 8.2%. The main purpose of these tests was to use different steel grades and reinforcement ratios, but varying only the product of the two (ρf_y) as the web reinforcement parameter. The study concluded that the load-deflection relationship and failure mechanisms of such squat RC walls are directly related to the product of reinforcement ratio and reinforcement yield strength regardless of the grade of steel. As of that time, Japan standards restricted the shear reinforcement yield strength to a maximum of 300 MPa. The authors recommended to allow the use of higher yield strength up to 500 MPa for the shear reinforcement in the design practice, as the walls behavior and performance resulted to be similar to those designed using lower yield strength.

Maier (1991)

Seven walls with flanged cross section and three walls with rectangular cross section were tested. All wall specimens had aspect ratio h_w/l_w = 1.02 (M/Vl_w = 1.12), 120 cm height and 10 cm web thickness. One flanged wall (S8) had an opening in the compression zone at the bottom of the wall. All walls were tested under combined constant axial load and increasing shear loading. Only two flanged specimens (S5 and S7) were tested under reversed cyclic loading. Concrete compressive strength ranged from 29.2 to 37.3 MPa while axial loads ranged from 6.8% to 27.9%. The study revealed that vertical reinforcement was effective in providing shear strength

while horizontal reinforcement had marginal contribution to lateral strength on the tested walls. Higher axial loads and higher vertical reinforcement ratios produced higher strength but decreased ductility. Horizontal reinforcement contributed to the improvement of wall deformation capacity. Cyclically loaded specimens with low axial load did not show significant change in behavior when compared to their monotonic companion specimens. However, decreased strength was observed on cyclically loaded walls with higher axial loads.

Rothe (1992)

Gulec and Whittaker (2009) collected and reported the test results of shear walls tested by Rothe. As reported by Gulec and Whittaker, six walls with barbell and five walls with rectangular cross-sections were tested. All walls had shear span-to-length ratio (M/Vl_w) of 1.5. Three walls were subject to constant axial forces ranging from 0.065 $A_g f'_c$ to 0.096 $A_g f'_c$. Five walls were tested under reversed cyclic loading, one wall was loaded monotonically, and 5 walls were tested under dynamic earthquake simulated loads.

Seki et al. (1995)

Six flanged walls were tested by pseudo-dynamic (hybrid simulated) loading method. Their objectives were to characterize the lateral force-displacement behavior and equivalent viscous damping of the walls, and to verify the feasibility of hybrid simulation testing for squat shear walls. Their test specimens had shear span-to-length ratios (M/Vl_w) of 0.6, 0.8 and 1.0. All specimens had uniform reinforcement ratios of 1.2% (vertical and horizontal) and thickness of 75 mm in both, web and flanges. All walls had similar compressive strength ranging from 28.9 to 31.6 MPa at the age of testing. Steel yield stress ranged from 349 to 381 MPa. Axial load ratio was varied from 0% to 3.5%. They found that the shear displacement component was predominant in all the tested specimens ranging from 90% to 60%. The shear displacement component percentage decreased as the shear span-to-length ratio increased. Lateral strength tended to increase with application of axial loads, as well as with decreasing shear span-to-length ratio. Equivalent viscous damping ratio generally fell between 2% and 6%, but was highly scattered for small displacement demands and for near-failure displacements. Equivalent viscous damping showed a tendency to increase at high displacement demands. The authors concluded

that the pseudo-dynamic loading was a feasible method to simulate seismic response of squat shearwall structures.

CNSI/NUPEC (1996)

In 1991, the Japanese Nuclear Power Engineering Corporation (NUPEC) conducted tests in two flanged wall specimens (U-1 and U-2) under dynamic excitation in one direction. These test results were published on 1996 by the OECD – NEA Committee on the Safety of Nuclear Installations (CSNI). Both wall models were identical and were subjected to the same dynamic input records to verify the reproducibility of the tests. The response of both walls was reported to be very similar in terms of force, deformation, crack pattern, and failure mode. Wall specimens were 202 cm high, 310 cm long, with 10 cm x 298 cm flanges and web thickness of 7.5 cm. Web reinforcement ratio was set to1.2% and concrete strength 28.6 MPa. Axial load was applied by additional mass attached to the top slab with a resultant axial load ratio of 3.9% of $f'_c A_g$. The study aimed to provide data on the seismic response characteristics of squat RC shear walls typically found in nuclear power plants under loading levels that ranged from the essentially elastic state to the elasto-plastic ultimate state. Their data were used to develop and calibrate analytical computer models by allowing to be utilized by several organizations and hosting workshops under a program named "Seismic Shear Wall International Standard Problem" (SSWISP).

Kabeyasawa and Hiraishi (1998)

A total of twenty-one high-strength reinforced concrete shear walls specimens were tested under reversed cyclic loading as part of a national research project in Japan. Concrete with compressive strength ranging from 54.6 MPa to 137.5 MPa, and reinforcing steel with yield strength ranging 761 MPa to 1,395 MPa were used. All specimens had barbell cross sections with 8 cm web panel thickness, 20 cm x 20 cm confined boundary elements and total wall length of 170 cm. Web reinforcement ratios varied from 0.20% to 1.45%, and axial load ratios ranging from approximately 10% to 14% of $A_g f'_c$ were applied to the wall specimens. The purpose of the program was to investigate the feasibility of the design and construction of reinforced concrete shearwall structures using ultra-high strength materials.

Salonikios et al. (1999)

The research program involved testing of eleven rectangular cross section walls with aspect ratios of 1.0 and 1.5 (M/Vl_w = 1.1 and 1.6) under reversed cyclic loading. Two specimens were tested with axial load corresponding to 7% $A_g f'_c$ while the other nine had zero axial load. All wall specimens had adequately confined reinforcement at the boundary element zones. Four of the specimens (two of each aspect ratio) included diagonal reinforcement. Pilot specimen MSW2 was reported to show out-of-plane buckling behavior due to the lack of lateral restrain in the test setup. Specimen MSW1 is considered flexure controlled after cross section analysis. The shear deformation components (sliding + web shear) contributed between 20% to 80% to the total wall deformation and usually increased with the ductility level. Sliding shear deformations increased substantially for displacement ductilities above 2.5. For most walls, sliding shear deformations were significantly higher than the diagonal (web distortion) shear deformations. Walls with diagonal reinforcement showed improved hysteretic behavior with higher energy dissipation and reduced sliding at the base. Compressive axial load had a favorable effect in reducing sliding shear. Walls with lower aspect ratio showed significantly higher sliding and strength degradation. Axially loaded members as well as those with increased reinforcement ratios showed less strength degradation.

XiangDong (1999)

The experimental program at the University of Houston, Texas included the testing of thirteen framed wall specimens and a frame specimen without wall panel. Specimens named FSW-1, FSW-2 and FSW-3 had different shortcomings and served as pilot specimens to test and improve the experimental setup. Wall specimen FSW-11 was also reported to fail prematurely and therefore is not included in the database on this research. All the specimens had the same dimensions and frame element longitudinal reinforcement: frame elements were 152.4 mm x 152.4 mm, wall thickness 76.2 mm and 914.4 x 914.4 mm of clear wall panel. Concrete target compressive strength was 55 MPa. However, it varied from 48.3 MPa to 57.1 MPa. Main parameters were the axial load ratio (varying from 1.3% to 9.3%), web reinforcement ratio (varying from 0.23% to 1.11%) and hoop spacing on the frame members. The authors reported that when the axial load ratio increased from about 1.4% to 4.5%, the lateral shear strength increased significantly by 40%. However, when axial load ratio increases from about 4.5% to

8.5%, the strength increased by only 13%. In contrast, varying the steel ratio of the wall panel from 0.25% to 0.5%, did not change the lateral strength appreciably but when panel reinforcement ratio was increased from 0.5% to 1.0%, the shear strength was improved by an average of 25%. As the panel reinforcement ratio increased, the spacing and width of cracks decreased and were more evenly distributed in the panel resulting in better ductility and hysteretic behavior. When minimum panel reinforcement was used, the diagonal tension failure mode - characterized by one or few substantially wide diagonal crack in the panel - was predominant. Thus, the authors suggested that a minimum reinforcement ratio of 0.5% would be more appropriate. Increasing boundary element confinement (hoops) helped to prevent crushing of concrete and longitudinal bar buckling at the boundary elements, and reduced pinching effect. Shear displacement component ranged from 68% to 95% of the total displacement.

Palermo and Vecchio (2002)

Two identical flanged wall specimens (DP1 and DP2) were tested under reversed cyclic loading. Axial load of 5.45% of $f'_c A_g$ was applied to specimen DP1 while specimen DP2 had no axial load. These wall specimens were similar to NUPEC's dynamic loaded specimens. Wall specimens were 202 cm high, 307.5 cm long, with 9.5 cm x 304.5 cm flanges and web thickness of 7.5 cm. Web reinforcement ratio was set to 0.73% and 0.79% in the horizontal and vertical directions, respectively. Concrete compressive strength was 21.7 MPa and 18.8 MPa for specimens DP1 and DP2, respectively. Test results show that axial load has a significant effect on wall behavior. In their case, a small amount of axial load (5.45% of $f'_c A_g$) significantly improved shear strength. In contrast to typically observed behavior on other experiments, the wall with axial load showed improved ductility and energy dissipation characteristics. The authors attributed this non-typical ductility behavior to the fact that both walls showed different failure modes. The wall without axial load showed sliding shear plane formed at the top of the wall web (possibly due to weaker concrete near the top of the wall section) while the wall with axial load showed web crushing failure mechanism.

Matsui et al. (2004)

Two identical specimens with barbell cross section were tested at the University of Tokyo under uni-directional dynamic shake table loading. Both specimens had a wall clear height of 180 cm,

web thickness of 8 cm, well confined boundary elements measuring 20 cm x 20 cm, web reinforcement ratios of 0.40%, and axial load ratios of nearly 6.5% of $A_g f'_c$. Only the height from the base to the top weight center of mass was changed on the two specimens which resulted in shear span-to-length ratio (M/Vl_w) of 1.38 and 1.76 for Wall-A and Wall-B, respectively. The two specimens were subjected to equal series of scaled earthquake motion records. The failure modes of both walls were different which shows the influence of the shear span-to-length ratio on the response of these walls. Wall A, with lower shear span-to-length ratio, resulted in higher shear strength and significantly higher shear deformation component. Wall B (M/Vl_w = 1.76) showed equally important flexural and shear deformation components, while for Wall A shear deformation was about twice the flexural deformation.

Dabbagh (2005)

A series of six squat walls with barbell cross section and high strength concrete were tested under reversed cyclic loading at the University of New South Wales, Sydney, Australia. All specimens had the same dimensions with thickness of 7.5 cm, length of 100 cm and aspect ratio of 1.0 (M/Vl_w = 1.10). Five specimens were tested with axial load ratio of nearly 10% of $A_g f'_c$ and one had no axial load. Boundary element reinforcement ratio was set to 6.43% while web reinforcement ratios varied from 0.45% to 1.34%. Concrete compressive strength ranged from 83 MPa to 96 MPa, while reinforcement yield strength varied from 498 MPa to 536 MPa. They observed that, at this aspect ratio, an increase only in the vertical reinforcement ratio led to an increase in peak shear strength but this effect was not as significant as in normal strength concrete walls. Horizontal reinforcement ratio did not have a significant effect on peak strength but caused an increase in wall's displacement capacity. Dabbagh's group also found that the axial load significantly increased peak shear strength, but at the same time reduced ductility.

Greifenhagen and Lestuzzi (2005)

Results of four lightly reinforced, reversed cyclic loading, rectangular cross section specimens were reported. Axial load ranged from 2.2% to 9.4% of $A_g f'_c$ and aspect ratio of 0.57 (M/Vl_w = 0.69 to 0.76). Vertical and horizontal reinforcement ratios were set to 0.003. Concrete strength ranged from 20 MPa to 51 MPa. Specimens M1 and M2 were excluded from database since the actuator reached the maximum capacity of 200 kN during the test, and the axial load level had to

be reduced in order to achieve strength degradation of the specimen at higher displacement levels. Specimen M3 was deemed to be controlled by flexure after cross section analysis. Shear deformation components (sliding + shear distortion) contributed between 20% to 47% (average 30%) to the total deformation, depending on the ductility level. The portion of total deflection due to flexure decreased as the lateral displacement increased, whereas sliding portions generally increased as ductility and drift increased. Higher axial loads prevented the sliding shear failure mode and thus, diagonal tension failure was induced because the walls had low reinforcement ratios. In the cases with lower axial loads, where sliding shear failure mode predominated, damage was concentrated at the bottom area near the foundation and the horizontal reinforcement became ineffective. Higher axial load ratios produced less drift capacity. By comparing their test results with other tests from literature, the authors suggested that the drift capacity of squat walls depends mostly on axial force ratio, vertical reinforcement arrangement, and degree of restraining at the top of the wall. They also found that cantilever shear walls without rotation restraints at the top are less susceptible to brittle shear failures than those with fixed top end.

Akita et al. (2006)

Two wall specimens with barbell cross section were tested under coexisting axial and shear loading. The two specimens were nominally identical to the specimens on the dynamic tests by Matsui et al. (2004), but these were subjected to quasi-static reversed cyclic loading. The main objective of their study was to compare the behavior of RC shear walls under quasi-static cyclic loading and dynamic loading. In general, the lateral load-displacement characteristics and failure modes observed on the quasi-static tests were similar to those of the dynamic tests.

Sanada and Kabeyasawa (2006)

Two companion walls with barbell cross-section were tested under reversed cyclic loading at the University of Tokyo. Constant axial load corresponding to nearly 0.10 of $A_g f'_c$ was applied to both walls during testing. Both walls had web reinforcement of 0.25% on each direction, web thickness of 8 cm, 140 cm clear height, 25 cm x 25 cm boundary elements and aspect ratio h_w/l_w of 0.68. One of the specimens (Type-N) was built with normal base consisting of a stiff continuous foundation beam, while the other (Type-S) had a special base split into four pieces.

Each piece of the base was individually anchored and equipped with a biaxial load cell to measure the local shear and axial forces. The hysteretic behavior, cracking pattern and failure mode were similar for both walls, and therefore, the split base specimen reproduced the behavior of the normal specimen. The authors found that about 70% of the total lateral force was carried around the boundary column on the compressive side at the shear failure damage state. At lower damage state (i.e. onset of shear cracking) the compression boundary column region carried around 40% of the total lateral force. The shear force transfer at the tensile boundary element zone was negligible at all damage states, which was to be expected because the cracks on the tensile side are open and shear friction forces cannot effectively develop. These observations suggested that forces were mainly transferred in a diagonal compression strut mechanism as the wall experienced higher demands.

Kuang and Ho (2008)

Kuang and Ho's group tested 8 walls with aspect ratios of 1.0 and 1.5, rectangular cross section of 100 mm x 1200 mm. The intent of their study was to evaluate the behavior of non-seismically detailed squat walls and the effectiveness of improved confinement detailing to enhance ductility of such walls for moderate earthquake hazard. Concrete strength ranged from 30.4 MPa to 37.7 MPa and steel yield strength was 520 MPa. Axial load ratios ranged from 10% to 30% of $A_g f'_c$. All specimens exhibited a flexural failure mode. The authors observed that providing confinement at the wall boundary zones resulted in significantly higher ductility and improved energy dissipation. This may be attributed to the added concrete confinement in the compression zone and the prevention of outer bars buckling as the bars lateral support becomes more closely spaced. In the same manner, addition of crossties throughout the cross-section of the wall panel provided confining stresses to the entire section, and thus, it enhanced walls ductility, energy dissipation as well as shear strength. Concentrating the longitudinal reinforcement at the boundary zones resulted in increased flexural strength but marginal improvement in ductility and energy dissipation. The increased flexural strength induced the formation of more diagonal shear cracks on the wall panel.

Xiang (2009)

Five walls with aspect ratio of 1.0 ($M/V/l_w$ = 1.125) and three walls with aspect ratio of 1.5 (M/Vl_w = 1.625) were tested under reversed cyclic loading at Nanyang Technological University in Singapore. Six of the walls were subjected to axial loads corresponding to 5% of $f'_c A_g$ while the other two were tested without axial load. All walls had the same cross section with a 200 cm length, 12 cm web thickness and boundary elements measuring 15 cm x 30 cm. The reinforcement arrangement was the same for all specimens. Web reinforcement ratio of 0.5% and boundary element reinforcement ratio of 1.4% were used. Most of the wall specimens were cast monolithically with the top beam and bottom foundation except for three wall spaecimens that included a construction joint at the base. All wall specimens had lower yield strength longitudinal reinforcement at the boundary elements and showed flexure-controlled failure mode. Higher confinement of the boundary elements produced higher ductility, higher energy dissipation, and less strength degradation. Walls with axial load ratio of 5% showed higher strength and higher energy dissipation and less pinching behavior due to the reduction of sliding. The presence of a construction joint at the wall base resulted in higher sliding displacements. Stiffness characteristics did not appear to be affected by the boundary element confinement. The authors found that walls stiffness is mostly influenced by the outermost (boundary element) reinforcement, axial load and aspect ratio.

Terzioğlu (2011) – As reported by Gutiérrez (2012) and Opazo (2012)

Eleven squat wall specimens with rectangular cross section were tested under reversed cyclic loading at the University of Bogaziçi, Turkey. All cross sections measured 12 cm x 150 cm. Aspect ratios ranged from 0.33 to 1.0. Two of the wall specimens carried axial loads corresponding to 5.1% and 9.9% of $A_g f'_c$ while the rest were tested without axial loads. Web reinforcement ratios were either 0.34% or 0.67%. Boundary element reinforcement ratios varied from 0% to 9.75%. Concrete strength varied from 19.3 MPa to 35 MPa and steel yield strength varied from 437 MPa to 572 MPa. All specimens showed shear failure modes. Test results showed that increasing boundary element reinforcement ratio can significantly increase the shear strength of shear-dominated walls with aspect ratios as low as 0.5. The presence of axial loads produced higher shear strengths. The authors noted that wall specimens with lower aspect ratios reached higher strengths and had predominant shear deformation components, whereas the wall

with higher aspect ratio (1.0) showed equally important flexural and shear deformation components. The authors also noted that the wall specimens with lower web reinforcement ratios tend to fail in diagonal tension, while higher panel reinforcement ratio suppressed the diagonal tension mechanism leading to either diagonal compression or sliding failure mechanisms. Wall specimens with diagonal compression failures showed the most brittle behavior.

Altin et al. (2013)

Altin's group tested five shear-deficient walls with aspect ratio of 1.5 (M/Vl_w = 1.65) and 100 mm X 1000 mm rectangular cross section. The aim of their study was to investigate the effect of different shear strengthening configurations using carbon fiber reinforced polymer (CFRP). One reference specimen without CFRP reinforcement and other four specimens with CFRP strengthening were tested. Steel yield strength ranged from 325 MPa to 425 MPa and concrete strength was around 15.5 MPa. Walls had considerable concentrated longitudinal reinforcement at the edges with no confining hoops and sub-minimum reinforcement ratios of 0.15% and 0.18% in the horizontal and vertical directions, respectively. No axial loads were applied to the specimens. The reference specimen showed a diagonal tension shear failure mode with typical wide and concentrated cracks along both of the diagonals. This failure mode was to be expected due to the low panel reinforcement ratios and suppression of flexural failure by the boundary longitudinal reinforcement. The CFRP strengthened specimens attained considerably higher strength, ductility and energy dissipation.

Carrillo and Alcocer (2013)

This experimental program carried out in Mexico involved the testing of 39 isolated rectangular cross section walls. The walls were full scale (10 cm thick and 250 cm height) models of typical walls found in housing construction in Latin American countries. Four specimens had large web openings representative of windows and doors. The tests included specimens with monotonic loading, reversed cyclic, and dynamic loading. Aspect ratios were set to 0.44, 1.0 and 1.94. Twelve of the specimens were reinforced with welded wire mesh made of cold drawn wire having low tensile strain at fracture. On these specimens reinforced with wire mesh, the fracture of web reinforcement led to brittle failure modes at lower displacements compared to specimens

with similar amount of mild rebar reinforcement. Therefore, these wall tests were not considered in the database shown on Appendix A of this document. Three types of concrete were used, namely, normalweight, lightweight and self-consolidating. Concrete strength ranged from 16.0 MPa to 24.7 MPa with the exception of few very low strength specimens whose concrete strength was as low as 5.2 MPa. All specimens had confined boundary elements within the rectangular cross section and were over-designed in flexure to induce shear failure modes. Equal horizontal and vertical web reinforcement ratios ranging from 0% to 0.28% were used. Constant axial stress of 0.25 MPa was applied to all specimens, which in general corresponded to axial load ratios below $0.03f'_cA_g$. Lower strength on reversed cyclic tests was noted when comparing similar specimens tested under monotonic load from this program. The authors proposed a shear strength predictive equation for walls with the characteristics found in one to two story concrete housing based on calibration of the ACI 318 seismic provisions equation with their experimental results. The authors found that shear strength increases as the shear span-to-length ratio (M/Vl_w) decreases; concrete strength corresponds to the diagonal tension strength of the wall; and that web steel contributed to the shear strength, though it was not fully efficient. The authors observed that the efficiency factor for the web steel ranged from 78% to 86%, but noted that as the reinforcement ratios increased the efficiency factor decreased. The efficiency factor accounted for the fact that the distribution of strains in the steel is not uniform along the wall height and not all steel crossing the cracks reached yielding. Diagonal cracks usually grew wider at the central panel zone and tended to be minimal near the top beam and bottom foundation. Thus, authors deemed that yield potential is higher for the bars around the center of the panel.

Whyte and Stojadinovic (2013)

Two walls nominally identical to specimen SW3 (tested under cyclic loading at the University at Buffalo) were tested under quasi-static hybrid-simulated earthquake loading at the NEES facilities at Berkeley, California. Concrete compressive strength at day of testing was 35.5 MPa and 37.3 MPa for Wall 1 and Wall 2, respectively. Reinforcement yield stress was 464 MPa. Equal horizontal and vertical reinforcement ratios of 0.71% were used. Neither wall had axial loading. By comparison of global responses of the walls tested at Berkeley and the nominally identical wall tested at Buffalo, the authors observed that the responses were very similar, and deemed that the quasi-static hybrid-simulated test method was adequate to represent the global

behavior of squat shear walls and very stiff members under ground motion sequences. They also pointed out that the main advantage of quasi-static hybrid-simulation over traditional quasi-static cyclic and dynamic methods is that it enables incorporation of ground motion inputs within a large-scale test. Both tested walls initially experienced shear and flexural deformations. With increased displacements, the flexural cracks from each end of the wall joined to form a continuous crack along the wall-foundation joint which triggered a sliding shear failure mechanism.

Park et al. (2015)

Seven walls with rectangular cross section and one with barbell cross section were tested. High strength reinforcing steel with yield stress ranging from 477 MPa to 667 MPa was used. Wall aspect ratio was set to 1.0 (M/Vl_w =1.17), constant axial load ratio was set to 7%, and thickness was 200 mm for all the specimens. Concrete strength was varied from 46.1 MPa to 70.3 MPa. All walls were designed to fail in shear with the exception of one which was designed to yield in flexure. The intent of their research was to verify the adequacy of the current shear design provisions of ACI 349 for RC squat walls with high strength (Grade 550 MPa) reinforcement. The specimen with barbell cross section resulted in 18% higher strength and better ductility than the similar specimen with rectangular cross-section which could be attributed to the confinement provided by hoops of the boundary elements and the additional confinement that the boundary elements themselves provided to the compressive zones of the wall panels. The authors noted that the failure modes in comparable specimens with Grade 420 and Grade 550 horizontal reinforcement bars were identical but that the specimen with Grade 420 showed marginally larger strength. The authors attributed the lesser strength of the wall with higher grade horizontal reinforcement to the greater spacing of the high strength bars which allowed an increase in crack widths and thus, reduced the frictional force transfer along cracks. It is important to note that the steel grade was changed only in the horizontal direction, whereas other studies suggest that vertical reinforcement is often more influential to shear strength than the horizontal reinforcement in walls with low aspect ratio. The shear controlled specimens without boundary confinement failed due to sliding followed by web crushing whereas the ones with boundary confinement failed due to web crushing without significant sliding. Walls with confinement

hoops at wall boundary elements showed significantly higher strength and enhanced ductility by restraining the diagonal cracking propagation into the wall boundaries.

Luna et al. (2015)/NEES-UB

Twelve large scale squat walls with rectangular cross section were tested under reversed cyclic loading and without axial load at the University at Buffalo, New York. All wall specimens' cross section measured 20.3 cm x 305 cm. All wall specimens were reinforced with two curtains of No. 13 (12.7 mm nominal diameter) mild rebars. Yield stress between 434 MPa and 462 MPa and reinforcement ratios ranging from 0.33% to 1.5% were used. Two of the wall specimens included confined boundary zones with concentrated reinforcement. Aspect ratios varied from 0.33 to 0.94 and concrete strength varied from 24.1 MPa to 53.8 MPa. The experimental setup did not fully prevent the out-of-plane twisting of the walls which, as reported, led to notable differences on the measured peak shear strength between the first and third quadrant of the hysteresis curves. Their study also aimed to evaluate the initial stiffness of squat walls and revealed that experimental stiffnesses were substantially lower than those calculated using current US standards. The following conclusions were also drawn by the authors:

- Horizontal reinforcement was considered effective up to a certain threshold value where sufficient confinement to the diagonal compression struts is provided. Above the threshold value the effect of horizontal reinforcement on shear strength was minimal.
- All web reinforcement provided confinement to the compression struts, and therefore contributed to the shear strength. Walls failing in diagonal compression mode showed higher strength when web reinforcement was increased.
- Confined boundary elements helped to maintain strength at displacement levels beyond peak strength. Walls without confined boundary elements showed rapid strength degradation with further cycling after peak strength was attained.
- Walls with low aspect ratio were more prone to base sliding, especially after reaching peak strength. Pinching in the hysteresis loops was mainly attributed to sliding.

1.7 Organization of Dissertation

This dissertation includes eight chapters. Chapter 1 presented the motivation, scope, objectives, and methodology of the conducted research, as well as a discussion on RC squat walls behavior

and summaries of experimental programs from which data was obtained for the elaboration of this dissertation. Chapter 2 describes the assembled database using reported data from the considered experimental studies; including statistical distribution of several parameters within the database (detailed data is included on Appendix A). Chapter 3 presents the development of an empirical equation for the prediction of peak shear strength of RC squat walls with rectangular cross sections, developed from the database described in Chapter 2; and investigates the performance of other widely used equations available in the literature and US standards. In Chapter 4 empirical equations for the prediction of displacement capacities of RC squat walls with rectangular cross sections at diagonal cracking (or principal stiffness degradation of the global force-displacement response), at peak strength, and at ultimate state (at 20% strength drop) are proposed. The development of the proposed equations is based on the assembled database described in Chapter 2. Chapter 4 also investigates the performance of other equations available in the literature. Chapters 5 and 6 are similar to Chapters 3 and 4, but focused on walls with boundary elements (i.e. barbell and flanged cross sections). Chapter 7 presents and compares two analytical modeling approaches for RC squat walls using the *OpenSees* analytical platform. The first model is based on the *OpenSees Hysteretic Material*, while the second is based on the *Flexure-Shear Interaction Displacement-Based Beam-Column Element*, developed by Massone et al. (2006). Sample *OpenSees* input files are included on Appendix B and Appendix C. Chapter 8 summarizes the key findings and conclusions, and provides recommendations for future studies.

CHAPTER 2. SQUAT WALLS DATABASE

2.1 Introduction

A database was assembled from reported experimental data of shear-controlled squat reinforced concrete walls tests found in the literature. A total of 207 walls tested in different countries including Australia, Canada, China, Germany, Greece, Japan, Korea, Mexico, New Zealand, Switzerland, Turkey, and United States have been included for the database. Only walls with symmetric cross sectional shapes were considered for this database. From them, 70 specimens had rectangular cross section, whereas 137 specimens had enlarged boundary elements (Figure 2-1). The group of walls with boundary elements consisted of 56 wall specimens with flanges (simulating intersecting walls) and 81 wall specimens with boundary columns (barbell shaped cross section).

It is known that walls with boundary elements can generally achieve higher peak shear stresses than those similar walls with rectangular cross section. Figure 2-2 shows the peak shear strength normalized by the gross shear area of the cross section (A_{cv}), and the square root of concrete compressive strength. Walls with flanged and barbell cross sections can attain about the same range of normalized shear stresses which are considerably higher than the stresses attained in walls with rectangular cross sections. The mean values for normalized peak shear stresses are 0.56, 1.10 and 1.18 for those walls with rectangular, barbell and flanged cross sections, respectively. Therefore, our database designed for the development of the predictive equations has been subdivided in two categories as follows: (1) walls with rectangular cross section and (2) walls with enlarged boundary elements (flanged/barbell cross section). Appendix A presents the tabulated data of the main properties of the wall specimens included in the database.

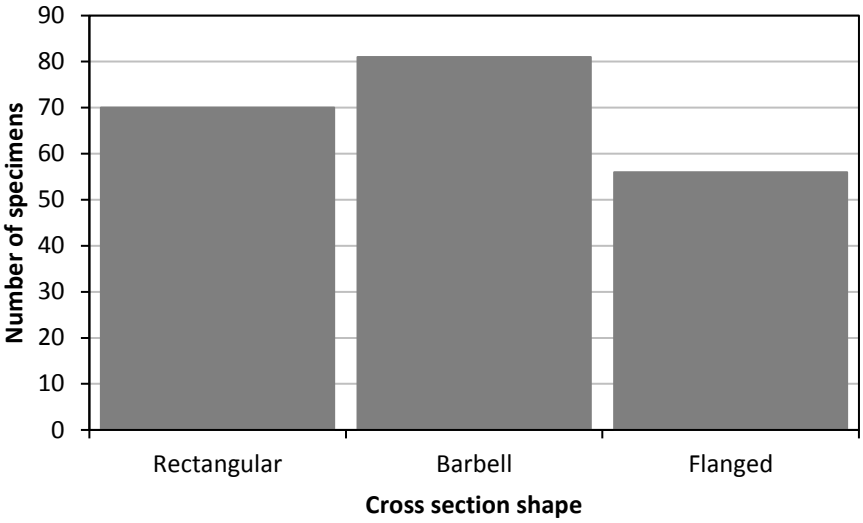

Figure 2-1. Histogram of cross section shape of specimens used in our assembled database.

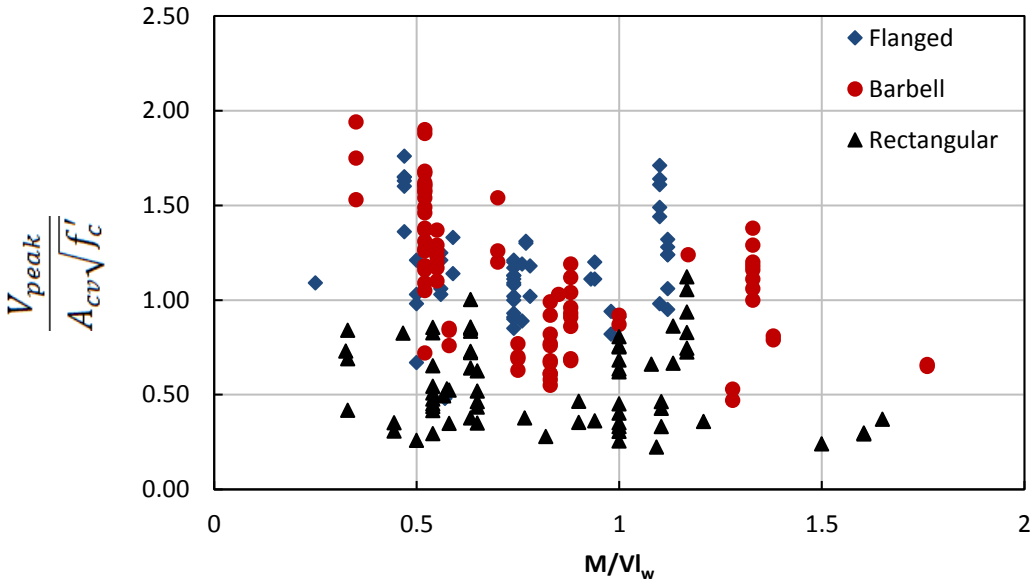

Figure 2-2. Variation of normalized maximum average shear stress with shear span-to-length ratio for different cross sectional shapes.

The assembled database considered only quasi-static cyclic, dynamic and hybrid-simulated dynamic loading experimental tests in order to minimize bias due to loading type in the shear strength and displacement capacity estimates (Figure 2-3). The loading types commonly used in experimental studies can be described as: *monotonic loading* - the application of a monotonically

increasing load in only one direction; *cyclic loading* - application of quasi-static lateral load reversals with increasing force or displacement (typically two to four cycles per load step are applied); *repeated loading* - similar to quasi-static cyclic loading but loaded only in one direction (no load reversals); *dynamic loading* - the use of "shake tables" which simulate earthquake loading by application of earthquake ground motion records at the foundation of the specimen; and *hybrid-simulated* that consists of the simulation of earthquake ground motion loading by application of a quasi-static lateral load (this method uses computational analysis to calculate the corresponding lateral load at each step of the simulated input ground motion). By evaluation of collected data, we have found that cyclic tests can yield lower shear strength than monotonically loaded similar specimens. Since the focus of this work is on earthquake loading, tests using monotonic or repeated loading schemes were excluded from the database as these can lead to higher strength and considerably larger drift capacities due to the lack of cyclic cumulative damage and/or the absence of cracking from loading in the opposite direction which may not be representative of earthquake loading.

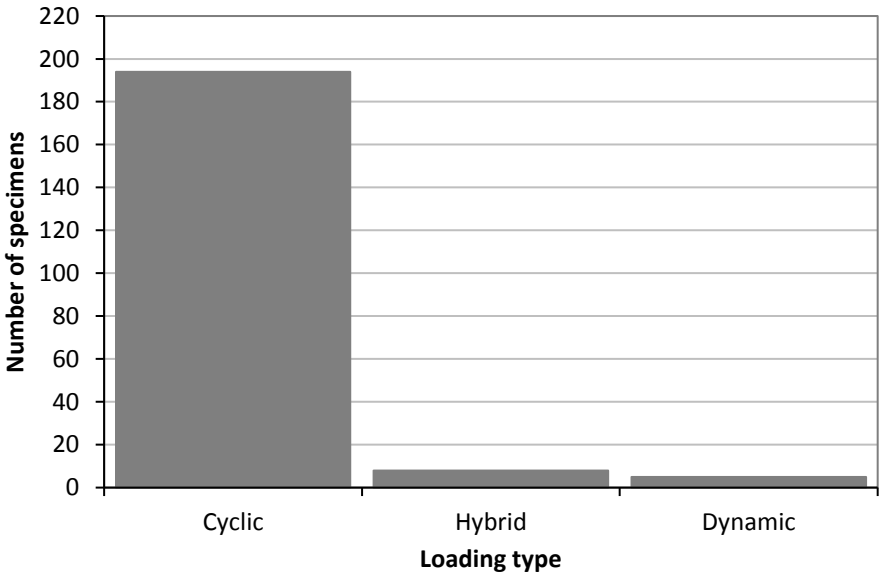

Figure 2-3. Histogram of loading type for the walls population included in the assembled database.

Only conventionally reinforced walls with symmetric horizontal and vertical reinforcement arrangements, no diagonal reinforcement, and no additional dowel reinforcement at foundation to wall interface have been considered, as commonly found in US design and construction

practice. Moderate to large scale tests, with minimum web thicknesses of 75 mm, were used here in order to reduce bias due to small scale and material properties. Also, only walls using conventional normalweight concrete were included in order to minimize the bias due to reduced strength and stiffness of lightweight concrete, or due to improved tensile stress-strain behavior of fiber-modified concrete. Only walls deemed as shear-controlled were included in the database. Walls were considered to be shear-controlled by comparing the shear load associated with flexural failure ($V_{flexure}$) with the peak strength (V_{peak}) measured from test. A ratio of $V_{flexure}/V_{peak}$ higher than one suggests that the wall is expected to have a shear-controlled failure. Walls with aspect ratios lower than 1.5 were selected in order to further minimize the possibilities of including flexure-controlled and mixed failure modes. Walls flexural strength was calculated by fiber cross-section analysis using an OpenSees code (code sample can be found on Appendix D); implementing reported steel and concrete materials properties.

OpenSees *Concrete04* material (Lowes and Berry, 2009) was used as constitutive model for concrete in the fiber cross section analyses. Conservatively, no strength increase due to transverse steel confinement was considered and concrete tensile strength was neglected. Reported values for the concrete parameters were used whenever possible, but when values were not reported in the literature then the following assumptions have been made:

- concrete modulus of elasticity, as per ACI 318-14 code provisions,
- concrete strain at peak compressive strength, 0.002,
- concrete ultimate strain, 0.004 as suggested by Mander et al. (1988).

OpenSees *ReinforcingSteel* material (Mohle and Kunnath, 2010) was used as the steel constitutive model in the fiber cross section analyses. Reported values for the steel parameters were used whenever possible, but when values were not reported in the literature then the following assumptions have been made:

- ultimate tensile strength of the steel reinforcement, $1.2f_y$,
- steel modulus of elasticity, 200 GPa,
- steel ultimate tensile strain, 0.12,
- steel strain at the onset strain hardening, 0.015,
- tangent at initial strain hardening, 8275 MPa.

Selected wall specimens were tested in a cantilever setup with a load applied in the direction of the plane of the wall so that the aspect ratio (h_w/l_w) was generally similar to M/Vl_w. Note that walls tested with restricted rotation at the top will have a h_w/l_w of nearly twice M/Vl_w thus, representing boundary conditions found in wall-piers which are connected to very stiff elements at both ends. Only cantilever (fixed-free) tests were selected to eliminate bias due to boundary conditions. Walls with openings and asymmetric cross sections were excluded from database.

Some of the walls from Carrillo and Alcocer (2013) were reinforced with non-ductile wire mesh and were reported to fail prematurely by fracture of web reinforcement. This type of non-ductile wire mesh reinforcement is not representative of the common US design and construction practice and therefore, corresponding wall specimens were excluded from database. Terzioglu tests data were reported by Opazo (2012) and Gutierrez (2012).

2.2 Walls with Rectangular Cross Section

Rectangular walls database was assembled using the results from 70 wall specimens meeting the selection criteria found in the literature. It includes wall specimens of moderate to large scale, built with normal and high strength concrete and steel materials. Sixty-seven of the 70 wall specimens were tested under cyclic loading, two were tested using hybrid-simulated earthquake loading, and one was tested using dynamic loading. Their thicknesses ranged from 76 mm to 203 mm. Aspect ratio of the walls (h_w/l_w) varied from 0.25 to 1.50 whereas the shear span-to-length ratio (M/Vl_w) varied from 0.33 to 1.65. About 90% of the wall specimens had aspect ratio between 0.25 and 1.0. Length-to-thickness ratio varied from 7.5 to 54.0, but more than 95 % of the wall specimens had a ratio below 30. Forty-two of the 70 wall specimens were tested without axial loads, in addition to the self-weight of the specimen (wall plus top slab or top beam). Axial load ratios were calculated as the additional applied load (P) divided by the product of the concrete compressive strength and the gross cross sectional area (f'_cA_g). The remaining walls had axial load ratios ranging from 1% to 14%. Figure 2-4 shows a summary of the geometric properties and axial loading values for the rectangular walls used in this study. Figure 2-5 shows a summary of the reinforcement and material properties for the same population of wall specimens.

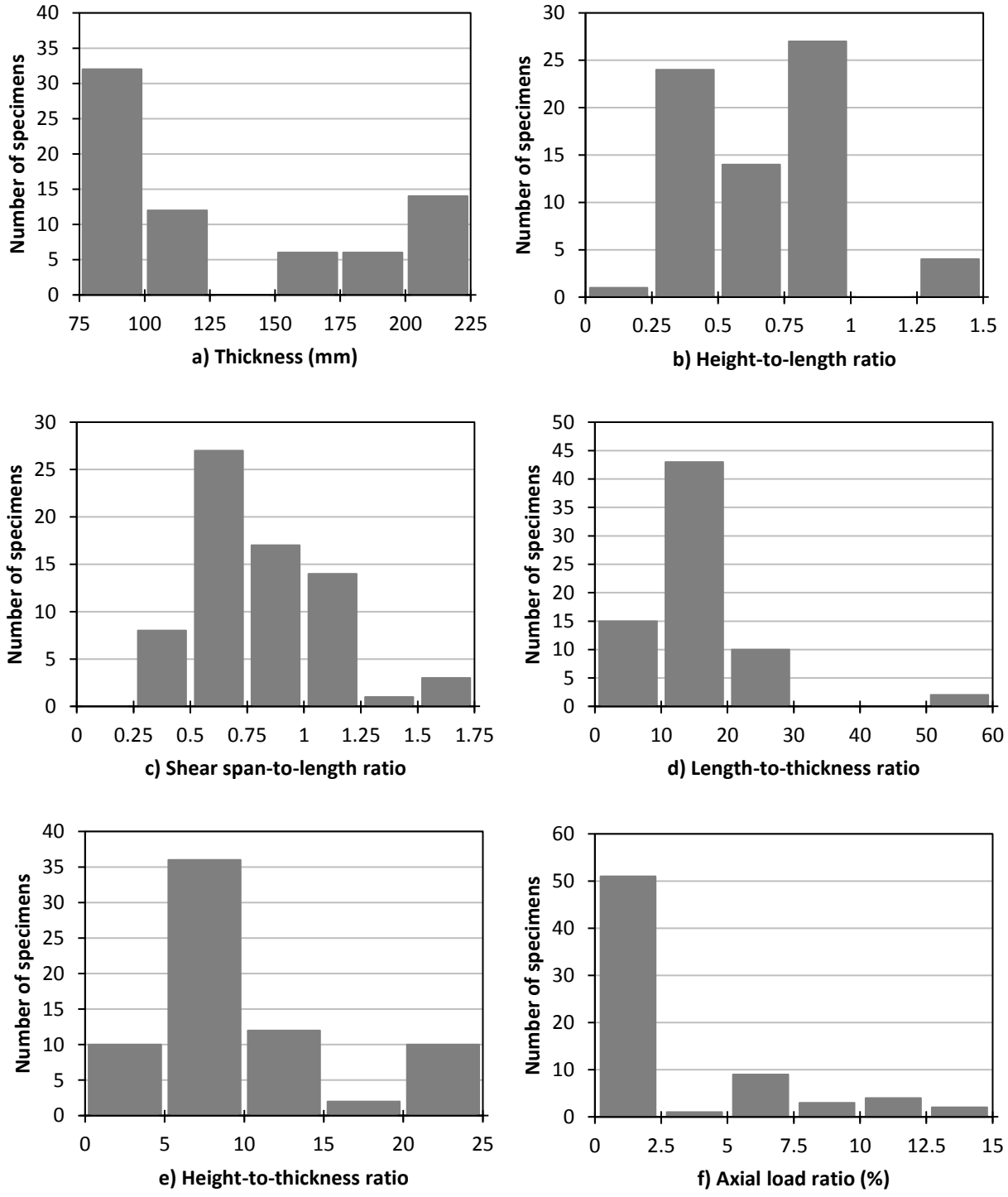

Figure 2-4. Histograms of geometric and loading properties of wall specimens with rectangular cross section.

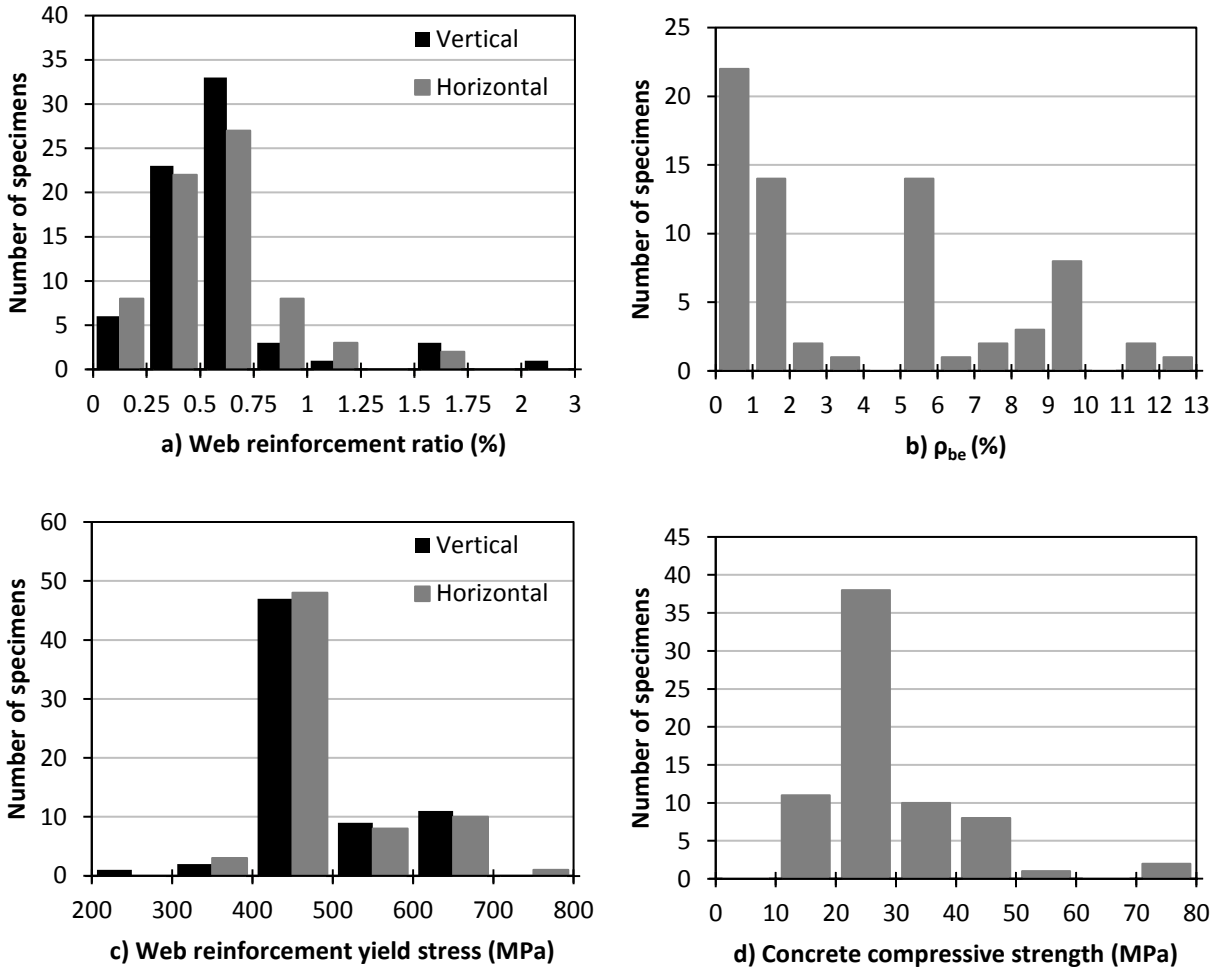

Figure 2-5. Histograms of reinforcement and material properties of wall specimens with rectangular cross section.

The concrete compressive strength varied from 13.7 MPa to 70.3 MPa. Approximately 70% of the specimens used concrete with strength between 20 MPa and 40 MPa and about 15% were constructed with high strength concrete (f'_c > 40MPa). The web reinforcement yield stress ranged from 300 MPa to 745 MPa. Nearly 30% of the wall specimens used high strength steel reinforcement with yield stress above 500 MPa. Web reinforcement ratios ranged from 0.14% to 2.93%, but approximately 90% of the specimens had web reinforcement ratios of 1% or less. Twenty-two of the 70 wall specimens (roughly 30%) did not have boundary elements with concentrated steel reinforcement. The remaining 48 walls had longitudinal boundary element reinforcement ratios varying from 1.1% to 12.4%. Longitudinal boundary element reinforcement ratio was taken as the concentrated vertical steel area at the boundary divided by the gross shear

area of the cross section (A_{cv}). Where the steel reinforcement was uniformly distributed along the length of the wall, the longitudinal boundary element reinforcement ratio was taken as zero.

2.3 Walls with Boundary Elements

The database of walls with boundary elements is populated with the results from 137 wall specimens meeting the selection criteria. Data from 81 barbell and 56 flanged cross section wall tests were collected from published literature. It includes data of moderate to large scale specimens, constructed with normal and high strength concrete and steel materials. One hundred and twenty-seven of the 137 wall specimens were tested under cyclic loading, six were tested using hybrid-simulated earthquake loading, and four were tested using dynamic loading. Their thicknesses ranged from 74 mm to 200 mm. Aspect ratio of the walls (h_w/l_w) varied from 0.21 to 1.22, whereas the shear span-to-length ratio (M/Vl_w) ranged from 0.25 to 1.76. About 90% of the specimens had aspect ratio between 0.25 and 1.0. Length-to-thickness ratio varied from 7.5 to 41.3, but roughly 90% of the specimens had a ratio falling below 30. Twenty of the 137 walls were tested without axial loads, in addition to the self-weight of the specimen (wall plus top slab or top beam). Axial load ratios were calculated in terms of the additional applied load (P) divided by the product of the concrete compressive strength and the gross cross sectional area (f'_cA_g). Only one wall was tested with a very high axial load ratio of 28%, and the rest of the walls with additional axial loading had axial load ratios ranging from 1.3% to 13.8%. Figure 2-6 shows a summary of the geometric properties and axial loading values for the walls with enlarged boundary elements considered in this study.

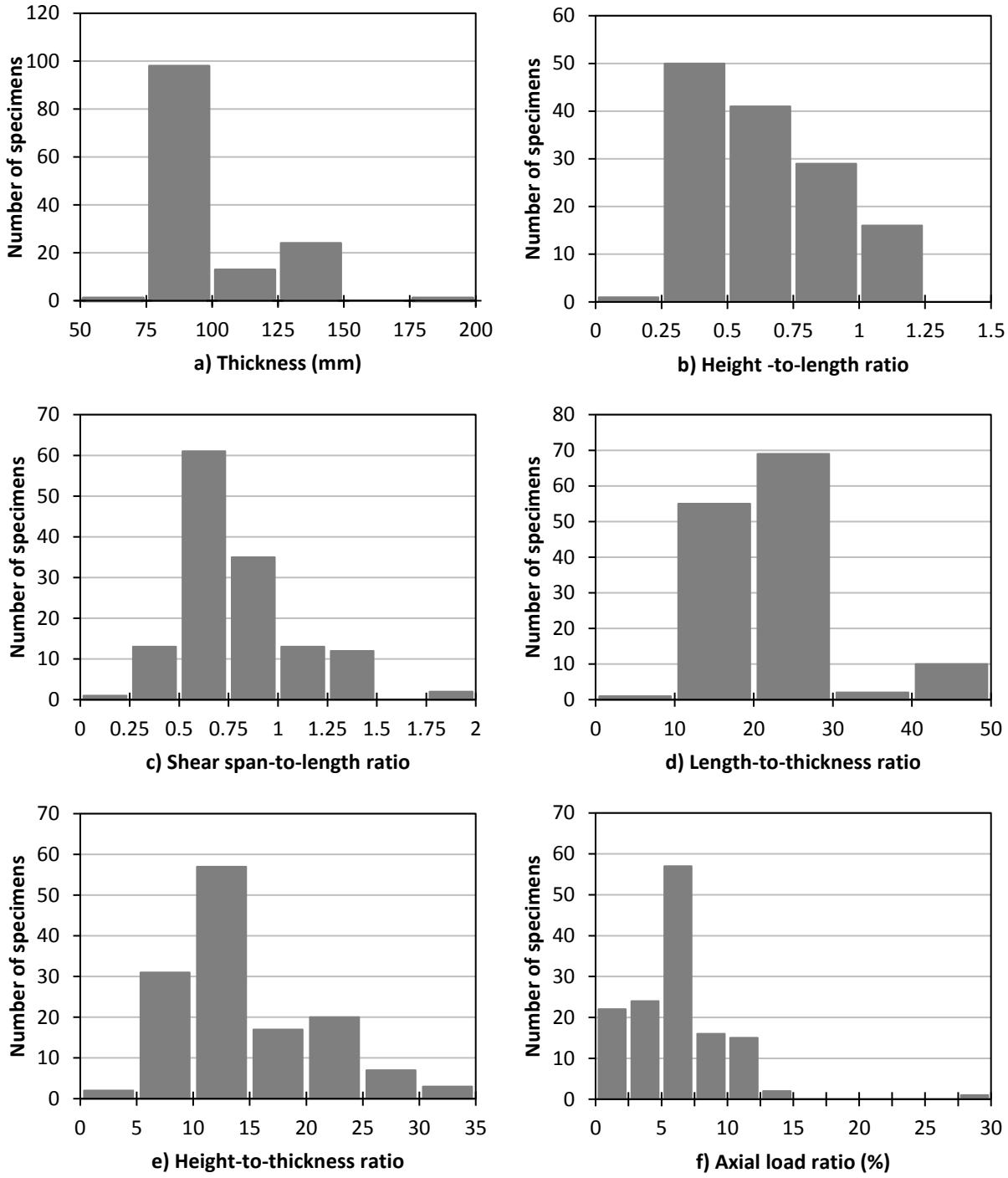

Figure 2-6. Histograms of geometric and loading properties of walls with flanged and barbell cross section.

The concrete compressive strength varied from 17.4 MPa to 103.4 MPa. Approximately 70% of wall specimens used concrete with strength between 20 MPa and 40 MPa, and about 25% of

them were constructed with high strength concrete (f'_c > 40MPa). The web reinforcement yield stress ranged from 296 to 1420 MPa. Nearly 20% of the specimens used high strength steel reinforcement with yield stress above 500 MPa. The web reinforcement ratios ranged from 0% to 2.76%, but approximately 80% of the specimens had web reinforcement ratios of 1.25% or less. Three wall specimens with barbell cross section lacked of vertical and horizontal web reinforcement, and the only vertical reinforcement was placed at the boundary elements. One flanged specimen did not have any horizontal web reinforcement and another flanged specimen did not have any vertical web reinforcement. All wall specimens had widened boundary elements with concentrated steel reinforcement. Their longitudinal boundary element reinforcement ratios varied from 0.4 % to 9.7%. Longitudinal boundary element reinforcement ratio was calculated in terms of the concentrated vertical steel area at the boundary divided by the gross shear area of the cross section (A_{cv}). Figure 2-7 shows a summary of the reinforcement and material properties of the same population of wall specimens.

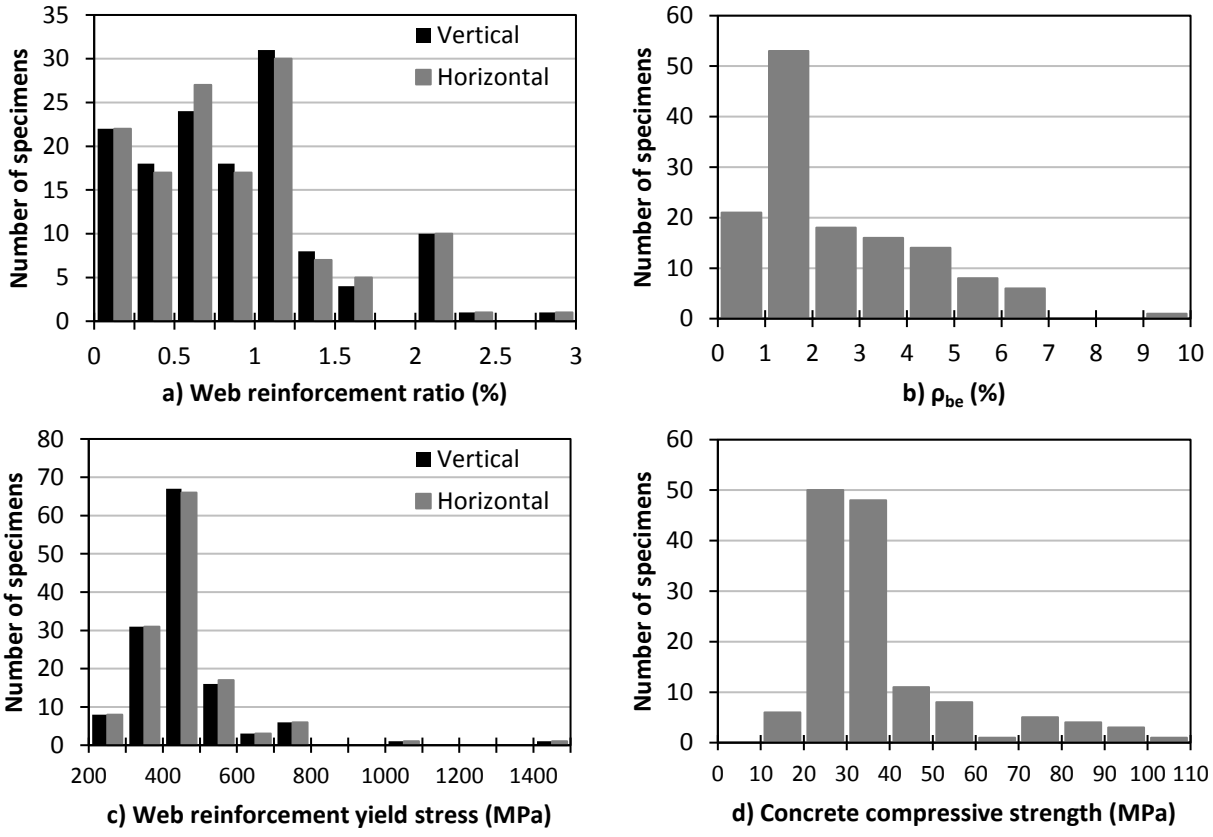

Figure 2-7. Histograms of reinforcement and material properties of walls with flanged and barbell cross section.

CHAPTER 3. SHEAR STRENGTH OF SQUAT WALLS WITH RECTANGULAR CROSS SECTION

3.1 Introduction

Statistical analyses have been carried out from the assembled database, as described in Chapter 2. As previously noted, wall specimens with enlarged boundary elements (i.e. barbell and flanged cross section) generally achieved higher shear strength than comparable specimens with rectangular cross section. Therefore, the assessment of available predictive equations and development of new predictive equations were addressed separately for both groups of walls. The discussion on the strength of walls with boundary elements is presented in Chapter 5.

It has been found that the commonly used equations, as described in US standards and literature, vary significantly in functional form as well as in predictive performance. Even when the behavior of squat walls is significantly different from walls with higher aspect ratios, these equations have been generated based on experimental data, including walls of different characteristics which do not necessarily focus on squat walls. Also, some of the commonly used equations do not differentiate between walls with rectangular or barbell cross section.

Many equations were found in current US design codes (ACI 318, ACI 349, ASCE 43-05) and in literature (e.g., Barda et al., 1977; Wood et al., 1990) for the prediction of the peak shear strength of reinforced concrete walls. However, comparison against experimental results show that these equations yield significantly scattered strength predictions for squat walls. Some reasons for their scattered predictions originate from the limited data on which the expressions are based. For example, ACI 318-14 equations are mostly based on data from moderate aspect ratio walls, and were modified by either imposing limits of reinforcement and/or incorporating a factor to include the strength characteristics of low aspect ratio walls (Cardenas et al., 1973). ASCE 43 equation is based on Barda's experiments (Barda, 1972; Barda et al., 1977) and was modified to provide a lower-bound solution when compared with some experiments available at that time. It is important to note that the US code equations have remained basically unchanged for over 30 years, while significant new experimental data is now available. Extensive research has been

performed during the past few years (e.g., Carrillo et al., 2013; Gulec and Whittaker 2009; Massone, 2010a; etc.) to address this situation, however the development of better equations to assess the peak shear strength of squat RC walls is still necessary, since the lateral strength and performance of these walls relies mostly on its shear strength.

This chapter presents an evaluation of current expressions for the prediction of peak shear strength of squat reinforced concrete walls with rectangular cross section available in US design codes and in literature. The performance of each of the selected equations is assessed by comparing the strength predictions with experimental strength from the assembled database for walls with rectangular cross section. The experimental peak shear strength of each wall was taken as the average of the peak strengths measured from the first and third quadrants (i.e. positive and negative loading directions, respectively). Key parameters influencing the peak shear strength were identified and a new equation to predict the peak shear strength of squat walls with rectangular cross sections is presented. The new equation was obtained from multivariable regression analyses using an assembled experimental database and aims to improve current peak shear estimates. The new expression presented herein is intended to be used in the design and assessment of structures with RC squat walls.

3.2 Current Expressions for Peak Shear Strength

The following subsections discuss the selected current equations for shear strength prediction. The equations shown are similar to those found on the corresponding references, but the names and subscripts for parameters have been modified to maintain uniformity within equations, database and manuscript. Also, the equations are expressed in terms of nominal loads and nominal strength (without applying any strength reduction factor) for the purpose of comparison.

3.2.1 ACI 318-14

The ACI 349-13 *Code Requirements for Nuclear Safety Related Concrete Structures* uses all the same provisions of the ACI 318-14 for evaluating peak shear strength of walls, with the difference that provisions for lightweight aggregates (i.e., λ factor) were omitted from the entire code and commentary, since the structural configuration and structural member sizing is typically controlled by live loads, seismic loads or shielding requirements, and not floor dead

loads. Section R21.2.4 of the ACI 349-13 commentary states that lightweight concrete is not permitted in nuclear safety-related structures.

The ACI 318-14 has two different sets of provisions for evaluating the peak shear strength of reinforced concrete walls. The first set, given in section 11.5 of the code, is intended to be used for shear walls with general loading. The second set, specified in section 18.10, is intended to be used specifically for special structural walls of earthquake resistant structures.

For design purposes, the strength shall be calculated by multiplying the nominal strength by the strength reduction factor (φ). This factor is determined according to section 9.3 of the code and is equal to 0.75 for most cases of shear and torsion. The code requires that, for any structural member designed to resist earthquake effects, the strength reduction factor (φ) shall be 0.60 if its nominal shear strength is less than the shear corresponding to the development of the nominal flexural strength of the member. This is commonly applicable to squat walls and other structural members with low shear span-to-length ratio (M/Vl_w), where the necessary reinforcement to provide shear strength in excess of the corresponding shear at flexural strength becomes impractical.

3.2.1.1 Chapter 11 of ACI 318-14

The provisions first appeared in Chapter 11 of ACI 318-71 and have remained unchanged since then. The wall nominal shear strength loaded in the direction of the plane of the wall is calculated using equation 3-1, which attributes part of the strength to the concrete and the rest to the web reinforcement as it has been typically used in the US design practice for many reinforced concrete members. Although research show that higher shear stresses can be obtained in some types of walls, an upper limit of $0.83\sqrt{f_c'}$ is conservatively imposed in the nominal shear stress to preclude diagonal compression failure and to limit the redistribution of shear force.

$$V_n = V_c + V_s \leq 0.83\sqrt{f_c'}t_w d \tag{3-1}$$

where V_n is the nominal shear strength (N); f'_c is the uniaxial compressive strength of concrete (MPa); t_w is the wall web thickness (mm); d is the effective depth of the cross section (mm) and

is taken as 80% of the length of wall ($0.8l_w$) or determined by strain compatibility analysis; V_c is the nominal shear strength carried by concrete (N); and V_s is the shear strength carried by steel reinforcement (N).

The nominal shear strength provided by concrete is taken as the lesser of the values obtained by equations 3-2 and 3-3. When the term $(M_u/V_u - l_w/2)$ is negative equation 3-3 shall not apply. The nominal shear strength provided by horizontal reinforcement can be calculated using equation 3-4.

$$V_c = 0.27\lambda\sqrt{f_c'}t_w d + \frac{Pd}{4l_w} \tag{3-2}$$

$$V_c = \left[0.05\lambda\sqrt{f_c'} + \frac{l_w\left(0.1\lambda\sqrt{f_c'} + 0.2\dfrac{P}{l_w t_w}\right)}{\dfrac{M}{V} - \dfrac{l_w}{2}} \right] t_w d \tag{3-3}$$

$$V_s = \frac{A_v f_y d}{s} \tag{3-4}$$

where P is the total applied axial load normal to the cross section (N); M is the flexural moment at section (N•mm); V is the shear loading at section (N); A_v is the area of shear reinforcement (mm^2) within spacing s; s is center-to-center spacing of horizontal reinforcement (mm); f_y is the yield stress of the shear reinforcement (MPa); and λ is the modification factor reflecting the reduced mechanical properties of lightweight concrete (1.0 for normalweight concrete, 0.85 for sand-lightweight concrete and 0.75 for all-lightweight concrete).

As reported by Cardenas et al. (1973), ACI 318 assumes that shear strength provided by concrete corresponds to shear force that would produce significant inclined cracking. Inclined cracks are generally classified as either “web-shear” or “flexure-shear”. Web shear cracks are those that form near the neutral axis of the cross section and propagate inclined to the member axis before any flexural cracking has occurred in their vicinity. On the other hand, flexure-shear cracks begin with a flexural crack at the extreme tension fiber and, as a result of the applied shear, becomes inclined in the direction of increasing moment as it propagates through the cross section.

Equation 3-2 has been derived based upon the assumption that the development of inclined or "web-shear" cracking of a wall with combined axial and shear loading will occurs when the maximum principal tensile stress in an interior point of the cross section reaches a value of $0.33\sqrt{f_c'}$. Equation 3-3 predicts flexure-shear cracking strength as the shear that produces flexural cracking stress of $0.5\sqrt{f_c'}$ at a section located $l_w/2$ above the section being investigated, plus the shear required to transform the incipient flexural crack into an inclined and fully developed flexure-shear crack (conservatively taken as $0.05\sqrt{f_c'}$). According to section 11.5.4.7 of the ACI 318-14, the critical section for design in the lower portions of the wall can be taken at a distance of the lesser of $l_w/2$ and $h_w/2$ from the base.

Sections 11.6 and 11.7 also establish limits on the quantity and spacing of reinforcement as follows:

- Spacing for horizontal reinforcement shall not exceed the smallest of $l_w/5$, $3t_w$ and 450 mm.
- Spacing of vertical reinforcement shall not exceed the smallest of $l_w/3$, $3t_w$ and 450 mm.
- The ratio of vertical reinforcement (ρ_v) shall not be smaller than 0.0025 and the calculated by equation 3-5. The value calculated with equation 3-5 need not be larger than the required to meet the design strength ($\varphi V_n \geq V_u$).
- Where $V_u \geq 0.5\ \varphi V_c$, the horizontal (transverse) reinforcement ratio shall be at least 0.0025 and the vertical (longitudinal) reinforcement ratio shall be the greater of 0.0025 and the value calculated with the following equation as established in code section 11.6.2.

$$\rho_v = 0.0025 + 0.5\left(2.5 - \frac{h_w}{l_w}\right)(\rho_h - 0.0025) \qquad (3\text{-}5)$$

- Where $V_u < 0.5\ \varphi V_c$, more relaxed reinforcement limits are allowed as per section 11.6.1.

As stated by Barda et al. (1977), horizontal reinforcement becomes less effective than vertical reinforcement for shear strength in low rise walls. Their findings also suggests that for walls with aspect ratios lower than 0.5 the shear strength was almost insensitive to the horizontal reinforcement ratio, but was effective to produce more distributed crack patterns with reduced crack widths, which enhances energy dissipation. In a similar manner, for walls with higher aspect ratios ($h_w/l_w \geq 1.0$), vertical reinforcement is less effective for shear strength, but promotes

a distributed crack pattern. In order to reflect this behavior, equation 3-5 was incorporated in the code, along with the upper and lower reinforcement limits and spacing limits. Equation 3-5, in combination with the applicable limits, require that if h_w/l_w is less than 0.5, the amount of vertical reinforcement should be equal to the amount of horizontal reinforcement; whereas if h_w/l_w is greater than 2.5, only a minimum amount of vertical reinforcement is required (i.e., 0.0025 s t_w). The required vertical reinforcement ratio varies linearly between aspect ratios of 0.5 and 2.5. Section 11.5.4 also allows the design of squat walls ($h_w/lw \leq 2.0$) using the strut and tie approach described in Chapter 23 of the code.

3.2.1.2 Chapter 18 of ACI 318-14

This set of provisions for the design of shear walls resisting seismic loads was incorporated for the first time in the ACI 318 code under Appendix A of ACI 318-83, and still practically unchanged in section 18.10 of the current version of ACI 318. The nominal shear strength is calculated using equation 3-6 and follows the same concept of the modified truss analogy used for the design of reinforced concrete beams (Wood, 1990).

$$V_n = A_{cv}\left(\alpha_c \lambda \sqrt{f_c'} + \rho_h f_y\right) \leq 0.83 A_{cw} \sqrt{f_c'} \tag{3-6}$$

where A_{cv} is the gross area of concrete section bounded by web thickness and length of section in the direction of shear force considered (mm^2); A_{cw} is the area of concrete section of an individual pier, horizontal wall segment, or coupling beam resisting shear (mm^2); α_c is the coefficient defining the relative contribution of concrete strength to nominal wall shear strength (varies linearly from 0.25 for h_w/l_w =1.5 to 0.17 for h_w/l_w = 2.0); and ρ_h is the horizontal (transverse) reinforcement ratio.

Equation 3-6 reflects the experimental observations for the higher unit shear strength of walls with low aspect ratio by incorporating the factor α_c. Section 18.10 of the code also imposes limits on the quantity and distribution of reinforcement as follows:

- Ratio of vertical (ρ_v) and horizontal reinforcement (ρ_h) shall not be less than 0.0025.

- Where $V_u \leq 0.083A_{cv}\lambda\sqrt{f_c'}$, the reinforcement ratios ρ_v and ρ_h shall be permitted to be reduced to the requirements of section 11.6 of the code.
- For squat walls (i.e., $h_w/l_w \leq 2.0$) vertical reinforcement ratio (ρ_v) shall not be less than the horizontal reinforcement (ρ_h).
- Spacing for horizontal and vertical reinforcement shall not exceed 450 mm.
- At least two curtains of reinforcement are required if $V_u > 0.17A_{cv}\lambda\sqrt{f_c'}$.

3.2.2 ASCE 43-05

Although ASCE 43-05 (*Seismic Design Criteria for Structures, Systems and Components in Nuclear Facilities and Commentary*) refers to the provisions of ACI 349-13 (similar to ACI 318) for the determination of shear strength of reinforced concrete walls, it also provides an alternate method for low rise reinforced concrete shear walls. ASCE 43-05 recognizes that ACI 349 method tends to underestimate the strength of low rise walls with enlarged boundary elements, and suggests the use of the method described below for walls with barbell or flanged cross sections and with a ratio of $h_w/l_w \leq 2.0$. Total shear capacity can be calculated with the following expressions:

$$V_n = v_n d t_w \tag{3-7}$$

$$v_n = 0.69\sqrt{f_c'} - 0.28\sqrt{f_c'}\left(\frac{h_w}{l_w} - 0.5\right) + \frac{P}{4l_w t_w} + \rho_{se} f_y \leq 1.67\sqrt{f_c'} \tag{3-8}$$

$$\rho_{se} = A\rho_v + B\rho_h \tag{3-9}$$

where v_n is the nominal shear stress capacity (MPa) calculated from equation 3-8; d is the distance from the extreme compression fiber to the center of the force of all reinforcement in tension (mm) which may be determined by strain compatibility analysis or taken as $0.6l_w$ in lieu of an analysis; ρ_{se} is the effective reinforcement ratio; and A and B are constants to quantify the contribution of the reinforcement in the vertical and horizontal direction, respectively.

Only the vertical reinforcement is considered effective for aspect ratios below 0.5, only the horizontal reinforcement is considered effective for aspect ratios above 1.5, and both

reinforcement contributions vary linearly for aspect ratios between 0.5 and 1.5. Constants A and B are calculated as follows based on the aspect ratio h_w/l_w:

if $h_w/l_w \leq 0.5$	A = 1	B = 0
if $0.5 < h_w/l_w < 1.5$	A = - h_w/l_w + 1.5	B = h_w/l_w – 0.5
if $h_w/l_w \geq 1.5$	A = 0	B = 1

According to ASCE 43-05, equation 3-8 is applicable to shear walls with reinforcement ratios (ρ_v and ρ_h) less than or equal to 0.01. When ρ_v or ρ_h exceeds 0.01, the effective reinforcement ratio (ρ_{se}) shall be limited to 0.01 in the calculation of strength. The ASCE 43 method is based on the equations proposed by Barda (Barda, 1972; Barda et al., 1977) and was modified to account for both horizontal and vertical steel, and provide a lower-bound solution when compared with some experiments available at that time.

3.2.3 Barda et al. (1977)

Eight RC squat wall specimens with heavily reinforced and well-confined flanges (end walls) were tested in under lateral load and without axial load. Their study involved six walls with cyclic loading, two walls with monotonic loading and one wall that was repaired and retested after attaining heavy damage. The shear span-to-length ratios of the test specimens varied from 0.25 to 1.0. They calibrated equation 3-10 to give a close prediction of the shear strength of the tested wall specimens. However, they proposed equation 3-11 for design purposes to include the effect of axial load.

$$V_n = \left(0.69\sqrt{f_c'} - 0.28\sqrt{f_c'}\left(\frac{h_w}{l_w} - \frac{1}{2}\right) + \rho_v f_y \right) t_w d \tag{3-10}$$

$$V_n = \left(0.67\sqrt{f_c'} - 0.21\sqrt{f_c'}\,\frac{h_w}{l_w} + \frac{P}{4 l_w t_w} + \rho_v f_y \right) t_w d \tag{3-11}$$

Equations 3-10 and 3-11 include only the vertical reinforcement ratio since the authors observed that the horizontal reinforcement did not show significant contribution to shear strength on the tested specimens with lower aspect ratios. However, they noted that horizontal reinforcement had

a considerable effect in generating more evenly distributed, closely spaced, and narrow width crack pattern that enhanced hysteretic behavior and post peak strength. Therefore, they recommended providing equal reinforcement ratio in both, vertical and horizontal directions. Also, based on the characteristics of the wall specimens tested in their experimental program, the authors suggested that the equations were applicable for aspect ratios equal or less than one; and reinforcement ratios ranging from 0.0025 to 0.005 and somewhat higher. For the calculations presented herein, d was assumed as $0.6l_w$.

3.2.4 Wood (1990)

Wood (1990) evaluated the results of 143 low-rise wall specimens which included rectangular, flanged and barbell cross sections. Wood proposed the equation 3-12 to estimate the shear strength of squat RC walls:

$$0.5\sqrt{f_c'}A_{cv} \le V_n = \frac{A_{vf} f_y}{4} \le 0.83A_{cv}\sqrt{f_c'} \tag{3-12}$$

where, A_{vf} is the total vertical reinforcement area in the wall (mm^2).

Wood observed that the maximum average shear stress tended to increase with an increase in the amount of vertical reinforcement in both web and boundary elements. The author proposed a semi-empirical expression (Equation 3-12), derived by using a shear-friction analogy, and calibrated against experimental data of squat RC walls tests collected from literature. The author found that lower bounds for the strength of the walls considered were well represented by $0.5A_{cv}\sqrt{f_c'}$ and $A_{vf}f_y/4$ but also established an upper limit of $0.83A_{cv}\sqrt{f_c'}$ to avoid failure modes associated with compressive strength of concrete.

3.3 Development of New Peak Shear Strength Predictive Equation

A statistical approach was used to develop and calibrate an equation that improves the actual estimates of peak shear strength of squat RC walls with rectangular cross section. Multivariable linear regression analyses were performed to produce an empirical equation that better fits the included database of 70 squat RC walls with rectangular cross section. The goal was to lower the

standard deviation and coefficient of variation of the predicted-to-measured shear strength ratio. The goal was also to obtain a mean predicted-to-measured strength ratio near to 1.0, while keeping the percentage of over-predictions around 50% which means that the predicted strength would be, on average, nearer to the experimental strength. Experimental peak strength was taken as the average of the peak strengths recorded in the positive (first quadrant of hysteresis) and negative (third quadrant of hysteresis) loading directions.

A functional equation form was selected based on Barda's proposed expressions and based on common ACI seismic design expressions. The parameters found on these equations are in general agreement with the parameters having important influence on shear strength as reported by several researchers. Additional predictive parameters were identified by reviewing the findings from numerous experimental programs and extended to account for the vertical, horizontal and boundary element reinforcement. To arrive to the final parameter selection, multivariable linear regression analysis was run using several different combinations of the previously identified parameters to generate a calibrated equation on each run. Finally, the calibrated equation with the parameter combination that yields less variability when compared to the assembled database was selected. The following set of expressions includes the parameters that were found to be better correlated to the experimental strength and is calibrated to best fit the data within the database:

$$V_n = \left(0.35 + 0.068 f_c^{'} - 0.080 f_c^{'} \frac{h_w}{l_w} + 0.41 \frac{P}{A_g} + 0.47 \rho_{se} f_{yse} + 0.39 \rho_{be} f_{ybe} \right) A_{cv} \qquad (3\text{-}13)$$

$$f_{yse} = A f_{yv} + B f_{yh} \qquad (3\text{-}14)$$

$$\rho_{se} = A \rho_v + B \rho_h \qquad (3\text{-}15)$$

$$\rho_{be} = A_{sbe} \Big/ A_{cv} \qquad (3\text{-}16)$$

where ρ_{be} is the longitudinal boundary element reinforcement ratio; A_{sbe} is the longitudinal boundary reinforcement area (mm^2); and constants A and B are calculated as follows depending on the aspect ratio h_w/l_w:

if $h_w/l_w \leq 0.5$	A = 1	B = 0
if $0.5 < h_w/l_w < 1.5$	A = - h_w/l_w + 1.5	B = h_w/l_w – 0.5
if $h_w/l_w \geq 1.5$	A = 0	B = 1

Figure 3-1 shows the portion of peak shear strength attributed to each of the parameters calculated with equation 3-13 for wall specimen MRN100C, tested by Carrillo and Alcocer (2013). The wall specimen had a low axial load ratio of 1.54%, aspect ratio of 0.44, concrete compressive strength of 16.2 MPa, horizontal and vertical reinforcement ratios of 0.29%, web reinforcement yield strength of 447 MPa, and boundary element yield strength of 430 MPa.

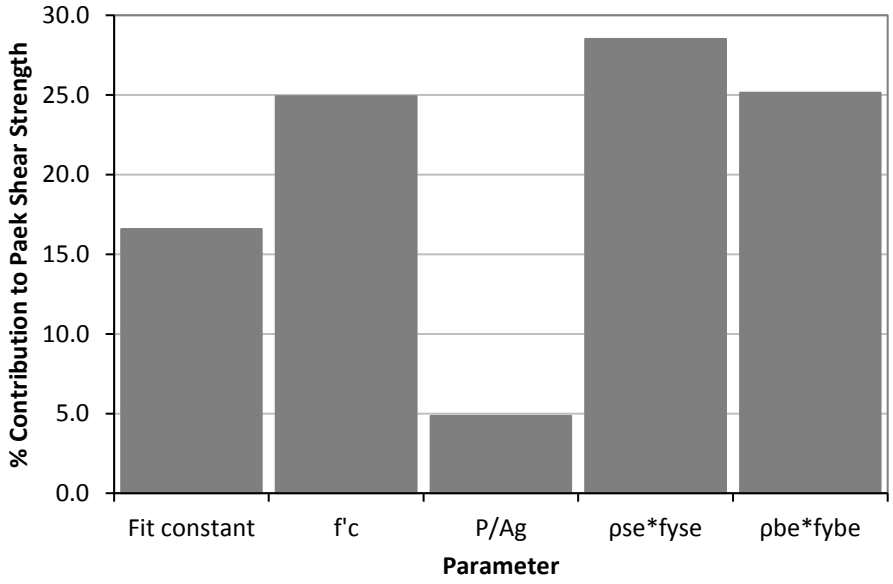

Figure 3-1. Contribution to peak shear strength attributed to each of the equation 3-13 parameters for wall specimen MRN100C.

Other failure modes yielding lower strength can occur. The occurrence of such failure modes may be related to differences between the actual conditions of the wall being evaluated and the experimental setup of walls considered in the database. The user should be aware of the characteristics and range of parameters of the wall specimens considered in the corresponding database (refer to Chapter 2) to determine adequate applicability of the predictive equation.

Some disagreement among research findings and common equations in terms of the effectiveness of the vertical and horizontal reinforcement to provide shear strength was found. The majority of researchers (e.g., Barda, 1977; Greifenhagen and Lestuzzi, 2005, etc.) agree in the fact that horizontal reinforcement contribution to shear strength is marginal while vertical reinforcement has significant effect on shear strength in walls with very low aspect ratios (e.g., 0.5 or less). However, the results of walls with aspect ratios around 1.0 show some inconsistency in terms of the effectiveness of vertical and horizontal reinforcements (Cardenas et al., 1980; Maier, 1991; Dabbagh, 2005; Luna et al., 2015; etc.). For walls with aspect ratios around 1.0, some researchers found both reinforcements to be effective in contributing to peak shear strength while others reported that horizontal reinforcement did not contribute significantly to the shear strength. However, those researchers who found horizontal reinforcement not very effective in providing shear strength, reported that horizontal reinforcement was more influent on improving crack distribution, energy dissipation and post-peak response. On the other hand, the effectiveness of horizontal reinforcement in providing shear strength on slender walls (e.g., aspect ratios of 2.0 or higher) has been well established in literature.

In general, it appears that the shear strength of walls with very low aspect ratios tend to be more influenced by the vertical reinforcement; and the horizontal reinforcement helps on improving the hysteretic behavior, energy dissipation and maintaining the strength at higher drift levels. However, the role of vertical and horizontal reinforcements seems to gradually invert as the aspect ratio increases. To address this issue ASCE 43-05 standard implements an effective reinforcement ratio, which varies the effectiveness of the vertical and horizontal reinforcement ratios as a function of the wall aspect ratio (Figure 3-2). ACI 318-14 and ACI 349-13 do not directly consider the vertical reinforcement contribution but require vertical reinforcement ratio to be at least equal to the calculated horizontal reinforcement ratio for squat walls with aspect ratios equal or less than 2.0 to assure adequate steel reinforcement.

In order to identify which parameter produced a better prediction, the parameter associated with the strength provided by the reinforcement was evaluated by one-at-a-time parameter variation. The use of vertical distributed reinforcement only, total vertical reinforcement (including boundary element reinforcement) only, horizontal reinforcement only, both horizontal and vertical distributed reinforcements in separate terms and an effective reinforcement ratio that

combines both distributed reinforcements in one term (in the same fashion as in ASCE 43-05) were considered. The last resulted to be a better predictive parameter for steel contribution to shear strength as it produced the least variability. Using the effective reinforcement ratio to consider the contribution of both steel reinforcements as a function of aspect ratio (Figure 3-2) seems to be a reasonable assumption and is in good general agreement with experimental findings.

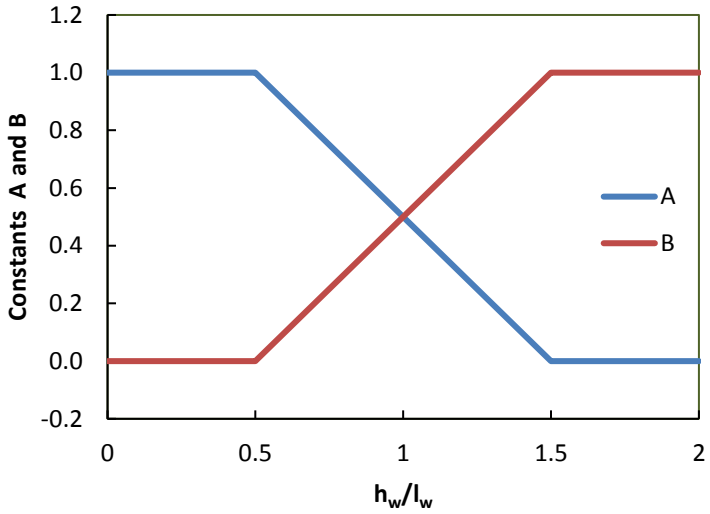

Figure 3-2. Variation of effective reinforcement constants with aspect ratio.

It has been consistently reported by researchers that walls with lower aspect ratios or lower shear span-to-length ratios can yield higher shear stress capacities. This has been commonly attributed to an increase in the shear carried by concrete as the aspect ratio decreases. In a preliminary study, the aspect ratio was treated as a separate term and compared to equation calibration using a term that considers the product of a concrete strength parameter and the aspect ratio. It was found that using the product of aspect ratio and a concrete strength parameter produced better predictions than using the aspect ratio separately. Additional to the term considering the product of aspect ratio and concrete strength, the use of another term with concrete strength parameter only was also considered, which further improved the predictions. Different combinations using the aspect ratio and the shear span-to-length ratio were evaluated. Also, the use of the square root

of the concrete compressive strength ($\sqrt{f_c'}$) versus using the compressive strength itself (f'_c) was considered.

The aspect ratio (h_w/l_w) was found to produce better correlation with the included database (with cantilever test setup) than the shear span (M/Vl_w). The aspect ratio is a more practical parameter for design purposes, since it does not depend on structural analysis to calculate values for moment and shear. However, if a wall pier with both ends fixed is being considered, then the use of the M/Vl_w would be more appropriate. The concrete compressive strength (f'_c) resulted to be a better strength prediction parameter; with best results when a concrete strength term and another term with the product of concrete strength and wall aspect ratio were included in the equation.

The boundary element reinforcement ratio is not considered in most equations. However, several researchers (e.g., Endo, 1980; Wood, 1990; and Terzioğlu, 2011) have found that the boundary element reinforcement affects both the shear load transfer mechanism and the peak shear strength even in shear-dominated walls with very low aspect ratios. Therefore, a term with the longitudinal boundary element reinforcement ratio (ρ_{be}), calculated as the ratio of longitudinal boundary reinforcement area in tension to the effective shear area (A_{sbe}/A_{cv}), was included resulting in an enhancement in the predictive performance of the equation. Another option where the ρ_{be} was calculated as the ratio of longitudinal boundary reinforcement area in tension to the gross area of the corresponding boundary element (A_{sbe}/A_{be}) was evaluated as well, but better predictions were obtained using (A_{sbe}/A_{cv}).

It has also been widely recognized that axial loads can enhance the shear load carrying capacity of reinforced concrete walls of higher aspect ratios. The same behavior was observed from different researchers for squat RC walls. Therefore, the axial load ratio (P/A_g) was incorporated in the equation form. The increase in shear strength due to axial loads may be attributed to two major mechanisms. First, the axial force enhances the frictional force transfer through cracks and construction joints. Secondly, the change in the biaxial stress state of the concrete panel can increase concrete shear strength. Results from several researchers (e.g., Salonikios et al., 1999; Palermo and Vecchio, 2002; Greifenhagen and Lestuzzi, 2005; Xiang, 2009; etc.) suggest that low axial load ratios in the order of 5% are enough to effectively reduce the base sliding

displacements (in walls with construction joints), and thus help prevent premature sliding failure of squat RC walls.

3.4 Evaluation of Selected Peak Shear Strength Equations

In this section the selected commonly used predictive equations and the new expression developed herein (presented in last section) will be evaluated in terms of their predictive performance by using a statistical approach and comparing to the experimental results compiled in the assembled database. In order to eliminate bias due to load amplification factors and resistance reduction factors between codes, the equations are modified to use nominal loads and nominal strengths. Also, the calculated peak and nominal shear strengths (V_{peak} and V_n) were then normalized with the effective shear area of the section (A_{cv}) to eliminate the test scale differences between different experimental programs, so that all the parameters were worked in terms of stress instead of force. The normalization of the shear force with A_{cv} also allows for a fair comparison between the available equations and the developed equation since different effective depth (d) definitions are suggested among the available expressions.

In order to evaluate the suitability of the proposed equation, it is compared against several widely-used equations in terms of the predicted-to-measured strength ratio. Figure 3-3 shows a graphic representation of the correlation of the calculated shear stress capacity vs the measured peak shear stress for the 70 rectangular cross section wall tests in the database, and for each of the equations discussed on section 3.2.

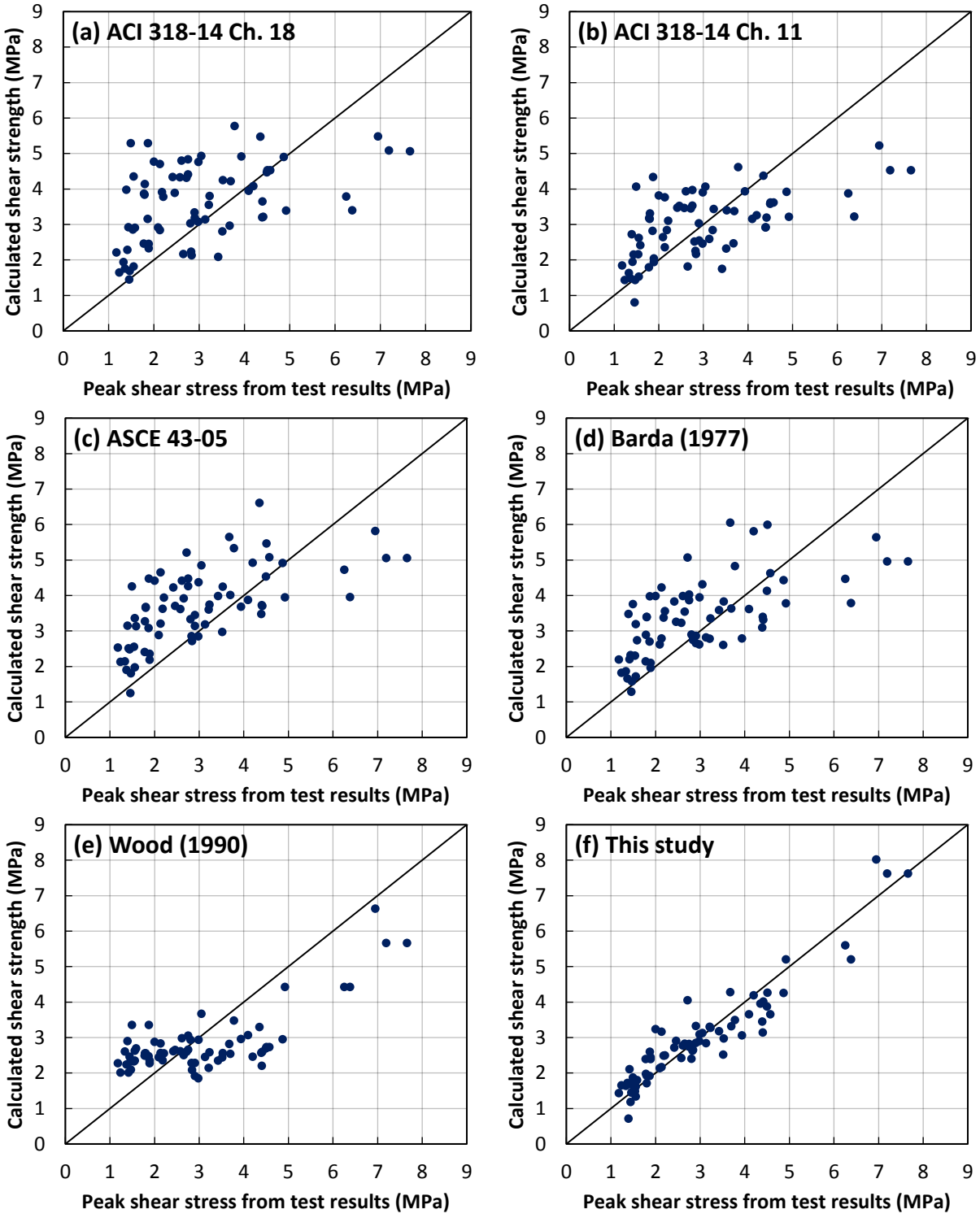

Figure 3-3. Correlation between calculated nominal shear stress and measured peak shear stress using various available equations: (a) to (e); and the new equation proposed in this study (f).

The diagonal line represents a ratio of predicted-to-measured strength of 1.0. Any point falling on the line means an exact prediction of the shear strength. Any point above the diagonal line represents an over-prediction of strength and vice-versa. The farther the point from the diagonal represents a larger error on the estimate. It can be noted from Figure 3-3 that the equation proposed in this study (equation 3-13) reduces the scatter of the results significantly over the rest of the evaluated equations.

In order to numerically compare the observed behavior of the predictions with each equation, Table 3-1 presents a summary of common central tendency and dispersion measures of the predicted-to-measured strength ratio, along with the percent of over-predictions. Mean and median values larger than 1.0 suggest that the equation tends to overestimate the strength. For example, ASCE 43-05 equation overestimates the strength, on average, by 39%. On the other hand, the standard deviation and coefficient of variation (COV) provide information on the dispersion (scatter) of the predicted-to-measured strength ratios. In other words, the mean and median values give useful information on the accuracy of the predictive equation while the standard deviation and coefficient of variation provide information regarding the precision of the equation. The % over-predictions provides information on the bias of the predictions. A non-biased equation will yield results having % over-predictions of around 50%. A lower % over-predictions would represent an equation producing biased estimates that tend to the conservative side while a higher % over-predictions indicates that the equation produces biased estimates that tend to the unconservative side.

Table 3-1. Summary of statistics of the ratio of predicted shear strength to the measured peak shear strength for walls included in the database.

	ACI Ch. 18	ACI Ch. 11	ASCE 43-05	Barda	Wood	This study
Mean	1.39	1.13	1.39	1.28	1.09	1.04
Median	1.25	1.03	1.36	1.25	1.00	1.01
Minimum	0.53	0.50	0.62	0.59	0.50	0.51
Maximum	3.53	2.72	2.84	2.51	2.24	1.61
Std. dev	0.60	0.44	0.47	0.45	0.42	0.20
COV	0.43	0.39	0.34	0.35	0.39	0.19
% Over-predictions	71.4	54.3	78.6	68.6	50.0	52.9

Figure 3-4 shows a typical box and whisker plot comparing the distribution of the predicted-to-measured strength for each presented equation model. The graph shows the lower quartile (25th percentile), median, upper quartile (75th percentile), the extreme values and the mean value marked with "+" symbol. The box in the box and whisker plot is constituted by the second and third quartile and represents the spread of the central 50% of the observations. The range of this box is commonly known as the inter-quartile range (IQR), midspread, or middle fifty. The narrower this range (or box in the graph) is, indicates the lesser the variability since the central 50% of the observations are nearer to the median value. The lower and upper whiskers of the plot represent the spread of the first and fourth quartile, being the ends of the whiskers the extreme (i.e. maximum and minimum) values marked with "-" tick mark.

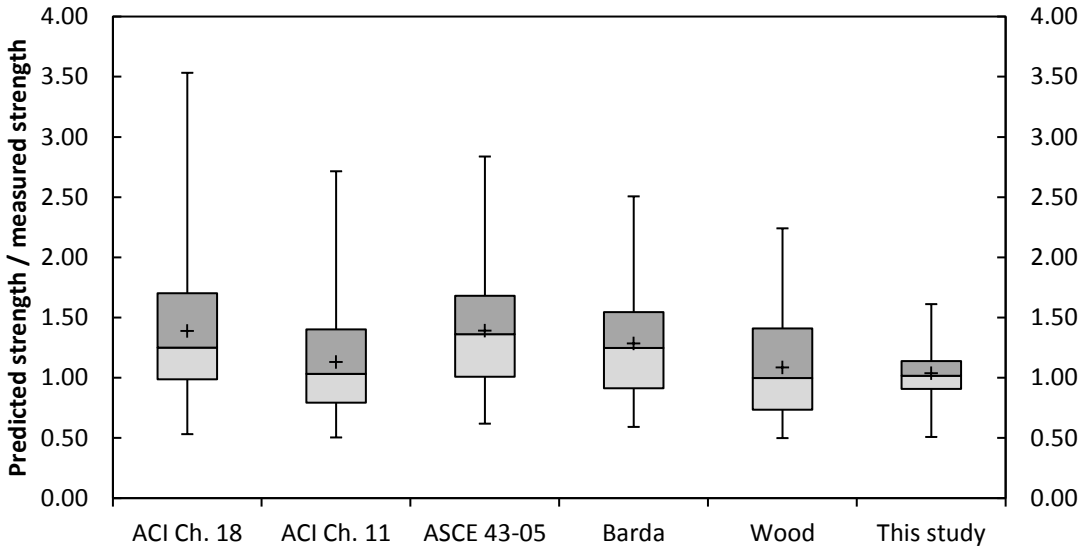

Figure 3-4. Distribution of the ratio of predicted-to-measured peak strength.

It can be observed that the proposed equation produces a significantly improved estimate of the shear strength since the mean and median values are very close to 1.0 and all the dispersion measures indicate that the scatter is considerably reduced in comparison with the rest of the evaluated equations. It is also observed that the midspread falls between 0.91 and 1.14, showing the smallest IQR. Also, the range (difference between maximum and minimum values) has been reduced, which suggests a reduction in scatter. In the same manner, the proposed equation yields 52.9% of over-predictions which is very near to the intended value. Note that ACI 318 Ch. 18, ASCE 43-05 and Barda expressions tend to over-predict shear strength of squat walls with

rectangular cross sections. This is observed on the box and whisker plot, central tendency statistics, and on the high % over-predictions. Generally, an equation yielding mean and median values near to 1.0 will produce nearly 50% over-predictions if the data is not severely skewed.

To further evaluate the proposed equation, a plot of the peak shear strength normalized with $A_{cv}\sqrt{f_c'}$ vs aspect ratio is presented in Figure 3-5. This figure shows that the upper strength limit of the ACI 318-14 ($0.83A_{cv}\sqrt{f_c'}$) is a reasonable value for squat shear walls with rectangular cross sections. Thus, the use of this limit with the proposed equation 3-13 is recommended for the estimation of peak shear strength. This limit has been traditionally imposed as an upper-bound to avoid non-ductile diagonal compression failure in walls, wall piers, deep beams and coupling beams. Figure 3-5 also suggests that the upper strength limit becomes more important for walls of lower aspect ratios. In addition, a good correlation between the predicted and measured normalized peak shear strengths can be noted.

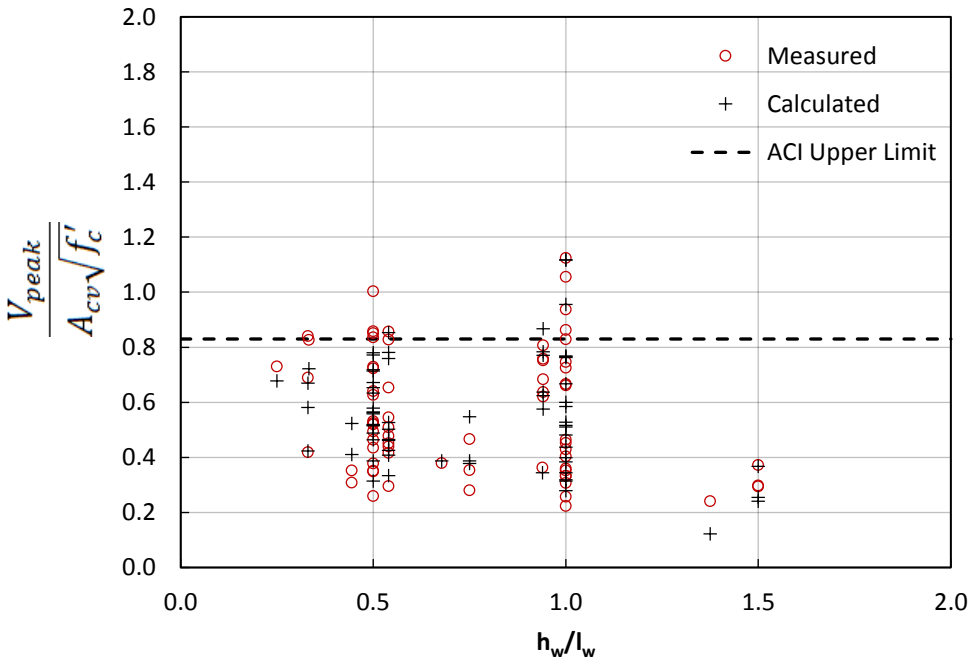

Figure 3-5. Variation of the predicted and measured normalized peak shear strength with wall aspect ratio compared to ACI 318 upper limit.

CHAPTER 4. DISPLACEMENT CAPACITY OF SQUAT WALLS WITH RECTANGULAR CROSS SECTION

4.1 Introduction

Many equations are found in current US design codes and literature for the prediction of the peak shear strength of reinforced concrete walls. However, the available expressions for the prediction of the displacement capacity of these structural systems are more limited. Current design codes and standards usually provide fixed values for the allowable drift to control structural damage. Duffey et al. (1994a, 1994b) found that design codes and standards tend to provide unconservative drift limits for the case of low-rise RC walls as most of them are focused on high rise buildings generally having slender walls. It has been generally accepted that squat walls tend to exhibit brittle shear controlled failures while slender walls tend to fail in more ductile flexural failure modes with less influence of shear deformations.

Some researchers (e.g. Hidalgo, 2000; Carrillo, 2010; Sánchez, 2013) have proposed different expressions to calculate the displacement or drift capacity of squat RC walls based on calibration against limited experimental data. While significant research has been performed during the past years to address this situation, the development of better equations to assess the displacement capacity of squat RC walls is still necessary. It is important to note that the scatter on the predictions of displacement capacity is considerable. The accurate prediction of the displacement capacity of squat walls is a challenging task since it involves several complex failure mechanisms and other displacement sources, which are individually highly variable in nature.

Squat RC walls are commonly shear controlled elements and generally its load displacement behavior does not show a clear yielding point. A major stiffness reduction is commonly observed prior to peak strength development and followed by prompt strength degradation with relatively low ductility. For structural analysis purposes, this behavior can be represented with a hysteretic model using a tri-linear backbone curve. This chapter presents an evaluation of current expressions for the prediction of the displacement capacity of squat reinforced concrete walls

with rectangular cross section found in the literature. The performance of each of the selected equations was assessed by comparing the displacement predictions with experimental displacements from the assembled database for walls with rectangular cross section. Key parameters influencing the displacement capacity were identified. The experimental displacements of each wall were taken as the average of the displacements measured from the first and third quadrants (i.e. positive and negative loading directions, respectively). New equations to predict the displacement capacities of squat walls at diagonal cracking, peak strength, and ultimate state, are presented to improve current displacement estimates. These displacement capacity estimates, in conjunction with the peak strength estimate presented in Chapter 3 can be used to define the backbone curve for a hysteretic model. The equations were obtained from multivariable linear regression analyses using an assembled experimental database from various experimental programs which is presented on Chapter 2 and Appendix A. The expressions presented herein are intended to apply for squat walls with rectangular cross section and a wide range of characteristics.

4.2 Current Expressions for Estimation of Displacement Capacity

The following subsections discuss the selected current equations for displacement capacity prediction. The equations shown are similar to those presented on the corresponding references but the names and subscripts of the parameters have been modified to maintain uniformity within equations, database and script throughout this document.

4.2.1 Hidalgo et al. (2000)

Hidalgo et al. (2000) developed a hysteretic model for the analysis of cyclic lateral load-displacement behavior of squat RC shearwalls. The authors used a tri-linear hysteresis envelope and proposed the following equations for the estimation of the drift at shear cracking, peak strength, and the ultimate drift, based on linear regression from experimental results.

$$\Delta_{cr} = \left(0.00175\frac{M}{Vl_w}\right)h_w \qquad \text{for} \qquad M/Vl_w \le 1.0 \qquad (4\text{-}1)$$

$$\Delta_{cr} = \left(0.00155 + 0.0002\frac{M}{Vl_w}\right)h_w \quad \text{for} \quad M/Vl_w > 1.0 \quad (4\text{-}2)$$

$$\Delta_{peak} = \left(0.0027 + 0.0033\frac{M}{Vl_w}\right)h_w \quad \text{for} \quad M/Vl_w \leq 1.0 \quad (4\text{-}3)$$

$$\Delta_{peak} = \left(0.0056 + 0.00033\frac{M}{Vl_w}\right)h_w \quad \text{for} \quad M/Vl_w > 1.0 \quad (4\text{-}4)$$

$$\Delta_u = \left(0.002 + 0.012\frac{M}{Vl_w}\right)h_w \quad \text{for} \quad M/Vl_w \leq 1.0 \quad (4\text{-}5)$$

$$\Delta_u = 0.014h_w \quad \text{for} \quad M/Vl_w > 1.0 \quad (4\text{-}6)$$

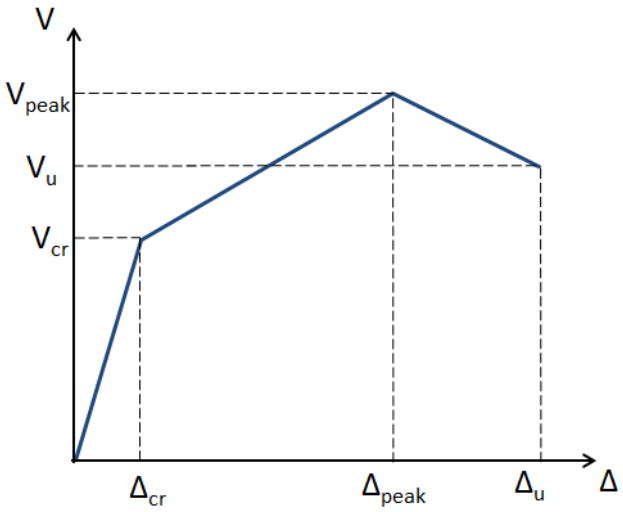

Figure 4-1. Tri-linear backbone model proposed by Hidalgo et al. (2000).

The authors recommended to use the ACI 318 seismic design provisions for determining the peak shear strength with slight modifications to increase the concrete strength coefficient (α_c) for walls with aspect ratios below 1.5 and taking the wall area (A_{cv}) as the thickness times the minimum of the wall length and wall height. Further information can be found on Hidalgo and Jordán (1996). The shear force corresponding to the cracking point was recommended to be

taken as the concrete contribution to strength of the ACI 318 seismic provisions and using the same recommendations as for peak strength. The ultimate displacement was defined as the displacement associated to a 20% decrease in strength (80% V_{peak}) after peak point.

4.2.2 Carrillo (2010)

Carrillo (2010) presented a tri-linear backbone model for the analysis of squat walls. The model was based on the observations from an experimental program carried-out at Universidad Nacional Autónoma de México (UNAM) which was focused on studying the seismic behavior of squat RC walls representative of typical housing in several Latin American countries. In the same manner as in Hidalgo et al. (2000), the model presented by Carrillo (2010) included a stiffness reduction which was deemed to be associated to the occurrence of significant diagonal web cracking. Model backbone shape is similar to the model presented by Hidalgo et al. (2000) but different expressions for the estimation of the cracking, peak and ultimate points were proposed (refer to Figure 4-1). Carrillo (2010) proposed the following equations to calculate the drift ratio at diagonal cracking as a percentage:

$$R_{cr}(\%) = \left(\frac{V_{cr}}{K_{cr}}\right)\frac{100}{h_w} \tag{4-7}$$

$$K_{cr} = \frac{1}{\left(\frac{h_w^3}{c_1 3E_c I_g} + \frac{h_w}{c_2 G_c A_{cv}}\right)} \tag{4-8}$$

where V_{cr} is the diagonal cracking strength, K_{cr} is the cracked stiffness of the wall considering both flexural and shear deformations, I_g is the strong axis gross moment of inertia of the wall cross section, G_c is the shear modulus of elasticity of concrete, E_c is the modulus of elasticity of concrete, c_1 is a factor to account for flexural stiffness reduction due to cracking, and c_2 is a factor to account for reduced shear stiffness due to cracking. Carrillo (2010) recommended taking both stiffness modifiers equal to 0.5 to represent the cracked stiffness. For an uncracked element both factors should be taken equal to 1.0.

Ultimate displacement was defined as the displacement associated to a 20% decrease in strength (80% V_{peak}) after peak point. Carrillo (2010) proposed the following equations to calculate the drift ratio at peak strength and ultimate drift ratio as a percentage:

$$R_{peak}(\%) = \frac{V_{peak}}{t_w\sqrt{f_c'}}\frac{1}{5200}e^{1.30\frac{M}{Vl_w}} \tag{4-9}$$

$$R_u(\%) = \frac{V_{peak}}{t_w\sqrt{f_c'}}\frac{1}{3650}e^{1.35\frac{M}{Vl_w}} \tag{4-10}$$

The peak shear strength can be calculated with the equation proposed by Carrillo (2010) which was based on calibration of the ACI 318 equation form against experimental data. The cracking strength was assumed as the concrete contribution to strength. Further information can be found on Carrillo (2010).

4.2.3 Sánchez (2013)

Sánchez (2013) proposed a backbone model similar to the proposed by Hidalgo et al. (2000) and Carrillo (2010) but modified to include a first stiffness reduction due to flexural cracking and a second stiffness reduction due to distributed diagonal cracking. An additional line segment to represent the initial uncracked stiffness and the reduced stiffness after flexural cracking was included. Based on the experimental results from RC shear walls with similar characteristics of those used for housing in Mexico, Sánchez (2013) proposed equations to estimate the strength and displacement at flexural cracking, diagonal cracking, peak strength and ultimate damage state as shown in Figure 4-2. Further information regarding the strength estimates can be found on Sánchez (2013).

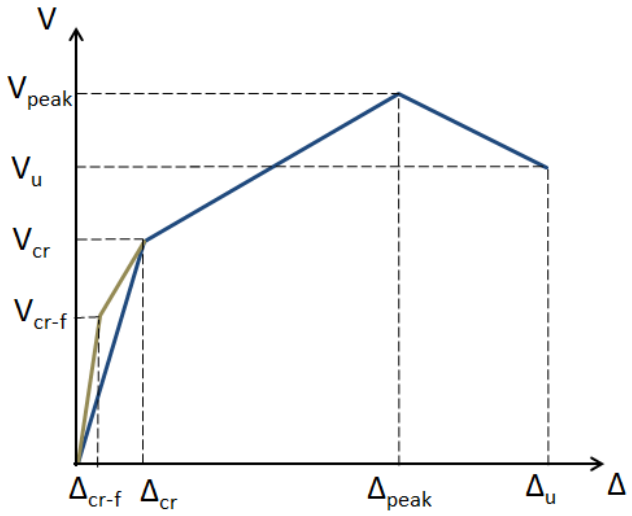

Figure 4-2. Backbone model proposed by Sánchez (2013).

Sánchez proposed to calculate the displacement at flexural cracking using the following expression:

$$\Delta_{cr-f} = \left(0.01 + 0.005\frac{h_w}{l_w}\right)\frac{h_w}{100} \tag{4-11}$$

Then, the flexural cracking strength would be calculated by multiplying the drift at flexural cracking by the elastic stiffness of a cantilever wall considering flexural and shear deformations and uncracked properties ($c_1 = c_2 = 1$).

Sánchez also proposed to calculate the displacement at diagonal cracking point using the following expression:

$$\Delta_{cr} = \left(0.025 + 0.13\frac{M}{Vl_w}\right)\frac{h_w}{100} \tag{4-12}$$

The diagonal cracking strength associated with this displacement was proposed to be calculated as:

$$V_{cr} = \left(0.32 - 0.045\frac{M}{Vl_w}\right)\sqrt{f_c'}A_{cw} \tag{4-13}$$

The author proposed to calculate the displacement at peak strength (Δ_{peak}) by calculating the flexural (Δ_f) and shear (Δ_s) displacement components (mm) separately using the following expressions:

$$\Delta_{peak} = \Delta_f + \Delta_s \tag{4-14}$$

$$\Delta_f = \frac{V_{peak} h_w^3}{3EI} \tag{4-15}$$

$$\Delta_s = \frac{V_{peak} l_w}{A_w \sqrt{f_c'}} \frac{1}{300} e^{1.33\frac{M}{Vl_w}} \tag{4-16}$$

where the modulus of elasticity (E) in MPa is defined as $4400\sqrt{f'c}$, the cracked moment of inertia (I) is taken as 70% of the gross moment of inertia (mm^4), V_{peak} is the peak strength (N), h_w is the height of the wall (mm), l_w is the length of the wall (mm) and A_w is the effective shear area of the cross section (mm^2). The proposed expression for the calculation of peak strength can be found on Sánchez (2013).

The author defined ultimate state as the point past the peak strength where a strength degradation of 20% was attained. As shown in the next equations, the ultimate displacement (Δ_u) was proposed to be calculated by adding the contribution of the horizontal reinforcement ($\Delta_{\rho h}$) to the peak displacement and multiplying by the displacement capacity ductility calibrated with the experimental data.

$$\Delta_u = \left(\Delta_f + \Delta_s + \Delta_{\rho h}\right) \times \left(0.6\frac{M}{Vl_w} + 0.5\right) \geq 1.2\Delta_{peak} \tag{4-17}$$

$$\Delta_{\rho h} = 9/\rho_h f_{yh} \leq 9mm \tag{4-18}$$

4.2.4 Gérin and Adebar (2004)

Gérin and Adebar (2004) proposed a model to calculate the load-displacement response of reinforced concrete elements controlled by brittle shear failure when subjected to reversed cyclic shear loading. The model was based on the experimental observations of 21 large-scale

membrane-type element tests. The backbone curve of the model can be represented by the curve shown on the following figure.

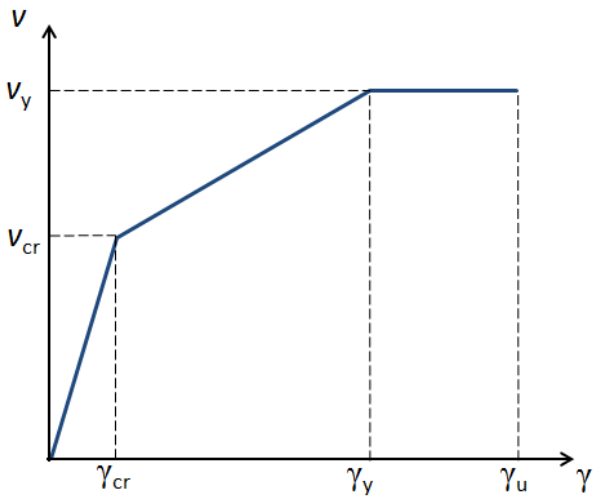

Figure 4-3. Backbone model proposed by Gérin and Adebar (2004).

The stress (v_{cr}) and shear strain (γ_{cr}) at shear cracking were proposed to be calculated with the following expressions:

$$v_{cr} = f_{cr}\sqrt{1+\frac{\sigma_v}{f_{cr}}} \tag{4-19}$$

$$\gamma_{cr} = \frac{v_{cr}}{G_c} \tag{4-20}$$

$$f_{cr} = 0.33\sqrt{f_c'} \tag{4-21}$$

$$G_c = 0.4E_c \tag{4-22}$$

where f_{cr} is the concrete tensile cracking stress, σ_v is the vertical axial stress (positive sign for compression), G_c is the uncracked shear modulus of elasticity of concrete and E_c is the modulus of elasticity of concrete.

On this model the yield (peak) stress (v_y) is recommended to be calculated per ACI 318-08 and the shear strain at yield (shear strain at peak strength - γ_y) is calculated using the following equation:

$$\gamma_y = \frac{f_{yh}}{E_s} + \frac{v_y - \sigma_v}{\rho_v E_s} + \frac{4v_y}{E_c} \tag{4-23}$$

where f_{yh} is the horizontal reinforcement yield stress, ρ_v is the vertical reinforcement ratio and E_s is the reinforcement modulus of elasticity.

At ultimate state, the shear stress remains the same as in the yield point and the ultimate shear strain (γ_u) is obtained by multiplying the shear strain at yield by the shear strain ductility with the following expression:

$$\gamma_u = \left(4 - 12\frac{v_y}{f_c^{'}}\right)\gamma_y \tag{4-24}$$

where the yield shear stress shall not be taken larger than 25% of the concrete compressive strength ($v_y \leq 0.25\, f'_c$). The authors conservatively imposed this limit in the shear ductility to consider the possibility of concrete diagonal compression failure.

4.2.5 ASCE 41-13

This version of the standard modifies the numerical modeling provisions for RC shear walls and associated components controlled by shear from the previous version (2006) of the ASCE 41 standard. The changes are based on recommendations by Wallace (2007) which incorporates a major stiffness reduction to consider the effect of typical inclined shear cracking. Therefore, the backbone curve changes from a bilinear to a tri-linear shape in order to provide a better representation of low-rise walls behavior; where shear deformations are very significant in comparison to flexural deformations. The backbone characteristics can be described with the following figure.

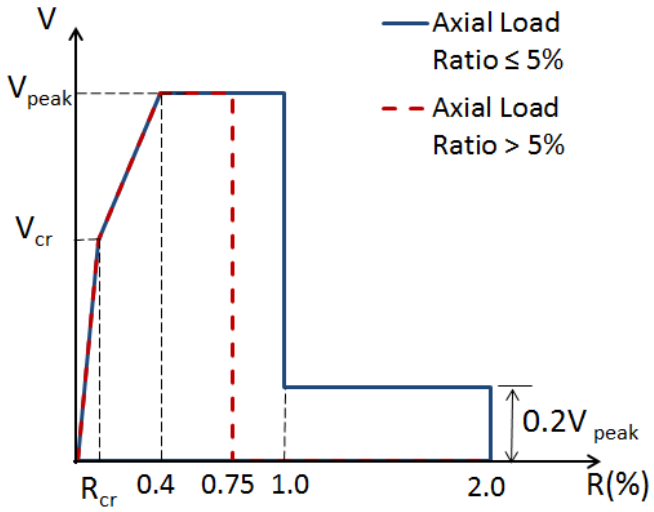

Figure 4-4. Backbone model proposed by Wallace (2007) and ASCE 41-13.

As suggested by Wallace (2007) and Elwood et al. (2007) walls with significant axial loading can show reduced drift capacity and residual strength. Therefore, the model reduces the drift capacity from 1% to 0.75% and the residual strength from $0.2V_{peak}$ to 0 for walls with axial load ratios (P/f'_cA_g) greater than 0.05.

Wallace (2007) suggested that the cracking strength be calculated by the following equation which was obtained based on simplified expressions for principal tensile stress limited to approximately $0.33\sqrt{f_c'}$.

$$V_{cr} = 0.33\sqrt{f_c^{'}}\sqrt{1+\frac{P/A_g f_c^{'}}{48.2\sqrt{f_c^{'}}}}A_w \le 0.6V_n \qquad (4\text{-}25)$$

However, the ASCE 41-13 standard approximates the inclined cracking strength as 0.6 V_{peak} which was considered typical for older buildings (Wallace, 2007). The corresponding drift can be calculated by dividing the inclined cracking strength by the elastic stiffness (K_e) of a cantilever wall considering flexural and shear deformations and uncracked properties ($c_1 = c_2 = 1.0$).

4.2.6 Duffey et al. (1994a, 1994b)

Duffey et al. (1994a, 1994b) suggested average values for drift ratio at peak strength and at several stages of strength degradation past the peak strength, based on statistical analysis of experimental data compiled from numerous experimental studies. They found mean and median drift ratio at peak strength of 0.80% and 0.72%, respectively. The authors also published the central tendency values for subsequent damage stages such as attaining 90, 80, 70, 60 and 50% of the peak strength. However, the authors stated that care must be exercised when modelling using values of drift beyond the peak strength since relatively small energy dissipation capacity may remain in the wall (due to rapid strength and stiffness degradation) while the earthquake motion may still impart significant energy. Even though some walls may have enough energy dissipation capacity after attaining peak strength, data for this advanced damage stage was scarcer since many of the early experimental studies presented data only up to the peak load. Therefore, they recommended using the drift ratio values associated to the peak strength as the ultimate drift capacity when performing analyses using hysteretic models. Duffey et al. (1994a, 1994b) also noted that the allowable drift limits on most design codes and standards tend to be unconservative for low-rise RC shearwalls because those are mainly focused on high rise buildings comprised of slender walls which generally have higher ductility.

4.3 Development of New Displacement Capacity Predictive Equations

The experimental load-displacement envelope of these type of shear-controlled walls does not typically show a clear yielding point, but major stiffness reduction is generally observed prior to the peak strength, and the post-peak response is characterized by rapid strength degradation showing relatively low ductility (see Figure 4-5). For structural analysis purposes, this behavior can be represented with a hysteretic model using a tri-linear backbone curve (see Figure 4-1).

Drift data was collected from numerous experiments found in literature and were included in the assembled database. The availability of displacement data is more limited than peak strength data since not all the references included in this study included displacements, drift or global force-displacement data. Drift data collection was possible for 63 of the 70 specimens with rectangular cross section listed in the database (Appendix A). The drift data for the ultimate state (20%

strength drop) was even scarcer since many of the early experimental studies presented data only up to the peak load. Therefore, only 58 qualifying datasets of ultimate drift could be obtained from the evaluated references for walls with rectangular cross section.

Most of the data was obtained from global force-displacement hysteresis curves found on the evaluated references. Therefore, it considers the total drift instead of separate shear and flexural displacement components. The vast majority of cyclic tests were displacement controlled, where the wall specimen is loaded to a specific displacement in one direction, then the load is reversed to the same displacement in the opposite direction. Typically, specimens were subjected to several load reversal cycles (2 or 3) at the same displacement level as shown on Figure 4-5. In order to obtain the drift data, first, the cyclic envelope was traced from the hysteresis curves, and the displacement data was converted to drift ratio (taken as the ratio between the lateral displacement to height where displacement was measured). Straight lines connecting the peaks of the first cycle at each displacement level were used to trace the experimental envelope (see Figure 4-5). The load-displacement envelope was not extrapolated further than the last loading peaks. Afterwards, the drift ratios corresponding to the assumed diagonal cracking condition (R_{cr}), peak strength (R_{peak}) and at ultimate state (R_u) were retrieved from the obtained cyclic envelope. The average drift ratio from 1st and 3rd quadrants of each wall were recorded for each of the three states. Cracking drift ratio was defined as that corresponding to the development of 60% of peak strength, while ultimate drift ratio was defined as that corresponding to the post-peak point where a strength degradation of 20% is attained. Further details are discussed in the next sub-sections. For tests where ultimate displacement data was not available for one of the loading directions (commonly when test is stopped due to sudden failure in the opposite direction), the single value available for the ultimate displacement was recorded.

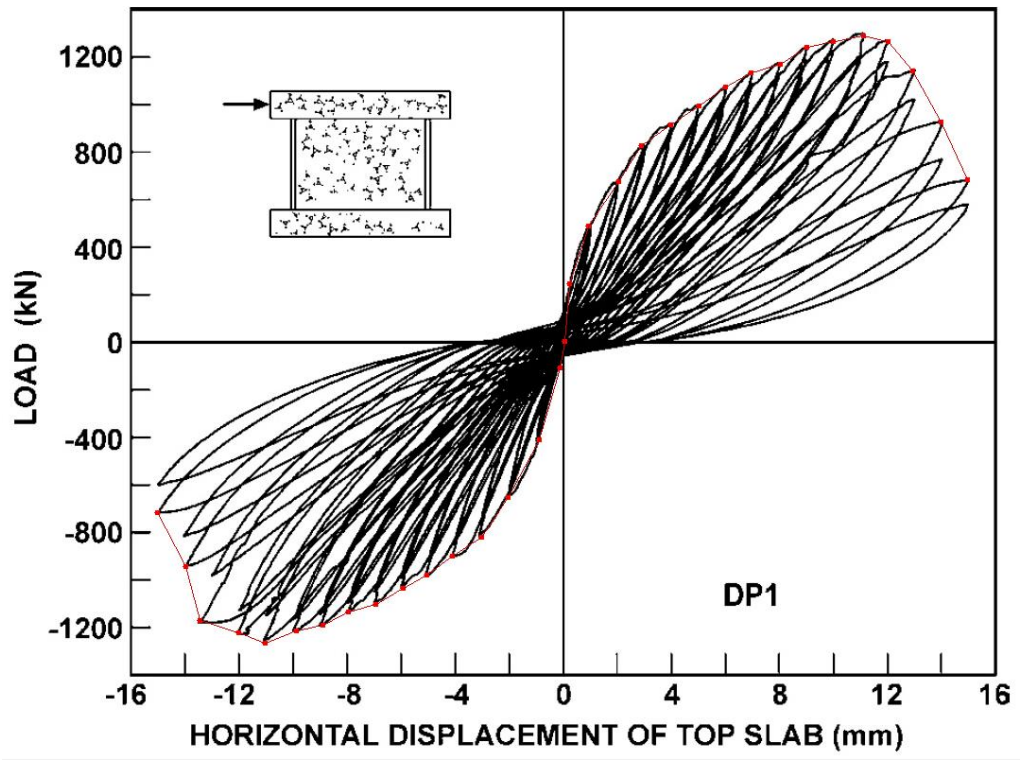

Figure 4-5. Representative experimental load-displacement envelope (adapted from Palermo and Vecchio, 2002).

Regression analyses were performed to develop empirical equations that better fits the collected drift data. The goal was to lower the coefficient of variation and to obtain a mean value near to 1.0 for the ratio of predicted-to-measured drift capacity. Key parameters were identified by evaluating the correlation coefficient with the drift capacity. The correlation coefficient can range from 0 to 1.0 and indicates the degree of linear relationship between two variables. A correlation coefficient with a value of 1 indicates a perfect correlation while a value of 0 indicates that no correlation exists. Multivariable linear regression analyses were carried to derive the equations with the selected parameters. In order to simplify the equations, the least meaningful parameters were eliminated (one at a time), based on the highest p-value, and the equation was recalibrated by regression. This process was repeated until the scatter of the prediction was observed to increase. In order to minimize bias due to test specimens' scale, the collected displacement data was converted to drift ratio, reinforcement spacing was normalized with wall thickness and any parameter involving forces was normalized with the effective shear area of the section (A_{cv}) for the calibration and development of equations. The following sub-

sections present the simplified expressions using the most significant parameters that were found to produce a better correlation with the database, and are proposed for the prediction of drift ratio at diagonal cracking, drift ratio at peak strength and at ultimate drift ratio, respectively.

4.3.1 Drift Ratio at Diagonal Cracking

Researchers have used different approaches to estimate the point at which the first main stiffness reduction occurs. It has been reported by some researchers (e.g. Salonikios et al., 2000; Carrillo, 2010; and Greifenhagen and Lestuzzi, 2005) that first significant yield generally occurred close to the development of 75 to 80% of the maximum lateral strength of RC squat walls specimens.

However, most researchers coincide on the assumption that the first major stiffness decrease is related to the occurrence of significant inclined cracking across the web with enough crack width as to start mobilizing a shear friction mechanism through crack surfaces. Carrillo and Alcocer (2012) suggested that distributed diagonal cracking occurs at a lateral load higher than that associated with the first inclined web crack and that it generally occur at load levels lower than that associated with onset yielding of reinforcement. Carrillo and Alcocer (2012) also proposed to assume the cracking shear equal to the concrete contribution to shear strength.

Sánchez (2013) points out that the first significant diagonal cracking does not cover the whole length of the wall and the typical crack width at this stage is in the order of 0.3 mm to 0.6 mm. Therefore, Sánchez (2013) defined the significant diagonal cracking strength as the lateral force at which the cracks have widened to 0.5 mm and cracking covers 40% of the wall length. Calibrated expressions for the cracking strength and cracking drift based on experimental observations were proposed by Sánchez (2013).

Wallace (2007) suggested modifications to the ASCE 41-06 standard to include a point of stiffness reduction associated to the concrete diagonal cracking into the backbone curves for shear-controlled walls and wall segments, and recommended an expression to calculate the cracking strength. ASCE 41-13 incorporated the recommendations by Wallace (2007) and provides fixed drift ratio values for determining the drift capacities, but allows the cracking strength to be taken as 60% of the peak strength.

For the purpose of simplicity, it was assumed in this study that both, the significant inclined cracking and ultimate damage states occur at a fixed portion of the peak strength. In order to better represent the squat shear walls behavior, two options for the estimation of the cracking or "first yield" point were considered. In the first option, the main decrease in stiffness was assumed to occur upon loading to 60% of peak strength, which has been considered to be the typical lateral force associated to significant inclined cracking (Wallace, 2007 and ASCE 41-13). On the second option, it was assumed that the main stiffness reduction occurs upon loading to 75% of the peak strength which could be representative of the onset reinforcement yielding. The definition of the first stiffness reduction point, based on the 60% of the peak strength (diagonal cracking), was found to generally better approximate the ascending branch of the experimental envelope and the initial stiffness. Therefore, the cracking drift equation was fitted based on the assumption that significant web cracking occurs at the point where 60% of the maximum strength is attained. The parameter selection and equation calibration approach by multiple linear regression analyses was described on previous section (4.3). The following simplified expression includes the most significant parameters that were found to produce a better correlation with the database and is proposed for the prediction of drift ratio at significant diagonal cracking state (R_{cr}) of squat RC walls with rectangular cross section.

$$R_{cr} = 0.0006 + 0.124\rho_{be} + 0.093\rho_h + 0.000024\frac{l_w}{t_w} \tag{4-26}$$

where ρ_{be} is the boundary element reinforcement ratio (A_{sbe}/A_{cv}), ρ_h is the horizontal reinforcement ratio, l_w is the wall length and h_w is the wall height.

4.3.2 Drift Ratio at Peak Strength

Different approaches to obtain the displacement capacity at peak strength have been used in other studies presented earlier. Carrillo (2010) and Sánchez (2013) calibrated their displacement capacity at peak strength expressions based on the observed peak strength and the moment-to-shear span ratio as main predictive parameters. Gérin and Adebar (2004) used a theoretical mechanics approach to determine the shear strain at peak strength. Hidalgo et al. (2000) used the moment-to-shear span ratio as the only predictive parameter for their expressions. ASCE 41-13 establishes a typical fixed value for the estimation of displacement at peak strength.

Based on the observed approaches made by other researchers, two main options were evaluated in this study for the development of equations to estimate the displacement capacity at peak strength of squat RC walls with rectangular cross section. The first option considered that the peak shear strength was an influential parameter on the displacement at peak strength, while other parameters were selected based on the correlation coefficient. On the second option, all the influential parameters were preliminarily selected based on their correlation coefficient with the displacement data. In both options the same general approach in terms of the iterative process of simplifying the equations by eliminating the least meaningful parameters based on the p-value as described earlier was employed.

While some researchers have found that the peak strength is a good predictive parameter, no strong correlation between the peak strength and the displacement at peak strength was found in the database included in this study. The following simplified equation includes the parameters found to produce a better correlation with experimental data considered in this study; and is proposed for the estimation of the drift ratio at peak strength (R_{peak}) of squat RC walls with rectangular cross sections.

$$R_{peak} = 0.0094 - 0.000006 f_{yh} + 0.000063 f_c^{'} - 0.00044 \frac{s_h}{t_w} \quad (4\text{-}27)$$

where f_{yh} is the horizontal reinforcement yield stress (MPa), f'_c is the concrete compressive strength (MPa), s_h is the horizontal reinforcement spacing (mm), and t_w is the wall thickness (mm).

4.3.3 Drift Ratio at Ultimate Damage State

The ultimate drift equation was fitted based on the definition of ultimate damage state as the point where the strength degrades to attain 80% of the peak strength. Similar assumptions have been used by numerous researchers to define the ultimate damage state. Kazaz et al. (2012) defined ultimate state as the point on the load-deformation curve where strength drops abruptly or degrades to 85% of the maximum strength. Several researchers (i.e. Sánchez, 2013; Carrillo, 2010; Kuang and Ho, 2008; Greifenhagen and Lestuzzi, 2005; Hidalgo, 1996; Park, 1989; among others) have defined the ultimate drift as that corresponding to a 20% strength drop after

peak strength. Salonikios et al. (2000) defined the ultimate damage state when the strength has dropped 25% of the peak strength. This ultimate state criterion has been conventionally used for RC walls and other type of concrete members subject to lateral loading.

Regarding the estimation of displacement capacity at ultimate state, different approaches have been used by other researchers as well. Carrillo (2010) based his estimated capacity on he observed peak strength and the moment-to-shear span ratio. Sánchez (2013) and Gérin and Adebar (2004) used a calibrated ductility expression to estimate the ultimate displacement. Hidalgo et al. (2000) used the moment-to-shear span ratio as the only predictive parameter for the ultimate drift capacity. ASCE 41-13 establishes a typical fixed value for the estimation of ultimate drift capacity for walls with low axial load ratio and for walls with significant axial load ratio, respectively.

In a similar fashion as for the displacement at peak strength, several options using multiple linear regressions were evaluated in this study. The two options used for the displacement at peak strength (i.e. considering a term related to the peak strength, and considering other parameters but peak strength) were evaluated for the ultimate displacement as well. An additional option based on the calibration of the observed displacement ductility (Δ_u/Δ_{peak}) was considered for this damage state. The same iterative approach for parameters selection and simplification of the final equation described on earlier sections was used herein for all three options.

The following expression is proposed for the estimation of ultimate displacement (R_u) of squat RC walls with rectangular cross section in terms of drift ratio:

$$R_u = 0.013 + 0.302\rho_v - 0.0046\frac{s_h}{t_w} + 0.0042\frac{s_v}{t_w} + 0.001\frac{P}{A_g} \geq R_{peak} \quad (4\text{-}28)$$

where ρ_v is the vertical reinforcement ratio, s_h is the horizontal reinforcement spacing (mm), s_v is the vertical reinforcement spacing (mm), P is the axial load (N), and A_g is the gross cross sectional area (mm^2).

4.4 Evaluation of Selected Displacement Capacity Equations

In this section the selected predictive equations found in literature and the new expressions developed herein were evaluated in terms of their predictive performance by using a statistical analysis approach and comparing to the experimental data compiled in the assembled database (Appendix A). In order to minimize bias due to test specimens scale, all the displacement predictions were converted to drift ratio for comparison.

The following subsections show detailed analysis of the performance of each of the equations developed in this study for each of the three defined damage states, and compares them to the performance of the corresponding equations found in literature. Tabulated summaries of common central tendency and dispersion measures of the predicted-to-measured drift ratios, along with the percent of over-predictions, are presented in the same fashion as presented on Chapter 3 for the strength predictions. Mean and median values larger than 1.0 suggest that the equation tends to overestimate the drift ratio. On the other hand, the standard deviation and coefficient of variation (COV) provide information on the dispersion (scatter) of the predicted-to-measured drift ratio. In other words, the mean and median values give useful information on the accuracy of the predictive equation while the standard deviation and coefficient of variation provide information regarding the precision of the equation. The % over-predictions provides information on the bias of the predictions. A non-biased equation will yield results having % over-predictions of around 50%. A lower % of over-predictions would represent an equation producing biased estimates that tend to underestimate drift ratios, while a higher % of over-predictions indicates that the equation produces biased estimates that tend to overestimate drift ratios.

Sections 4.4.1, 4.4.2 and 4.4.3 will discuss the findings for the displacement at diagonal cracking, displacement at peak strength and ultimate displacement, respectively.

4.4.1 Drift Ratio at Diagonal Cracking

The performance of the equations for the prediction of the cracking or “first yield” displacement will not be compared as all of them are based on different assumptions of the corresponding strength at which the stiffness reduction occurs, and therefore, are not directly comparable. Thus,

only statistical analysis of the drift ratio at diagonal cracking predictions using the equation developed in this study is presented. The equation was calibrated based on the assumption that the first major decrease in stiffness takes place upon development of 60% of the peak strength. This assumption is more likely to represent the significant diagonal cracking condition than the onset of reinforcement yielding. Figure 4-6 shows a graphic representation of the correlation of the calculated drift ratio at diagonal cracking vs. the measured drift ratio at diagonal cracking for the 63 rectangular cross section wall tests with available drift data included in the database.

The diagonal line represents a ratio of predicted-to-measured cracking drift ratio of 1.0. Any point falling on the line means an exact prediction of the cracking drift ratio. Any point above the diagonal line represents an over-prediction of strength and vice-versa. The farther the point from the diagonal represents a larger error on the estimate. It can be noted from Figure 4-6 that the equation proposed in this study (equation 4-26) provides a reasonable estimate of the experimental values.

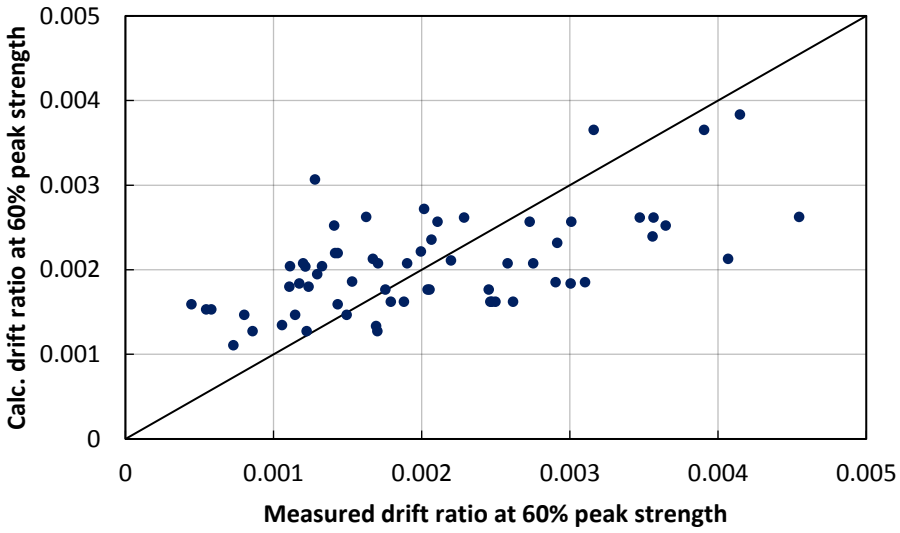

Figure 4-6. Correlation between calculated drift ratio at 60% peak strength and measured drift ratio at 60% peak strength for walls with rectangular cross section included in the database.

Table 4-1 presents a summary of common central tendency and dispersion measures of the predicted-to-measured cracking drift ratio, along with the percent of over-predictions. It can be

noted that the variability of the calculated-to-measured drift at diagonal cracking strength is relatively high but the equation can produce reasonable estimates on an average sense.

Table 4-1. Summary of statistics of the ratio of predicted-to-measured drift at 60% peak strength for walls with rectangular cross section included in the database.

	This study
Mean	1.20
Median	1.09
Minimum	0.52
Maximum	3.56
Std. dev.	0.58
COV	0.48
% Over-predictions	54.0

4.4.2 Drift Ratio at Peak Strength

In order to evaluate the suitability of the proposed equation 4-27 for the estimation of the drift ratio at peak strength, it is compared against several equations/models found in literature. Figure 4-7 shows a graphic representation of the correlation of the calculated drift ratio at peak strength vs the measured drift ratio at peak strength for the 63 obtained datasets of walls with rectangular cross section in the considered database, and for each of the equations presented on section 4.2.

The diagonal line represents a ratio of predicted-to-measured strength of 1.0 and any point above or below the diagonal line represents an over-prediction or an under-prediction, respectively. Figure 4-7 shows that the scatter on the predictions is significant. However, it is observed that the equation proposed in this study (equation 4-27) reduces the scatter of the drift ratio at peak strength estimate over most of the evaluated equations. It seems that Hidalgo et al. (2000) equation produces similar scatter as equation 4-27 but tends to underestimate the predictions. On the other side, fixed drift ratio provided by ASCE 41-13 tends to underestimate actual value in most cases. ASCE 41-13 suggests a drift ratio of 0.004 at the development of peak strength while the average drift ratio from test data resulted to be 0.0076.

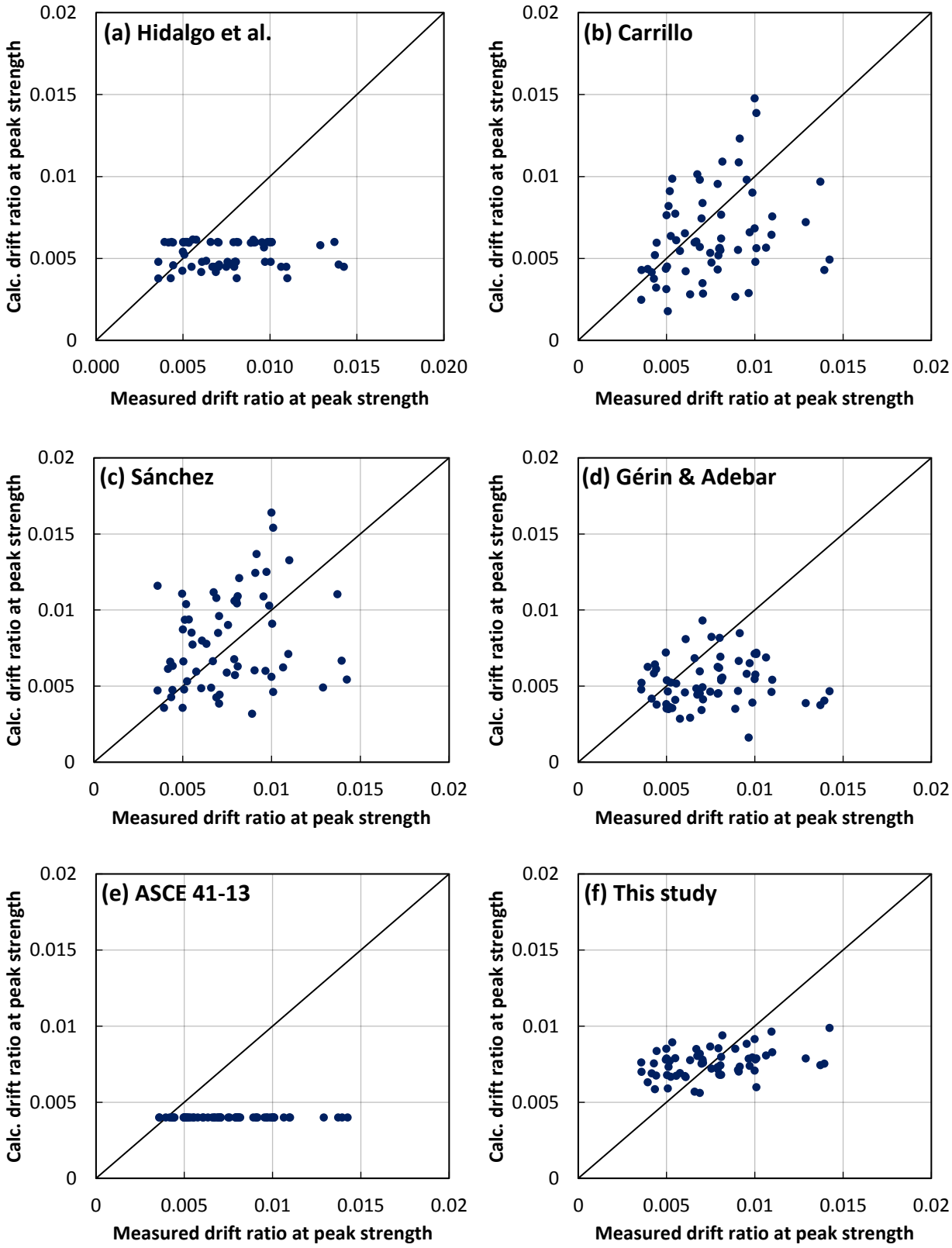

Figure 4-7. Correlation between calculated drift ratio at peak strength and measured drift ratio at peak strength using various available equations: (a) to (e); and the new equation proposed in this study (f).

In order to numerically compare the predictive performance of each equation, Table 4-2 presents a summary of common central tendency and dispersion measures of the predicted-to-measured drift ratio at peak strength, along with the percent of over-predictions. Figure 4-8 shows a typical box and whisker plot comparing the distribution of the predicted-to-measured drift ratio for each selected equations/models. The graph shows the lower quartile (25^{th} percentile), median, upper quartile (75^{th} percentile), the extreme values and the mean value marked with "+" symbol. The central box in the box and whisker plot is constituted by the second and third quartile and represents the spread of the central 50% of the observations. The range of this box is commonly known as the inter-quartile range (IQR), midspread or middle fifty. The narrower this range (or box in the graph) is, indicates the lesser the variability since the central 50% of the observations are nearer to the median value. The lower and upper whiskers of the plot represent the spread of the first and fourth quartile, being the ends of the whiskers the extreme (i.e. maximum and minimum) values marked with "-" tick mark.

Table 4-2. Summary of statistics of the ratio of predicted-to-measured drift at peak strength for walls with rectangular cross section included in the database.

	Hidalgo et al.	Carrillo	Sánchez	Gérin & Adebar	ASCE 41-13	This study
Mean	0.78	0.90	1.14	0.77	0.59	1.11
Median	0.67	0.87	1.19	0.70	0.56	1.08
Minimum	0.31	0.30	0.36	0.17	0.28	0.54
Maximum	1.52	1.84	3.23	1.58	1.12	2.13
Std. dev.	0.29	0.38	0.50	0.33	0.21	0.36
COV	0.38	0.42	0.44	0.42	0.35	0.33
% Over-predictions	27.0	36.5	58.7	22.2	4.8	52.4

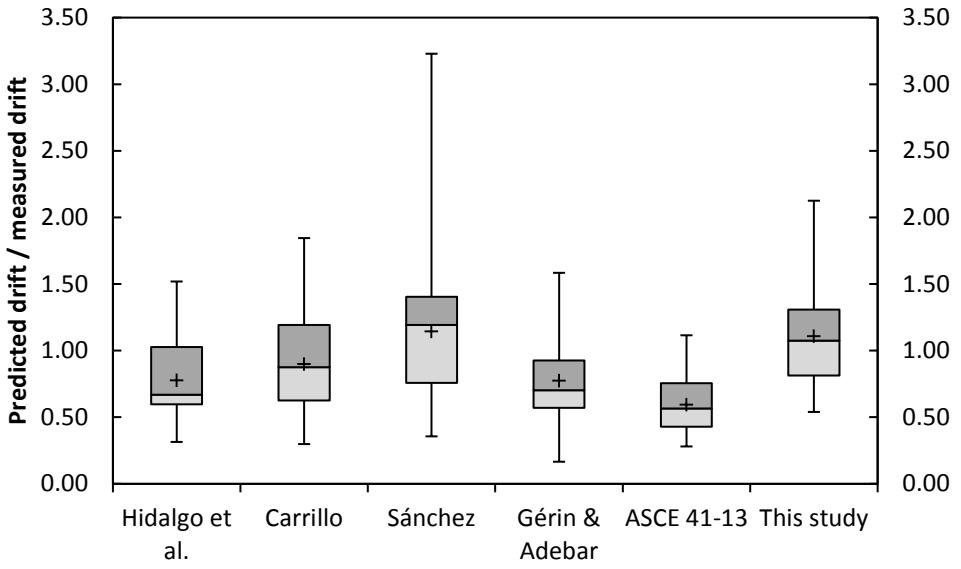

Figure 4-8. Distribution of the ratio of predicted-to-measured drift at peak strength.

From the statistics presented on Table 4-2 and from Figure 4-8 it can be observed that the proposed equation produces an improved estimate of the drift ratio at peak strength since the mean and median predicted-to-measured values are closer to 1.0, whereas the coefficient of variation (COV) is kept in a similar level or lower than that of other predictions. It is also observed that the midspread falls between 0.81 and 1.31, which means that the ratio of predicted-to-measured values for 50% of the observations is closer to the median, and thus closer to a value of 1.0. In terms of the range (difference between maximum and minimum values), the equation proposed in this study is on par with the rest of the equations with the exception of ASCE 41-13 provision which underestimated the drift ratio in most cases; and Sánchez (2013) equation which tends to slightly over-predict (on an average sense) and shows the highest scatter. In the same manner, the proposed equation yields 52.4% of over-predictions which is very near to the intended value of 50%. Note that ASCE 41-13 and Hidalgo et al. (2000) expressions tend to under-predict drift ratio at peak strength of squat walls with rectangular cross sections. This is observed on the box and whisker plot, central tendency statistics, and on the low % over-predictions.

It is important to note that obtaining a low COV for the prediction of displacement capacity of RC squat shear walls is difficult due to the stochastic nature of the several factors contributing to the lateral displacement and different failure modes involved. Also, the systematic error induced

by the difference in testing and measuring conditions between each of the experimental programs or research groups plays an important role on adding variability.

4.4.3 Drift Ratio at Ultimate Damage State

In order to evaluate the suitability of the proposed equation 4-28 for the estimation of the drift ratio at ultimate damage state, it is compared against several equations/models found in literature. Figure 4-9 shows a graphic representation of the correlation of the calculated ultimate drift ratio vs the measured ultimate drift ratio for the 58 obtained datasets of walls with rectangular cross section in the database, and for each of the equations presented on section 4.2.

As noted on previous sections, the diagonal line represents a ratio of predicted-to-measured strength of 1.0 and any point above or below the diagonal line represents an over-prediction or an under-prediction, respectively. It can be noted from Figure 4-9 that the scatter on the predictions is significant. However, it is observed that the equation proposed in this study (equation 4-28) reduces the scatter of the ultimate drift ratio estimate over most of the evaluated equations as the points appear to be closer to the diagonal line. ASCE 41-13 provides fixed values of the drift ratio at the ultimate (abrupt strength drop) state of 0.0075 and 0.010 for walls with low axial loads and walls with significant axial loads, respectively. These provisions tend to underestimate the actual value in most cases since the average drift ratio from test data resulted to be 0.013.

In order to numerically compare the predictive performance of each equation, Table 4-3 presents a summary of common central tendency and dispersion measures of the predicted-to-measured drift ratio at peak strength, along with the percent of over-predictions. In the same fashion as discussed on previous section (4.4.2), Figure 4-10 shows a typical box and whisker plot comparing the distribution of the predicted-to-measured drift ratio at for each selected equations/models. This graph provides valuable information regarding the central tendency, spread of values and extreme values.

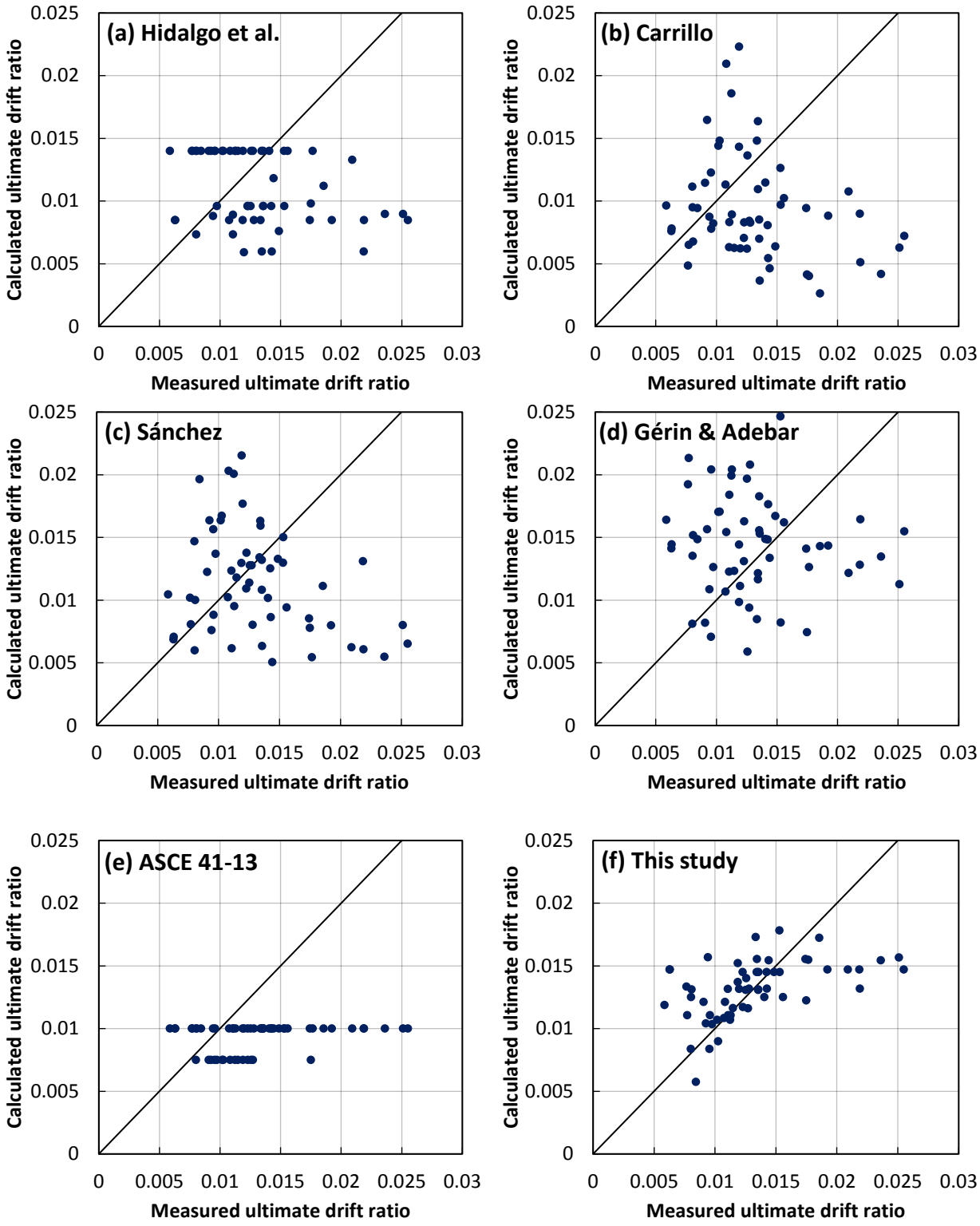

Figure 4-9. Correlation between calculated ultimate drift ratio and measured ultimate drift ratio using various available equations: (a) to (e); and the new equation proposed in this study (f).

Table 4-3. Summary of statistics of the ratio of predicted-to-measured ultimate drift for walls with rectangular cross section included in the database.

	Hidalgo et al.	Carrillo	Sánchez	Gérin & Adebar	ASCE 41-13	This study
Mean	0.96	0.82	0.99	1.22	0.79	1.09
Median	0.86	0.71	0.96	1.09	0.74	1.02
Minimum	0.27	0.14	0.23	0.17	0.39	0.58
Maximum	2.38	1.93	2.33	2.79	1.70	2.34
Std. dev.	0.46	0.45	0.49	0.58	0.29	0.36
COV	0.47	0.55	0.49	0.47	0.36	0.33
% Over-predictions	39.7	32.8	46.6	60.3	17.2	55.2

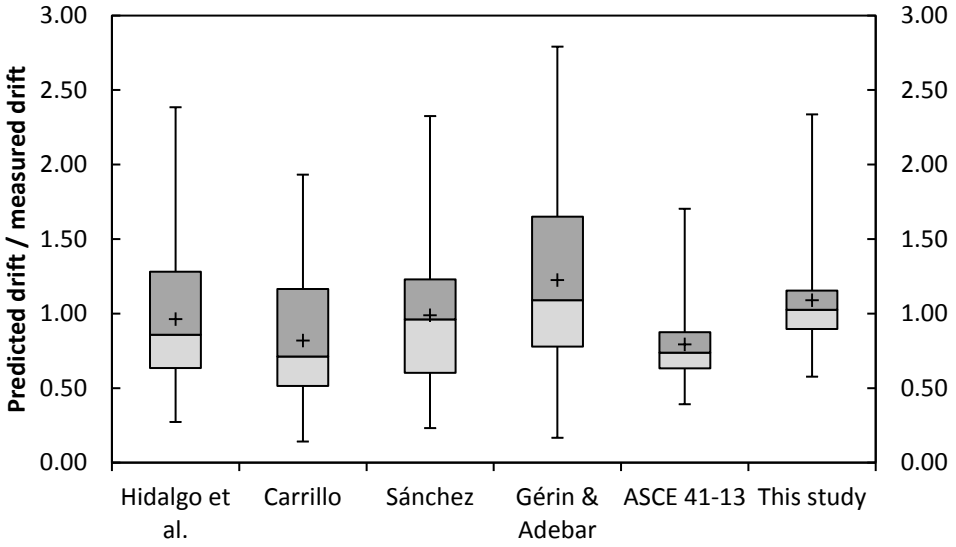

Figure 4-10. Distribution of the ratio of predicted-to-measured ultimate drift.

From the statistics presented on Table 4-3 and from Figure 4-10 it can be observed that the proposed equation produces an improved estimate of the ultimate drift ratio. The mean and median predicted-to-measured values are closer to 1.0 than the rest of the predictive models but the proposed by Sánchez (2013). While the estimates using the equations proposed by Sánchez (2013) produce mean and median predicted-to-measured values relatively close to 1.0, the scatter on its predictions (in terms of range, IQR, and COV) is significantly larger than that of the

equation proposed in this study. Similarly, the equation 4-28 (this study) produced lower COV of the predicted-to-measured drift ratio than other predictions. It is also observed that the midspread falls between 0.90 and 1.16, which means that the ratio of predicted-to-measured values for 50% of the observations is closer to the median, and thus closer to a value of 1.0. In terms of the range (difference between maximum and minimum values), the equation proposed in this study is on par or narrower than the rest of the equations with the exception of ASCE 41-13 provision which, in most cases, underestimated the drift ratio. This is observed on the box and whisker plot, central tendency statistics, and on the low % over-predictions. The proposed equation yields 55.2% of over-predictions which is close to the intended value of 50%.

In the same manner as in the drift ratio at peak strength case, obtaining a low COV for the prediction of displacement capacity of RC squat shear walls is challenging due to the stochastic nature of the several factors contributing to the post-peak lateral displacement and the different failure modes involved. Also, the systematic error induced by the difference in testing and measuring conditions between each of the experimental programs or research groups appears to be an influent source of variability.

On the other hand, drift limits have been conventionally imposed in building codes for the purpose of controlling damage and as a measure of collapse prevention during an earthquake event. The allowable drift ratios for RC shearwall building systems provided on most current building design codes tend to be unconservative since they appear to be mainly focused on tall buildings, where the main earthquake force resisting system commonly consists of slender shearwalls. For example, ASCE 7-10 seismic provisions allow a drift ratio of 0.02, which is far beyond the typical ultimate drift capacity of squat RC walls. The average ultimate drift ratio obtained from the experimental values on the collected database of squat walls with rectangular cross sections was 0.013. At a drift ratio of 0.02 most squat walls would be expected to have undergone very severe damage where structural stability would be compromised. Duffey el al. (1994a, 1994b) also noted that the characteristic lower ductility and lower drift capacity of squat (low-rise) RC shearwalls was not recognized in building design codes. Further research is needed to establish reasonable drift limits for damage control of squat RC wall structural systems.

CHAPTER 5. SHEAR STRENGTH OF SQUAT WALLS WITH BOUNDARY ELEMENTS

5.1 Introduction

Statistical analyses have been carried out from the assembled database described in Chapter 2. As previously noted, walls with enlarged boundary elements (i.e. barbell and flanged cross section) can generally achieve higher shear strength than comparable specimens with rectangular cross section. Therefore, the assessment of available predictive equations and development of new predictive equations were addressed separately for both groups of walls. The discussion on strength of walls with rectangular cross section was presented on Chapter 3.

This chapter presents an evaluation of current expressions for the prediction of peak shear strength of squat reinforced concrete walls with enlarged boundary elements available in US design codes and in the literature. The performance of each of the selected equations was assessed by comparing the strength predictions with experimental strength from the assembled database for walls with boundary elements. The experimental peak shear strength of each wall was taken as the average of the peak strengths measured from the first and third quadrants (i.e. positive and negative loading directions, respectively). Key parameters influencing the peak shear strength were identified and a new equation to predict the peak shear strength of squat walls with boundary elements (flanged or barbell) is presented. The new equation was obtained from multivariable regression analyses using an assembled experimental database and aimed to improve current peak shear estimates. The improved expression presented herein was intended to be used in the design and assessment of structures with RC squat walls.

5.2 Current Expressions for Peak Shear Strength

The current equations selected for evaluation are available in US standards and codes and in literature. These include ACI 318-14 (*Building Code Requirements for Structural Concrete and commentary*), ASCE 43-05 (*Seismic Design Criteria for Structures, Systems and Components in Nuclear Facilities and Commentary*), Barda et al. (1977) and Wood (1990). A brief introduction

of the provisions included on these references is given on this section and a detailed discussion was presented on Chapter 3 (section 3.2) of this document.

The selected references from US standards are ACI 318-14 and ASCE 43-05. On ACI 318-14, two sets of equations for the shear strength prediction are presented: one in Chapter 11 and another in Chapter 18. The provisions of Chapter 11 were intended for non-seismic loading, whereas the provisions of Chapter 18 were intended for seismic loading. ASCE 43-05 presents a set of predictive equations for squat RC walls with boundary elements, which is mainly based on Barda et al. (1977) study. For walls with rectangular cross section, ASCE 43-05 refers to ACI 349-06 *Code Requirements for Nuclear Safety Related Concrete Structures* which uses all the same provisions as in ACI 318-14 for evaluating peak shear strength of walls, with the difference that provisions for lightweight aggregates (i.e., λ factor) are omitted from the entire code and commentary.

The selected references from literature are Wood (1990) and Barda (1977). Wood (1990) evaluated the results of 143 low-rise wall specimens which included rectangular, flanged and barbell cross sections. A semi-empirical equation, derived by using a shear-friction analogy and calibrated against experimental data from squat wall tests was proposed. Barda (1977) developed an empirical expression based on the experimental results of eight RC squat walls with heavily reinforced and well-confined flanges (end walls) tested in shear and without axial load.

The following sections present the development of a new improved equation to predict shear strength of squat RC walls with boundary elements (flanges and barbell) and evaluate the performance of the selected current equations for shear strength prediction. The equations shown are similar to the presented on the corresponding references but are presented in terms of nominal loads and nominal strength (without applying any strength reduction factor) for the purpose of comparison.

5.3 Development of New Peak Shear Strength Predictive Equation

A statistical approach was used to develop and calibrate an equation that improves the actual estimates of peak shear strength of squat RC walls with boundary elements. Multivariable linear regression analyses were performed to produce an empirical equation that fits better to the

included database of 137 squat RC walls with boundary elements. The goal was to lower the standard deviation and coefficient of variation (COV) of the predicted-to-measured shear strength ratio. The intent was also to obtain a mean predicted-to-measured strength ratio near to 1.0 while keeping the percentage of over-predictions around 50% which means that the predicted strength would be, on average, nearer to the experimental strength. Experimental peak strength was taken as the average of the peak strengths recorded in the positive (first quadrant) and negative (third quadrant) loading directions.

A functional equation form was selected based on Barda's proposed expressions and based on common ACI seismic design expressions. The parameters found on these equations are in general agreement with the parameters having important influence on shear strength as reported by several researchers. Additional predictive parameters were identified by reviewing the findings from numerous experimental programs and extended to account for the vertical, horizontal and boundary element reinforcement. To arrive to the final parameter selection, the multivariable linear regression analysis was run using several different combinations of the previously identified parameters to generate a calibrated equation on each run. Finally, the calibrated equation with the parameter combination that yields less variability when compared to the assembled database was selected. The following set of expressions includes the parameters that were found to be better correlated to the experimental strength and is calibrated to best fit the data within the database:

$$V_n = \left(0.54 + 0.19 f_c^{'} - 0.17 f_c^{'} \frac{h_w}{l_w} + 0.45 \frac{P}{A_g} + 0.39 \rho_{se} f_{yse} + 0.31 \rho_{be} f_{ybe} \right) A_{cv} \quad (5\text{-}1)$$

$$f_{yse} = A f_{yv} + B f_{yh} \quad (5\text{-}2)$$

$$\rho_{se} = A \rho_v + B \rho_h \quad (5\text{-}3)$$

$$\rho_{be} = A_{sbe} / A_{cv} \quad (5\text{-}4)$$

where ρ_{be} is the longitudinal boundary element reinforcement ratio; A_{sbe} is the effective longitudinal boundary reinforcement area (mm^2); and constants A and B are calculated as follows depending on the aspect ratio h_w/l_w:

if $h_w/l_w \leq 0.5$	A = 1	B = 0
if $0.5 < h_w/l_w < 1.5$	A = - h_w/l_w + 1.5	B = h_w/l_w – 0.5
if $h_w/l_w \geq 1.5$	A = 0	B = 1

The effective longitudinal boundary reinforcement area shall be taken as the total longitudinal reinforcement area of boundary element in tension for barbell shaped walls; and as the longitudinal reinforcement area within the effective width (b_{eff}) of the flange in tension for walls with flanged cross section. In the case of flanged cross sections, the effective flange width is taken as the minimum of: one half the wall height ($h_w/2$) and actual flange width (b_f). The basis for this criterion is explained later in this section. The behavior regarding the effectiveness of vertical and horizontal reinforcements in RC squat walls with boundary elements is similar to that of squat walls with rectangular cross-section, which was discussed on section 3.3.

Figure 5-1 shows the portion of the peak shear strength attributed to each of the parameters calculated with equation 5-1 for wall specimen U-1, tested by CNSI/NUPEC (1996). The wall specimen had flanged cross section, an axial load ratio of 3.9%, aspect ratio of 0.65, concrete compressive strength of 28.6 MPa, horizontal and vertical reinforcement ratios of 1.21%, and web and boundary reinforcement yield strength of 383 MPa.

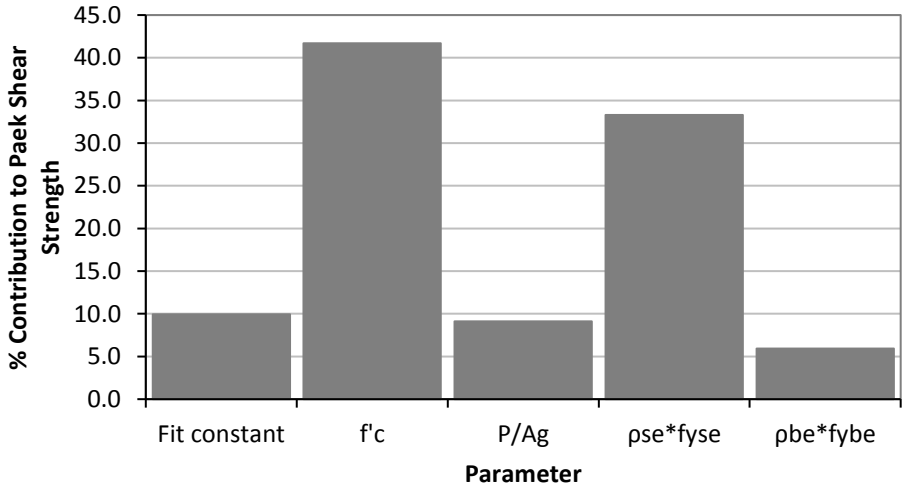

Figure 5-1. Contribution to peak shear strength attributed to each of the equation 3-13 parameters for wall specimen U-1.

Other failure modes yielding lower strength can occur. The occurrence of such failure modes may be related to differences between the actual conditions of the wall being evaluated and the experimental setup of walls considered in the database. The user should be aware of the characteristics and range of parameters of the wall specimens considered in the corresponding database to determine applicability of the predictive equation.

In the same manner as for the rectangular squat walls, the parameter associated with the strength provided by the reinforcement was evaluated by one-at-a-time parameter variation. The use of vertical distributed reinforcement only, total vertical reinforcement (including boundary element reinforcement) only, horizontal reinforcement only, both horizontal and vertical distributed reinforcements in separate terms, and an effective reinforcement ratio that combines both distributed reinforcements in one term (in the same fashion as in ASCE 43-05) were considered. The last resulted to be a better predictive parameter for steel contribution to shear strength as it produced the least variability. Using the effective reinforcement ratio to consider the contribution of both steel reinforcements as a function of aspect ratio seems to be a reasonable assumption and is in good general agreement with experimental findings (Figure 3-2).

It has been consistently reported by researchers that walls with lower aspect ratios or lower shear span-to-length ratios can yield higher shear stress capacities. This has been commonly attributed to an increase in the shear carried by concrete as the aspect ratio decreases. In a preliminary study (Adorno-Bonilla and Vidot-Vega, 2015), the aspect ratio was treated as a separate term and compared to equation calibration using a term that considers the product of a concrete strength parameter and the aspect ratio. It was found that using the product of aspect ratio and a concrete strength parameter produced better predictions than using the aspect ratio separately. Additional to the term considering the product of aspect ratio and concrete strength, the use of another term with concrete strength parameter only was also considered, which further improved the predictions. Different combinations using the aspect ratio and the shear span-to-length ratio were evaluated. Also, the use of the square root of the concrete compressive strength ($\sqrt{f'_c}$) versus using the compressive strength itself (f'_c) was considered.

The aspect ratio (h_w/l_w) was found to produce better correlation with the included database (with cantilever test setup) than the shear span (M/Vl_w). The aspect ratio is a more practical parameter

for design purposes, since it does not depend on structural analysis to calculate values for moment and shear. However, if a wall pier with both ends fixed is being considered, then the use of the M/Vl_w would be more appropriate. The concrete compressive strength (f'_c) resulted to be a better strength prediction parameter; with best results when a concrete strength term and another term with the product of concrete strength and wall aspect ratio were included in the equation.

The boundary element reinforcement ratio is not considered in most currently available equations. However, several researchers (e.g., Endo, 1980; Wood, 1990; and Terzioğlu, 2011) have found that the boundary element reinforcement affects both the shear load transfer mechanism and the peak shear strength even in shear-dominated walls with very low aspect ratios. Therefore, a term with the longitudinal boundary element reinforcement ratio (ρ_{be}), calculated as the ratio of longitudinal boundary reinforcement area in tension to the effective shear area (A_{sbe}/A_{cv}), was included resulting in an enhancement in prediction performance. Another option where the ρ_{be} was calculated as the ratio of longitudinal boundary reinforcement area in tension to the gross area of the corresponding boundary element (A_{sbe}/A_{be}) was evaluated as well, but better predictions were obtained using A_{sbe}/A_{cv}.

This group of walls is comprised of barbell and flange cross sections which, in general, can reach higher shear stresses than those of rectangular cross section. Specifically, the walls with flanged cross section can have a shear lag effect which makes the tensile steel stresses to be non-uniform along the flange width. These stresses are higher at the center of the flange width (nearer to the web), and decrease with increasing distance from the web in the outward direction as shown in Figure 5-2. Therefore, if we consider all the steel within the whole flange width to be effective, we might be using an unrealistic assumption especially for the case of walls with wide flanges.

A typical approach used in design codes and standards, is to assume an effective flange width where the steel is fully effective. In order to address this effect, and to obtain a more accurate predictive equation, different criteria found in standards and in literature for determining the effective flange width were considered. Then, the boundary element reinforcement ratios were calculated for each case and the equations were fitted by multiple linear regression against the data of walls with flanged cross section. This allowed determining which assumption of the effective flange width would give a better predictive performance by comparing the variability of

the predictions. Boundary element reinforcement ratio (ρ_{be}) for flanged walls was defined in the same fashion as for barbell and rectangular cross sections (A_{sbe}/A_{cv}); with the only difference being that the effective boundary longitudinal reinforcement area (A_{sbe}) is the area within the effective flange width (b_{eff}) of the flange in tension, instead of the longitudinal reinforcement within the whole boundary element. The assessed calculations for the effective flange width are shown in Table 5-1 and were taken as the actual flange width or the calculated value (b_{eff}), whichever is less.

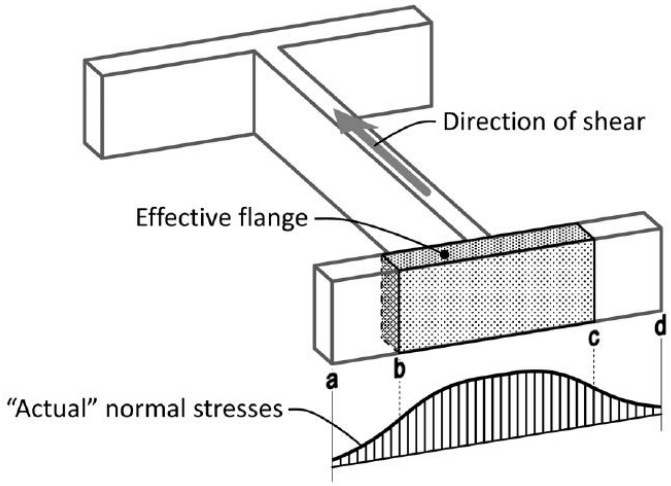

Figure 5-2. Effective flange width concept (adapted from Moehle et al., 2011).

Table 5-1. Trials for effective flange width determination.

Effective flange width	Comments
$b_{eff} = ½\ h_w$	from SEAOC, 1999
$b_{eff} = ¼\ h_w$	from ACI 318-14 section 18.10.5.2 - walls
$b_{eff} = 16\ t_f + t_w$	from ACI 318-14 section 6.3.2.1 - T-beams
$b_{eff} = 0.3\ h_w$	from UBC 97
$b_{eff} = \begin{Bmatrix} 0.71 l_w \ if\ {}^{P}/_{A_g f_c'} = 0 \\ 0.46 l_w \ if\ {}^{P}/_{A_g f_c'} > 0 \end{Bmatrix}$	Based on Hassan and El-Tawil (2003). They found that effective flange width was better correlated to wall length and presence of axial load for slender walls.
$b_{eff} = 0.25\ l_w$	Additional trial based on wall length.
$b_{eff} = 0.15\ l_w$	Additional trial based on wall length.

The equation fitted using the effective flange width equal to half the wall height (b_{eff} = ½ h_w) yielded the most accurate prediction with the lesser variability, and thus it was used in the final equation. However, the differences found on the overall variability between the different flange width assumptions were not very significant since the database does not include a large quantity of specimens with very wide flanges as those from Palermo and Vecchio (2002) and CNSI/NUPEC (1996).

It has also been widely recognized that axial loads can enhance the shear load carrying capacity of reinforced concrete walls of higher aspect ratios. The same behavior was observed from different researchers for squat RC walls. Therefore, the axial load ratio (P/A_g) was incorporated in the equation form. The increase in shear strength due to axial loads may be attributed to two major mechanisms. First, the axial force enhances the frictional force transfer through cracks and construction joints. Secondly, the change in the biaxial stress state of the concrete panel can increase concrete shear strength. Results from several researchers (e.g., Salonikios et al., 1999; Palermo and Vecchio, 2002; Greifenhagen and Lestuzzi, 2005; Xiang, 2009) suggest that low axial load ratios in the order of 5% are enough to effectively reduce the base sliding displacements (in walls with construction joints), and thus help prevent premature sliding failure of squat RC walls.

5.4 Evaluation of Selected Peak Shear Strength Equations

In this section the selected commonly used predictive equations presented on sections 5.2 and 3.2 and the new expression developed herein (equation 5-1) are evaluated in terms of their predictive performance by using a statistical approach and comparing to the experimental results compiled in the assembled database. In order to eliminate bias due to load amplification factors and resistance reduction factors between codes, the equations were modified to use nominal loads and nominal strengths. Also, the calculated peak and nominal shear strengths (V_{peak} and V_n) were then normalized with the effective shear area of the section (A_{cv}) to eliminate the test scale differences between different experimental programs, so that all the parameters were worked in terms of stress instead of force. The normalization of the shear force with A_{cv} also allows for a fair comparison between the available equations and the developed equation since the available expressions suggest different effective depth (d) definitions.

In order to evaluate the suitability of the proposed equation, it is compared against several widely-used equations in terms of the predicted-to-measured strength ratio. Figure 5-3 shows a graphic representation of the correlation of the calculated shear stress capacity vs the measured peak shear stress for the 137 walls with boundary elements tests in the database, and for each of the equations discussed on sections 5.2 and 3.2. The diagonal line represents a ratio of predicted-to-measured strength of 1.0. Any point falling on the line means an exact prediction of the shear strength. Any point above the diagonal line represents an over-prediction of strength and vice-versa. The farther the point from the diagonal represents a larger error in the estimate. It can be noted from Figure 5-3 that the equation proposed in this study (equation 5-1) reduces the scatter of the results significantly over the rest of the evaluated equations.

In order to numerically compare the observed behavior of the predictions with each equation, Table 5-2 presents a summary of common central tendency and dispersion measures of the predicted-to measured strength ratio, along with the percent of over-predictions. Mean and median values larger than 1.0 suggest that the equation tends to overestimate the strength. For example, Wood's equation underestimates the strength, on average, by around 47%. On the other hand, the standard deviation and coefficient of variation (COV) provide information on the dispersion (scatter) of the predicted-to-measured strength ratios. In other words, the mean and median values give useful information on the accuracy of the predictive equation while the standard deviation and coefficient of variation provide information regarding the precision of the equation. The % over-predictions provides information on the bias of the predictions. A non-biased equation will yield results having % over-predictions of around 50%. A lower % of over-predictions would represent an equation producing biased estimates that tend to the conservative side, while a higher % of over-predictions indicates that the equation produces biased estimates that tend to the unconservative side.

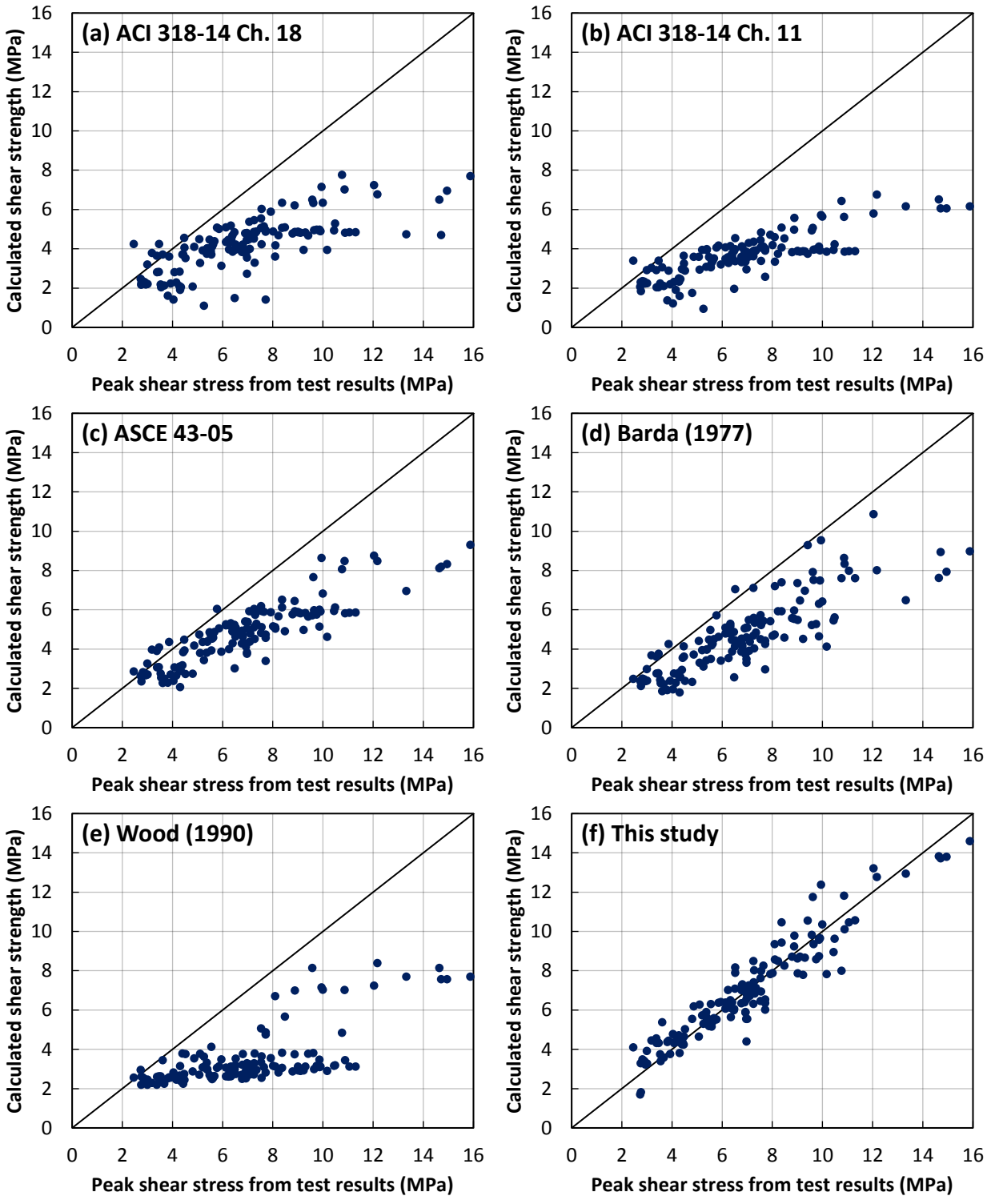

Figure 5-3. Correlation between calculated nominal shear stress and measured peak shear stress using various available equations: (a) to (e); and the new equation proposed in this study (f).

Table 5-2. Summary of statistics of the ratio of predicted shear strength to the measured peak shear strength for walls included in the database.

	ACI Ch. 18	ACI Ch. 11	ASCE 43-05	Barda	Wood	This study
Mean	0.65	0.56	0.73	0.70	0.53	1.02
Median	0.64	0.55	0.72	0.69	0.49	1.00
Minimum	0.18	0.18	0.44	0.38	0.28	0.62
Maximum	1.72	1.38	1.24	1.15	1.07	1.67
Std. dev.	0.20	0.15	0.15	0.15	0.17	0.15
COV	0.30	0.27	0.21	0.22	0.32	0.15
% Over-predictions	5.1	0.7	5.1	4.4	1.5	48.9

Figure 5-4 shows a typical box and whisker plot comparing the distribution of the predicted-to-measured strength for each presented equation model. The graph shows the lower quartile (25^{th} percentile), median, upper quartile (75^{th} percentile), the extreme values and the mean value marked with "+" symbol. The box in the box and whisker plot is constituted by the second and third quartile and represents the spread of the central 50% of the observations. The range of this box is commonly known as the inter-quartile range (IQR), midspread or middle fifty. The narrower this range (or box in the graph) is, indicates the lesser the variability since the central 50% of the observations are nearer to the median value. The lower and upper whiskers of the plot represent the spread of the first and fourth quartile, being the ends of the whiskers the extreme (i.e. maximum and minimum) values marked with "-" tick mark.

It can be observed that the proposed equation produces a significantly improved estimate of the shear strength since the mean and median values are very close to 1.0. While the variability in terms of standard deviation does not seem to be significantly reduced with the equation developed on this study, the resulting COV is considerably lower which indicates that the scatter is reduced in comparison with the rest of the evaluated equations. It is also observed that the midspread falls between 0.94 and 1.10, showing the second-smallest IQR after ACI Chapter 11 equation. Also, resulting maximum and minimum values are 0.62 and 1.67, respectively; which is a reasonable range. In the same manner, the proposed equation yields 48.9% of over-predictions which is very near to the intended value of 50%.

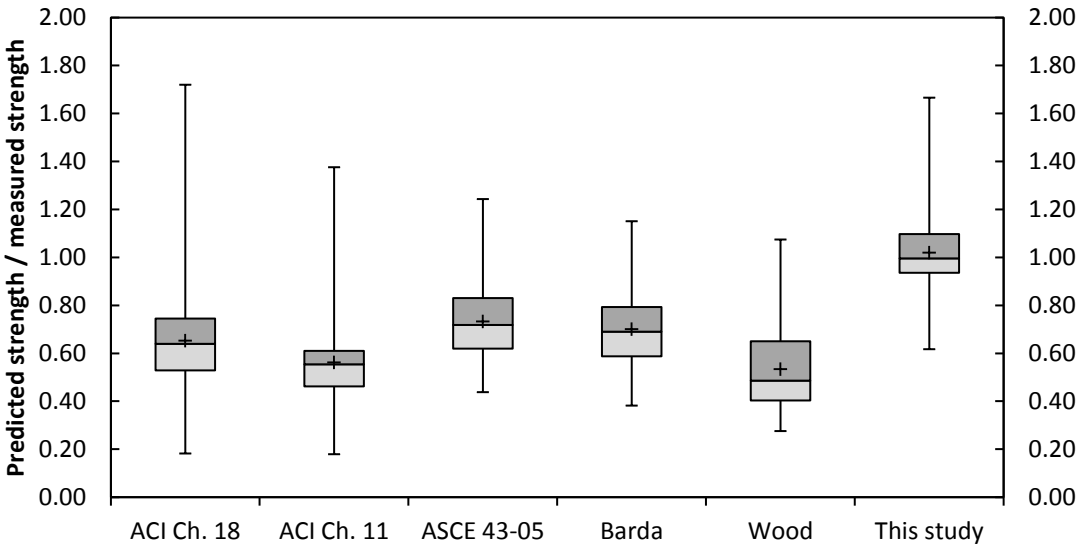

Figure 5-4. Distribution of the ratio of predicted-to-measured peak strength.

Note that ACI 318 Ch. 18, ACI 318 Ch. 11 and Wood tend to under-predict shear strength of squat walls with flanged and barbell cross sections. Barda and ASCE 43-05 tend to under-predict as well but in a lesser degree since these equations were developed based on flanged walls tests. The degree of under-prediction can be better observed in the low central tendency values (i.e. mean and median). Also, the degree of under prediction is observed on the box and whisker plot where the IQR box is far below 1.0, and on the low % over-predictions. Therefore, these equations tend to fall into the conservative side for squat RC walls with flanges or barbells. Generally, an equation yielding mean and median values near to 1.0 will produce nearly 50% over-predictions if the data is not severely skewed.

To further evaluate the proposed equation, a plot of the peak shear strength normalized with $A_{cv}\sqrt{f_c'}$ is presented in . In contrast to the case of squat RC walls with rectangular cross sections, this figure shows that the upper strength limit of the ACI 318 ($0.83A_{cv}\sqrt{f_c'}$) is not a reasonable value for squat shear walls with boundary elements. On the other hand, the upper strength limit established in ASCE 43-05 ($1.67A_{cv}\sqrt{f_c'}$) is a reasonable limit for squat RC walls with flanged and barbell cross sections. Thus, it is recommended to use a limit strength of $1.67A_{cv}\sqrt{f_c'}$ when using the proposed equation 5-1 to predict wall's peak shear strength. This limit has been traditionally imposed as an upper-bound to avoid non-ductile diagonal compression failure in

walls, wall piers, deep beams and coupling beams. In the same manner as for squat walls with rectangular cross section, , suggests that the upper strength limit becomes more important for walls of lower aspect ratios. In addition, a good correlation between the predicted and measured normalized peak shear strengths can be observed.

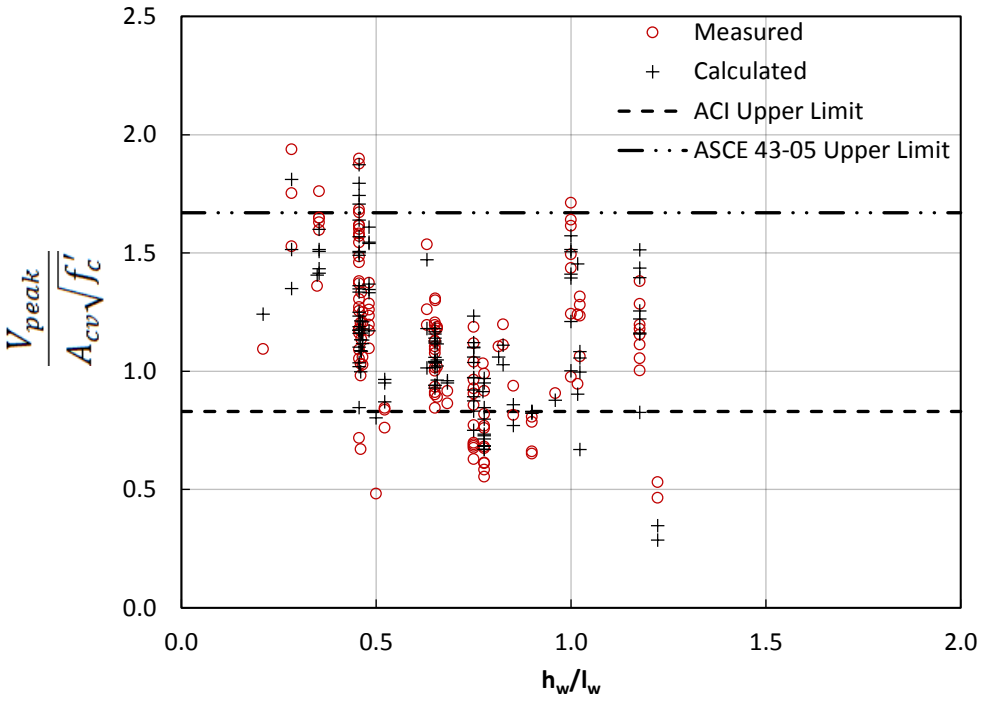

Figure 5-5. Variation of the predicted and measured normalized peak shear strength with wall aspect ratio compared to ACI 318 and ACI 43-05 upper limits.

CHAPTER 6. DISPLACEMENT CAPACITY OF SQUAT WALLS WITH BOUNDARY ELEMENTS

6.1 Introduction

It was noted on Chapters 3 and 5 that squat RC walls with enlarged boundary elements can show different behavior than those with rectangular cross section. This difference was mainly observed in the strength but, in order to maintain uniformity, the assessment of available predictive equations and development of new predictive equations was addressed separately for both groups of walls.

This chapter presents an evaluation of current expressions for the prediction of the displacement capacity of squat reinforced concrete walls with enlarged boundary elements (i.e. flanged and barbell-shaped cross section) found in the literature. The performance of each of the selected equations was assessed by comparing the displacement predictions with experimental displacements from the assembled database for walls with enlarged boundary elements. Key parameters influencing the displacement capacity were identified. The experimental displacements of each wall were taken as the average of the displacements measured from the first and third quadrants (i.e. positive and negative loading directions, respectively). New equations to predict the cracking, peak, and ultimate displacement capacities of squat walls with boundary elements are presented to improve current displacement estimates. These displacement capacity estimates, in conjunction with the peak strength estimate presented in Chapter 5 can be used to define the backbone curve for a hysteretic model. The equations were obtained from multivariable linear regression analyses using an assembled experimental database from various experimental programs which is presented on Chapter 2 and Appendix A. The expressions presented herein were intended to apply for squat walls with rectangular cross section and a wide range of characteristics.

6.2 Current Expressions for Estimation of Displacement Capacity

The selected predictive equations for displacement capacity were found in US standards and in literature. The models proposed by Hidalgo et al. (2000), Carrillo (2010), Sánchez (2013), Gérin

and Adebar (2004) and ASCE 41-13 were considered. A brief introduction to these models is given in this section and section 4.2 presents a detailed discussion of the selected current equations for displacement capacity prediction.

Hidalgo et al. (2000) developed a hysteretic model for the analysis of cyclic lateral load-displacement behavior of squat RC shear walls. The authors used a tri-linear hysteresis envelope and proposed equations 4-1 to 4-6 for the estimation of the drift at shear cracking, peak strength, and the ultimate drift based on linear regression from experimental results. The authors recommended using a modified version of ACI 318 seismic design provisions for determining the peak shear strength. The shear force corresponding to the cracking point was recommended to be taken as the calculated concrete contribution to strength. The ultimate displacement was defined as that associated to a 20% drop in strength (80% V_{peak}) past the peak point.

Carrillo (2010) presented a tri-linear backbone model for the analysis of squat walls. The model was based on the observations from experimental tests representative of typical squat RC walls of housing construction in several Latin American countries. In the same manner as in the model by Hidalgo et al. (2000), the model presented by Carrillo (2010) has a tri-linear backbone with a stiffness reduction point associated to significant diagonal web cracking. Carrillo (2010) proposed equations 4-7 to 4-10 equations to calculate the drift ratio at diagonal cracking, peak strength and ultimate state as a percentage. Ultimate displacement was defined as the displacement associated to a 20% decrease in strength (80% V_{peak}) after peak point. The cracking strength was assumed as the concrete contribution to shear strength.

Sánchez (2013) proposed a backbone model similar to that proposed by Hidalgo et al. (2000) and Carrillo (2010), but modified to include a first stiffness reduction due to flexural cracking and a second stiffness reduction due to distributed diagonal cracking. An additional line segment to represent the initial uncracked stiffness and the reduced stiffness after flexural cracking was included. Based on the experimental results from RC shear walls with similar characteristics of those used for housing construction in Mexico, Sánchez (2013) proposed equations 4-11 to 4-18 to estimate the points of the backbone curve corresponding to flexural cracking, diagonal cracking, peak strength and ultimate damage state. The author proposed to estimate the displacement at peak strength (Δ_{peak}) by adding the flexural (Δ_f) and shear (Δ_s) displacement

components and proposed separate equations for their calculation. Sánchez (2013) used the same 20% strength degradation criterion to define the ultimate damage state as used by other researchers. Sánchez (2013) used a ductility-based approach to calibrate the expressions for estimation of the ultimate displacement (Δ_u).

Gérin and Adebar (2004) proposed a model to calculate the load-displacement response of reinforced concrete elements controlled by brittle shear failure under reversed cyclic shear loading. The model was based on theoretical mechanics and the experimental observations of 21 large-scale membrane-type element tests. The backbone curve shows major stiffness degradation due to diagonal cracking and a yield plateau after attaining peak strength. Equations 4-19 to 4-24 were proposed by Gérin and Adebar (2004) to calculate the backbone points corresponding to diagonal cracking, yield (peak strength) and ultimate damage state. On this model, the yield (peak) stress (v_y) is recommended to be calculated per seismic provisions of ACI 318-08. The model assumes that shear yielding is associated to the yield of reinforcement. A ductility expression calibrated with experimental data was proposed to obtain ultimate shear strain (γ_u); associated to a concrete shear failure due to large displacements along cracks. A conservative limit in the shear ductility was imposed to consider the possibility of concrete diagonal compression failure which could occur in walls with high reinforcement ratios.

ASCE 41-06 standard has been updated to ASCE 41-13 which now incorporates a major stiffness reduction prior to peak strength in the backbone curve to consider the effect of typical inclined shear cracking and provide a better representation of low-rise walls behavior. The changes are based on recommendations by Wallace (2007). Shear cracking is assumed to occur at the development of 60% of the peak strength and the corresponding displacement is calculated using the elastic stiffness of a cantilever wall considering flexural and shear deformations and uncracked properties. Shear strength is calculated using ACI 318 seismic provisions. The model provides fixed drift ratio values for the drift capacity. In order to consider the effects of axial load, the model reduces the drift capacity from 1% to 0.75% and the residual strength from $0.2V_{peak}$ to 0 for walls with axial load ratios (P/f'_cA_g) greater than 0.05.

Duffey et al. (1994a, 1994b) suggested average values for drift ratio at peak strength and at several post-peak strength degradation stages, based on statistical analysis of experimental data

compiled from numerous experimental studies. Due to the typical brittle response of squat RC walls, and the lack of sufficient experimental data of post-peak response, the authors recommended using the drift ratio values associated to the peak strength as the ultimate drift capacity when performing analyses using hysteretic models. Duffey et al. (1994a, 1994b) also noted that the allowable drift limits on most design codes and standards tend to be unconservative for low-rise RC shear walls since those are mainly focused on high rise buildings comprised of slender walls, which generally have higher ductility.

6.3 Development of New Displacement Capacity Predictive Equations

As discussed on section 4.3 the lateral load-displacement envelopes of squat RC walls can be adequately represented by a tri-linear backbone as shown in Figure 4-1. Therefore, drift data was collected from numerous experiments found in literature and were included in the assembled database for the three main points defining the tri-linear backbone (i.e. significant diagonal cracking, peak strength, and ultimate damage state). The availability of displacement data is more limited than peak strength data since no drift data was reported on some of the evaluated references, while for some other tests only data of drift at peak strength was available. From the 137 wall specimens with enlarged boundary elements (barbell and flanged cross section) listed in the database, drift data collection was possible for 67 and 82 specimens for the cracking and peak points, respectively. The drift data for the ultimate damage state was even scarcer since many of the early experimental studies presented data only up to the peak strength. Therefore, only 59 qualifying datasets could be obtained from the evaluated references for ultimate drift of walls with enlarged boundary elements.

In the same manner as for the walls with rectangular cross section, most of the data was obtained from global force-displacement hysteresis curves, including the contribution of both shear and flexural deformations, found on the evaluated references. The vast majority of cyclic loading tests were displacement controlled, typically with two or three cycles at each displacement level as shown on Figure 4-5. The drift data was obtained from the experimental envelopes which were extracted by tracing straight lines connecting all the first cycle peaks of the hysteresis loops (see Figure 4-5). The load-displacement envelope was not extrapolated beyond the last loading

peaks. The data was converted to drift ratio to make all the measurements comparable. Afterwards, the drift ratios corresponding to the assumed diagonal cracking condition (R_{cr}), peak strength (R_{peak}) and ultimate state (R_u) were retrieved from the obtained cyclic envelope. The average drift ratio from 1st and 3rd quadrants of each wall was recorded for each of the three states. Cracking drift ratio was defined as that corresponding to the development of 60% of peak strength, while ultimate drift ratio was defined as that corresponding to the post-peak point where a strength degradation of 20% is attained. For tests where ultimate displacement data was not available for one of the loading directions (commonly when test is stopped due to sudden failure in the opposite direction), the single value available for the ultimate displacement was recorded. Further details are discussed in the next sub-sections and in Chapter 4.

The same methodology used in Chapter 4 for the walls with rectangular cross sections is used in this chapter for the walls with enlarged boundary elements. Regression analyses were performed to develop empirical equations that better fits the collected drift data. The goal was to lower the coefficient of variation and to obtain a mean value near to 1.0 for the ratio of predicted-to-measured drift capacity. Key parameters were identified by evaluating the correlation coefficient with the drift capacity. Multivariable linear regression analyses were carried to derive the equations with the selected parameters. An iterative process of eliminating the least meaningful parameter based on the highest p-value, and re-calibration until the scatter of the prediction was observed to increase, was used to simplify the equations. In order to minimize bias due to test specimens' scale, the collected displacement data was converted to drift ratio, reinforcement spacing was normalized with wall thickness and any parameter involving forces was normalized with the effective shear area of the cross section (A_{cv}) for the calibration and development of equations. The following sub-sections present the simplified expressions using the most significant parameters that were found to produce a better correlation with the barbell/flanged walls database, and are proposed for the prediction of drift ratio at diagonal cracking, drift ratio at peak strength and at ultimate drift ratio, respectively.

6.3.1 Drift Ratio at Diagonal Cracking

As previously discussed, it was considered that the main stiffness reduction on the load-displacement envelope of squat RC shear walls is related to the development of significant

diagonal cracking of the wall web; and that this effect can be reasonably approximated by assuming the significant cracking occurs at the development of 60% of the peak strength. Further discussion on this first stiffness reduction is provided on section 4.3.1.

For the purpose of simplicity, it was assumed in this study that both, the significant inclined cracking and ultimate damage states occur at a fixed portion of the peak strength. In order to better represent the squat shear walls behavior, two options for the estimation of the cracking or "first yield" point were considered. In the first option, the main decrease in stiffness was assumed to occur upon loading to 60% of peak strength, which has been considered to be the typical lateral force associated to significant inclined cracking (Wallace, 2007 and ASCE 41-13). On the second option, it was assumed that the main stiffness reduction occurs upon loading to 75% of the peak strength which could be representative of the onset reinforcement yielding. The definition of the first stiffness reduction point, based on the 60% of the peak strength (diagonal cracking), was found to generally better approximate the ascending branch of the experimental envelope and the initial stiffness. Therefore, the cracking drift equation was fitted based on the assumption that significant web cracking occurs at the point where 60% of the maximum strength is attained. The parameter selection and equation calibration approach by multiple linear regression analyses was described on previous section (6.3). The following simplified expression include the most significant parameters that were found to produce a better correlation with the database, and thus is proposed for the prediction of drift ratio at significant diagonal cracking state (R_{cr}) of squat RC walls with enlarged boundary elements in terms of the drift ratio.

$$R_{cr} = 0.0008 + 0.0012\rho_{be} + 0.00041\frac{h_w}{l_w} - 0.00031\frac{s_v}{t_w} \qquad (6\text{-}1)$$

where ρ_{be} is the boundary element reinforcement ratio (A_{sbe}/A_{cv}), l_w is the wall length, h_w is the wall height, s_v is the spacing of vertical reinforcement and t_w is the wall web thickness. Note that the effective longitudinal boundary reinforcement area was taken as the total longitudinal reinforcement area of boundary element in tension for barbell shaped walls; and as the longitudinal reinforcement area within the effective width (b_{eff}) of the flange in tension for walls with flanged cross section. In the case of flanged cross sections, the effective flange width is taken as the minimum of: one half the wall height ($h_w/2$) and actual flange width (b_f).

6.3.2 Drift Ratio at Peak Strength

Based on the observed approaches made by other researchers, two main options were evaluated in this study for the development of equations to estimate the displacement capacity at peak strength of squat RC walls with enlarged boundary elements, in a similar fashion as presented on section 4.3.2. The first option considered that the peak shear strength was an influential parameter on the displacement at peak strength, while other parameters were selected based on the correlation coefficient. On the second option, all the influential parameters were preliminarily selected based on their correlation coefficient with the displacement data. In both options the same general approach described earlier in terms of the iterative process for simplifying the equations by eliminating the least meaningful parameters based on the p-value was employed.

While some researchers have found that the peak strength is a good predictive parameter, no strong correlation between the peak strength and the displacement at peak strength was found in the database included in this study. The following simplified equation includes the parameters found to produce a better correlation with experimental data in this study, and thus is proposed for the estimation of the drift ratio at peak strength (R_{peak}) of squat RC walls with enlarged boundary elements.

$$R_{peak} = 0.0067 + 0.0024\frac{M}{Vl_w} - 0.000077\frac{l_w}{t_w} + 0.00006 f_c^{'} - 0.000005\ f_{ybe} \qquad (6\text{-}2)$$

where M/Vl_w is the shear span-to-length ratio, l_w is the wall length (mm), and t_w is the wall thickness (mm), f'_c is the concrete compressive strength (MPa), and f_{ybe} is the boundary element reinforcement yield stress (MPa).

6.3.3 Drift Ratio at Ultimate Damage State

The ultimate drift equation was fitted based on the definition of ultimate damage state as the point where the strength degrades to attain 80% of the peak strength. This ultimate state criterion based on a small drop in strength has been conventionally used for RC walls and other type of concrete members subject to lateral loading. Different approaches to estimate the shear walls

displacement capacity at ultimate damage state (e.g. based on peak strength and moment to shear ratio as main predictive parameters, based on calibration of the observed displacement ductility, based on typical average values, etc.) were found in literature. Further discussion on the different methodologies used by previous researchers can be found on section 4.3.3.

In a similar fashion as for the displacement at peak strength, several options using multiple linear regressions were evaluated in this study. The two options used for the displacement at peak strength (i.e. considering a term related to the peak strength, and considering other parameters but peak strength) were evaluated for the ultimate displacement as well. An additional option based on the calibration of the observed displacement ductility (Δ_u/Δ_{peak}) was considered for this damage state. The same iterative approach for parameters selection and simplification of the final equation described on earlier sections was used herein for all three options.

In contrast to the findings for squat RC walls with rectangular cross sections, the best estimate for walls with enlarged boundary elements was obtained with the calibration of the displacement ductility approach. The following set of expressions is proposed for the estimation of ultimate displacement capacity (R_u) of squat RC walls with enlarged boundary elements in terms of drift ratio:

$$\mu_u = 2.39 - 0.001 f_{yh} - 0.146 \rho_{be} - 31.3 \rho_h - 0.38 \frac{s_h}{t_w} + 0.32 \frac{s_v}{t_w} \geq 1.0 \quad (6\text{-}3)$$

$$R_u = \mu_u \times R_{peak} \quad (6\text{-}4)$$

where μ_u is the calculated displacement ductility, f_{yh} is the horizontal reinforcement yield stress (MPa), ρ_{be} is the boundary element reinforcement ratio (A_{sbe}/A_{cv}), ρ_h is the horizontal reinforcement ratio, s_v is the spacing of vertical reinforcement (mm), s_h is the horizontal reinforcement spacing (mm), and t_w is the wall web thickness (mm). As it is also noted on section 6.3.1, the effective longitudinal boundary reinforcement area was taken as the total longitudinal reinforcement area of boundary element in tension for barbell shaped walls; and as the longitudinal reinforcement area within the effective width (b_{eff}) of the flange in tension for walls with flanged cross section. In the case of flanged cross sections, the effective flange width is taken as the minimum of: one half the wall height ($h_w/2$) and actual flange width (b_f).

6.4 Evaluation of Selected Displacement Capacity Equations

In this section the selected predictive equations found in literature and the new expressions developed herein are evaluated in terms of their predictive performance by using a statistical analysis approach and comparing to the experimental data compiled in the assembled database (Appendix A). In order to minimize bias due to test specimens scale, all the displacement predictions were converted to drift ratio for comparison.

The following subsections show detailed analysis of the performance of each of the equations developed in this study for the prediction of displacement capacity of squat RC walls with enlarged boundary elements, at each of the three defined damage states, and compared to the performance of the corresponding equations found in literature. Tabulated summaries of common central tendency and dispersion measures of the predicted-to-measured drift ratios, along with the percent of over-predictions are presented in the same fashion as presented on Chapter 4 for the prediction of displacement capacity of squat RC walls with rectangular cross sections. Mean and median values larger than 1.0 suggest that the equation tends to overestimate the drift ratio. Standard deviation and coefficient of variation (COV) provide information on the dispersion (scatter) of the predicted-to-measured drift ratio, where lower values mean less variability. The % over-predictions provides information on the bias of the predictions where a non-biased equation will yield around 50% over-predictions. A lower % of over-predictions would represent an equation producing biased estimates that tend to underestimate drift ratios, while a higher % of over-predictions indicates that the equation produces biased estimates that tend to overestimate drift ratios.

Sections 6.4.1, 6.4.2 and 6.4.3 will discuss the findings for the displacement at diagonal cracking, displacement at peak strength and ultimate displacement, respectively.

6.4.1 Drift Ratio at Diagonal Cracking

The performance of the equations for the prediction of the cracking or “first yield” displacement will not be compared because all of them are based on different assumptions of the corresponding strength at which the stiffness reduction occurs, and therefore, are not directly comparable. Thus, only statistical analysis of the drift ratio at diagonal cracking predictions

using the equation developed in this study is presented. The equation was calibrated based on the assumption that the first major decrease in stiffness due to significant diagonal cracking takes place upon development of 60% of the peak strength.

Figure 6-1 shows a graphic representation of the correlation of the calculated drift ratio at diagonal cracking vs. the measured drift ratio at diagonal cracking for the 67 barbell and flanged cross section wall tests with available drift data included in the database. The diagonal line represents a ratio of predicted-to-measured cracking drift ratio of 1.0, where any point above the diagonal line represents an over-prediction of strength and vice-versa. The farther the point from the diagonal represents a larger error on the estimate. It can be noted from Figure 6-1 that the equation proposed in this study (equation 6-1) provides a reasonable estimate of the experimental values.

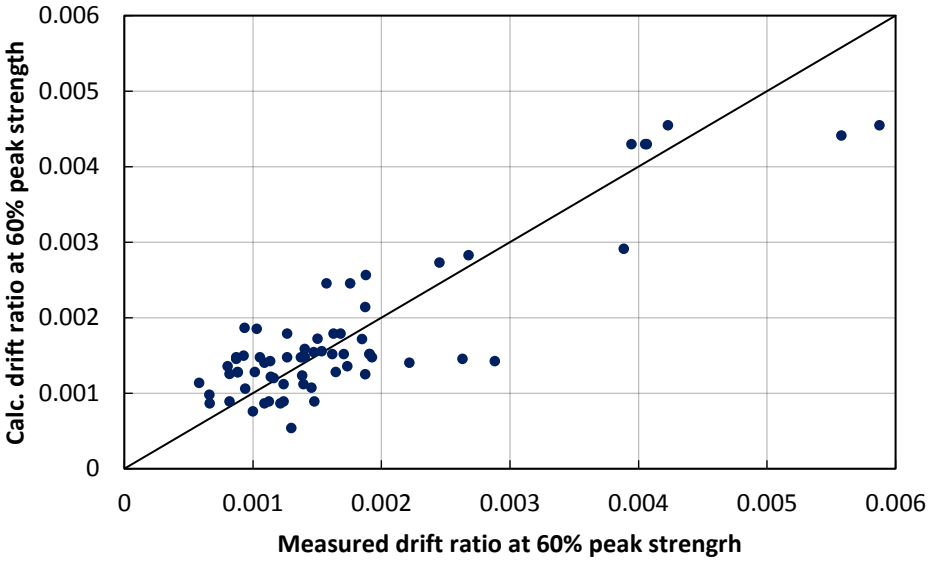

Figure 6-1. Correlation between calculated drift ratio at 60% peak strength and measured drift ratio at 60% peak strength for walls with boundary elements included in the database.

Table 6-1 presents a summary of common central tendency and dispersion measures of the predicted-to-measured cracking drift ratio, along with the percent of over-predictions. It can be noted that the equation can produce reasonable estimates of the drift at diagonal cracking strength on an average sense.

Table 6-1. Summary of statistics of the ratio of predicted-to-measured drift at 60% peak strength for walls with boundary elements included in the database.

	This study
Mean	1.08
Median	1.06
Minimum	0.41
Maximum	1.99
Std. dev	0.35
COV	0.32
% Over-predictions	61.2

The equation for the drift at diagonal cracking obtained for walls with enlarged boundary elements in this section produced a better correlation with experimental data than the developed on section 4.3.1 for walls with rectangular cross section since the mean and median values are closer to 1.0 and yields a lower COV in terms of the ratio of predicted-to-measured cracking drift. The % of over-predictions is slightly high which means that the backbone model would tend to slightly underestimate the initial stiffness.

6.4.2 Drift Ratio at Peak Strength

In order to evaluate the suitability of the proposed equation 6-2 for the estimation of the drift ratio at peak strength, it is compared against several equations/models found in literature. Figure 6-2 shows a graphic representation of the correlation of the calculated drift ratio at peak strength vs. the measured drift ratio at peak strength for the 82 obtained datasets of walls with enlarged boundary elements in the database, and for each of the equations presented on section 4.2.

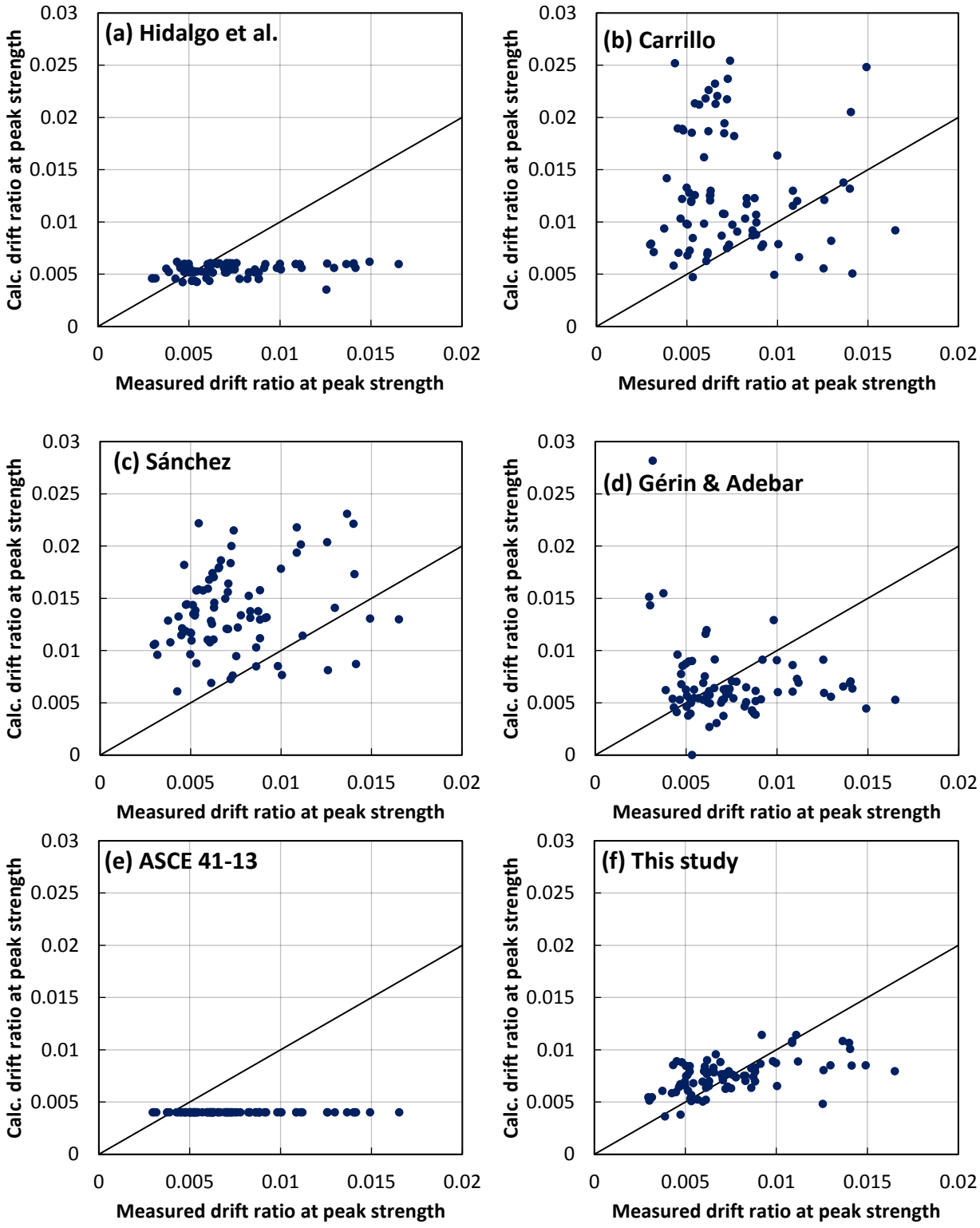

Figure 6-2. Correlation between calculated drift ratio at peak strength and measured drift ratio at peak strength using various available equations: (a) to (e); and the new equation proposed in this study (f).

As noted on previous section, the diagonal line represents a ratio of predicted-to-measured strength of 1.0 and any point above or below the diagonal line represents an over-prediction or an under-prediction, respectively. It can be noted from Figure 6-2 that the scatter on the predictions is significant. However, it is observed that the equation proposed in this study (equation 6-2) reduces the scatter of the drift ratio at peak strength estimate over most of the evaluated equations. It seems that Hidalgo et al. (2000) equation produces similar scatter as equation 6-2 but tends to underestimate the predictions. On the other side, fixed drift ratio provided by ASCE 41-13 tend to underestimate actual value in most cases. ASCE 41-13 suggests a conservative drift ratio of 0.004 at the development of peak strength while the average drift ratio from test data of walls with flanged and barbell cross sections resulted to be 0.0074. In order to numerically compare the predictive performance of each equation, Table 6-2 presents a summary of common central tendency and dispersion measures of the predicted-to-measured drift ratio at peak strength, along with the percent of over-predictions.

Table 6-2. Summary of statistics of the ratio of predicted-to-measured drift at peak strength for flanged/barbell walls included in the database.

	Hidalgo et al.	Carrillo	Sánchez	Gérin & Adebar	ASCE 41-13	This study
Mean	0.83	1.97	2.08	1.15	0.62	1.10
Median	0.82	1.61	2.02	0.89	0.60	1.03
Minimum	0.28	0.36	0.61	0.30	0.24	0.38
Maximum	1.54	5.80	4.07	8.87	1.34	1.96
Std. dev.	0.29	1.09	0.79	1.19	0.23	0.34
COV	0.35	0.55	0.38	1.03	0.37	0.31
% Over-predictions	20.7	84.1	91.5	32.1	6.1	54.9

Figure 6-3 shows a typical box and whisker plot comparing the distribution of the predicted-to-measured drift ratio at peak strength for each of the selected equations/models. The graph shows the lower quartile (25^{th} percentile), median, upper quartile (75^{th} percentile), the extreme values and the mean value marked with "+" symbol. The central box (inter quartile range – IQR) in the box and whisker plot is constituted by the second and third quartile and represents the spread of the central 50% of the observations. The narrower the IQR (or box in the graph) is, indicates the

lesser the variability since the central 50% of the observations are nearer to the median value. The lower and upper whiskers of the plot represent the spread of the first and fourth quartile, being the ends of the whiskers the extreme (i.e. maximum and minimum) values marked with "-" tick mark.

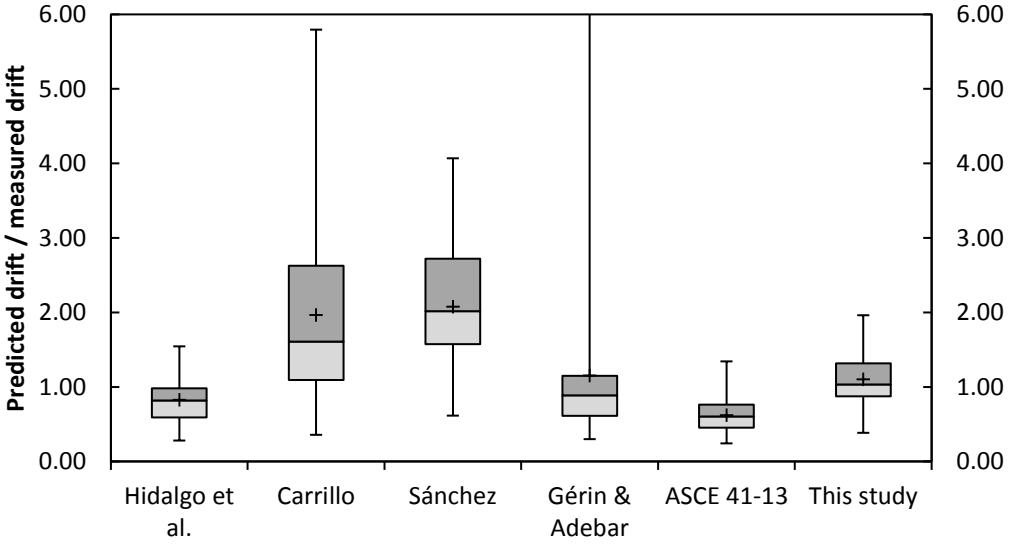

Figure 6-3. Distribution of the ratio of predicted-to-measured drift at peak strength.

From the statistics presented on Table 6-2 and from Figure 6-3, it can be observed that the proposed equation produces an improved estimate of the drift ratio at peak strength since the mean and median predicted-to-measured values are closer to 1.0, while the coefficient of variation (COV) is kept in a similar level or lower than other predictions. It is also observed that the midspread falls between 0.87 and 1.31, which means that the ratio of predicted-to-measured values for 50% of the observations is closer to the median, and thus closer to a value of 1.0. In the same manner, the proposed equation yields 54.9% of over-predictions which is very near to the intended value of 50%.

In terms of the range (difference between maximum and minimum values), the equation proposed in this study is on par with the estimates using ASCE 41-13 provisions and Hidalgo et al. (2000) equations. However, these last two tend to underestimate the drift ratio at peak strength as it can be noted from the low values of mean, median and % of over-predictions. On the contrary, the predictions using the equations proposed by Carrillo (2010), Sánchez (2013),

and Gérin and Adebar (2004) seem to produce considerably high scatter in terms of range, COV, and by inspection of Figure 6-2.

By observing the mean and median values from Table 6-2 and Figure 6-3, it is noted that the predictions using Carrillo (2010) and Sánchez (2013) equations tend to substantially over-estimate the displacement capacity at peak strength of squat RC walls with enlarged boundary elements. These two models also yield the wider IQR in terms of the predicted-to-measured ratio and the highest % of over-predictions. Carrillo (2010) and Sánchez (2013) equations were calibrated with peak strength as a main predictive parameter, but the data was oriented to walls with rectangular cross sections which strength is comparatively lower. Therefore, such degree of over-estimation can be attributed to the higher strength commonly attained by walls with barbell and flanged cross sections.

While the predictions using the equation by Gérin and Adebar (2004) may produce fairly reasonable mean and median values of predicted-to-measured ratio, it produced highly scattered predictions denoted by the widest range and the highest COV. Gérin and Adebar (2004) model performed significantly better for the prediction displacement capacity at peak strength of walls with rectangular cross sections. It should be noted that the model proposed by Gérin and Adebar (2004) was based on the experimental results of membrane-type elements. It appears that the behavior of membrane-type panels can be similar to cantilever walls with rectangular cross sections, but incongruent with that of cantilever walls with flanges and barbell cross sections.

6.4.3 Drift Ratio at Ultimate Damage State

In order to evaluate the suitability of the set of equations proposed in this study for the estimation of the drift ratio ultimate damage state (equations 6-3 and 6-4), its predictive performance is compared against several equations/models found in the literature. Figure 6-4 shows a graphic representation of the correlation of the calculated ultimate drift ratio vs. the measured ultimate drift ratio for the 59 obtained datasets of walls with enlarged boundary elements in the database, and for each of the equations presented on section 4.2.

As noted on previous section, the diagonal line represents a ratio of predicted-to-measured strength of 1.0 and any point above or below the diagonal line represents an over-prediction or

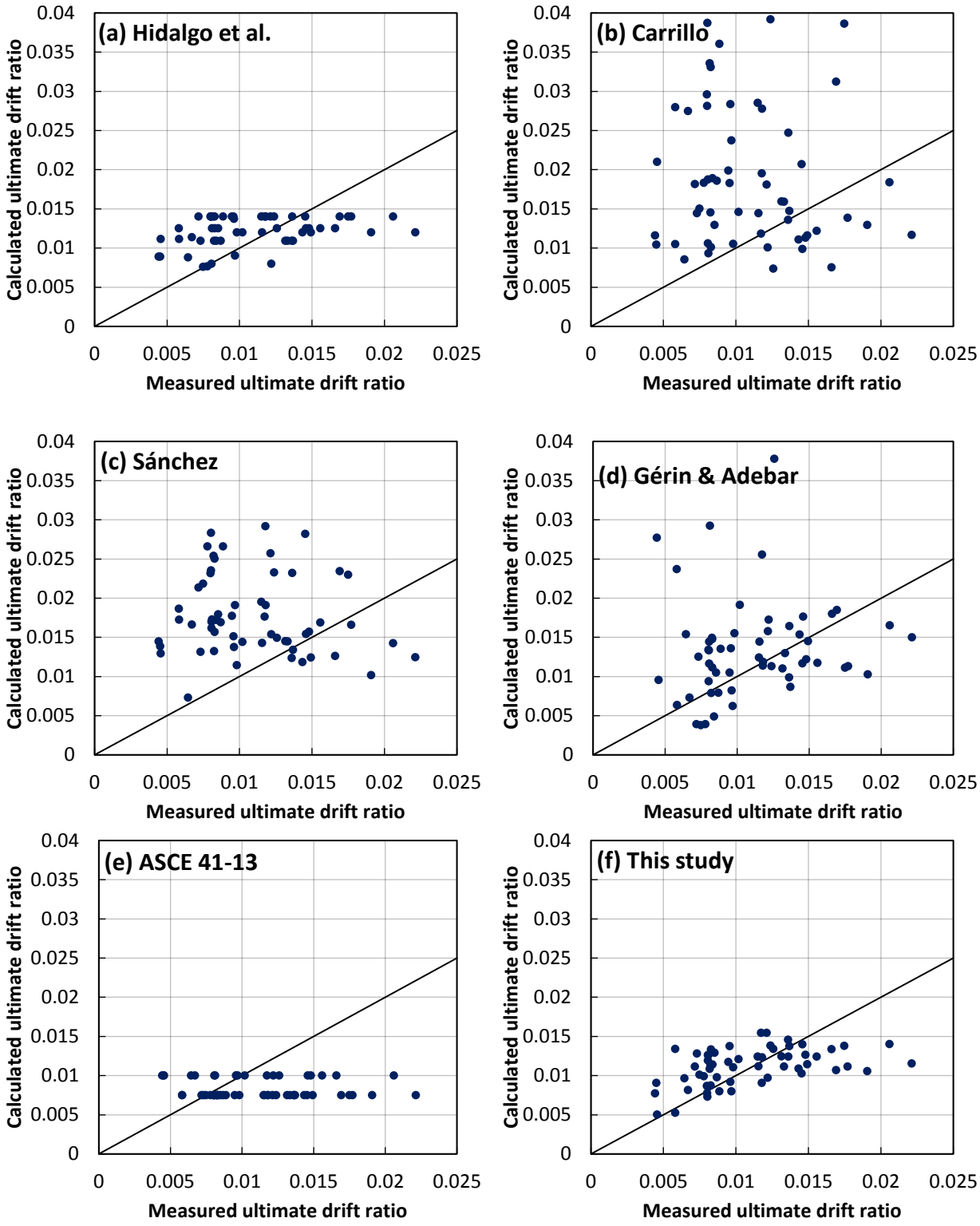

Figure 6-4. Correlation between calculated ultimate drift ratio and measured ultimate drift ratio using various available equations: (a) to (e); and the new equation proposed in this study (f).

an under-prediction, respectively. It can be noted from Figure 6-4 that the scatter on the predictions is significant. However, it is observed that the set of equations proposed in this study (equations 6-3 and 6-4) reduces the scatter of the drift ratio at peak strength estimate over most of the evaluated equations.

It seems that Hidalgo et al. (2000) equation produces similar scatter as equations 6-3 and 6-4, but tends to over-estimate the predictions. On the other side, ASCE 41-13 provides fixed values of the drift ratio at the ultimate state (abrupt strength drop) of 0.0075 and 0.010 for walls with low axial loads and walls with significant axial loads, respectively. These provisions tend to underestimate the actual value in most cases since the average drift ratio from test data resulted to be 0.011. Also, by observing Figure 6-4(e) it is noted that most of the points fall below the diagonal line.

Table 6-3. Summary of statistics of the ratio of predicted-to-measured ultimate drift for flanged/barbell walls included in the database.

	Hidalgo et al.	Carrillo	Sánchez	Gérin & Adebar	ASCE 41-13	This study
Mean	1.23	1.93	1.83	1.56	0.87	1.10
Median	1.19	1.76	1.70	1.09	0.85	1.06
Minimum	0.13	0.21	0.53	0.34	0.27	0.28
Maximum	2.44	4.82	3.52	13.59	2.26	2.30
Std. dev.	0.45	1.17	0.84	1.84	0.42	0.37
COV	0.37	0.61	0.46	1.19	0.48	0.34
% Over-predictions	61.0	76.3	83.1	59.3	25.4	55.9

In order to numerically compare the predictive performance of each equation, Table 6-3 presents a summary of common central tendency and dispersion measures of the predicted-to-measured drift ratio at peak strength, along with the percent of over-predictions. In the same fashion as discussed on previous section (6.4.2), Figure 6-5 shows a typical box and whisker plot comparing the distribution of the predicted-to-measured drift ratio for each selected equations/models. The graph provides valuable information regarding the central tendency, spread of values and extreme values.

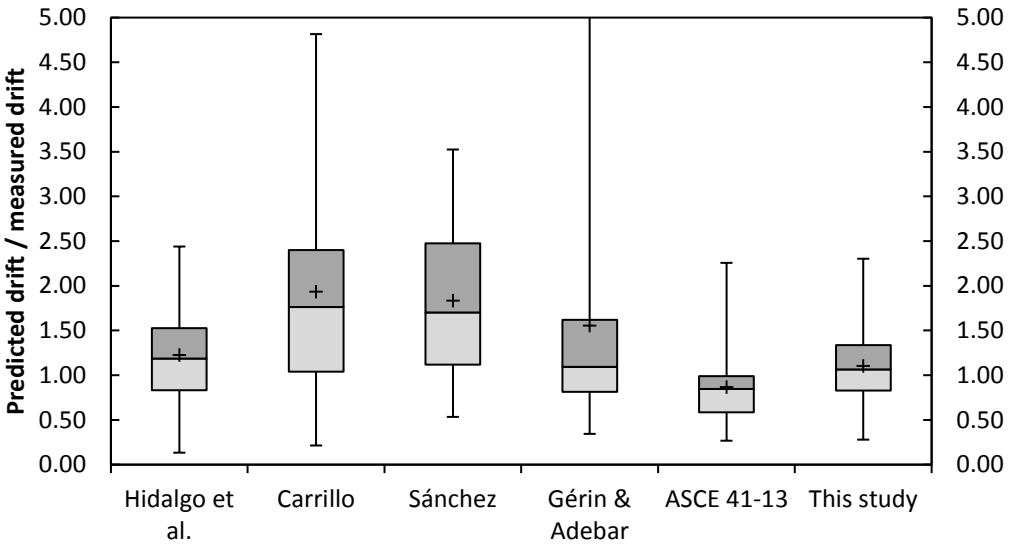

Figure 6-5. Distribution of the ratio of predicted-to-measured ultimate drift.

From the statistics presented on Table 6-3 and from Figure 6-5, it can be observed that the proposed set of equations produce an improved estimate of the drift ratio at peak strength since the mean and median predicted-to-measured values are closer to 1.0, while the coefficient of variation (COV) is kept in a similar level or lower than other predictions. It is also observed that the midspread falls between 0.83 and 1.34, which means that the ratio of predicted-to-measured values for 50% of the observations is closer to the median, and thus closer to a value of 1.0. In the same manner, the proposed equation yields 55.9% of over-predictions which is very near to the intended value of 50%.

In terms of the range (difference between maximum and minimum values), the equation proposed in this study is on par with the estimates using ASCE 41-13 provisions and Hidalgo et al. (2000) equations. However, ASCE 41-13 provisions tend to underestimate the drift ratio at peak strength as it can be noted from the low values of mean, median, % of over-predictions, and by inspection of Figure 6-4(e).

On the contrary, the predictions using the equations proposed by Carrillo (2010), Sánchez (2013), and Gérin and Adebar (2004) seem to produce considerably high scatter in terms of range, COV, and by inspection of Figure 6-4. Hidalgo et al. (2000) equations tend to slightly over-estimate the ultimate drift capacity on an average sense.

By observing the mean and median values from Table 6-3 and Figure 6-5, it is noted that the predictions using Carrillo (2010) and Sánchez (2013) equations tend to substantially over-estimate the displacement capacity at peak strength of squat RC walls with enlarged boundary elements. These two models also yield the widest IQR in terms of the predicted-to-measured ratio and the highest % of over-predictions. The range of the predicted-to-measured ratio of these two models is wider than all but the obtained using Gérin and Adebar (2004) equation. In the same manner as for the displacement at peak strength, the higher strength commonly attained by walls with barbell and flanged cross sections seems to bias the predictions of these two models since both use the peak strength to predict the ultimate drift capacity.

While the predictions using the equation by Gérin and Adebar (2004) may produce fairly reasonable median value of predicted-to-measured ratio, a considerable disparity is observed between its mean and median values of 1.09 and 1.56, respectively, which represents a significantly biased distribution. The equation by Gérin and Adebar (2004) produces highly scattered predictions represented by the widest range and the highest COV. It is again observed that Gérin and Adebar (2004) model performed significantly better for the prediction ultimate drift capacity of walls with rectangular cross sections. It appears that the behavior of membrane-type panels can be similar to cantilever walls with rectangular cross sections, but significantly different to that of cantilever walls with flanges and barbell cross sections.

Finally, it was noted that the allowable drift ratios for RC shear wall building systems provided on most current building design codes tend to be unconservative for squat RC walls with enlarged boundary elements as well as for squat RC walls with rectangular cross sections. For example, ASCE 7-10 seismic provisions allow a drift ratio of 0.02, while the average drift ratio at ultimate damage state (20% strength degradation) obtained from the experimental values on the collected database of squat walls with enlarged boundary elements was 0.011. This issue was discussed in more detail on section 4.4.3.

CHAPTER 7. ANALYTICAL MODELING OF SQUAT WALLS

7.1 Introduction

As noted previously, squat RC shear walls tend to have shear-dominated behavior and to exhibit strong coupling between flexural and shear responses. An adequate understanding of the lateral load vs. deformation behavior along with analytical modeling tools that can simulate such behavior is essential for the seismic design and performance assessment of nuclear power plant structures and other low rise shear wall civil structures. This chapter evaluates the applicability of two simplified modeling approaches for further calibration; and assesses their feasibility for design and evaluation of squat RC walls.

Monotonic and cyclic analyses were performed within the OpenSees analytical platform. Data from existing experimental tests of squat RC walls were used to develop and calibrate the models. This chapter discusses the advantages and disadvantages of each method and provides recommendations for future research in this topic. A Fiber-Based Model with flexure-shear interaction and a Macro-Hysteretic Model available in the OpenSees analytical platform were studied by comparing the simulated behavior with experimental data from several large scale tests of RC squat walls with rectangular cross sections. Performed analyses show that both, the Fiber-Based Model with shear-flexure interaction and the Macro-Hysteretic models can be calibrated to obtain a reasonable prediction of the lateral load-displacement behavior of squat reinforced concrete walls. Finally, the backbones for the presented Macro-Hysteretic model were calculated using the expressions for the prediction of strength and displacement capacity developed in previous chapters (Chapters 3 to 6) and analyses were performed to simulate the cyclic behavior of several large scale RC squat walls with rectangular cross sections. The obtained analysis results were then compared to experimental data for the corresponding test specimens.

The experimental data considered on this chapter was obtained from experimental tests of twelve large-size, low aspect ratio, RC shear walls that were conducted at the University at Buffalo

(Rocks, 2012; Luna et al., 2015). The digital test data has been published on the Network for Earthquake Engineering Simulation (NEES) website. The wall specimens had rectangular cross sections with a length of 304.8 cm and thickness of 20.3 cm with conventional reinforcement placed in two curtains. The specimens had varying aspect ratios ranging from 0.33 to 0.94, varying reinforcement ratios ranging from 0.33% to 1.5% and concrete strength varying from 24.1 to 53.8 MPa; and were tested under quasi-static cyclic lateral loading without axial load. The loading protocol consisted of increasing drift levels with 3 cycles on the first load step (drift level) and two cycles at every other load step. The drift was increased at each load step and ranged from about 0.01% to measure initial stiffness and up to maximum drifts of around 3% (severe strength degradation or failure). This chapter presents the analytical modeling of the lateral load vs. displacement behavior of six of these specimens, namely SW1, SW3, SW6, SW7, SW9 and SW11. Table 7-1 summarizes the basic properties of the studied wall specimens.

Table 7-1. Properties of the studied specimens.

Wall	h_w/l_w	ρ_v (%)	ρ_h (%)	f'_c (MPa)	f_y (MPa)	f_u (MPa)
SW1	0.94	0.67	0.67	24.8	462	703
SW3	0.54	0.67	0.67	53.8	434	600
SW6	0.33	0.67	0.67	26.2	462	703
SW7	0.33	0.33	0.33	26.2	462	703
SW9	0.54	1.5	0.67	29.7	462	703
SW11	0.54	0.67	0.67	34.5	462	703

7.2 Fiber-Based Flexure-Shear Interaction Model

On this modeling approach the OpenSees *Flexure-Shear Interaction Displacement-Based Beam-Column Element* (Orackal et al., 2006; Massone et al., 2012) was used. The wall is modeled using *m* stacked elements (Figure 7-1) composed of *n* strips each (Figure 7-2b). Each strip consists of vertical fibers corresponding to the steel and concrete tributary areas, and a horizontal fiber representing the total area of horizontal steel within one element. The interaction between flexure and shear is incorporated at the strip level, where the constitutive laws for concrete and steel are applied treating each strip as a reinforced concrete panel or membrane element (Figure 7-2a). A shear spring is assigned to each vertical uniaxial element, and then the strip is treated as

an RC panel with membrane action (i.e., with uniform normal and shear stresses applied in the plane) as shown in Figure 7-2(a). A rotating-angle softened-truss-model (Pang and Hsu, 1995) approach is implemented to represent the membrane (panel) behavior. Constitutive stress-strain material models are applied along the principal strain field, to obtain the stresses in the principal directions and then transformed to the reference (x, y) coordinates in order to obtain forces in the global directions. In this formulation, it is assumed that the principal stress and strain directions coincide. The parameter *c* (Figure 7-2(a)) is called the element center of rotation factor and is defined as the relative distance from the bottom of the element to the center of rotation. Massone (2006) suggested a value of $c = 0.4$ which was adopted in this study.

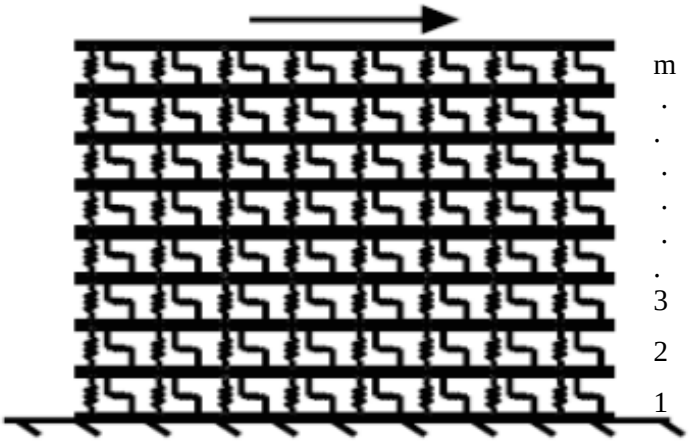

Figure 7-1. Wall model using Flexure-Shear Interaction Displacement-Based Beam-Column Element (Adapted from Massone, 2010a).

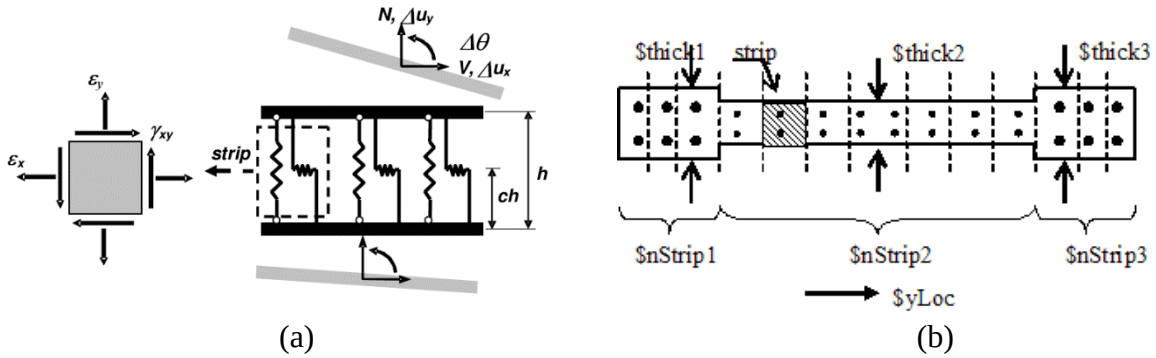

Figure 7-2. Flexure-Shear Interaction Displacement-Based Beam-Column Element: (a) model element (adapted from Orackal et al., 2006), and (b) element section modeling (Massone et al., 2012).

By using the membrane (panel) formulation, the model is capable of recording the following quantities at the strip level: *eX* (horizontal strain), *eY* (axial strain), *e1* (principal strain in direction 1), *e2* (principal strain in direction 2), alpha (angle for principal axis, measured counterclockwise from *eY* to *e1*), *sX* (average horizontal steel stress), *sY* (average vertical steel stress), *s1* (average principal concrete stress in direction 1) and *s2* (average principal concrete stress in direction 2). Also, at the section level, axial strain, curvature, shear strain, resultant axial force, moment and shear force can be recorded.

It is important to note that this model, as implemented in OpenSees, is intended for 2D monotonic static analysis and is not able to model the cyclic response of a wall. A new element model including the capability to calculate cyclic shear-flexure interaction, developed by Kolozvari et al. (2015) has been recently implemented in the OpenSees analysis platform, but its evaluation for the analysis of squat RC walls is out of the scope of this study.

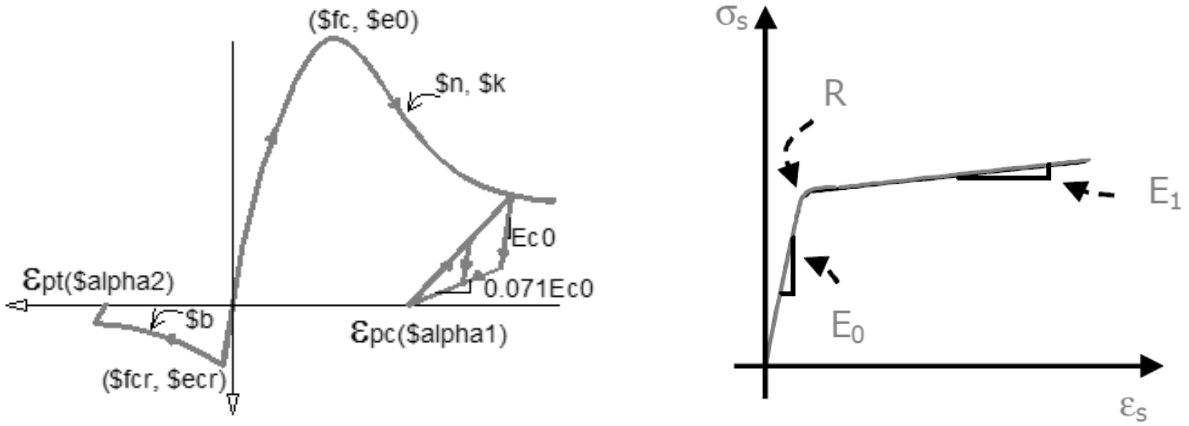

Figure 7-3. Constitutive models for concrete and steel: (a) *Concrete06* (adapted from Massone, 2010b) and (b) *Steel02* (adapted from Massone et al., 2004).

The constitutive models for concrete and steel materials used are the *Concrete06* (Massone, 2010b) and *Steel02* (Filippou and Mazzoni, 2012) which are available in OpenSees (Figure 7-3). The concrete constitutive model uses a Thorenfeldt-based curve to describe the compressive stress strain behavior of concrete, and the tension stiffening equation proposed by Belarbi and Hsu (1994) for the tensile portion of the curve. The compressive branch envelope of this

constitutive relationship is described by equation 7-1, which is the same base equation form used by Mander et al. (1988). Mander's model use k = 1 and incorporates the increase in compressive strength and ultimate strain due to transverse steel confinement into this base equation.

$$\sigma_c = f'_c \frac{n\left(\frac{\varepsilon_c}{\varepsilon_0}\right)}{n - 1 + \left(\frac{\varepsilon_c}{\varepsilon_0}\right)^{nk}} \tag{7-1}$$

where ε_0 is the strain at compressive strength, n is the compressive shape factor and k is the post peak compressive shape factor. The tensile branch of the stress strain relationship is described by the equations (7-2) and (7-3) proposed by Belarbi and Hsu (1994) which considers the tension stiffening.

$$\varepsilon_c \leq \varepsilon_{cr} \qquad \sigma_c = E_c \varepsilon_c \tag{7-2}$$

$$\varepsilon_c > \varepsilon_{cr} \qquad \sigma_c = f_{cr}\left(\frac{\varepsilon_{cr}}{\varepsilon_c}\right)^b \tag{7-3}$$

where ε_{cr} is the tensile strain at peak tensile stress, f_{cr} is the tensile cracking stress and b is the exponent of the tension stiffening curve. An example of the stress-strain relationship for Concrete06 is shown in Figure 7-3(a). The tension stiffening is represented by the post cracking tensile stress in the concrete tensile constitutive model. This residual tensile strength is provided by the concrete that remains bonded to reinforcement between cracks. Further information regarding the constitutive models can be found on the OpenSees documentation.

The calibration of concrete constitutive model parameters was done by using the reported material properties and other typical values. The post peak compressive shape factor was taken as k = 1.0 as suggested by Mander et al. (1988), while the compressive shape factor (n) was selected to match the compressive model curve with the reported compressive stress-strain curve. The concrete tensile cracking stress was taken as $7.5(f'_c)^{1/2}$, while the value of the tensile cracking strain was taken as 0.00008 as proposed by Belarbi and Hsu (1994). The model was found to be sensitive to the tension envelope exponent b and the calibration of this parameter is discussed later in this section. Parameters *alpha1* and *alpha2* are related to the cyclic unloading and reloading of concrete, thus not significant for monotonic analyses. Therefore, default values

were used. Table 7-2 shows the parameters used in the analyses for the concrete constitutive model. Negative values on Table 7-2 indicate compressive concrete related parameters.

Table 7-2. *Concrete06* constitutive model calibrated parameters.

Wall	fc (MPa)	e0	n	k	alpha1	fcr	ecr	b	alpha2
SW1	- 24.8	-0.003	2.0	1.0	0.32	450.0	0.00008	4.0	0.08
SW3	- 53.8	-0.003	3.75	1.0	0.32	662.4	0.00008	4.0	0.08
SW6	- 26.2	-0.003	2.0	1.0	0.32	462.3	0.00008	4.0	0.08

The reinforcement is modeled using the monotonic branch of uniaxial material model *Steel02* available in OpenSees. This constitutive model is based on the model described by Filippou et al. (1983) and uses a simple bi-linear relationship with a softened transition between the initial and post-yield tangents as shown in Figure 7-3(b). Further information regarding the constitutive models can be found on the OpenSees documentation.

Calibration of constitutive model parameters for the reinforcing steel was obtained from the reported material properties. Nevertheless, some parameters require experimental data from cyclic tests which is not usually available. Therefore, the values of *R0, cR1* and *cR2* were taken from recommended values found on the OpenSees documentation and the values for the hardening parameters *a1* and *a2* calibrated with experimental data by prior researchers were obtained from Elmorsi et al. (1998). Default values were used for *a3* and *a4* (no hardening in tension was considered). However, these isotropic hardening parameters are not as significant for monotonic analyses as they are for cyclic analyses. Table 7-3 presents the parameters used for the steel constitutive model.

Table 7-3. *Steel02* constitutive model calibrated parameters.

Wall	fy (MPa)	E0 (MPa)	bs	R0	cR1	cR2	a1	a2	a3	a4
SW1	462	$200x10^3$	0.018	15	0.925	0.15	18.5	0.0015	0	1.0
SW3	434	$200x10^3$	0.013	15	0.925	0.15	18.5	0.0015	0	1.0
SW6	462	$200x10^3$	0.018	15	0.925	0.15	18.5	0.0015	0	1.0

The selected specimens studied in this section (SW1, SW3 and SW6) had vertical and horizontal reinforcement ratios of 0.67% which results in two curtains of #3 reinforcing bars spaced at nearly 7 in. on center. The cross section was modeled with one strip at the location of every vertical bar along the length of the wall (Figure 7-4). Wall models were initially discretized with one element per horizontal bar location along the height resulting in 14, 10 and 5 elements for the specimens SW1, SW3 and SW6, respectively. Orackal et al. (2006) suggested that the model was sensitive to the number of vertical elements. Therefore, walls SW1, SW3 and SW6, were modeled to 7, 5 and 3 elements for the specimens, respectively. This resulted in a better representation of the displacement capacity while maintaining a good approximation of the peak strength. The obtained results for the Fiber-Based Model with flexure-shear interaction, using the reduced number of elements, and the materials constitutive model parameters shown on Table 7-2 and Table 7-3, are illustrated in the next figures and compared to the experimental data.

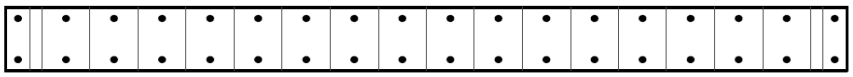

Figure 7-4. Cross section discretization model for the studied specimens SW1, SW3 and SW6.

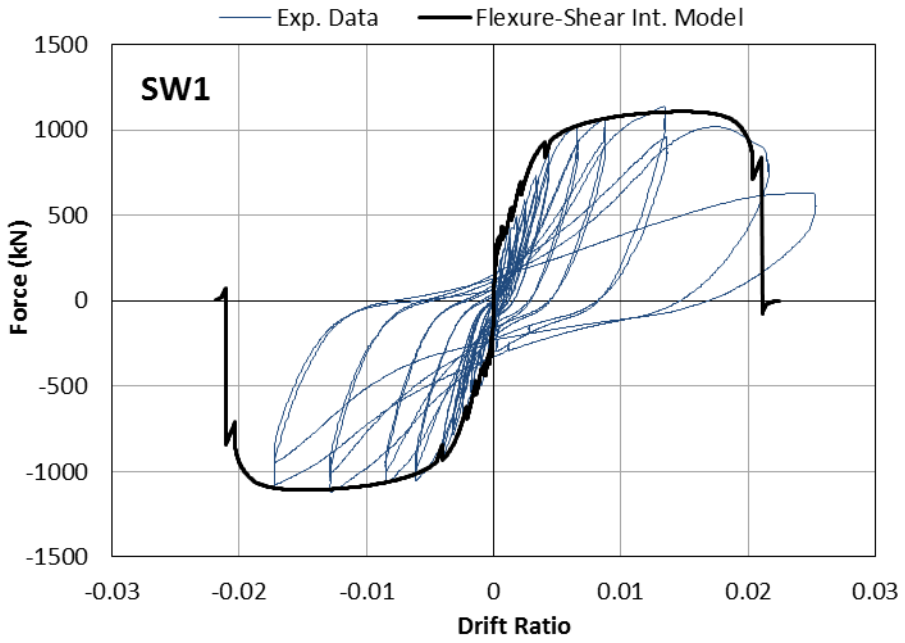

Figure 7-5. Experimental and flexure-shear interaction model load-displacement results for wall SW1.

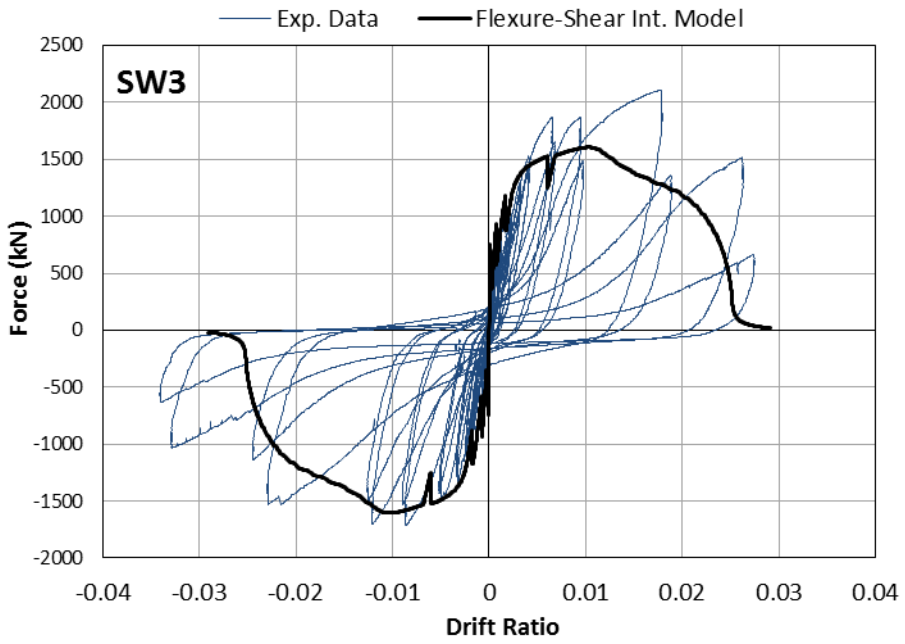

Figure 7-6. Experimental and flexure-shear interaction model load-displacement results for wall SW3.

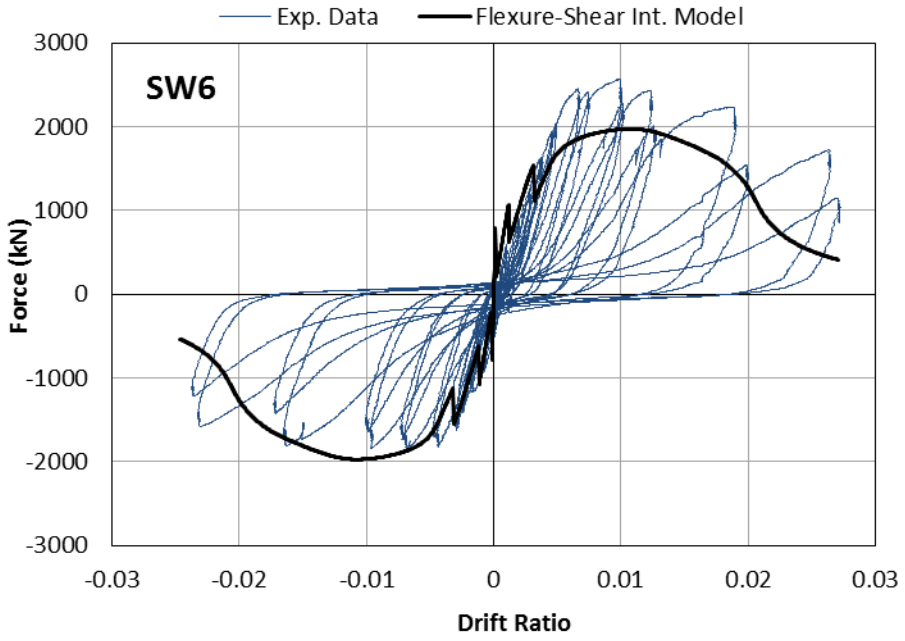

Figure 7-7. Experimental and flexure-shear interaction model load-displacement results for wall SW6.

The obtained results show that the flexure-shear interaction model can reasonably predict the experimental cyclic load-displacement envelope for the studied walls with aspect ratios ranging from 0.33 to 0.94 and rectangular cross section. However, the model calibration and performance assessment was conducted for a small number of experimental tests and would need to be validated and/or further calibrated against a larger database to obtain more reliable predictions.

As mentioned before, the flexure-shear model was found to be very sensitive to the number of elements in which the wall is discretized and to the concrete tension stiffening curve exponent (parameter *b*). In order to illustrate the effect of these parameters, the wall specimen SW3 has been modeled using three different values of *b* and then using three different number of elements. The rest of the parameters were kept constant using the calibrated values. Results of the monotonic analytical responses are plotted against experimental data on Figure 7-8 showing the effect of wall discretization; and on Figure 7-9 showing the effect of parameter *b*. Only the first quadrant of the response is shown for clarity.

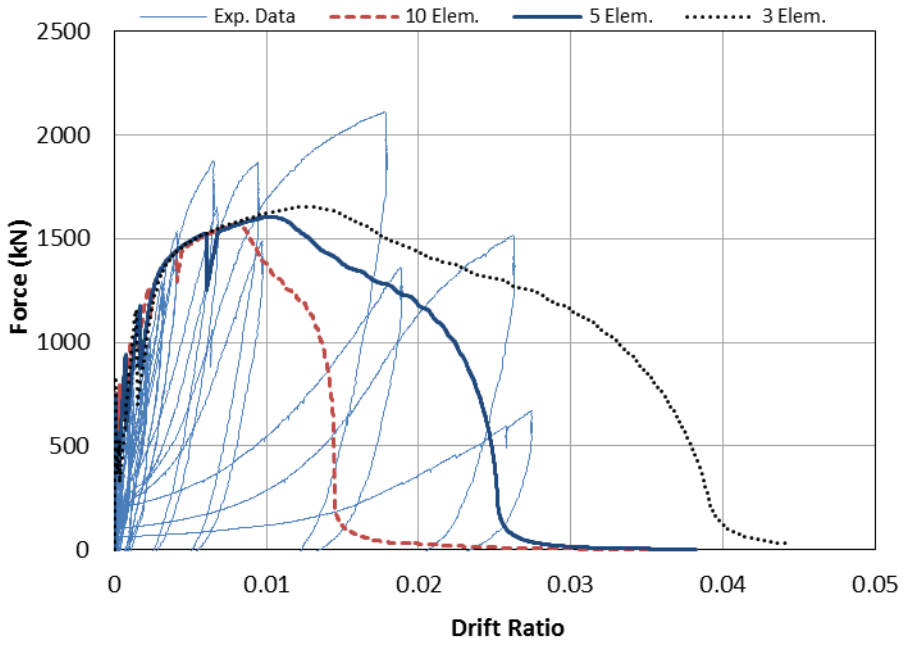

Figure 7-8. Sensitivity of the Fiber-Based Flexure-Shear Interaction Model to vertical wall discretization (No. vertical elements) on wall specimen SW3.

Figure 7-8 shows the sensitivity to the number of vertical elements in which the model was discretized. The number of stacked elements used to represent the wall affected mostly the

predicted displacement capacity of the wall but did not have a significant effect on the peak strength. As the wall was modeled using fewer elements, the predicted drift capacity increased substantially. This effect may be attributed to the localization of stresses and damage as the model is further discretized, which causes earlier failure of the element leading to loss of overall stability of the model.

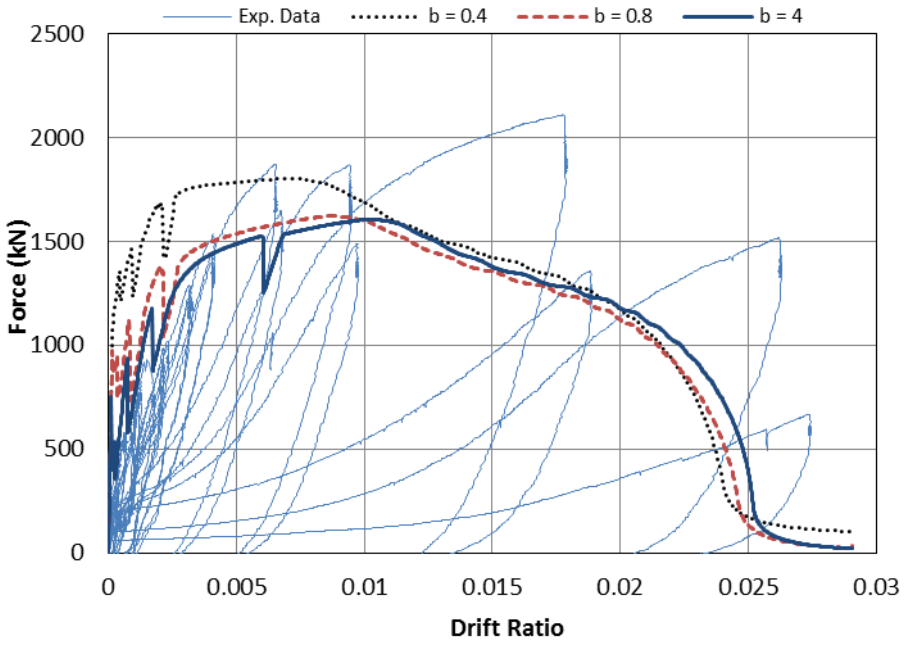

Figure 7-9. Sensitivity of the Fiber-Based Flexure-Shear Interaction Model to concrete tension stiffening curve exponent (*b*) on wall specimen SW3.

From Figure 7-9, it can be observed that the concrete parameter *b* has a major effect on the apparent initial stiffness of the wall model and also has a moderate effect on its peak strength. When the value of *b* was increased the apparent initial stiffness, as well as the peak strength, decreases since the tension stiffening curve was decreasing more rapidly. The effect of this parameter on the response was more pronounced for values of about 0.8 and less. A value of *b* equal to 0.4 was suggested by Belarbi and Hsu (1994, 1995), however by adjusting this parameter to a higher value (e.g. 4.0 as also found by Whyte and Stojadinovic, 2013) produced a better fit to the evaluated experimental data.

Finally, Table 7-4 shows the ratio of the predicted-to-measured peak shear strength for the Fiber-Based Model. The experimental peak strength was taken as the average of the peaks from first and third quadrants since, on specimens with lower aspect ratios, these values can be substantially different. The difference in strength measured on both positive and negative directions mostly occur due to sudden failure of the wall specimen after attaining peak strength in one direction. Also, Luna et al. (2015) reported that significant out of plane displacements were observed in some of the tests performed at the University at Buffalo due to insufficient lateral restrain in the test rig.

Table 7-4. Experimental vs. Fiber-Based Model peak shear strength.

Wall	V_{peak}^{+}	V_{peak}^{-}	V_{peak}^{avg}	V_{model}	V_{model}/V_{peak}^{avg}
SW1	1139	1112	1125	1108	0.98
SW3	2108	1717	1913	1606	0.84
SW6	2571	1841	2206	1975	0.90

*Force units: kN

The obtained results suggest that the flexure-shear interaction model is feasible to be calibrated and used to simulate the lateral load vs. displacement behavior of squat RC walls with rectangular cross sections since it was able to reasonably predict the peak strength and drift capacity of the studied experiments. Table 7-4 shows that the strength was predicted with reasonable accuracy for the studied specimens. However, great care should be taken in the selection of the number of elements to model squat RC walls using the flexure-shear interaction element if the prediction of ultimate displacement capacity is considered important in the analysis. In a similar manner, judgment is advised on the selection of the concrete tension stiffening curve exponent (*b* parameter) when the prediction of initial stiffness is of particular interest. Further calibration against a larger database is still necessary to obtain more reliable results. Also, assessment of the model performance for walls with enlarged boundary elements is needed. The availability of published cyclic testing experimental data is a major source of difficulty to perform this task.

7.3 Macro-Hysteretic Model

In this modeling approach the cyclic lateral load vs. displacement behavior of the wall was modeled as a single degree of freedom structure and the experimental displacements were applied at the free end. The hysteretic material model from OpenSees called *Hysteretic Material* (Scott and Filippou, 2013) was used. This model requires the definition of a backbone curve as shown in Figure 7-10, which was calibrated with the experimental data.

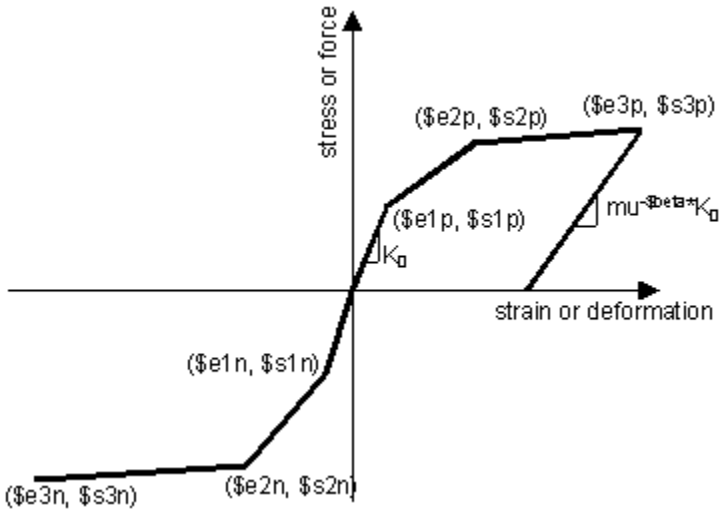

Figure 7-10. Backbone curve definition parameters for the hysteretic material model (Scott and Filippou, 2013).

The *Hysteretic Material* model has the capability to capture commonly observed pinching and strength and stiffness degradation of hysteresis loops. This can be accomplished by the calibration of the model with experimental data. In order to illustrate the effect of each of the model parameters Figure 7-11 is presented. Figure 7-11(a) shows an example of the effect of the pinching parameters (*pinchX* and *pinchY*) where the black line corresponds to both parameters set to a value of 1.0 (no pinching), while the red line corresponds to *pinchX* = 0.8 and *pinchY* = 0.2. Note that the *pinchX* parameter is the pinching factor for deformation during reloading, while the *pinchY* parameter corresponds to the pinching factor for force during reloading.

The model has two strength-reducing damage parameters referred to as *damage1* and *damage2*. The *damage1* parameter incorporates strength deterioration due to ductility, whereas the *damage2* parameter incorporates strength deterioration damage due to the energy dissipated by

inelastic deformation. This means that the first produces a strength reduction proportional to the cumulative plastic deformation, while the second produces a strength reduction proportional to the cumulative inelastic energy dissipation. Figure 7-11(b) shows an example of the effect of strength degradation parameters where the black line corresponds to both damage parameters set to zero (no damage) and the red line corresponds to damage parameters higher than zero.

This model also includes a parameter to adjust unloading stiffness degradation based on the ductility demand (*beta*). This parameter is the power used to determine ductility-dependent degraded unloading stiffness as a portion of the initial unloading stiffness (μ^{-beta}). Figure 7-11(c) shows an example of the effect of unloading stiffness degradation parameter where the black line corresponds to *beta* = 0 (no damage), and the red line corresponds to *beta* = 0.5.

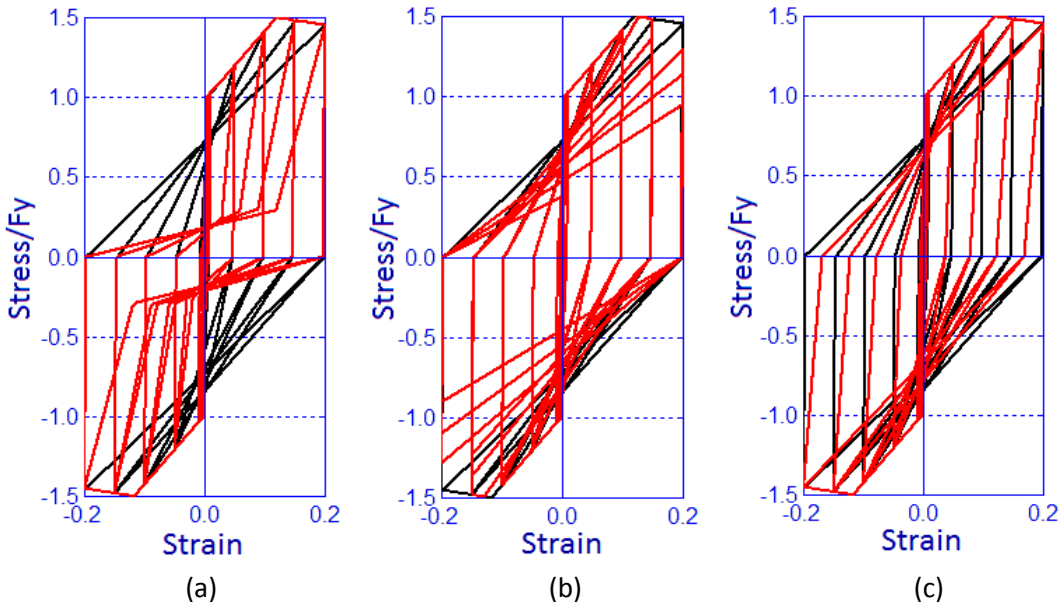

Figure 7-11. Effect of hysteretic parameters on the Hysteretic Material model: (a) pinching, (b) strength degradation, (c) and unloading stiffness degradation (Scott and Filippou, 2013).

7.3.1 Basic Parameters Calibration

The calculated backbone curve was optimized by taking the peak strength and maximum drift points equal to the experimental values. The initial stiffness was also set to be equal to the obtained experimentally. The control point associated with the "yielding", or cracking in the case

of shear-controlled squat RC walls, was adjusted so that the area under the experimental cyclic envelope equals the area under the calculated backbone (Figure 7-12).

Table 7-5 shows the calculated backbone parameters for the considered walls. The intent of calibrating the backbone curve to the experimental envelope was to evaluate if the tri-linear backbone is capable of reasonably represent the experimental load-displacement envelopes, and afterwards, to assess the model's ability to capture the hysteretic behavior of the considered walls by calibrating the hysteretic parameters. From this calibration, initial values for the *Hysteretic Model* parameters were identified for modeling squat RC walls. The intent was not to provide a statistically robust calibration of the hysteresis parameters, but to identify a reasonable range of values for the parameters and show the capability of the simple model to capture the typical hysteretic behavior of these walls.

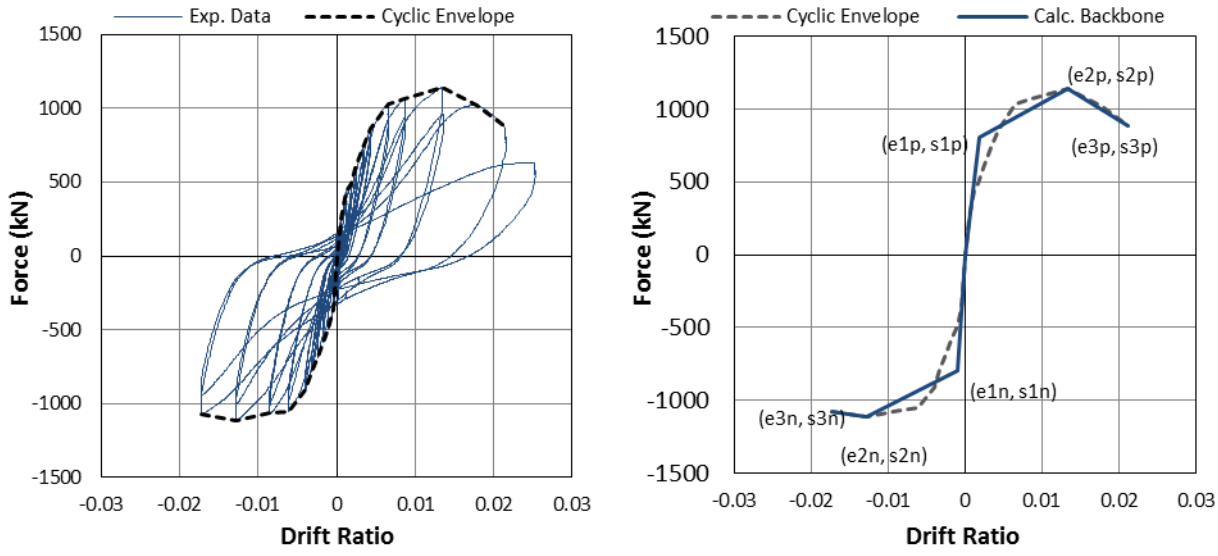

(a) Experimental cyclic envelope (b) Backbone curve fitting

Figure 7-12. Example backbone curve fitting for the Macro-Hysteretic Model (SW1).

Table 7-5. Calibrated backbone control points parameters.

Wall	s1p	e1p	s2p	e2p	s3p	e3p	s1n	e1n	s2n	e2n	s3n	e3n
SW1	805	0.00193	1139	0.0134	890	0.0212	-796	-0.00093	-1112	-0.0128	-1076	-0.0173
SW3	1410	0.00121	2108	0.0177	1512	0.0262	-1076	-0.00073	-1717	-0.0086	-1526	-0.0228
SW6	1957	0.00221	2571	0.0096	1726	0.0264	-1566	-0.00119	-1841	-0.0073	-1588	-0.0232

*All values of force are in kN and deformation is taken as drift ratio.

As discussed earlier, the hysteretic model is defined by several parameters that control pinching in force (*pinchY*) and deformation (*pinchX*), damage based on ductility (*damage1*) and energy (*damage2*), and unloading stiffness degradation (*beta*) based on ductility. It was noted that similar results were obtained if the model was calibrated using dissipated energy-based damage, or if calibrated using a ductility-based damage. To be consistent with the unloading stiffness degradation approach, the damage was calibrated based on ductility. Using strength degradation based only on ductility produced a reasonable approximation of the studied squat RC wall specimens' behavior. In this way, only four parameters would be necessary to calibrate the model for this type of walls. Table 7-6 shows the calibrated hysteresis parameters.

Table 7-6. Calibrated pinching and damage parameters.

Wall	pinchX	pinchY	damage1	damage2	Beta
SW1	0.6	0.15	0.010	0	0.3
SW3	0.6	0.15	0.012	0	0.4
SW6	0.75	0.15	0.016	0	0.4

The model results compared to experimental test data of the hysteresis are shown in Figure 7-13. It can be noted that the tri-linear backbone model is capable of reasonably represent shape of experimental load-displacement envelope for the studied specimens if well calibrated. It is also observed that the model loading and unloading rules are simple but capable enough to reasonably capture the characteristic features of the hysteretic behavior such as pinching, strength degradation and stiffness degradation. In this study these parameters are calibrated against a very limited amount of experiments for the purpose of assessing the feasibility of the model to be further calibrated for use in squat RC walls modeling; and to identify basic values for such parameters.

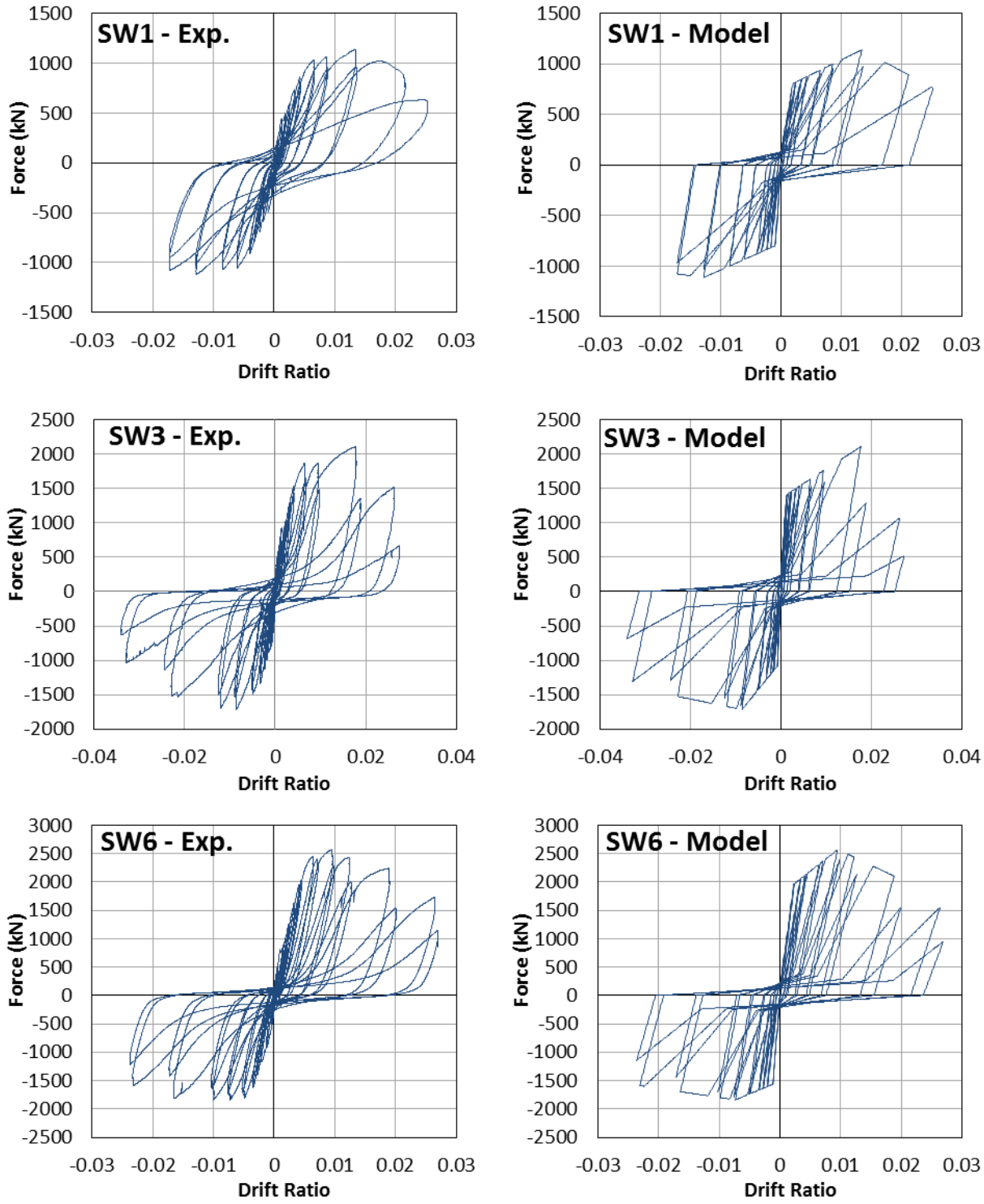

Figure 7-13. Experimental and calibrated Macro-Hysteretic model results of the cyclic load-displacement behavior for walls SW1, SW3 and SW6.

One of the limitations of the *Hysteretic Material* model is that the backbone curve has only three linear segments. These types of walls and other shear-controlled RC structural members tend to show an initial stiffness reduction upon flexural cracking. Then they would experience a larger reduction in stiffness at the "yielding" point (which is not necessarily related to the yielding of the reinforcement but more likely to significant diagonal cracking) until it reaches the peak strength or "capping point", where the strength degradation becomes more pronounced and the slope of the envelope becomes negative until reaching failure. While this behavior would be more accurately modeled with the incorporation of a fourth line segment into the backbone curve to include the flexural cracking point, the stiffness reduction due to diagonal cracking appears to be more significant, and therefore, the tri-linear backbone can reasonably capture the typical experimental load-displacement envelope shape of members controlled by shear.

Among the most significant advantages of Macro-Hysteretic model over the Fiber-Based Flexure-Shear Interaction Model presented herein are the substantially less computational effort and the ability to simulate the cyclic performance of a wall with reasonable accuracy. Also, the use of simplified Macro-Hysteretic models for structures that include squat walls would be generally preferred for performance based assessment of structures due to their ability to represent the cyclic force-deformation behavior at the story level with relative simplicity. This model can be conveniently calibrated to fit a given experimental dataset since it has fewer pinching and degradation parameters than other hysteretic models that have been proposed in literature. Despite the few parameters required, it is shown that the *Hysteretic Material* can reasonably capture the key characteristics of the hysteretic behavior of squat walls with rectangular cross sections. Having a calibrated model to determine the backbone control points, such as the equations proposed in Chapters 3 to 6, is key to use this model for the simulation of squat RC walls behavior. The simplicity of the model makes it suitable for empirical calibration of the backbone and hysteresis parameters with a larger database which would allow to use this model to simulate the behavior of squat RC walls with reasonable accuracy and without the need of having experimental data available.

7.3.2 Developed Backbone Model

On previous section (7.3.1) it was shown that the experimental load displacement envelope of a squat RC wall can be reasonably represented with a tri-linear backbone. On Chapters 4 and 6 it was noted that these walls show a first major stiffness reduction that is associated with the occurrence of significant diagonal cracking. This point was associated to a characteristic lateral force level of 0.6 V_{peak}. Then the wall would keep developing lateral strength until reaching the peak strength, where the strength degradation becomes more noticeable, and the strength envelope will start to decrease in a pronounced manner as the displacement is increased. This behavior can be represented with a straight line of negative slope. While several walls were taken to extreme strength degradation levels showing considerable energy dissipation, data for these advanced damage states was very scarce, and therefore predictions of behavior derived thereof would be considered unreliable. To these effects, ultimate damage state was defined using a conventional 20% strength drop criterion (when attaining $0.8V_{peak}$).

Calibrated expressions obtained from multiple linear regression analyses were proposed on Chapters 4 and 6 for the determination of the drift ratio capacity at each of the control points (i.e. diagonal cracking, peak strength, and ultimate damage state), for walls with rectangular cross sections and with enlarged boundary elements, respectively. Likewise, expressions were proposed on Chapters 3 and 5, for the prediction of the peak strength of squat RC walls with rectangular cross section and with enlarged boundary elements, respectively. Using the aforementioned sets of expressions, the proposed tri-linear backbone curve can be estimated by determining the three control points: cracking point (R_{cr} , $0.6V_{peak}$), peak point (R_{peak} , V_{peak}), and ultimate state point (R_u , $0.8V_{peak}$).

Figure 7-14 and Figure 7-15 show the calculated backbones using the methodology proposed herein, compared to the experimental load-drift ratio envelope for several squat RC walls of rectangular cross sections and with enlarged boundary elements, respectively. The studied wall specimens were selected from different research programs within the assembled database and have variety of characteristics (e.g. aspect ratio, reinforcement ratios concrete strength, etc.). The specimens with rectangular cross section shown on Figure 7-14 were selected from the test programs by Carrillo and Alcocer (2013), Terzioğlu (2011), Luna et al. (2015), Saatcioglu/Wiradinata (1985), and Park et al. (2015). The specimens with enlarged boundary

elements shown on Figure 7-15 were selected from the experimental programs by Akita et al. (2006), Barda (1972), Palermo and Vecchio (2002), Park et al. (2015), Dabbagh (2005), Endo (1980), and XiangDong (1999).

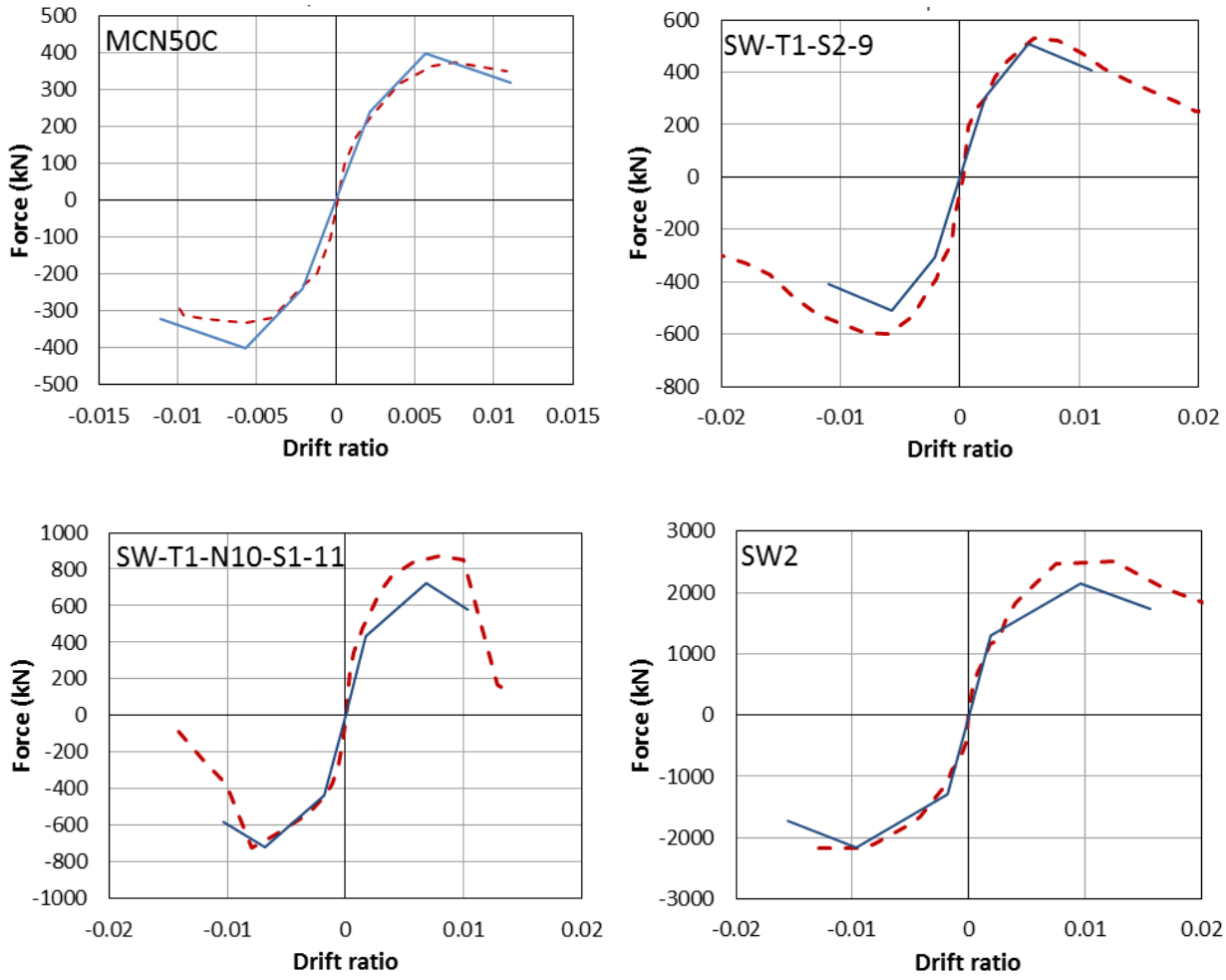

Figure 7-14. Calculated backbone (—) compared to experimental (- - -) load-drift ratio envelope for squat RC walls with rectangular cross section.

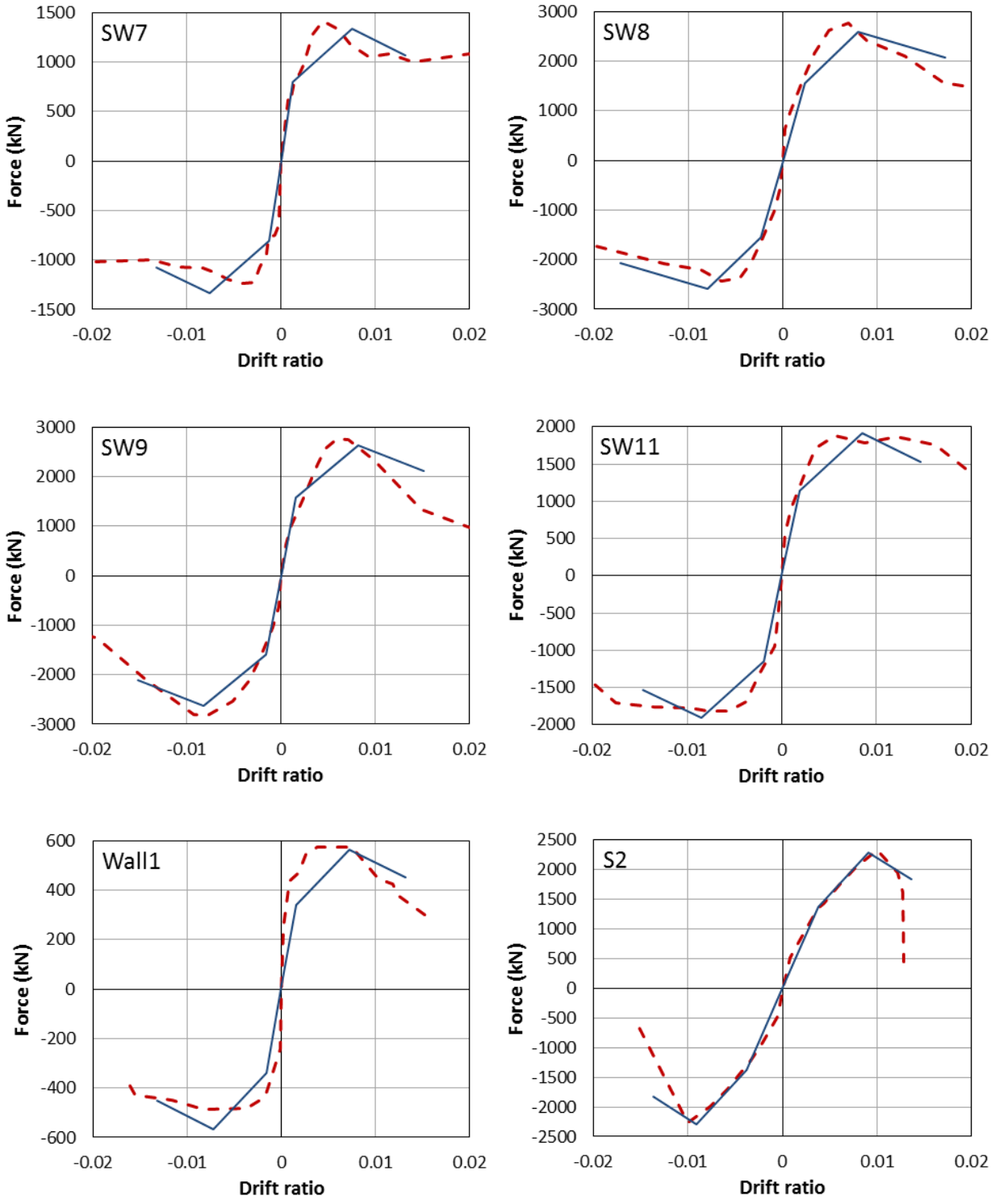

Figure 7.14. Continued.

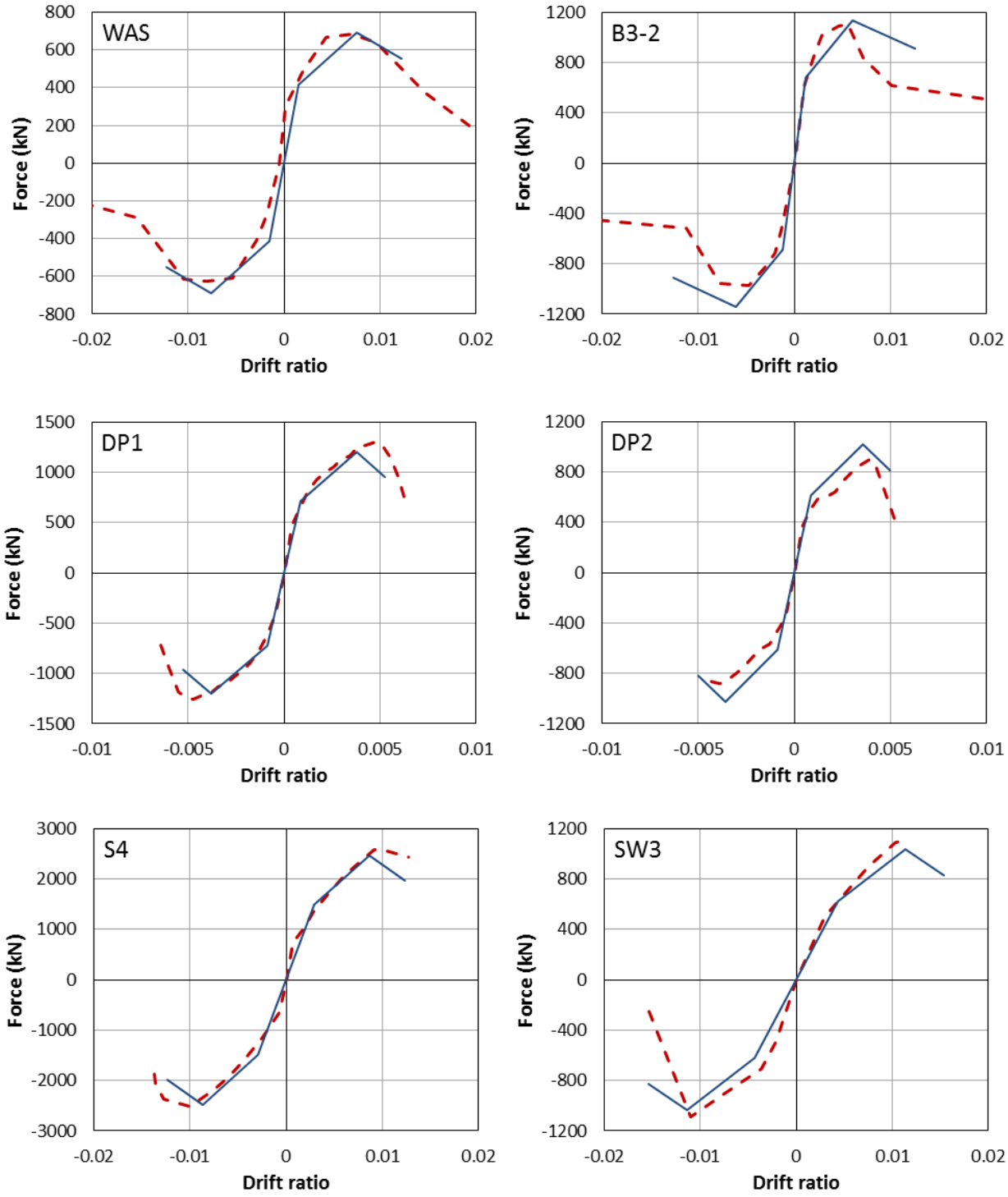

Figure 7-15. Calculated backbone (—) compared to experimental (- - -) load-drift ratio envelope for squat RC walls with enlarged boundary elements.

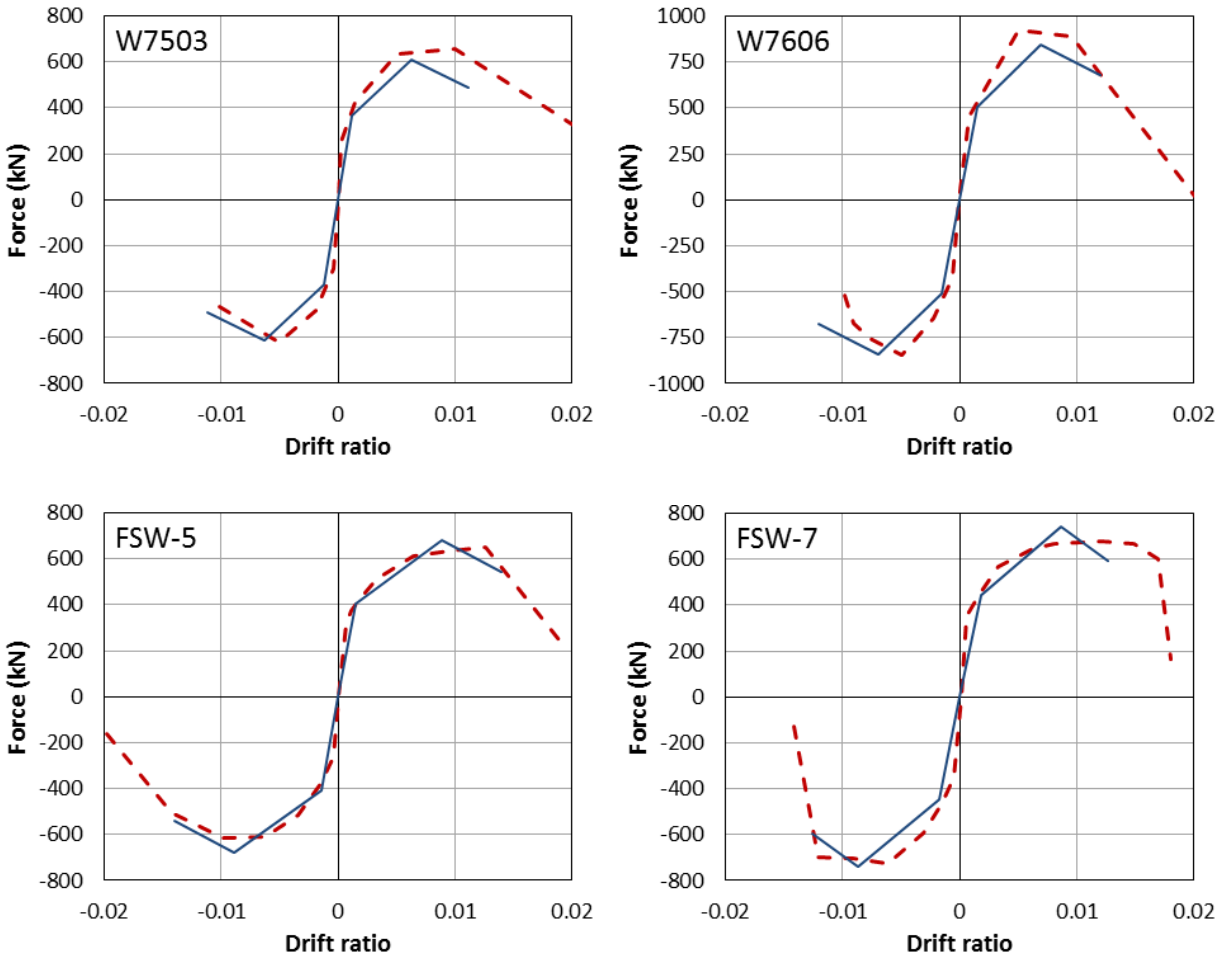

Figure 7-15. Continued.

From Figure 7-14 and Figure 7-15, it can be noted that the proposed backbone model is able to predict the experimental load-drift ratio envelope behavior with relatively good accuracy. The peak strength, initial stiffness, and the area under the curve (up to the defined ultimate point) can be reasonably estimated with the proposed backbone model. The studied specimens were selected with a wide variety in characteristics and from several different experimental programs so that they would be representative of the average model performance within the assembled database. Notwithstanding, due to the variability in the predictions, the model may yield less reasonable results for some cases.

While the prediction of the displacement capacity can have significant scatter, the area under the backbone curve, up to the defined ultimate state, appears to be similar to that of the experimental

envelope. This indicates that the proposed backbone model can adequately simulate the energy dissipation characteristics of squat RC walls under monotonic lateral loading. In the same manner, these findings suggest that the proposed backbone model, when used in conjunction with a hysteretic model, can reasonably represent the cyclic energy dissipation of squat RC walls; provided that the hysteresis damage parameters of the model (i.e. pinching, strength degradation and stiffness degradation) are well calibrated.

The next section discusses the analysis results for several walls using the Macro-Hysteretic model (OpenSees *Hysteretic Material* model) presented earlier in this chapter, with the basic calibration of hysteretic parameters presented on section 7.3.1 in conjunction with the backbone model proposed herein.

7.3.3 Macro-Hysteretic Model using Developed Backbone Model

As it was shown on previous section, the proposed tri-linear backbone model, using the equations developed in Chapters 3 to 6 to determine its control points, is capable of reasonably estimate the experimental load-drift ratio behavior of the studied walls. Furthermore, if the backbone and hysteretic parameters are well calibrated against experimental data, the presented Macro-Hysteretic model is capable of simulating the experimental hysteretic behavior with very good accuracy. In this section an additional three walls from the Luna et al. (2015)/NEES-UB experimental program were modeled using the proposed Macro-Hysteretic model (OpenSees *Hysteretic Material* model) presented earlier in this chapter, with the hysteretic parameters identified by the basic calibration presented on section 7.3.1, and with the calibrated backbone model discussed on previous section (7.3.2). The calculated backbone control points are shown on Table 7-7 and the selected hysteretic parameters are shown on Table 7-8.

Table 7-7. Calculated backbone control points parameters.

Wall	s1p	e1p	s2p	e2p	s3p	e3p	s1n	e1n	s2n	e2n	s3n	e3n
SW7	803	0.0013	1338	0.0076	1071	0.0132	-803	-0.0013	-1338	-0.0076	-1071	-0.0132
SW9	1581	0.0016	2635	0.0082	2108	0.0152	-1581	-0.0016	-2635	-0.0082	-2108	-0.0152
SW11	1147	0.0019	1912	0.0085	1529	0.0147	-1147	-0.0019	-1912	-0.0085	-1529	-0.0147

*All values of force are in kN and deformation is taken as drift ratio.

Table 7-8. **Selected pinching and damage parameters.**

Wall	pinchX	pinchY	damage1	damage2	Beta
SW7	0.75	0.15	0.016	0	0.4
SW9	0.6	0.15	0.016	0	0.4
SW11	0.6	0.15	0.016	0	0.4

Figure 7-16 shows the experimental hysteresis data compared to the proposed Macro-Hysteretic model results. The studied test specimens were subjected to a displacement-controlled lateral load protocol. In order to assess the predictive performance of the model proposed in this study, the lateral loading on the wall models was taken as a displacement input at the free end with the same experimental displacement protocol as in the experiments.

The results shown on Figure 7-16, suggest that the proposed model can reasonably simulate the experimental behavior of the studied wall specimens and other walls with similar characteristics when using the strength and drift capacity equations proposed in this study to estimate the tri-linear backbone curve, in combination with the basic hysteretic parameter values identified on section 7.3.1. Specifically, the pinching parameters identified on section 7.3.1 appear to be well suited to represent the pinching of the experimental hysteresis loops for the studied RC squat walls specimens.

On the other hand, the model with the selected parameters was not able to consistently capture the cyclic strength degradation. It can be observed that the modeled response of wall SW7 captured the cyclic strength degradation after the peak point with good accuracy. Wall SW11 model captured some of the experimentally observed post-peak cyclic strength degradation. However, cyclic strength degradation is barely observed on the modeled response of wall SW9.

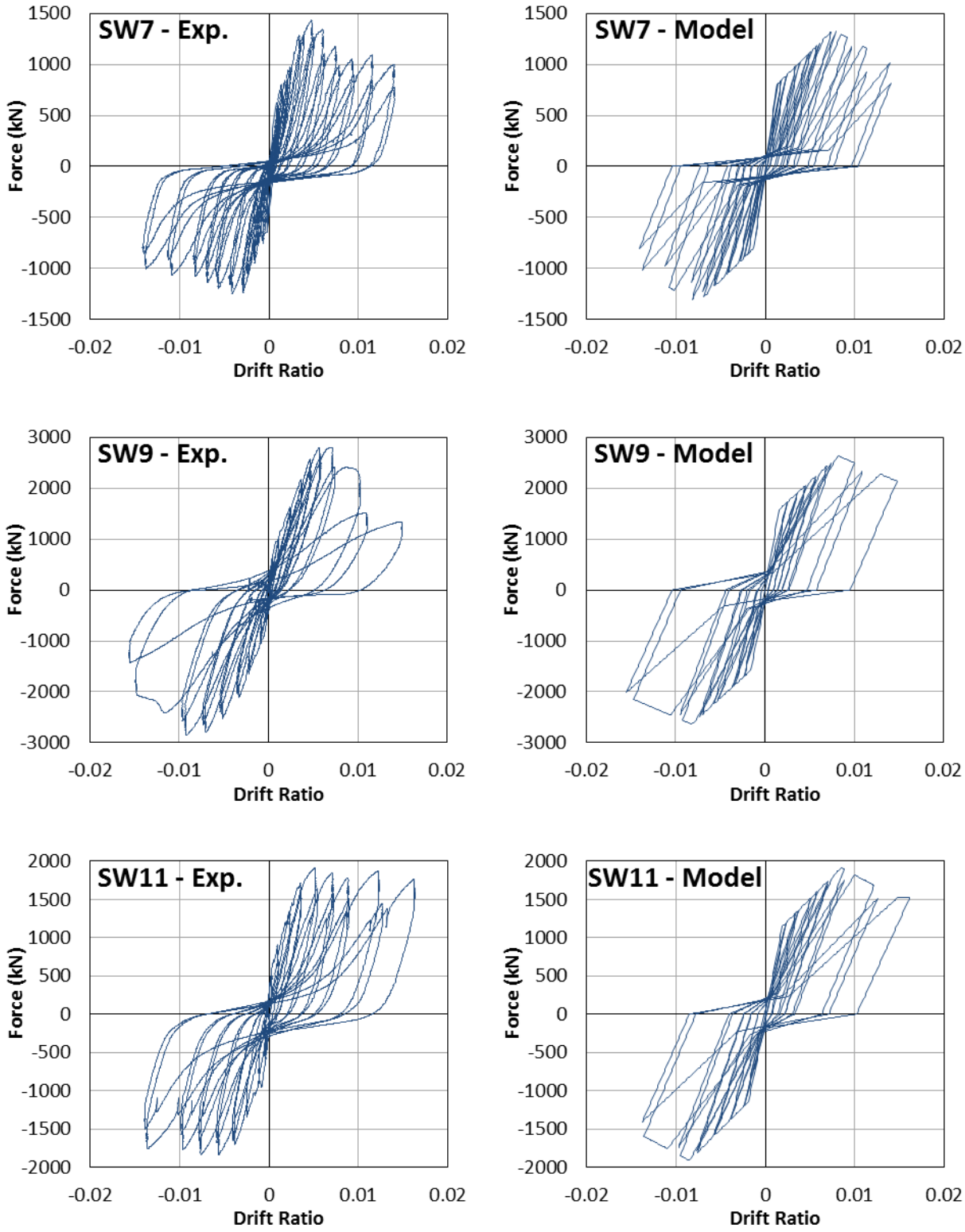

Figure 7-16. Experimental and Macro-Hysteretic model results of the cyclic load- displacement behavior for walls SW7, SW9 and SW11 using calculated backbone and base hysteretic parameters.

The Macro-Hysteretic model starts to show significant strength degradation after the peak point is reached. Prior to the peak point the model does not show noticeable strength degradation. The strength degradation on the model increases with further cycling past the peak point, which is also observed on the experimental response. However, due to the differences between the displacement at peak strength of the estimated backbone and the actual (experimental) displacement at peak strength, the model may start to degrade in strength at a different stage than in the test. It is observed that the estimated displacement at peak strength is larger than the corresponding experimental value for all the three walls studied in this section. Notwithstanding, walls SW7, SW11 and SW9 undertook six, four, and three full cycles past the peak control point, respectively. That explains the observed differences in cyclic strength degradation where wall SW7 showed the highest degradation while wall SW9 showed the lowest degradation.

In terms of the unloading stiffness degradation, the selected value of *beta* = 0.4 produced a reasonable but slightly underestimated prediction in the modeled response. It appears that a lower value (e.g. *beta* = 0.3) would produce a better estimate of the unloading stiffness of the three specimens modeled in this section. Notwithstanding, considering the values found on section 7.3.1 (Table 7-6) it seems that a value of *beta* between 0.3 and 0.4 could be a reasonable assumption for the studied walls and walls with similar characteristics.

In order to improve this Macro-Hysteretic model for modeling of squat RC walls, further calibration of the hysteretic damage parameters against experimental data is needed. In this manner, the user could select adequate hysteretic degradation parameters for the analysis, based on the main features of the wall. A first step would be to identify wall features (e.g. aspect ratio, reinforcement ratios, wall boundary element to wall web sectional area, axial load ratio, concrete strength, etc.) that could be correlated to pinching, cyclic strength degradation and stiffness degradation. Then characteristic parameters may be obtained by calibration against experimental data. Such calibration should be performed with a larger database including walls with enlarged boundary elements. The availability of further digital cyclic test data is key for the calibration of the hysteretic model parameters.

CHAPTER 8. SUMMARY AND CONCLUSIONS

8.1 Summary

An experimental database was assembled for this study by collecting data from published literature and compiled into a database. Database is described in Chapter 2 and tabulated data is presented on Appendix A. The database was divided in two groups (i.e. walls with rectangular cross sections and with enlarged boundary elements) due to significant differences in characteristics, strength and behavior found between the two types of walls. Therefore, both groups of walls were treated individually throughout the research work in order to produce more accurate results.

For both groups of walls, new equations for the prediction of peak shear strength were developed based on multiple linear regressions of the compiled experimental data. The expressions include the parameters that were found more meaningful in the prediction of peak shear strength. The predictive performance of the new proposed equations was compared with some of the widely used equations found in the literature and US codes and standards by means of statistical analysis. It was found that the evaluated existing equations, except that proposed by Wood (1990), tend to over-estimate the peak shear strength of squat RC walls with rectangular cross section considered in the assembled database. All the evaluated existing equations tend to considerably under-estimate the peak shear strength of the squat RC walls with enlarged boundary elements considered in the assembled database. Better correlation with the experimental data and reduced variability of the predicted-to-measured strength ratio was found with the new equations proposed in this study for each group of walls.

In a similar fashion as for the peak shear strength of squat RC walls, new predictive equations to estimate the displacement (drift ratio) capacity of squat RC walls were developed for both groups of walls by means of multiple linear regressions with the compiled experimental data. The equations for the prediction of displacement capacity proposed in this study were compared with other equations found in the literature and produced a better correlation with the experimental data in the collected database. Predictive expressions were developed for the displacement

capacity in terms of drift ratio at diagonal cracking (at development of 0.6 V_{peak}), peak strength, and at ultimate damage state (at 20% strength degradation); for each group of walls.

Finally, two analytical modeling approaches for the analysis of squat RC walls were evaluated. The first is a Fiber-Based Model with flexure-shear interaction, and the second is a Macro-Hysteretic Model. A backbone curve, calculated with the equations developed in this study for the prediction of strength and displacement capacity, was proposed. The backbone curve was used with the hysteretic model to assess its feasibility to model the non-linear cyclic response of squat RC walls.

8.2 Conclusions

Chapter 3 evaluated the peak shear strength of squat RC walls with rectangular cross sections using the experimental data from an assembled database including 70 walls tests found in the literature. Chapter 5 evaluated the peak shear strength of squat RC walls with enlarged boundary elements (i.e. flanged and barbell cross sections) using the experimental data from an assembled database including 137 walls tests found in the literature. The assembled experimental database considered only quasi-static cyclic, dynamic and hybrid-simulated dynamic loading squat walls tested in a cantilever setup with no restrain at top. Several equations to predict peak shear strength that are available in the literature (i.e. Wood, 1990 and Barda et al. 1977) and on several design standards (i.e. ASCE 43-05 and ACI 349-13 / ACI 318-14) were evaluated. From this evaluation, significant scatter was found in the peak shear strength predictions among existing equations. It was also found that the peak shear strength equations in ASCE 43-05 standard and in seismic provisions of ACI 318-14 / ACI 349-13 codes tend to over-estimate the strength of squat RC walls with rectangular cross section. The best estimates for squat RC walls of rectangular cross section, using the existing equations, were obtained using the expressions proposed by Wood (1990). For the case of squat RC walls with enlarged boundary elements, all the existing equations tend to under-estimate peak strength. The provisions of ASCE 43-05 yield the best estimates among existing equations. New equations to predict peak shear strength of squat walls with rectangular cross sections and with flanged/barbell cross sections were proposed in Chapters 3 and 5, respectively. Equations were developed using multivariable linear regression analyses, considering the parameters that were found to produce a better correlation

with the database. The new equations produced results of predicted-to-measured strength ratios with less variability (e.g. lower coefficient of variation) and average values nearer to 1.0, when compared with the other equations evaluated in this study. An improved correlation of the predicted peak shear strength to the measured peak shear strength was obtained with the proposed equations. Therefore, equations 3-13 and 5-1 are recommended for the prediction of squat RC shear walls having rectangular cross sections and enlarged boundary elements, respectively.

In addition, it was found that the upper shear strength limit established on ACI 318-14 ($0.83A_{cv}\sqrt{f_c'}$), intended to avoid non-ductile diagonal compression failure in walls with high web reinforcement ratios, is a reasonable value for squat shear walls with rectangular cross sections. However, this limit tends to be too conservative for squat RC walls with enlarged boundary elements, which can generally achieve higher strength. On the other hand, the upper strength limit established in ASCE 43-05 ($1.67A_{cv}\sqrt{f_c'}$) was found to be a more reasonable limit for squat RC walls with flanged and barbell cross sections. This limit becomes more important as the aspect ratio of the wall decreases. Therefore, the upper strength limits established in ACI 318-14 and ASCE 43-05 are recommended for squat RC shear walls having rectangular cross sections and enlarged boundary elements, respectively.

Chapter 4 evaluated the drift capacity of squat RC walls with rectangular cross sections while Chapter 6 evaluated the drift capacity of squat walls with enlarged boundary elements, using the data from the assembled database. Several equations to predict drift capacities at cracking strength, peak shear strength, and ultimate drift that are available in the literature (i.e. Hidalgo et al., 2000; Carrillo, 2010; Sánchez, 2013; and Gérin and Adebar, 2004) and the model proposed on ASCE 41-13 were evaluated. From this evaluation, it was found significant scatter in the drift ratio capacities predictions among the equations. New equations to predict the drift capacity at diagonal cracking state, peak shear strength, and at ultimate state (20% strength drop) were proposed, based on multivariable linear regression analyses. Parameters that were found to produce a better correlation with the database were considered. The evaluation of equations for displacement capacity was carried in the same fashion as it was done for peak shear strength. The new equations produced results for ratio of predicted-to-measured drift capacity with lower coefficient of variation and central tendency values nearer to 1.0 when compared with the other

equations evaluated in this study. The proposed equations for displacement capacity of squat RC walls with rectangular cross sections and with enlarged boundary elements are presented on Chapters 4 and 6, respectively.

The developed equations for the prediction of displacement capacity showed higher coefficients of variation (COV) than the strength prediction equations. Obtaining a low COV for the prediction of displacement capacity of RC squat shear walls is difficult due to the stochastic nature of the several factors contributing to the lateral displacement and different failure modes involved. Also, the systematic error induced by the difference in testing and measuring conditions between each of the experimental programs or research groups appears to be a significant source of variability.

The ASCE 41-13 load displacement backbone model suggests fixed values for the estimation of the drift ratio capacity at each of the aforementioned damage states depending on whether the wall has significant axial loading or not. These suggested values appeared to be reasonable in terms of scatter as they yield comparatively low coefficients of variation in the predicted-to-measured ratio, but the prediction seems to be conservative since it underestimated the drift capacity at peak strength and at ultimate state for most tests.

On the other hand, it was found that the allowable drift limits for damage control of shear wall structural systems suggested on ASCE 7-10 design code tend to be unconservative for low-rise RC shear walls. ASCE 7-10 drift limits are mainly focused on high rise buildings comprised of slender walls which generally have higher ductility. Thus, the use of ASCE 7-10 drift limits are not recommended for use with squat RC wall structural systems. A much lower value should be recommended, but further research on this topic is still necessary to establish a reasonable drift limit.

A Fiber-Based Model and a Macro-Hysteretic Model were evaluated on Chapter 7. The Fiber-Based Model with flexure-shear interaction model (OpenSees *Flexure-Shear Interaction Displacement-Based Beam-Column Element*) as presented herein, is not capable of calculating the hysteretic response, but was able to reasonably calculate the load-displacement envelope for the studied wall specimens. While the shear flexure interaction model may predict the monotonic response of the studied specimens, it still needs to be calibrated and validated against

considerable amount of experimental squat RC walls data in order to consider it more reliable. The modeled post-peak response using flexure-shear interaction model was found to be sensitive to the vertical discretization of the wall (number of stacked elements). The modeled initial stiffness using the flexure-shear interaction model was found to be sensitive to the tension stiffening parameter (*b*) of the concrete constitutive model.

On the other hand, the hysteretic model (OpenSees *Hysteretic Material* model) is capable of calculating the cyclic response of squat shear walls with good accuracy if the backbone and hysteretic parameters are well calibrated. The model is simple in terms of computational effort and output assessment. However, this model needs the definition of a backbone curve in order to perform an analysis. A tri-linear backbone is proposed to be used in conjunction with the hysteretic model for the analysis of squat RC walls. For the proposed backbone, the control points associated to diagonal cracking, peak strength, and ultimate state are calculated using the shear strength and displacement capacity predictive equations developed in this study. Diagonal cracking was assumed to occur at the development of 60% of the peak strength, while ultimate damage state was defined as the point where the strength drops by 20% after attaining peak strength. The calculated backbones showed generally good agreement with experimental cyclic load-drift ratio envelopes. Values for the hysteretic parameters were obtained by calibration with experimental data. The results of the modeled cyclic response using the calculated backbone in combination with the presented Macro-Hysteretic model showed reasonably good agreement with experimental data for the studied tests. The hysteretic parameters related to cyclic damage can be further calibrated against experimental data to obtain characteristic values for walls with other features such as barbell/flanged cross section, significant axial loads, among others.

8.3 Future Work

In order to improve the capability of the Macro-Hysteretic model presented on Chapter 7 for modeling of squat RC walls, additional calibration of the hysteretic damage parameters against experimental data is needed. Further work can be done in the calibration of the hysteretic model using more experimental data as to better characterize the loading and unloading parameters (i.e. strength degradation, loading stiffness degradation, unloading stiffness degradation, pinching characteristics, etc.). In this manner, the user could select adequate hysteretic degradation

parameters for the analysis, based on the main features of the wall. A first step might be to identify wall features (e.g. aspect ratio, reinforcement ratios, wall boundary element to wall web sectional area, axial load ratio, concrete strength, etc.) that could be correlated to pinching, cyclic strength degradation and stiffness degradation. Then characteristic parameters may be obtained by calibration against experimental data. Such calibration should be performed with a larger database including walls with enlarged boundary elements. However, this task seems to be limited by the availability of digital data for sufficient number of tests.

Further calibration is needed to validate the ability of the flexure shear interaction model to represent the behavior of squat RC walls with other features such as: axial load, different reinforcement ratios and enlarged boundary elements, etc. Additional sensitivity analysis of the tension stiffening curve exponent (*b* parameter) and model discretization should be performed to put forward recommendations.

The assessment of other analytical modeling approaches for squat RC walls such as: OpenSees *Cyclic Shear-Flexure Interaction Model for RC Walls* (SFI MVLEM) developed by Kolozvari et al. (2015), the cyclic softened membrane model (CSMM) proposed by Hsu and Mo (2010), and other finite element models would be valuable for the identification of adequate modeling methods.

Additional research aiming to establish appropriate drift limits for common design performance levels (i.e. immediate occupancy, life protection and collapse prevention) for squat RC wall systems under seismic loading needs to be conducted. Also, further research on the behavior of squat RC walls at more advanced damage states is necessary. The availability of load - displacement test data of squat RC walls subjected to advanced strength degradation stages is limited at the present time. More experimental data on the hysteretic behavior of squat walls at very advanced damage states (i.e. residual strength region) needs to become available to the research community, in order to expand the general knowledge on this topic.

REFERENCES

ACI Committee 318, 1971, "Building Code Requirements for Structural Concrete and Commentary (ACI 318-71)," American Concrete Institute, Detroit, MI.

ACI Committee 318, 1983, "Building Code Requirements for Structural Concrete and Commentary (ACI 318-83)," American Concrete Institute, Detroit, MI.

ACI Committee 349, 2006, "Code Requirements for Nuclear Safety Related Concrete Structures (ACI 349-06) and Commentary (ACI 349R-06)," American Concrete Institute, Farmington Hills, MI.

ACI Committee 318, 2008, "Building Code Requirements for Structural Concrete and Commentary (ACI 318-08)," American Concrete Institute, Farmington Hills, MI.

ACI Committee 349, 2014, "Code Requirements for Nuclear Safety Related Concrete Structures (ACI 349-13) and Commentary (ACI 349R-13)," American Concrete Institute, Farmington Hills, MI.

ACI Committee 318, 2014, "Building Code Requirements for Structural Concrete and Commentary (ACI 318-14)," American Concrete Institute, Farmington Hills, MI.

Adorno, C., and Vidot, A., 2015, "Shear Strength of Squat Reinforced Concrete Walls Under Cyclic Loading" *Proceedings*, Eleventh Canadian Conference on Earthquake Engineering, Victoria, BC, Canada.

Akita, T., Kuramoto, H., Matsui, T., and Kabeyasawa, T., 2006, "Hysteresis Modeling of RC Shear Walls Based on Static Loading Test" *Proceedings*, Eighth U.S. National Conference on Earthquake Engineering, No. 1291, San Francisco, CA.

Alexander, C. M., Heidebrecht, A. C., and Tso, W. K., 1973, "Cyclic Load Tests on Shear Wall Panels," *Proceedings*, Fifth World Conference on Earthquake Engineering, Rome, Italy, pp. 1116-1119.

Altin, S., Anil, Ö., Kopraman, Y., and Kara, M. E., 2012, "Hysteretic Behavior of RC Shear Walls Strengthened with CFRP Strips," *Composites Part B: Engineering*, Elsevier, Vol. 44, No. 1, pp. 321-329.

American Society of Civil Engineers, 2005, "Seismic Design Criteria for Structures, Systems, and Components in Nuclear Facilities (ASCE/SEI 43-05)," ASCE, Reston, VA.

American Society of Civil Engineers, 2007, "Seismic Rehabilitation of Existing Buildings (ASCE/SEI 41-06)," ASCE, Reston, VA.

American Society of Civil Engineers, 2007, “Supplement to *Seismic Rehabilitation of Existing Buildings (ASCE/SEI 41-06)*”, pp. S1-S498.

American Society of Civil Engineers, 2010, “Minimum Design Loads for Buildings and Other Structures (ASCE/SEI 7-10)”, ASCE, Reston, VA.

American Society of Civil Engineers, 2014, "Seismic Rehabilitation and Retrofit of Existing Buildings (ASCE/SEI 41-13)," ASCE, Reston, VA.

ATC, 1998, "Evaluation of Earthquake Damaged Concrete and Masonry Buildings - Basic Procedures Manual (FEMA 306)," Federal Emergency Management Agency, Washington, DC.

Barda, F., 1972, “Shear Strength of Low-Rise Walls with Boundary Elements,” PhD Dissertation, Lehigh University, Bethlehem, PA.

Barda, F., Hanson, J. M., and Corley, W. G., 1977, "Shear Strength of Low-Rise Walls with Boundary Elements," *Reinforced Concrete Structures in Seismic Zones*, SP 53-8, American Concrete Institute, Farmington Hills, MI, pp. 149-202.

Belarbi, A., and Hsu, T. T. C., 1994, “Constitutive Laws of Concrete in Tension and Reinforcing Bars Stiffened by Concrete,” *ACI Structural Journal*, Vol. 91, No. 4, Jul.-Aug., pp. 465–474.

Belarbi, A., and Hsu, T. T. C., 1995, “Constitutive Laws of Softened Concrete in Biaxial Tension Compression,” *ACI Structural Journal*, Vol. 92, No. 5, Sept.-Oct., pp. 562–573.

Cardenas, A. E., Hanson, J. M., Corley, W. G., and Hognestad, E., 1973, "Design Provisions for Shear Walls," *ACI Journal*, Vol. 70-23, March, pp. 221-230.

Cardenas, A. E., Russell, H. G., and Corley, W. G., 1980, "Strength of Low Rise Structural Walls," *Reinforced Concrete Structures Subjected to Wind and Earthquake Forces*, SP 63-10, American Concrete Institute, Farmington Hills, MI, pp. 221-241.

Carrillo, J., 2010, “Evaluación del Comportamiento a Cortante de Muros de Concreto para Vivienda por Medio de Ensayos Dinámicos,” PhD Dissertation, Instituto de Ingeniería, Universidad Nacional Autónoma de México, Mexico City, Mexico, 474 pp. (in Spanish)

Carrillo, J., and Alcocer, S., 2012, “Backbone Model for Performance-Based Seismic Design of RC Walls for Low-Rise Housing,” *Earthquake Spectra*, Vol. 28, No. 3, August, pp. 943-964.

Carrillo, J., and Alcocer, S. M., 2013, “Shear Strength of Reinforced Concrete Walls for Seismic Design of Low-Rise Housing,” *ACI Structural Journal*, Vol. 110, No. 3, May-June, pp. 415-426.

Chiba, O., Fukuzawa, R., Hatori, T., and Yagishita, K., 1985, “Experimental Study on Heavily Reinforced Concrete Shear Walls,” *Transactions*, Eighth International Conference on Structural Mechanics in Reactor Technology, H4/1, Brussels, Belgium.

Dabbagh, H., 2005, "Strength and Ductility of High-Strength Concrete Shear Walls Under Reversed Cyclic Loading," PhD Dissertation, School of Civil and Environmental Engineering, The University of New South Wales, Sydney, Australia.

Duffey, T. A., Farrar, C. R., and Goldman, A., 1994a, "Shear Wall Ultimate Drift Limits," *Report* No. NUREG/CR-6104, Los Alamos National Laboratory, Los Alamos, NM.

Duffey, T. A., Farrar, C. R., and Goldman, A., 1994b, "Low-Rise Shear Wall Ultimate Drift Limits," *Earthquake Spectra*, Vol. 10, No. 4, Nov., pp. 655-674.

Elmorsi, M., Kianush, M. R., and Tso, W. K.., 1998, "Nonlinear Analysis of Cyclically Loaded Reinforced Concrete Structures," *ACI Structural Journal*, Vol. 95, No. 6, Nov.-Dec., pp. 725–739.

Elwood, K., Matamoros, A., Wallace, J., Lehman, D., Heintz, J., Mitchell, A., Moore, M., Valley, M., Lowes, L., Comartin, C., and Moehle, J., 2007, "Update to ASCE/SEI 41 concrete provisions," *Earthquake Spectra*, Vol. 23, No. 3, pp. 493–523.

Endo, T. Adachi H., and Nakanishi, M., 1980, "Force-Deformation Hysteresis Curves of Reinforced Concrete Shear Walls," *Proceedings*, Seventh World Conference on Earthquake Engineering, Istanbul, Turkey, Vol. 6, pp. 315-322.

Filippou, F., Mazzoni, S., *Steel02 Material - Giuffré-Menegotto-Pinto Model with Isotropic Strain Hardening*, OpenSees, September 20, 2012. http://opensees.berkeley.edu/wiki/index.php/Steel02_Material_--_Giuffr%C3%A9-Menegotto-Pinto_Model_with_Isotropic_Strain_Hardening (accessed November 16, 2013).

Filippou, F. C., Popov, E. P., Bertero, V. V., 1983, "Effects of Bond Deterioration on Hysteretic Behavior of Reinforced Concrete Joints". *Report* No. EERC 83-19, Earthquake Engineering Research Center, University of California, Berkeley, CA.

Fukuzawa, R., Chiba, O., Hatori, T., Yagishita, K., and Watabe, M., 1988, "Study on Load-Deflection Characteristics of Heavily Reinforced Concrete Shear Walls," *Proceedings*, Ninth World Conference on Earthquake Engineering, Tokyo-Kyoto, Japan, pp. 4/517-4/522.

Gérin, M., and Adebar, P., 2004, "Accounting for Shear in Seismic Analysis of Concrete Structures," *Proceedings*, Thirteenth World Conference on Earthquake Engineering, No. 1747, Vancouver, BC, Canada.

Greifenhagen, C., Lestuzzi, P., 2005, "Static Cyclic Tests on Lightly Reinforced Concrete Shear Walls," *Engineering Structures*, Vol. 27, pp. 1703-1712.

Gulec, C. K., and Whittaker, A. S., 2009, "Performance-Based Assessment and Design of Squat Reinforced Concrete Shear Walls," *Report* No. MCEER-09-0010, Multidisciplinary Center for Earthquake Engineering Research, Buffalo, NY.

Gutiérrez, S. A., 2012, "Estudio del Comportamiento de Muros Cortos de Hormigón Armado con Carga Axial por un Modelo de Interacción de Corte-flexión", Thesis, Departamento de Ingeniería Civil, Universidad de Chile, Santiago, Chile, 110 pp. (in Spanish)

Hassan, M., and El-Tawil, S., 2003, "Tension Flange Effective Width in Reinforced Concrete Shear Walls," *ACI Structural Journal*, Vol. 100, No. 3, May-Jun., pp. 349-356.

Hernández, O. B., 1980, "Diseño de Muros de Concreto con Falla por Cortante," PhD Dissertation, Instituto de Ingeniería, Universidad Nacional Autónoma de México, Mexico City, Mexico, 165 pp. (in Spanish)

Hidalgo, P. A., and Jordán, R. M., 1996, "Strength and Energy Dissipation Characteristics of Reinforced Concrete Walls Under Shear Failure" *Proceedings*, Eleventh World Conference on Earthquake Engineering, No. 816, Acapulco, Mexico.

Hidalgo, P. A., Jordán, R. M., and Martínez, R. P., 2000, "Development and Use of an Analytical Model to Predict the Inelastic Seismic Behavior of Shear Wall, Reinforced Concrete Buildings" *Proceedings,* Twelfth World Conference on Earthquake Engineering, No. 472, Auckland, New Zealand.

Hirosawa, M., 1975, "Past Experimental Results on Reinforced Concrete Shear Walls and Analysis on Them," *Kenchiku Kenkyu Shiryo*, No. 6, Building Research Institute, Ministry of Construction, Tokyo, Japan, 277 pp. (in Japanese)

Hsu, T.T.C., Mo, Y.L., 2010, *Unified Theory of Concrete Structures, 2nd Ed*., John Wiley and Sons.

Huang, C. C., and Sheu, M. S., 1988, "Experimental and Theoretical Study on Aseismic Behaviors of Low-Rise RC Shear Walls," *Proceedings*, Ninth World Conference on Earthquake Engineering, Tokyo-Kyoto, Japan, pp. 6/35-6/40.

International Council of Building Officials (ICBO), 1997, "Uniform Building Code", Vol. 2, Whittier, CA.

Kabeyasawa, T., and Hiraishi, T., 1998, "Tests and Analyses of High-Strength Reinforced Concrete Shear Walls in Japan," *High-Strength Concrete in Seismic Regions*, SP 176-13, American Concrete Institute, Farmington Hills, MI, pp. 281-310.

Kazaz, İ., Gülkan, P., and Yakut, A., 2012, "Deformation Limits for Structural Walls with Confined Boundaries," *Earthquake Spectra*, Vol. 28, No. 3, August, pp. 1019-1046.

Kolozvari K., Orakcal K., and Wallace J. W., 2015, "Shear-Flexure Interaction Modeling of reinforced Concrete Structural Walls and Columns under Reversed Cyclic Loading", *Report* No. PEER 2015/12, Pacific Earthquake Engineering Research Center, University of California, Berkeley, CA, 116 pp.

Kuang, J. S., and Ho, Y. B., 2008, "Seismic Behavior and Ductility of Squat Reinforced Concrete Shear Walls with Nonseismic Detailing," *ACI Structural Journal,* Vol. 105, No. 2, Mar.-Apr., pp. 225–231.

Li, Y., Manoly, K., 2012, "GI 199 and 2011 Mineral VA Earthquake Impact to North Anna Nuclear Power Plant," Fifteenth World Conference on Earthquake Engineering, Lisbon, Portugal.

Lowes, L., and Berry M., *Concrete04 Material – Popovics Concrete Material*, OpenSees, October 23, 2009.
http://opensees.berkeley.edu/wiki/index.php/Concrete04_Material_--_Popovics_ Concrete_ Material

Luna, B. N., Rivera, J. P., and Whittaker, A. S., 2015, "Seismic Behavior of Low-Aspect-Ratio Reinforced Concrete Shear Walls," *ACI Structural Journal*, Vol. 112, No. 5, Sep.-Oct., pp. 593–604.

Maier, J., 1991, "Shear Wall Tests," *Preliminary Proceedings Volume,* International Workshop on Concrete Shear in Earthquake, Department of Civil and Environmental Engineering, University of Houston, Houston, TX.

Mander, J. B.; Priestley, M. J. N.; and Park, R., 1988, "Theoretical Stress-Strain Model for Confined Concrete," *Journal of Structural Engineering,* Vol. 114, No. 8, pp. 1804-1826.

Massone, L. M., Orakcal, K., and Wallace, J. W., 2004, "Flexural and Shear Responses In Slender RC Shear Walls," *Proceedings,* Thirteenth World Conference on Earthquake Engineering, No. 1067, Vancouver, BC, Canada.

Massone, L. M., 2006, "RC Wall Shear-Flexure Interaction: Analytical and Experimental Responses," PhD Dissertation, Department of Civil and Environmental Engineering, University of California, Los Angeles, CA.

Massone, L. M.; Orakcal, K.; and Wallace, J. W. , 2006; "Shear - Flexure Interaction for Structural Walls"; SP-236, ACI Special Publication – Deformation Capacity and Shear Strength of Reinforced Concrete Members Under Cyclic Loading, editors: Adolfo Matamoros & Kenneth Elwood, p. 127-150.

Massone, L. M., 2010a, "Strength Prediction of Squat Structural Walls Via Calibration of a Shear-Flexure Interaction Model," *Engineering Structures*, Vol. 32, pp. 922-932.

Massone, L., *Concrete06 Material,* OpenSees, March 24, 2010b.
http://opensees.berkeley.edu/wiki/index.php/Concrete06_Material (accessed November 16, 2013.

Massone L, Orakcal K, Wallace J., *Flexure-Shear Interaction Displacement-Based Beam-Column Element*, OpenSees, December 12, 2012. http://opensees.berkeley.edu/wiki/index.php/Flexure-Shear_Interaction_Displacement-Based_Beam-Column_Element (accessed November 16, 2013).

Matsui, T., Kabeyasawa, T., Koto, A., Kuramoto, H., and Nagashima, I., 2004, "Shaking Table Test and Analysis of Reinforced Concrete Walls," *Proceedings*, Thirteenth World Conference on Earthquake Engineering, No. 419, Vancouver, BC, Canada.

Moehle, J. P., Ghodsi, T., Hooper, J. D., Fields, D. C., and Gedhada, R., 2011. "Seismic Design of Cast-in-Place Concrete Special Structural Walls and Coupling Beams: A Guide for Practicing Engineers," *NEHRP Seismic Design Technical Brief No. 6, Report* No. NIST GCR 11-917-11REV-1, National Institute of Standards and Technology, Gaithersburg, MD.

Mohle, J. and Kunnath, S., *Reinforcing Steel Material*, OpenSees, June 16, 2010. http://opensees.berkeley.edu/wiki/index.php/Reinforcing_Steel_Material (Accessed 16 November 2013).

Mohammadi-Doostdar, H., 1994, "Behavior and Design of Earthquake Resistant Low-Rise Shear Walls," PhD Thesis, Department of Civil Engineering, University of Ottawa, Ottawa, ON, Canada, 234 pp.

OECD/NEA/CSNI, 1996, "Seismic Shear Wall ISP NUPEC's Seismic Ultimate Dynamic Response Test, Comparison Report," *Report* No. OCDE/GD(96)188, Committee on the Safety of Nuclear Installations OECD Nuclear Energy Agency, Issy-Les-Moulineaux, France, 412 pp.

Opazo, G. A., 2012, "Análisis y Modelación de Ensayos de Muros Cortos de Hormigón Armado", Thesis, Departamento de Ingeniería Civil, Universidad de Chile, Santiago, Chile, 105 pp. (in Spanish)

OpenSees. Open System for Earthquake Engineering Simulation. Pacific Earthquake Engineering Research Center, University of California. Berkeley, California.

Orakcal, K., Massone, L. M., and Wallace, J. W., 2006, "Analytical Modeling of Reinforced Concrete Walls for Predicting Flexural and Coupled-Shear-Flexural Responses," *Report* No. PEER 2006/07, Pacific Earthquake Engineering Research Center, University of California, Los Angeles, CA.

Orbovic, N., 2007, "The Comparison of Design Code Provisions for the Seismic Capacity of Reinforced Concrete Squat Shear Walls in Nuclear Facilities," *Proceedings*, 7ème Colloque National AFPS, A048, Ecole Centrale, Paris.

Palermo, D., and Vecchio, F. J., 2002, "Behavior of Three-Dimensional Reinforced Concrete Shear Walls," *ACI Structural Journal*, Vol. 99, No. 1, Jan.-Feb., pp. 81-89.

Pang, X. D., and Hsu, T. T. C., 1995, "Behavior of Reinforced Concrete Membrane Elements in Shear," *ACI Structural Journal*, Vol. 92, No. 6, Nov.-Dec., pp. 665–679.

Park, R., 1989, "Evaluation of Ductility of Structures and Structural Assemblages from Laboratory Testing," *Bulletin of the New Zealand National Society for Earthquake Engineering*, Vol. 22, No. 3, pp. 155-166.

Park, H. G., Baek, J. W., Lee, J. H., and Shin, H. M., 2015, "Cyclic Loading Tests for Shear Strength of Low-Rise Reinforced Concrete Walls with Grade 550 MPa Bars," *ACI Structural Journal*, Vol. 112, No. 3, May-June, pp. 299-310.

Paulay, T., Priestley, M. J. N., and Synge, A. J., 1982, "Ductility in Earthquake Resisting Squat Shearwalls," *ACI Journal*, Vol. 79, No. 4, Jul.-Aug., pp. 257-269.

Paulay, T., and Priestley, M. J. N., 1992, *Seismic Design of Reinforced Concrete and Masonry Buildings*, John Wiley & Sons.

Pilette, F. C., 1987, "Behavior of Earthquake Resistant Squat Shear Walls," MS Thesis, Department of Civil Engineering, University of Ottawa, Ottawa, ON, Canada, 177 pp.

Rocks J. F., 2012, "Large Scale Testing of Low Aspect Ratio Reinforced Concrete Walls," MS Thesis, Department of Civil, Structural and Environmental Engineering, University at Buffalo, Buffalo, NY, 164 pp.

Rothe, D., 1992, "Untersuchungen zum Nichtlinearen Verhalten von Stahlbeton Wandschieben unter Erdbebenbeanspruchung," PhD Dissertation, Fachbereich Konstruktiver Ingenieurbau, der Technischen Hochschule Darmstadt, Darmstadt, Germany, 161 pp. (in German)

Saito, H., Kikuchi, R., Kanechika, M., and Okamoto, K., 1989, "Experimental Study of the Effect of Concrete Strength on Shear Wall Behavior," *Transactions*, Tenth International Conference on Structural Mechanics in Reactor Technology, H08/292, Anaheim, CA.

Salonikios, T. N., Kappos, A. J., Tegos, I. A., and Penelis, G. G., 1999, "Cyclic Load Behavior of Low-Slenderness Reinforced Concrete Walls: Design Basis and Test Results," *ACI Structural Journal*, Vol. 96, No. 4, Jul.-Aug., pp. 649-660.

Salonikios, T. N., Kappos, A. J., Tegos, I. A., and Penelis, G. G., 2000, "Cyclic Load Behavior of Low-Slenderness Reinforced Concrete Walls: Failure Modes, Strength and Deformation Analysis, and Design Implications," *ACI Structural Journal*, Vol. 97, No. 1, Jan.-Feb., pp. 132-142.

Sanada, Y., and Kabeyasawa, T., 2006, "Local Force Characteristics of Reinforced Concrete Shear Wall" *Proceedings*, Eighth U.S. National Conference on Earthquake Engineering, No. 324, San Francisco, CA.

Sánchez, A., 2013, "Comportamiento Sísmico de Muros de Concreto para Vivienda," PhD Dissertation, Instituto de Ingeniería, Universidad Nacional Autónoma de México, Mexico City, Mexico, 436 pp. (in Spanish)

Sato S., Ogata Y., Yoshizaki S., Kanata K., Yamaguchi T., Nakayama T., Inada Y., and Kadoriku J., 1989, "Behavior of Shear Wall Using Various Yield Strength of Rebar Part 1: An Experimental Study," *Transactions*, Tenth International Conference on Structural Mechanics in Reactor Technology, H09/293, Anaheim, CA.

Scott, M., Filippou, F., *Hysteretic Material*, OpenSees, September 30, 2013. http://opensees.berkeley.edu/wiki/index.php/Hysteretic_Material (Accessed 16 November 2013).

SEAOC, 1999, *Recommended Lateral Force Requirements and Commentary, 7th Ed*., Structural Engineers Association of California, Sacramento, CA.

Seki, M., Kobayashi, J., Shibata, A., Kubo, T., Taira, T., and Akino, K., 1995, "Restoring Force Verification Test on RC Shear Wall," *Transactions*, Thirteenth International Conference on Structural Mechanics in Reactor Technology, H06/1, Porto Alegre, Brazil.

Synge, A. J., 1980, "Ductility of Squat Shear Walls," *Report* No. 80-8, Department of Civil Engineering, University of Canterbury, Christchurch, New Zealand, 142 pp.

Takada, T., 2012, "On Seismic Design Qualification of NPPs After Fukushima Event in Japan," Fifteenth World Conference on Earthquake Engineering, Lisbon, Portugal.

Wallace, J. W., 2007, "Modeling Issues for Tall Reinforced Concrete Core Wall Buildings". *Journal of Structural Design of Tall and Special Buildings*, Vol. 16, No. 5, pp. 615–632.

Wasiewicz, Z. F., 1988, "Sliding Shear in Low-Rise Walls under Lateral Load Reversals," MS Thesis, Department of Civil Engineering, University of Ottawa, Ottawa, ON, Canada, 127 pp.

Whittaker A., Lowes L., and Stojadinovic B., "Performance-Based Design of Squat Concrete Walls of Conventional and Composite Construction," *NEEShub Project Warehouse, Project 676.* Retrieved from: https://nees.org/warehouse/project/676.

Whyte C.A., Stojadinovic B., 2013, "Hybrid Simulation of Seismic Response of Squat Reinforced Concrete Shear Walls," *Report* No. PEER 2013/02, Pacific Earthquake Engineering Research Center, University of California, Los Angeles, CA, 196 pp.

Wiradinata, S., 1985, "Behavior of Squat Walls Subjected to Load Reversals," MS Thesis, Department of Civil Engineering, University of Toronto, Toronto, ON, Canada, 171 pp.

Wood, S. L., 1990, "Shear Strength of Low-Rise Reinforced Concrete Walls," *ACI Structural Journal*, Vol. 87, No. 1, Jan.-Feb., pp. 99-107.

XiangDong, G., 1999, "Framed Shear Walls under Cyclic Loading," PhD Dissertation, Department of Civil and Environmental Engineering, University of Houston, Houston, TX, 285 pp.

Xiang, W. Z., 2009, “Seismic Performance of RC Structural Squat Walls with Limited Transverse Reinforcement,” PhD Dissertation, School of Civil and Environmental Engineering, Nanyang Technological University, Singapore, 261 pp.

Xu, J., Nie, J., Braverman J., and Hofmayer, C., 2007, “Assessment of Analysis Methods for Seismic Shear Wall Capacity Using JNES/NUPEC Multi-Axial Cyclic and Shaking Table Test Data,” *Report* No. BNL-NUREG-77370-2006, Brookhaven National Laboratory, Upton, NY.

APPENDIX A SQUAT RC WALLS DATABASE

The following two sections will include tables with the compiled data for the considered experimental tests meeting the criteria discussed on Chapter 2. Appendix A.1 shows the data for the considered squat RC walls with rectangular cross sections while Appendix A.2 shows the data for the considered squat RC walls with enlarged boundary elements (i.e. flanges and barbells). The used notation is intended to be consistent with the rest of the discussion on previous chapters and definitions can be found on the glossary at the beginning of this document. The data on Appendix A.1 and Appendix A.2 is organized in four groups, namely, wall geometric properties, reinforcement configuration, materials properties, and loading and displacement data.

A.1 Squat RC Walls with Rectangular Cross Sections

Tables A-1 to A-4 show the compiled data for the considered squat RC wall tests with rectangular cross section mentioned on Chapter 2.

Table A-1. Geometric properties of squat RC walls with rectangular cross section.

Researcher	Wall ID	h_w (mm)	h_L (mm)	l_w (mm)	t_w (mm)	h_w/l_w	M/Vl_w	l_w/t_w	l_{be} (mm)
Carrillo/Alcocer	MCN50C	2400	2400	2400	100	1.00	1.00	24.00	200
Carrillo/Alcocer	MCN100C	2400	2400	2400	100	1.00	1.00	24.00	200
Carrillo/Alcocer	MCS50C	2400	2400	2400	100	1.00	1.00	24.00	200
Carrillo/Alcocer	MCS100C	2400	2400	2400	100	1.00	1.00	24.00	200
Carrillo/Alcocer	MRN100C	2400	2400	5400	100	0.44	0.44	54.00	200
Carrillo/Alcocer	MRN50C	2400	2400	5400	100	0.44	0.44	54.00	200
Carrillo/Alcocer	MCN50C-2	2400	2400	2400	100	1.00	1.00	24.00	200
Carrillo/Alcocer	MCS50C-2	2400	2400	2400	100	1.00	1.00	24.00	200
Carrillo/Alcocer	MCN100D	1920	2320	1920	80	1.00	1.21	24.00	160
Terzioglu	SW-T2-S1-1	750	950	1500	120	0.50	0.63	12.50	130
Terzioglu	SW-T1-S1-2	750	950	1500	120	0.50	0.63	12.50	130
Terzioglu	SW-T2-S2-3	750	950	1500	120	0.50	0.63	12.50	130
Terzioglu	SW-T2-S3-4	750	950	1500	120	0.50	0.63	12.50	130
Terzioglu	SW-T3-S1-5	750	950	1500	120	0.50	0.63	12.50	80
Terzioglu	SW-T4-S1-6	500	700	1500	120	0.33	0.47	12.50	130
Terzioglu	SW-T5-S1-7	1500	1700	1500	120	1.00	1.13	12.50	130

Researcher	Wall ID	h_w (mm)	h_L (mm)	l_w (mm)	t_w (mm)	h_w/l_w	M/Vl_w	l_w/t_w	l_{be} (mm)
Terzioglu	SW-T6-S1-8	1500	1700	1500	120	1.00	1.13	12.50	130
Terzioglu	SW-T1-S2-9	750	950	1500	120	0.50	0.63	12.50	130
Terzioglu	SW-T1-N5-S1-10	750	950	1500	120	0.50	0.63	12.50	130
Terzioglu	SW-T1-N10-S1-11	750	950	1500	120	0.50	0.63	12.50	130
NEES-UB	SW1	2865	2865	3048	203	0.94	0.94	15.01	N/A
NEES-UB	SW2	1646	1646	3048	203	0.54	0.54	15.01	N/A
NEES-UB	SW3	1646	1646	3048	203	0.54	0.54	15.01	N/A
NEES-UB	SW4	1646	1646	3048	203	0.54	0.54	15.01	N/A
NEES-UB	SW5	1006	1006	3048	203	0.33	0.33	15.01	N/A
NEES-UB	SW6	1006	1006	3048	203	0.33	0.33	15.01	N/A
NEES-UB	SW7	1006	1006	3048	203	0.33	0.33	15.01	N/A
NEES-UB	SW8	1646	1646	3048	203	0.54	0.54	15.01	N/A
NEES-UB	SW9	1646	1646	3048	203	0.54	0.54	15.01	N/A
NEES-UB	SW10	1646	1646	3048	203	0.54	0.54	15.01	N/A
NEES-UB	SW11	1646	1646	3048	203	0.54	0.54	15.01	380
NEES-UB	SW12	1646	1646	3048	203	0.54	0.54	15.01	380
Whyte	Wall 1	1646	1646	3048	203	0.54	0.54	15.01	N/A
Whyte	Wall 2	1646	1646	3048	203	0.54	0.54	15.01	N/A
Salonikios	MSW3	1800	1925	1200	100	1.50	1.60	12.00	240
Salonikios	MSW6	1800	1925	1200	100	1.50	1.60	12.00	240
Salonikios	LSW1	1200	1325	1200	100	1.00	1.10	12.00	240
Salonikios	LSW2	1200	1325	1200	100	1.00	1.10	12.00	240
Salonikios	LSW3	1200	1325	1200	100	1.00	1.10	12.00	240
Wiradinata	Wall 1	1000	1150	2000	100	0.50	0.58	20.00	320
Wiradinata	Wall 2	500	650	2000	100	0.25	0.33	20.00	320
Pilette	Wall4	1000	1160	2000	100	0.50	0.58	20.00	320
Pilette	Wall 5	1000	1160	2000	100	0.50	0.58	20.00	250
M. Doostdar	Wall 7	1500	1638	2000	100	0.75	0.82	20.00	320
M. Doostdar	Wall 8	1500	1638	1500	100	1.00	1.09	15.00	360
Synge	Wall 1	1500	1700	3000	100	0.50	0.57	30.00	200
Cardenas	SW-13	1905	2057	1905	76	1.00	1.08	25.00	N/A
Greifenhagen	M4	610	690	900	80	0.68	0.77	11.25	N/A
Park	S1	1500	1750	1500	200	1.00	1.17	7.50	300
Park	S2	1500	1750	1500	200	1.00	1.17	7.50	300
Park	S3	1500	1750	1500	200	1.00	1.17	7.50	300
Park	S5	1500	1750	1500	200	1.00	1.17	7.50	200
Park	S6	1500	1750	1500	200	1.00	1.17	7.50	200
Park	S7	1500	1750	1500	200	1.00	1.17	7.50	200
Hirosawa	72	1600	1700	1700	160	0.94	1.00	10.63	170

Researcher	Wall ID	h_w (mm)	h_L (mm)	l_w (mm)	t_w (mm)	h_w/l_w	M/Vl_w	l_w/t_w	l_{be} (mm)
Hirosawa	73	1600	1700	1700	160	0.94	1.00	10.63	170
Hirosawa	74	1600	1700	1700	160	0.94	1.00	10.63	170
Hirosawa	75	1600	1700	1700	160	0.94	1.00	10.63	170
Hirosawa	76	1600	1700	1700	160	0.94	1.00	10.63	170
Hirosawa	77	1600	1700	1700	160	0.94	1.00	10.63	170
Altin	1	1500	1650	1000	100	1.50	1.65	10.00	150
Alexander	1	1372	1372	2743	102	0.50	0.50	27.00	N/A
Rothe	T10	1100	1200	800	80	1.38	1.50	10.00	150
Hwang/Sheu	SWN-1D	500	650	1000	100	0.5	0.65	10	N/A
Hwang/Sheu	SWN-5D	750	900	1000	100	0.75	0.9	10	N/A
Sheu	SW-2	500	650	1000	100	0.5	0.65	10	N/A
Sheu	SW-5	500	650	1000	100	0.5	0.65	10	N/A
Sheu	SW-6	500	650	1000	100	0.5	0.65	10	N/A
Sheu	SW-11	500	650	1000	100	0.5	0.65	10	N/A
Sheu	SW-17	750	900	1000	100	0.75	0.9	10	N/A

N/A – Not Applicable

Table A-2. Reinforcement configuration of squat RC walls with rectangular cross section.

Researcher	Wall ID	A_{sbe} (mm^2)	ρ_{be} (%)	s_v (mm)	s_h (mm)	ρ_v (%)	ρ_h (%)	No. Vertical Curtains	No. Horiz. Curtains
Carrillo/Alcocer	MCN50C	1584	7.92	500	500	0.14	0.14	1	1
Carrillo/Alcocer	MCN100C	2280	11.40	250	250	0.29	0.29	1	1
Carrillo/Alcocer	MCS50C	1584	7.92	500	500	0.14	0.14	1	1
Carrillo/Alcocer	MCS100C	2280	11.40	250	250	0.29	0.29	1	1
Carrillo/Alcocer	MRN100C	1710	8.55	250	250	0.29	0.29	1	1
Carrillo/Alcocer	MRN50C	1188	5.94	500	500	0.14	0.14	1	1
Carrillo/Alcocer	MCN50C-2	1710	8.55	500	500	0.14	0.14	1	1
Carrillo/Alcocer	MCS50C-2	1710	8.55	500	500	0.14	0.14	1	1
Carrillo/Alcocer	MCN100D	1584	12.38	320	320	0.28	0.28	1	1
Terzioglu	SW-T2-S1-1	804	5.16	125	125	0.67	0.67	2	2
Terzioglu	SW-T1-S1-2	804	5.16	250	250	0.34	0.34	2	2
Terzioglu	SW-T2-S2-3	804	5.16	125	125	0.67	0.67	2	2
Terzioglu	SW-T2-S3-4	804	5.16	125	125	0.67	0.67	2	2
Terzioglu	SW-T3-S1-5	101	1.05	125	125	0.67	0.67	2	2
Terzioglu	SW-T4-S1-6	616	3.95	125	125	0.67	0.67	2	2
Terzioglu	SW-T5-S1-7	1521	9.75	250	125	0.34	0.67	2	2
Terzioglu	SW-T6-S1-8	1521	9.75	125	125	0.67	0.67	2	2
Terzioglu	SW-T1-S2-9	804	5.16	250	250	0.34	0.34	2	2
Terzioglu	SW-T1-N5-S1-10	804	5.16	250	250	0.34	0.34	2	2
Terzioglu	SW-T1-N10-S1-11	804	5.16	250	250	0.34	0.34	2	2
NEES-UB	SW1	0	0	175	175	0.71	0.71	2	2
NEES-UB	SW2	0	0	130	130	0.96	0.96	2	2
NEES-UB	SW3	0	0	175	175	0.71	0.71	2	2
NEES-UB	SW4	0	0	370	370	0.34	0.34	2	2
NEES-UB	SW5	0	0	130	130	0.96	0.96	2	2
NEES-UB	SW6	0	0	175	175	0.71	0.71	2	2
NEES-UB	SW7	0	0	370	370	0.34	0.34	2	2
NEES-UB	SW8	0	0	83	83	1.50	1.50	2	2
NEES-UB	SW9	0	0	83	175	1.50	0.71	2	2
NEES-UB	SW10	0	0	83	370	1.50	0.34	2	2
NEES-UB	SW11	1191	1.54	175	175	0.71	0.71	2	2
NEES-UB	SW12	1588	2.06	370	370	0.34	0.34	2	2
Whyte	Wall 1	0	0	175	175	0.71	0.71	2	2
Whyte	Wall 2	0	0	175	175	0.71	0.71	2	2
Salonikios	MSW3	311	1.29	100	100	0.28	0.28	2	2
Salonikios	MSW6	414	1.73	74	100	0.565	0.565	3	3
Salonikios	LSW1	414	1.73	74	100	0.565	0.565	3	3

Researcher	Wall ID	A_{sbe} (mm^2)	ρ_{be} (%)	s_v (mm)	s_h (mm)	ρ_v (%)	ρ_h (%)	No. Vertical Curtains	No. Horiz. Curtains
Salonikios	LSW2	311	1.29	100	100	0.28	0.28	2	2
Salonikios	LSW3	311	1.29	100	100	0.28	0.28	2	2
Wiradinata	Wall 1	401	1.25	284	300	0.71	0.21	2	2
Wiradinata	Wall 2	401	1.25	284	300	0.71	0.21	2	2
Pilette	Wall4	401	1.25	284	250	0.71	0.80	2	2
Pilette	Wall 5	401	1.60	175	175	1.15	1.15	2	2
M. Doostdar	Wall 7	401	1.25	284	250	0.71	0.80	2	2
M. Doostdar	Wall 8	401	1.11	285	250	0.70	0.80	2	2
Synge	Wall 1	452	2.26	140	120	0.81	1.68	1	1
Cardenas	SW-13	0	0.00	89	95.3	2.93	0.98	1	1
Greifenhagen	M4	0	0.00	219	122	0.32	0.26	2	2
Park	S1	5819	9.70	300	250	0.66	0.51	2	2
Park	S2	5819	9.70	300	180	0.66	0.70	2	2
Park	S3	5819	9.70	300	250	0.66	0.51	2	2
Park	S5	3879	9.70	550	500	0.36	0.25	2	2
Park	S6	3879	9.70	550	500	0.36	0.25	2	2
Park	S7	3879	9.70	550	500	0.36	0.25	2	2
Hirosawa	72	1546	5.68	132	264	0.52	0.26	2	2
Hirosawa	73	1546	5.68	132	264	0.52	0.26	2	2
Hirosawa	74	1546	5.68	132	132	0.52	0.52	2	2
Hirosawa	75	1546	5.68	132	132	0.52	0.52	2	2
Hirosawa	76	1546	5.68	132	66	0.52	1.04	2	2
Hirosawa	77	1546	5.68	132	66	0.52	1.04	2	2
Altin	1	1005	6.70	250	400	0.23	0.14	2	2
Alexander	1	0	0	114	114.3	0.30	0.30	1	1
Rothe	T10	169	1.41	120	158	0.71	0.51	2	2
Hwang/Sheu	SWN-1D	0	0	180	133	0.40	0.54	1	1
Hwang/Sheu	SWN-5D	0	0	180	130	0.40	0.55	1	1
Sheu	SW-2	0	0	180	133	0.40	0.54	1	1
Sheu	SW-5	0	0	180	133	0.71	0.97	1	1
Sheu	SW-6	0	0	180	133	0.71	0.97	1	1
Sheu	SW-11	0	0	225	133	0.70	0.54	1	1
Sheu	SW-17	0	0	225	130	0.70	0.55	1	1

Table A-3. Materials properties of squat RC walls with rectangular cross section.

Researcher	Wall ID	f'_c (MPa)	f_{ybe} (MPa)	f_{ube} (MPa)	f_{yv} (MPa)	f_{uv} (MPa)	f_{yh} (MPa)	f_{uh} (MPa)
Carrillo/Alcocer	MCN50C	17.5	433	698	447	672	447	672
Carrillo/Alcocer	MCN100C	17.5	430	685	447	672	447	672
Carrillo/Alcocer	MCS50C	22	433	698	447	672	447	672
Carrillo/Alcocer	MCS100C	22	430	685	447	672	447	672
Carrillo/Alcocer	MRN100C	16.2	430	685	447	672	447	672
Carrillo/Alcocer	MRN50C	16.2	433	698	447	672	447	672
Carrillo/Alcocer	MCN50C-2	20	430	685	447	672	447	672
Carrillo/Alcocer	MCS50C-2	27.1	430	685	447	672	447	672
Carrillo/Alcocer	MCN100D	24.7	411	656	435	659	435	659
Terzioglu	SW-T2-S1-1	19.3	437	545	473	567	473	567
Terzioglu	SW-T1-S1-2	23.7	437	545	473	567	473	567
Terzioglu	SW-T2-S2-3	25.8	437	545	473	567	473	567
Terzioglu	SW-T2-S3-4	29	525	775	572	678	572	678
Terzioglu	SW-T3-S1-5	32.1	572	678	572	678	572	678
Terzioglu	SW-T4-S1-6	34.8	509	632	572	678	572	678
Terzioglu	SW-T5-S1-7	35	536	667	572	678	572	678
Terzioglu	SW-T6-S1-8	22.6	536	667	572	678	572	678
Terzioglu	SW-T1-S2-9	24	525	775	572	678	572	678
Terzioglu	SW-T1-N5-S1-10	26.3	525	775	572	678	572	678
Terzioglu	SW-T1-N10-S1-11	27	525	775	572	678	572	678
NEES-UB	SW1	24.8	N/A	N/A	462	703	462	703
NEES-UB	SW2	48.3	N/A	N/A	434	600	434	600
NEES-UB	SW3	53.8	N/A	N/A	434	600	434	600
NEES-UB	SW4	29	N/A	N/A	462	703	462	703
NEES-UB	SW5	29.7	N/A	N/A	462	703	462	703
NEES-UB	SW6	26.2	N/A	N/A	462	703	462	703
NEES-UB	SW7	26.2	N/A	N/A	462	703	462	703
NEES-UB	SW8	24.1	N/A	N/A	462	703	462	703
NEES-UB	SW9	29.7	N/A	N/A	462	703	462	703
NEES-UB	SW10	31.7	N/A	N/A	462	703	462	703
NEES-UB	SW11	34.5	462	703	462	703	462	703
NEES-UB	SW12	34.5	462	703	462	703	462	703
Whyte	Wall 1	35.5	N/A	N/A	464	633	464	633
Whyte	Wall 2	37.3	N/A	N/A	464	633	464	633
Salonikios	MSW3	24.1	585	-	610	-	610	-
Salonikios	MSW6	27.5	585	-	610	-	610	-
Salonikios	LSW1	22.2	585	-	610	-	610	-

Researcher	Wall ID	f'_c (MPa)	f_{ybe} (MPa)	f_{ube} (MPa)	f_{yv} (MPa)	f_{uv} (MPa)	f_{yh} (MPa)	f_{uh} (MPa)
Salonikios	LSW2	21.6	585	-	610	-	610	-
Salonikios	LSW3	23.9	585	-	610	-	610	-
Wiradinata	Wall 1	25.0	435	650	435	650	425	565
Wiradinata	Wall 2	22.0	435	650	435	650	425	565
Pilette	Wall4	33	480	770	480	770	480	770
Pilette	Wall 5	27	480	770	480	770	480	770
M. Doostdar	Wall 7	45.0	450	658	450	658	450	658
M. Doostdar	Wall 8	45.0	450	658	450	658	450	658
Synge	Wall 1	27.2	300	460	300	460	380	576
Cardenas	SW-13	43.4	N/A	N/A	448	-	455	-
Greifenhagen	M4	24.4	N/A	N/A	504	634	745	800
Park	S1	46.5	617	-	653	-	667	-
Park	S2	46.5	617	-	653	-	477	-
Park	S3	70.3	617	-	653	-	667	-
Park	S5	46.1	617	-	653	-	667	-
Park	S6	70.3	617	-	653	-	667	-
Park	S7	46.5	617	-	653	-	667	-
Hirosawa	72	17.3	377	-	407	-	419	-
Hirosawa	73	20.8	377	-	407	-	419	-
Hirosawa	74	20.8	377	-	407	-	422	-
Hirosawa	75	13.7	377	-	407	-	422	-
Hirosawa	76	14.7	377	-	407	-	415	-
Hirosawa	77	18.3	377	-	407	-	415	-
Altin	1	15.5	425	520	325	420	325	420
Alexander	1	20.7	N/A	N/A	359	-	359	-
Rothe	T10	33.6	500	550	500	550	500	550
Hwang/Sheu	SWN-1D	26.7	N/A	N/A	468	-	468	-
Hwang/Sheu	SWN-5D	28.0	N/A	N/A	468	-	468	-
Sheu	SW-2	26.0	N/A	N/A	483	-	483	-
Sheu	SW-5	27.3	N/A	N/A	481	-	481	-
Sheu	SW-6	28.2	N/A	N/A	481	-	481	-
Sheu	SW-11	26.0	N/A	N/A	432	-	467	-
Sheu	SW-17	26.0	N/A	N/A	432	-	467	-

N/A: Not Applicable

- Value Not Reported

Table A-4. Loading, strength and drift ratio of squat RC walls with rectangular cross section.

Researcher	Wall ID	Loading Type	P/f'_cA_g (%)	V_{peak} (kN)	R_{cr}	R_{peak}	R_u
Carrillo/Alcocer	MCN50C	Cyclic	1.43	354	0.0017	0.0066	-
Carrillo/Alcocer	MCN100C	Cyclic	1.43	454	0.0016	0.0081	0.0141
Carrillo/Alcocer	MCS50C	Cyclic	1.14	374	0.0041	0.0101	-
Carrillo/Alcocer	MCS100C	Cyclic	1.14	454	0.0045	0.0100	0.0156
Carrillo/Alcocer	MRN100C	Cyclic	1.54	766	0.0027	0.0061	0.0080
Carrillo/Alcocer	MRN50C	Cyclic	1.54	670	0.0029	0.0069	0.0111
Carrillo/Alcocer	MCN50C-2	Cyclic	1.25	329	0.0014	0.0044	0.0096
Carrillo/Alcocer	MCS50C-2	Cyclic	0.92	321	0.0014	0.0040	0.0077
Carrillo/Alcocer	MCN100D	Dynamic	1.01	274	0.0020	0.0053	0.0059
Terzioglu	SW-T2-S1-1	Cyclic	0	793	0.0026	0.0097	0.0153
Terzioglu	SW-T1-S1-2	Cyclic	0	633	0.0025	0.0076	0.0136
Terzioglu	SW-T2-S2-3	Cyclic	0	666	0.0028	0.0100	0.0123
Terzioglu	SW-T2-S3-4	Cyclic	0	810	0.0017	0.0081	0.0142
Terzioglu	SW-T3-S1-5	Cyclic	0	385	0.0004	0.0036	0.0136
Terzioglu	SW-T4-S1-6	Cyclic	0	877	0.0013	0.0050	0.0149
Terzioglu	SW-T5-S1-7	Cyclic	0	709	0.0021	0.0071	0.0153
Terzioglu	SW-T6-S1-8	Cyclic	0	738	0.0030	0.0091	0.0134
Terzioglu	SW-T1-S2-9	Cyclic	0	565	0.0021	0.0061	0.0125
Terzioglu	SW-T1-N5-S1-10	Cyclic	5.1	791	0.0020	0.0080	0.0123
Terzioglu	SW-T1-N10-S1-11	Cyclic	9.9	796	0.0018	0.0080	0.0098
NEES-UB	SW1	Cyclic	0	1116	0.0026	0.0129	0.0209
NEES-UB	SW2	Cyclic	0	2342	0.0029	0.0110	0.0174
NEES-UB	SW3	Cyclic	0	1888	0.0025	0.0143	0.0255
NEES-UB	SW4	Cyclic	0	983	0.0009	0.0071	0.0219
NEES-UB	SW5	Cyclic	0	2831	0.0031	0.0110	0.0135
NEES-UB	SW6	Cyclic	0	2184	0.0025	0.0081	0.0219
NEES-UB	SW7	Cyclic	0	1323	0.0012	0.0043	0.0143
NEES-UB	SW8	Cyclic	0	2600	0.0021	0.0068	0.0134
NEES-UB	SW9	Cyclic	0	2791	0.0025	0.0069	0.0119
NEES-UB	SW10	Cyclic	0	2275	0.0017	0.0055	0.0108
NEES-UB	SW11	Cyclic	0	1850	0.0015	0.0067	0.0192
NEES-UB	SW12	Cyclic	0	1737	0.0014	0.0107	-
Whyte	Wall 1	Hybrid	0	1618	0.0019	0.0079	0.0063
Whyte	Wall 2	Hybrid	0	1705	0.0018	0.0075	0.0063
Salonikios	MSW3	Cyclic	7.0	173	0.0015	0.0058	0.0127
Salonikios	MSW6	Cyclic	0	187	0.0030	0.0091	0.0136
Salonikios	LSW1	Cyclic	0	262	0.0012	0.0050	0.0081

Researcher	Wall ID	Loading Type	P/f'_cA_g (%)	V_{peak} (kN)	R_{cr}	R_{peak}	R_u
Salonikios	LSW2	Cyclic	0	185	0.0011	0.0044	0.0077
Salonikios	LSW3	Cyclic	7.0	252	0.0008	0.0042	0.0115
Wiradinata	Wall 1	Cyclic	0	531	0.0005	0.0079	0.0100
Wiradinata	Wall 2	Cyclic	0	685	0.0006	0.0036	0.0120
Pilette	Wall4	Cyclic	0	401	0.0019	0.0071	0.0204
Pilette	Wall 5	Cyclic	0	545	0.0036	0.0140	0.0251
M. Doostdar	Wall 7	Cyclic	0	375	0.0012	0.0050	0.0144
M. Doostdar	Wall 8	Cyclic	0	225	0.0012	0.0089	0.0177
Synge	Wall 1	Cyclic	0	774	0.0013	0.0044	0.0094
Cardenas	SW-13	Cyclic	0	632	0.0022	0.0053	-
Greifenhagen	M4	Cyclic	4.3	135	0.0007	0.0051	0.0186
Park	S1	Cyclic	7.0	2158	0.0039	0.0101	0.0108
Park	S2	Cyclic	7.0	2298	0.0041	0.0100	0.0119
Park	S3	Cyclic	7.0	2085	0.0032	0.0082	0.0093
Park	S5	Cyclic	7.0	1478	0.0023	0.0079	0.0102
Park	S6	Cyclic	7.0	1876	0.0036	0.0095	0.0101
Park	S7	Cyclic	7.0	1916	0.0035	0.0092	0.0112
Hirosawa	72	Cyclic	11.3	773	0.0012	0.0051	0.0096
Hirosawa	73	Cyclic	9.4	770	0.0011	0.0070	0.0080
Hirosawa	74	Cyclic	9.4	790	0.0011	0.0050	0.0091
Hirosawa	75	Cyclic	14.3	812	0.0013	0.0137	-
Hirosawa	76	Cyclic	13.4	791	0.0014	0.0052	0.0126
Hirosawa	77	Cyclic	10.7	875	0.0036	0.0099	-
Altin	1	Cyclic	0.0	146	0.0020	0.0056	0.0084
Alexander	1	Cyclic	0.0	329	-	-	-
Rothe	T10	Cyclic	0.0	89	-	-	-
Hwang/Sheu	SWN-1D	Cyclic	12	323	0.0017	0.0063	0.0175
Hwang/Sheu	SWN-5D	Cyclic	12	247	0.0011	0.0097	-
Sheu	SW-2	Cyclic	0	179	-	-	-
Sheu	SW-5	Cyclic	0	242	-	-	-
Sheu	SW-6	Cyclic	0	276	-	-	-
Sheu	SW-11	Cyclic	0	222	-	-	-
Sheu	SW-17	Cyclic	0	180	-	-	-

- Corresponding drift ratio value could not be obtained from the reported data.

A.2 Squat RC Walls with Enlarged Boundary Elements

Tables A-5 to A-8 show the compiled data for the considered squat RC wall tests with rectangular cross section mentioned on Chapter 2.

Table A-5. Geometric properties of squat RC walls with enlarged boundary elements.

Researcher	ID	Shape	h_w (mm)	h_L (mm)	l_w (mm)	t_w (mm)	h_w/l_w	M/Vl_w	l_{be} (mm)	h_{be} (mm)
Kabe./Hira.	NW-2	Bar.	2000	2261	1700	80	1.18	1.33	200	200
Kabe./Hira.	No. 1	Bar.	2000	2261	1700	80	1.18	1.33	200	200
Kabe./Hira.	No. 2	Bar.	2000	2261	1700	80	1.18	1.33	200	200
Kabe./Hira.	No. 3	Bar.	2000	2261	1700	80	1.18	1.33	200	200
Kabe./Hira.	No. 4	Bar.	2000	2261	1700	80	1.18	1.33	200	200
Kabe./Hira.	No. 6	Bar.	2000	2261	1700	80	1.18	1.33	200	200
Kabe./Hira.	No. 7	Bar.	2000	2261	1700	80	1.18	1.33	200	200
Kabe./Hira.	No. 8	Bar.	2000	2261	1700	80	1.18	1.33	200	200
Sanada/Kabe.	Type N	Bar.	1400	2050	2050	80	0.68	1.00	250	250
Sanada/Kabe.	Type S	Bar.	1400	2050	2050	80	0.68	1.00	250	250
Matsui	Wall-A	Bar.	1800	2761	2000	80	0.90	1.38	200	200
Matsui	Wall-B	Bar.	1800	3526	2000	80	0.90	1.76	200	200
Akita	WAS	Bar.	1800	2761	2000	80	0.90	1.38	200	200
Akita	WBS	Bar.	1800	3526	2000	80	0.90	1.76	200	200
Kabeyasawa	K1	Bar.	1500	1500	2000	80	0.75	0.75	200	200
Kabeyasawa	K2	Bar.	1500	1500	2000	80	0.75	0.75	200	200
Kabeyasawa	K3	Bar.	1500	1500	2000	80	0.75	0.75	200	200
Kabeyasawa	K4	Bar.	1500	1500	2000	80	0.75	0.75	200	200
Maier	S5	Flan.	1200	1320	1180	100	1.02	1.12	100	400
Maier	S7	Flan.	1200	1320	1180	100	1.02	1.12	100	400
Barda	B3-2	Flan.	876	953	1905	101.6	0.46	0.50	102	610
Barda	B4-3	Flan.	876	953	1905	101.6	0.46	0.50	102	610
Barda	B5-4	Flan.	876	953	1905	101.6	0.46	0.50	102	610
Barda	B6-4	Flan.	876	953	1905	101.6	0.46	0.50	102	610
Barda	B7-5	Flan.	400	476	1905	101.6	0.21	0.25	102	610
Barda	B8-5	Flan.	1829	1905	1905	101.6	0.96	1.00	102	610
Synge	Wall-3	Flan.	1500	1700	3000	100	0.50	0.57	100	500
Palermo/Vecc.	DP1	Flan.	2020	2340	3075	75	0.66	0.76	95	3045
Palermo/Vecc.	DP2	Flan.	2020	2340	3075	75	0.66	0.76	95	3045
Saito	W-15-1	Flan.	750	1000	2150	150	0.35	0.47	150	500
Saito	W-12-1	Flan.	750	1000	2120	120	0.35	0.47	120	500
Saito	W-12-2	Flan.	750	1000	2120	120	0.35	0.47	120	500

Researcher	ID	Shape	h_w (mm)	h_L (mm)	l_w (mm)	t_w (mm)	h_w/l_w	M/Vl_w	l_{be} (mm)	h_{be} (mm)
Saito	W-12-3	Flan.	750	1000	2120	120	0.35	0.47	120	500
Saito	W-12-4	Flan.	750	1000	2120	120	0.35	0.47	120	500
Saito	W-12-5	Flan.	750	1000	2120	120	0.35	0.47	120	500
Saito	W-15-2	Flan.	1750	2000	2150	150	0.81	0.93	150	500
Saito	W-12-6	Flan.	1750	2000	2120	120	0.83	0.94	120	500
Saito	W-12-7	Flan.	1750	2000	2120	120	0.83	0.94	120	500
Sato	18M 12-40	Flan.	2200	2400	2150	150	1.02	1.12	150	1000
Sato	24M 8-30	Flan.	1400	1600	2150	150	0.65	0.74	150	1000
Sato	24M 8-40	Flan.	1400	1600	2150	150	0.65	0.74	150	1000
Sato	24M 8-50	Flan.	1400	1600	2150	150	0.65	0.74	150	1000
Sato	24M 6-30	Flan.	1000	1200	2150	150	0.47	0.56	150	1000
Sato	24M 6-40	Flan.	1000	1200	2150	150	0.47	0.56	150	1000
Sato	36M 12-30	Flan.	2200	2400	2150	150	1.02	1.12	150	1000
Sato	36M 12-40	Flan.	2200	2400	2150	150	1.02	1.12	150	1000
Sato	36M 12-50	Flan.	2200	2400	2150	150	1.02	1.12	150	1000
Sato	36L 8-30	Flan.	1400	1600	2150	150	0.65	0.74	150	1000
Sato	36L 8-40	Flan.	1400	1600	2150	150	0.65	0.74	150	1000
Sato	36M 8-30	Flan.	1400	1600	2150	150	0.65	0.74	150	1000
Sato	36M 8-40	Flan.	1400	1600	2150	150	0.65	0.74	150	1000
Sato	36M 8-50	Flan.	1400	1600	2150	150	0.65	0.74	150	1000
Sato	36M 6-30	Flan.	1000	1200	2150	150	0.47	0.56	150	1000
Sato	36M 6-40	Flan.	1000	1200	2150	150	0.47	0.56	150	1000
Sato	48M 8-30	Flan.	1400	1600	2150	150	0.65	0.74	150	1000
Sato	48M 8-40	Flan.	1400	1600	2150	150	0.65	0.74	150	1000
Sato	48M 8-50	Flan.	1400	1600	2150	150	0.65	0.74	150	1000
Sato	48H 8-30	Flan.	1400	1600	2150	150	0.65	0.74	150	1000
Sato	48H 8-40	Flan.	1400	1600	2150	150	0.65	0.74	150	1000
Sato	48H 8-50	Flan.	1400	1600	2150	150	0.65	0.74	150	1000
Seki	RA-00P	Flan.	1420	1800	3075	75	0.46	0.59	75	1500
Seki	RA-15P	Flan.	1420	1800	3075	75	0.46	0.59	75	1500
Seki	RB-00P	Flan.	2020	2400	3075	75	0.66	0.78	75	1500
Seki	RB-15P	Flan.	2020	2400	3075	75	0.66	0.78	75	1500
Seki	RC-00P	Flan.	2620	3000	3075	75	0.85	0.98	75	1500
Seki	RC-15P	Flan.	2620	3000	3075	75	0.85	0.98	75	1500
Park	S4	Bar.	1500	1750	1500	200	1.00	1.17	200	300
Dabbagh	SW1	Flan.	1000	1100	1000	75	1.00	1.10	100	375
Dabbagh	SW2	Flan.	1000	1100	1000	75	1.00	1.10	100	375
Dabbagh	SW3	Flan.	1000	1100	1000	75	1.00	1.10	100	375
Dabbagh	SW4	Flan.	1000	1100	1000	75	1.00	1.10	100	375

Researcher	ID	Shape	h_w (mm)	h_L (mm)	l_w (mm)	t_w (mm)	h_w/l_w	M/Vl_w	l_{be} (mm)	h_{be} (mm)
Dabbagh	SW5	Flan.	1000	1100	1000	75	1.00	1.10	100	375
Dabbagh	SW6	Flan.	1000	1100	1000	75	1.00	1.10	100	375
Ryo/Hiros.	30	Bar.	1200	1325	2300	75	0.52	0.58	250	250
Ryo/Hiros.	31	Bar.	1200	1325	1550	80	0.77	0.85	250	250
Sugano/Hiros.	70	Bar.	1200	1325	2300	74	0.52	0.58	250	250
Sugano/Hiros.	71	Bar.	1200	1325	2300	83	0.52	0.58	250	250
Endo	W7101	Bar.	1750	1875	2250	80	0.78	0.83	250	250
Endo	W7102	Bar.	1750	1875	2250	80	0.78	0.83	250	250
Endo	W7103	Bar.	1750	1875	2250	80	0.78	0.83	250	250
Endo	W7402	Bar.	1750	1875	2250	80	0.78	0.83	250	250
Endo	W7404	Bar.	1750	1875	2250	80	0.78	0.83	250	250
Endo	W7501	Bar.	1750	1875	2250	80	0.78	0.83	250	250
Endo	W7503	Bar.	1750	1875	2250	80	0.78	0.83	250	250
Endo	W7601	Bar.	1750	1875	2250	80	0.78	0.83	250	250
Endo	W7602	Bar.	1750	1875	2250	100	0.78	0.83	250	250
Endo	W7603	Bar.	1750	1875	2250	100	0.78	0.83	250	250
Endo	W7604	Bar.	2750	2875	2250	80	1.22	1.28	250	250
Endo	W7605	Bar.	2750	2875	2250	100	1.22	1.28	250	250
Endo	W7606	Bar.	1750	1875	2250	100	0.78	0.83	250	250
NUPEC	U-1	Flan.	2020	2400	3100	75	0.65	0.77	100	2980
NUPEC	U-2	Flan.	2020	2400	3100	75	0.65	0.77	100	2980
Xiang Dong	FSW-4	Bar.	914.4	1066.8	1219.2	76.2	0.75	0.88	152	152
Xiang Dong	FSW-5	Bar.	914.4	1066.8	1219.2	76.2	0.75	0.88	152	152
Xiang Dong	FSW-6	Bar.	914.4	1066.8	1219.2	76.2	0.75	0.88	152	152
Xiang Dong	FSW-7	Bar.	914.4	1066.8	1219.2	76.2	0.75	0.88	152	152
Xiang Dong	FSW-8	Bar.	914.4	1066.8	1219.2	76.2	0.75	0.88	152	152
Xiang Dong	FSW-9	Bar.	914.4	1066.8	1219.2	76.2	0.75	0.88	152	152
Xiang Dong	FSW-10	Bar.	914.4	1066.8	1219.2	76.2	0.75	0.88	152	152
Xiang Dong	FSW-12	Bar.	914.4	1066.8	1219.2	76.2	0.75	0.88	152	152
Xiang Dong	FSW-13	Bar.	914.4	1066.8	1219.2	76.2	0.75	0.88	152	152
Chiba	CW-0.6-1.2-20	Bar.	1050	1200	2300	80	0.46	0.52	300	300
Chiba	CW-0.6-0.6-20	Bar.	1050	1200	2300	80	0.46	0.52	300	300
Chiba	CW-0.6-0.8-20	Bar.	1050	1200	2300	80	0.46	0.52	300	300
Chiba	CW-0.6-1.6-20	Bar.	1050	1200	2300	80	0.46	0.52	300	300
Chiba	CW-0.6-2.0-20	Bar.	1050	1200	2300	80	0.46	0.52	300	300
Chiba	CW-0.6-1.2-40	Bar.	1050	1200	2300	80	0.46	0.52	300	300
Chiba	CW-0.4-1.2-20	Bar.	650	800	2300	80	0.28	0.35	300	300
Chiba	CW-0.8-1.2-20	Bar.	1450	1600	2300	80	0.63	0.70	300	300
Yagishita	CW-0.6-0.6-20a	Bar.	1050	1200	2300	80	0.46	0.52	300	300

Researcher	ID	Shape	h_w (mm)	h_L (mm)	l_w (mm)	t_w (mm)	h_w/l_w	M/Vl_w	l_{be} (mm)	h_{be} (mm)
Yagishita	CW-0.6-0.8-20a	Bar.	1050	1200	2300	80	0.46	0.52	300	300
Yagishita	CW-0.6-1.2-0	Bar.	1050	1200	2300	80	0.46	0.52	300	300
Fukuzawa	CW-0.6-0-20	Bar.	1050	1200	2300	80	0.46	0.52	300	300
Fukuzawa	CW-0.6-0.3-20	Bar.	1050	1200	2300	80	0.46	0.52	300	300
Fukuzawa	CW-0.6-2.4-20	Bar.	1050	1200	2300	80	0.46	0.52	300	300
Fukuzawa	CW-0.6-2.8-20	Bar.	1050	1200	2300	80	0.46	0.52	300	300
Fukuzawa	CW-0.6-0-0	Bar.	1050	1200	2300	80	0.46	0.52	300	300
Fukuzawa	CW-0.6-0-40	Bar.	1050	1200	2300	80	0.46	0.52	300	300
Fukuzawa	CW-0.6-0.6-0	Bar.	1050	1200	2300	80	0.46	0.52	300	300
Fukuzawa	CW-0.6-0.6-40	Bar.	1050	1200	2300	80	0.46	0.52	300	300
Fukuzawa	CW-0.4-0.6-20	Bar.	650	800	2300	80	0.28	0.35	300	300
Fukuzawa	CW-0.8-0.6-20	Bar.	1450	1600	2300	80	0.63	0.70	300	300
Fukuzawa	CW-0.4-2.0-20	Bar.	650	800	2300	80	0.28	0.35	300	300
Fukuzawa	CW-0.8-2.0-20	Bar.	1450	1600	2300	80	0.63	0.70	300	300
Hatori	CW-0.6-2-0	Bar.	1050	1200	2300	80	0.46	0.52	300	300
Hatori	CW-0.6-2-40	Bar.	1050	1200	2300	80	0.46	0.52	300	300
Hatori	CW-0.6-2-20B	Bar.	1050	1200	2300	80	0.46	0.52	300	300
Hatori	CW-0.6-0.6-20L	Bar.	1050	1200	2300	80	0.46	0.52	300	300
Hatori	CW-0.6-1.2-20L	Bar.	1050	1200	2300	80	0.46	0.52	300	300
Hatori	CW-0.6-2-20L	Bar.	1050	1200	2300	80	0.46	0.52	300	300
Taga	No 1	Bar.	1050	1200	2180	80	0.48	0.55	180	180
Taga	No 2	Bar.	1050	1200	2180	80	0.48	0.55	180	180
Taga	No 3	Bar.	1050	1200	2180	80	0.48	0.55	180	180
Taga	No 4	Bar.	1050	1200	2180	80	0.48	0.55	180	180
Taga	No 5	Bar.	1050	1200	2180	80	0.48	0.55	180	180
Taga	No 6	Bar.	1050	1200	2180	80	0.48	0.55	180	180

Bar. – Barbell cross section
Flan. – Flanged cross section

Table A-6. Reinforcement configuration of squat RC walls with enlarged boundary elements.

Researcher	ID	A_{sbe} (each)	ρ_{be} (%)	s_v (mm)	s_h (mm)	ρ_v (%)	ρ_h (%)	No. Vertical Curtains	No. Horiz. Curtains
Kabeyasawa/Hiraishi	NW-2	856	2.14	150	150	0.53	0.53	2	2
Kabeyasawa/Hiraishi	No. 1	2033	5.08	400	400	0.20	0.20	2	2
Kabeyasawa/Hiraishi	No. 2	2033	5.08	230	230	0.35	0.35	2	2
Kabeyasawa/Hiraishi	No. 3	2033	5.08	150	150	0.53	0.53	2	2
Kabeyasawa/Hiraishi	No. 4	2033	5.08	150	150	0.53	0.53	2	2
Kabeyasawa/Hiraishi	No. 6	2033	5.08	122	122	0.66	0.66	2	2
Kabeyasawa/Hiraishi	No. 7	2033	5.08	80	80	1.00	1.00	2	2
Kabeyasawa/Hiraishi	No. 8	2033	5.08	55	55	1.45	1.45	2	2
Sanada/Kabeyasawa	Type N	1134	1.81	130	130	0.25	0.25	2	2
Sanada/Kabeyasawa	Type S	1134	1.81	130	130	0.25	0.25	2	2
Matsui	Wall-A	1525	3.81	200	200	0.40	0.40	2	2
Matsui	Wall-B	1525	3.81	200	200	0.40	0.40	2	2
Akita	WAS	1525	3.81	200	200	0.40	0.40	2	2
Akita	WBS	1525	3.81	200	200	0.40	0.40	2	2
Kabeyasawa	K1	284	0.71	150	150	0.27	0.27	2	2
Kabeyasawa	K2	572	1.43	150	150	0.53	0.53	2	2
Kabeyasawa	K3	856	2.14	100	100	0.80	0.80	2	2
Kabeyasawa	K4	572	1.43	100	100	0.80	0.80	2	2
Maier	S5	503	1.26	100	100	1.01	1.01	2	2
Maier	S7	503	1.26	100	100	1.01	1.01	2	2
Barda	B3-2	2534	4.09	284	117	0.50	0.48	2	2
Barda	B4-3	2534	4.09	284	N/A	0.50	0.00	2	0
Barda	B5-4	2534	4.09	N/A	117	0.00	0.48	0	2
Barda	B6-4	2534	4.09	213	117	0.26	0.48	2	2
Barda	B7-5	2534	4.09	284	114	0.50	0.49	2	2
Barda	B8-5	2534	4.09	284	111	0.50	0.50	2	2
Synge	Wall-3	905	1.81	200	120	0.39	1.68	1	1
Palermo/Vecchio	DP1	1078	0.37	130	140	0.79	0.73	2	2
Palermo/Vecchio	DP2	1078	0.37	130	140	0.79	0.73	2	2
Saito	W-15-1	2850	3.80	90	90	1.06	1.06	2	2
Saito	W-12-1	2850	4.75	90	90	1.32	1.32	2	2
Saito	W-12-2	2850	4.75	130	130	0.91	0.91	2	2
Saito	W-12-3	2850	4.75	70	70	1.70	1.70	2	2
Saito	W-12-4	2850	4.75	90	90	1.32	1.32	2	2
Saito	W-12-5	2850	4.75	90	90	1.32	1.32	2	2
Saito	W-15-2	2850	3.80	90	90	1.06	1.06	2	2
Saito	W-12-6	2850	4.75	90	90	1.32	1.32	2	2

Researcher	ID	A_{sbe} (each)	ρ_{be} (%)	s_v (mm)	s_h (mm)	ρ_v (%)	ρ_h (%)	No. Vertical Curtains	No. Horiz. Curtains
Saito	W-12-7	2850	4.75	90	90	1.32	1.32	2	2
Sato	18M 12-40	3281	2.19	211	211	0.45	0.45	2	2
Sato	24M 8-30	1141	0.76	119	119	0.80	0.80	2	2
Sato	24M 8-40	856	0.57	159	159	0.60	0.60	2	2
Sato	24M 8-50	713	0.48	198	198	0.48	0.48	2	2
Sato	24M 6-30	1141	0.76	119	119	0.80	0.80	2	2
Sato	24M 6-40	856	0.57	159	159	0.60	0.60	2	2
Sato	36M 12-30	8702	5.80	82	82	1.16	1.16	2	2
Sato	36M 12-40	6705	4.47	106	106	0.90	0.90	2	2
Sato	36M 12-50	5421	3.61	132	132	0.72	0.72	2	2
Sato	36L 8-30	1712	1.14	82	82	1.16	1.16	2	2
Sato	36L 8-40	1284	0.86	106	106	0.90	0.90	2	2
Sato	36M 8-30	1712	1.14	82	82	1.16	1.16	2	2
Sato	36M 8-40	1284	0.86	106	106	0.90	0.90	2	2
Sato	36M 8-50	999	0.67	132	132	0.72	0.72	2	2
Sato	36M 6-30	1712	1.14	82	82	1.16	1.16	2	2
Sato	36M 6-40	1284	0.86	106	106	0.90	0.90	2	2
Sato	48M 8-30	2425	1.62	59	59	1.61	1.61	2	2
Sato	48M 8-40	1712	1.14	82	82	1.16	1.16	2	2
Sato	48M 8-50	1427	0.95	99	99	0.96	0.96	2	2
Sato	48H 8-30	2425	1.62	59	59	1.61	1.61	2	2
Sato	48H 8-40	1712	1.14	82	82	1.16	1.16	2	2
Sato	48H 8-50	1427	0.95	99	99	0.96	0.96	2	2
Seki	RA-00P	1389	1.23	70	70	1.20	1.20	2	2
Seki	RA-15P	1389	1.23	70	70	1.20	1.20	2	2
Seki	RB-00P	1389	1.23	70	70	1.20	1.20	2	2
Seki	RB-15P	1389	1.23	70	70	1.20	1.20	2	2
Seki	RC-00P	1389	1.23	70	70	1.20	1.20	2	2
Seki	RC-15P	1389	1.23	70	70	1.20	1.20	2	2
Park	S4	5819	9.70	367	250	0.54	0.51	2	2
Dabbagh	SW1	2413	6.43	160	167	0.47	0.45	2	2
Dabbagh	SW2	2413	6.43	100	100	1.34	1.34	2	2
Dabbagh	SW3	2413	6.43	160	100	0.84	0.75	2	2
Dabbagh	SW4	2413	6.43	160	100	0.84	0.75	2	2
Dabbagh	SW5	2413	6.43	100	167	1.34	0.45	2	2
Dabbagh	SW6	2413	6.43	133	143	1.01	0.94	2	2
Ryo/Hirosawa	30	1592	2.55	200	200	0.19	0.19	1	1
Ryo/Hirosawa	31	1592	2.55	200	200	0.18	0.18	1	1
Sugano/Hirosawa	70	1592	2.55	200	200	0.19	0.19	1	1

Researcher	ID	A_{sbe} (each)	ρ_{be} (%)	s_v (mm)	s_h (mm)	ρ_v (%)	ρ_h (%)	No. Vertical Curtains	No. Horiz. Curtains
Sugano/Hirosawa	71	1592	2.55	200	200	0.08	0.08	1	1
Endo	W7101	508	0.81	50	50	0.71	0.71	1	1
Endo	W7102	508	0.81	150	150	0.24	0.24	1	1
Endo	W7103	508	0.81	150	150	0.24	0.24	1	1
Endo	W7402	508	0.81	150	150	0.24	0.24	1	1
Endo	W7404	508	0.81	150	150	0.24	0.24	1	1
Endo	W7501	1017	1.63	150	150	0.24	0.24	1	1
Endo	W7503	1017	1.63	150	150	0.24	0.24	1	1
Endo	W7601	1017	1.63	100	100	0.71	0.71	2	2
Endo	W7602	1525	2.44	125	125	0.23	0.23	1	1
Endo	W7603	1525	2.44	80	80	0.71	0.71	2	2
Endo	W7604	1017	1.63	150	150	0.24	0.24	1	1
Endo	W7605	1525	2.44	125	125	0.23	0.23	1	1
Endo	W7606	1525	2.44	125	125	0.23	0.23	1	1
NUPEC	U-1	1393	0.47	70	70	1.21	1.21	2	2
NUPEC	U-2	1393	0.47	70	70	1.21	1.21	2	2
Xiang Dong	FSW-4	774	3.33	152	152	0.56	0.56	2	2
Xiang Dong	FSW-5	774	3.33	152	152	0.56	0.56	2	2
Xiang Dong	FSW-6	774	3.33	152	152	0.56	0.56	2	2
Xiang Dong	FSW-7	774	3.33	76	76	1.11	1.11	2	2
Xiang Dong	FSW-8	774	3.33	152	152	0.23	0.23	2	2
Xiang Dong	FSW-9	774	3.33	76	76	1.11	1.11	2	2
Xiang Dong	FSW-10	774	3.33	76	76	1.11	1.11	2	2
Xiang Dong	FSW-12	774	3.33	152	152	0.23	0.23	2	2
Xiang Dong	FSW-13	774	3.33	152	152	0.23	0.23	2	2
Chiba	CW-0.6-1.2-20	936	1.04	67	67	1.20	1.20	2	2
Chiba	CW-0.6-0.6-20	936	1.04	133	133	0.60	0.60	2	2
Chiba	CW-0.6-0.8-20	936	1.04	100	100	0.80	0.80	2	2
Chiba	CW-0.6-1.6-20	1296	1.44	50	50	1.60	1.60	2	2
Chiba	CW-0.6-2.0-20	1584	1.76	40	40	2.00	2.00	2	2
Chiba	CW-0.6-1.2-40	936	1.04	67	67	1.20	1.20	2	2
Chiba	CW-0.4-1.2-20	936	1.04	67	67	1.20	1.20	2	2
Chiba	CW-0.8-1.2-20	936	1.04	67	67	1.20	1.20	2	2
Yagishita	CW-0.6-0.6-20a	936	1.04	133	133	0.60	0.60	2	2
Yagishita	CW-0.6-0.8-20a	936	1.04	100	100	0.80	0.80	2	2
Yagishita	CW-0.6-1.2-0	936	1.04	67	67	1.20	1.20	2	2
Fukuzawa	CW-0.6-0-20	936	1.04	N/A	N/A	0.00	0.00	0	0
Fukuzawa	CW-0.6-0.3-20	936	1.04	267	267	0.30	0.30	2	2
Fukuzawa	CW-0.6-2.4-20	1584	1.76	34	34	2.36	2.36	2	2

Researcher	ID	A_{sbe} (each)	ρ_{be} (%)	s_v (mm)	s_h (mm)	ρ_v (%)	ρ_h (%)	No. Vertical Curtains	No. Horiz. Curtains
Fukuzawa	CW-0.6-2.8-20	1584	1.76	29	29	2.76	2.76	2	2
Fukuzawa	CW-0.6-0-0	936	1.04	N/A	N/A	0.00	0.00	0	0
Fukuzawa	CW-0.6-0-40	936	1.04	N/A	N/A	0.00	0.00	0	0
Fukuzawa	CW-0.6-0.6-0	936	1.04	133	133	0.60	0.60	2	2
Fukuzawa	CW-0.6-0.6-40	936	1.04	133	133	0.60	0.60	2	2
Fukuzawa	CW-0.4-0.6-20	936	1.04	133	133	0.60	0.60	2	2
Fukuzawa	CW-0.8-0.6-20	936	1.04	133	133	0.60	0.60	2	2
Fukuzawa	CW-0.4-2.0-20	1584	1.76	40	40	2.00	2.00	2	2
Fukuzawa	CW-0.8-2.0-20	1584	1.76	40	40	2.00	2.00	2	2
Hatori	CW-0.6-2-0	1584	1.76	40	40	2.00	2.00	2	2
Hatori	CW-0.6-2-40	1584	1.76	40	40	2.00	2.00	2	2
Hatori	CW-0.6-2-20B	936	1.04	40	40	2.00	2.00	2	2
Hatori	CW-0.6-0.6-20L	936	1.04	133	133	0.60	0.60	2	2
Hatori	CW-0.6-1.2-20L	936	1.04	67	67	1.20	1.20	2	2
Hatori	CW-0.6-2-20L	1584	1.76	40	40	2.00	2.00	2	2
Taga	No 1	936	2.89	67	67	1.20	1.20	2	2
Taga	No 2	936	2.89	67	67	1.20	1.20	2	2
Taga	No 3	936	2.89	67	67	1.20	1.20	2	2
Taga	No 4	936	2.89	133	133	0.60	0.60	2	2
Taga	No 5	936	2.89	40	40	2.00	2.00	2	2
Taga	No 6	936	2.89	40	40	2.00	2.00	2	2
Taga	No 7	936	2.89	40	40	2.00	2.00	2	2

N/A – Not Applicable

Table A-7. Material properties of squat RC walls with enlarged boundary elements.

Researcher	ID	f'_c (MPa)	f_{ybe} (MPa)	f_{ube} (MPa)	f_{yv} (MPa)	f_{uv} (MPa)	f_{yh} (MPa)	f_{uh} (MPa)
Kabeyasawa/Hiraishi	NW-2	93.6	776	968	1001	1128	1001	1128
Kabeyasawa/Hiraishi	No. 1	65.1	1009	-	792	-	792	-
Kabeyasawa/Hiraishi	No. 2	70.8	1009	-	792	-	792	-
Kabeyasawa/Hiraishi	No. 3	71.8	1009	-	792	-	792	-
Kabeyasawa/Hiraishi	No. 4	103.4	1009	-	792	-	792	-
Kabeyasawa/Hiraishi	No. 6	74.1	1009	-	1420	-	1420	-
Kabeyasawa/Hiraishi	No. 7	71.5	1009	-	792	-	792	-
Kabeyasawa/Hiraishi	No. 8	76.1	1009	-	792	-	792	-
Sanada/Kabeyasawa	Type N	22.4	398	557	340	560	340	560
Sanada/Kabeyasawa	Type S	24.5	398	557	340	560	340	560
Matsui	Wall-A	28.2	434	605	377	493	377	493
Matsui	Wall-B	27.4	434	605	377	493	377	493
Akita	WAS	27	434	605	377	493	377	493
Akita	WBS	27	434	605	377	493	377	493
Kabeyasawa	K1	19.2	392	557	395	526	395	526
Kabeyasawa	K2	19.2	392	557	395	526	395	526
Kabeyasawa	K3	19.2	392	557	395	526	395	526
Kabeyasawa	K4	20.8	392	557	395	526	395	526
Maier	S5	37.3	574	-	574	-	574	-
Maier	S7	34.1	555	-	555	-	555	-
Barda	B3-2	27.0	414	667	545	850	513	672
Barda	B4-3	19.0	527	808	535	825	N/A	N/A
Barda	B5-4	28.9	527	807	N/A	N/A	495	678
Barda	B6-4	21.2	529	802	496	654	496	654
Barda	B7-5	25.7	539	794	531	830	501	662
Barda	B8-5	23.4	489	778	527	755	496	675
Synge	Wall-3	26	300	460	315	440	380	576
Palermo/Vecchio	DP1	21.7	605	652	605	652	605	652
Palermo/Vecchio	DP2	18.8	605	652	605	652	605	652
Saito	W-15-1	24.8	369	526	369	526	369	526
Saito	W-12-1	35.2	369	526	369	526	369	526
Saito	W-12-2	38.1	369	526	369	526	369	526
Saito	W-12-3	35.8	369	526	369	526	369	526
Saito	W-12-4	35.8	369	526	369	526	369	526
Saito	W-12-5	40.4	369	526	369	526	369	526
Saito	W-15-2	25.9	369	526	369	526	369	526

Researcher	ID	f'_c (MPa)	f_{ybe} (MPa)	f_{ube} (MPa)	f_{yv} (MPa)	f_{uv} (MPa)	f_{yh} (MPa)	f_{uh} (MPa)
Saito	W-12-6	33.1	369	526	369	526	369	526
Saito	W-12-7	33.9	369	526	369	526	369	526
Sato	18M 12-40	43.1	422	-	422	-	422	-
Sato	24M 8-30	38	296	-	296	-	296	-
Sato	24M 8-40	35.8	422	-	422	-	422	-
Sato	24M 8-50	35	528	-	528	-	528	-
Sato	24M 6-30	40.1	296	-	296	-	296	-
Sato	24M 6-40	41.0	422	-	422	-	422	-
Sato	36M 12-30	36.3	296	-	296	-	296	-
Sato	36M 12-40	34.4	422	-	422	-	422	-
Sato	36M 12-50	37.2	528	-	528	-	528	-
Sato	36L 8-30	24.5	296	-	296	-	296	-
Sato	36L 8-40	27.8	422	-	422	-	422	-
Sato	36M 8-30	39.3	296	-	296	-	296	-
Sato	36M 8-40	38.8	422	-	422	-	422	-
Sato	36M 8-50	37.5	528	-	528	-	528	-
Sato	36M 6-30	33.4	296	-	296	-	296	-
Sato	36M 6-40	34.6	422	-	422	-	422	-
Sato	48M 8-30	27.4	296	-	296	-	296	-
Sato	48M 8-40	27.5	422	-	422	-	422	-
Sato	48M 8-50	28	528	-	528	-	528	-
Sato	48H 8-30	41.8	296	-	296	-	296	-
Sato	48H 8-40	43.1	422	-	422	-	422	-
Sato	48H 8-50	44.6	528	-	528	-	528	-
Seki	RA-00P	31.6	349	-	349	-	349	-
Seki	RA-15P	29.5	349	-	349	-	349	-
Seki	RB-00P	28.9	381	-	381	-	381	-
Seki	RB-15P	28.9	381	-	381	-	381	-
Seki	RC-00P	30.1	349	-	349	-	349	-
Seki	RC-15P	29.2	349	-	349	-	349	-
Park	S4	46.5	617	-	653	-	667	-
Dabbagh	SW1	86	535	638	536	597	536	597
Dabbagh	SW2	86	535	638	498	535	498	535
Dabbagh	SW3	96	535	638	498	535	536	597
Dabbagh	SW4	96	535	638	498	535	536	597
Dabbagh	SW5	83	535	638	498	535	536	597
Dabbagh	SW6	83	535	638	498	535	498	535

Researcher	ID	f'_c (MPa)	f_{ybe} (MPa)	f_{ube} (MPa)	f_{yv} (MPa)	f_{uv} (MPa)	f_{yh} (MPa)	f_{uh} (MPa)
Ryo/Hirosawa	30	33.0	468	-	335	-	335	-
Ryo/Hirosawa	31	17.4	468	-	485	-	485	-
Sugano/Hirosawa	70	24.1	419	-	549	-	549	-
Sugano/Hirosawa	71	25.2	419	-	461	-	461	-
Endo	W7101	26.0	359	-	447	-	447	-
Endo	W7102	24.6	359	-	447	-	447	-
Endo	W7103	26.0	359	-	447	-	447	-
Endo	W7402	23.0	297	-	414	-	414	-
Endo	W7404	23.9	297	-	414	-	414	-
Endo	W7501	27.4	318	-	367	-	367	-
Endo	W7503	21.8	318	-	367	-	367	-
Endo	W7601	20.0	409	-	443	-	443	-
Endo	W7602	20.0	409	-	443	-	443	-
Endo	W7603	23.8	409	-	443	-	443	-
Endo	W7604	34.6	328	-	423	-	423	-
Endo	W7605	27.1	328	-	423	-	423	-
Endo	W7606	26.1	328	-	423	-	423	-
NUPEC	U-1	28.6	383	485	383	485	383	485
NUPEC	U-2	28.6	383	485	383	485	383	485
Xiang Dong	FSW-4	49.5	425	540	419	563	419	563
Xiang Dong	FSW-5	56.3	425	540	419	563	419	563
Xiang Dong	FSW-6	49.8	425	540	419	563	419	563
Xiang Dong	FSW-7	52.8	425	540	419	563	419	563
Xiang Dong	FSW-8	48.3	425	540	600	650	600	650
Xiang Dong	FSW-9	50.2	425	540	419	563	419	563
Xiang Dong	FSW-10	55.9	425	540	419	563	419	563
Xiang Dong	FSW-12	57.1	425	540	600	650	600	650
Xiang Dong	FSW-13	56.9	425	540	600	650	600	650
Chiba	CW-0.6-1.2-20	34.0	379	575	412	536	412	536
Chiba	CW-0.6-0.6-20	29.5	379	575	412	536	412	536
Chiba	CW-0.6-0.8-20	39.7	379	575	412	536	412	536
Chiba	CW-0.6-1.6-20	33.6	379	570	412	536	412	536
Chiba	CW-0.6-2.0-20	34.6	374	578	412	536	412	536
Chiba	CW-0.6-1.2-40	31.8	379	575	412	536	412	536
Chiba	CW-0.4-1.2-20	33.0	379	575	412	536	412	536
Chiba	CW-0.8-1.2-20	33.4	379	575	412	536	412	536
Yagishita	CW-0.6-0.6-20a	29.1	379	575	412	536	412	536

Researcher	ID	f'_c (MPa)	f_{ybe} (MPa)	f_{ube} (MPa)	f_{yv} (MPa)	f_{uv} (MPa)	f_{yh} (MPa)	f_{uh} (MPa)
Yagishita	CW-0.6-0.8-20a	29.6	379	575	412	536	412	536
Yagishita	CW-0.6-1.2-0	28.7	379	575	412	536	412	536
Fukuzawa	CW-0.6-0-20	35.2	379	575	N/A	N/A	N/A	N/A
Fukuzawa	CW-0.6-0.3-20	35.2	379	575	412	536	412	536
Fukuzawa	CW-0.6-2.4-20	33.6	374	578	412	536	412	536
Fukuzawa	CW-0.6-2.8-20	31.7	374	578	412	536	412	536
Fukuzawa	CW-0.6-0-0	31.7	379	575	N/A	N/A	N/A	N/A
Fukuzawa	CW-0.6-0-40	31.7	379	575	N/A	N/A	N/A	N/A
Fukuzawa	CW-0.6-0.6-0	35.2	379	575	412	536	412	536
Fukuzawa	CW-0.6-0.6-40	34.0	379	575	412	536	412	536
Fukuzawa	CW-0.4-0.6-20	33.6	379	575	412	536	412	536
Fukuzawa	CW-0.8-0.6-20	33.5	379	575	412	536	412	536
Fukuzawa	CW-0.4-2.0-20	34.0	374	578	412	536	412	536
Fukuzawa	CW-0.8-2.0-20	34.3	374	578	412	536	412	536
Hatori	CW-0.6-2-0	33.7	374	578	412	536	412	536
Hatori	CW-0.6-2-40	33.9	374	578	412	536	412	536
Hatori	CW-0.6-2-20B	35.5	379	575	412	536	412	536
Hatori	CW-0.6-0.6-20L	25.2	379	575	412	536	412	536
Hatori	CW-0.6-1.2-20L	25.9	379	575	412	536	412	536
Hatori	CW-0.6-2-20L	25.2	374	578	412	536	412	536
Taga	No 1	27.2	387	531	412	536	412	536
Taga	No 2	38.3	387	531	412	536	412	536
Taga	No 3	58.4	387	531	412	536	412	536
Taga	No 4	36.5	387	531	412	536	412	536
Taga	No 5	25.7	387	531	412	536	412	536
Taga	No 6	37.2	387	531	412	536	412	536
Taga	No 7	58.2	387	531	412	536	412	536

N/A: Not Applicable

- Value Not Reported

Table A-8. Loading, strength and drift ratio of squat RC walls with enlarged boundary elements.

Researcher	ID	Loading Type	P/f'_cA_g (%)	V_{peak} (kN)	R_{cr}	R_{peak}	R_u
Kabeyasawa/Hiraishi	NW-2	Cyclic	10.2	1464	0.0026	0.0141	0.0169
Kabeyasawa/Hiraishi	No. 1	Cyclic	13.1	1101	0.0019	0.0071	-
Kabeyasawa/Hiraishi	No. 2	Cyclic	12.0	1208	0.0019	0.0071	0.0080
Kabeyasawa/Hiraishi	No. 3	Cyclic	11.9	1360	0.0018	0.0072	-
Kabeyasawa/Hiraishi	No. 4	Cyclic	13.8	1656	0.0016	0.0067	-
Kabeyasawa/Hiraishi	No. 6	Cyclic	11.5	1353	0.0019	0.0066	-
Kabeyasawa/Hiraishi	No. 7	Cyclic	11.9	1478	0.0025	0.0073	-
Kabeyasawa/Hiraishi	No. 8	Cyclic	11.2	1638	0.0027	0.0074	0.0080
Sanada/Kabeyasawa	Type N	Cyclic	10.8	712	0.0011	0.0050	0.0095
Sanada/Kabeyasawa	Type S	Cyclic	9.8	702	0.0022	0.0063	-
Matsui	Wall-A	Dynamic	6.3	686	0.0016	0.0062	0.0115
Matsui	Wall-B	Dynamic	6.5	554	0.0017	0.0043	0.0124
Akita	WAS	Cyclic	6.6	654	0.0019	0.0076	0.0118
Akita	WBS	Cyclic	6.6	542	0.0019	0.0149	0.0175
Kabeyasawa	K1	Cyclic	9.8	441	-	-	-
Kabeyasawa	K2	Cyclic	9.8	480	-	-	-
Kabeyasawa	K3	Cyclic	9.8	541	-	-	-
Kabeyasawa	K4	Cyclic	9.1	510	-	-	-
Maier	S5	Cyclic	6.8	683	0.0029	0.0165	0.0177
Maier	S7	Cyclic	27.9	855	0.0011	0.0063	0.0072
Barda	B3-2	Cyclic	0.0	1039	0.0014	0.0052	0.0081
Barda	B4-3	Cyclic	0.0	1017	0.0014	0.0053	0.0065
Barda	B5-4	Cyclic	0.0	699	0.0003	0.0053	0.0134
Barda	B6-4	Cyclic	0.0	876	0.0009	0.0061	0.0122
Barda	B7-5	Cyclic	0.0	1075	0.0013	0.0126	0.0374
Barda	B8-5	Cyclic	0.0	851	0.0009	0.0047	0.0096
Synge	Wall-3	Cyclic	0.0	738	0.0010	0.0043	0.0065
Palermo/Vecchio	DP1	Cyclic	5.4	1277	0.0012	0.0048	0.0058
Palermo/Vecchio	DP2	Cyclic	0.0	892	0.0011	0.0039	0.0046
Saito	W-15-1	Cyclic	7.9	2187	0.0015	0.0047	0.0075
Saito	W-12-1	Cyclic	5.6	2658	0.0019	0.0055	0.0078
Saito	W-12-2	Cyclic	5.1	2511	-	-	-
Saito	W-12-3	Cyclic	5.5	2511	-	-	-
Saito	W-12-4	Cyclic	2.7	2481	-	-	-
Saito	W-12-5	Cyclic	4.9	2668	-	-	-
Saito	W-15-2	Cyclic	7.6	1814	-	-	-
Saito	W-12-6	Cyclic	5.9	1755	-	-	-

Researcher	ID	Loading Type	P/f'_cA_g (%)	V_{peak} (kN)	R_{cr}	R_{peak}	R_u
Saito	W-12-7	Cyclic	2.9	1648	-	-	-
Sato	18M 12-40	Cyclic	4.6	2250	-	0.0048	-
Sato	24M 8-30	Cyclic	5.3	1680	0.0006	0.0086	-
Sato	24M 8-40	Cyclic	5.6	1740	0.0007	0.0051	-
Sato	24M 8-50	Cyclic	5.7	1740	0.0007	0.0060	-
Sato	24M 6-30	Cyclic	5.0	2100	-	0.0088	-
Sato	24M 6-40	Cyclic	4.9	2190	-	0.0078	-
Sato	36M 12-30	Cyclic	5.5	2490	-	0.0062	-
Sato	36M 12-40	Cyclic	5.8	2490	-	0.0066	-
Sato	36M 12-50	Cyclic	5.4	2430	-	0.0060	-
Sato	36L 8-30	Cyclic	8.2	1800	-	0.0088	-
Sato	36L 8-40	Cyclic	7.2	1830	-	0.0083	-
Sato	36M 8-30	Cyclic	5.1	1890	0.0008	0.0088	-
Sato	36M 8-40	Cyclic	5.2	2040	0.0012	0.0070	0.0132
Sato	36M 8-50	Cyclic	5.3	1980	0.0015	0.0071	-
Sato	36M 6-30	Cyclic	6.0	2250	-	0.0082	-
Sato	36M 6-40	Cyclic	5.8	2370	-	0.0088	-
Sato	48M 8-30	Cyclic	7.3	1980	0.0014	0.0051	0.0084
Sato	48M 8-40	Cyclic	7.3	2040	0.0017	0.0063	-
Sato	48M 8-50	Cyclic	7.1	2040	0.0019	0.0063	-
Sato	48H 8-30	Cyclic	4.8	2280	-	0.0053	-
Sato	48H 8-40	Cyclic	4.6	2340	-	0.0053	-
Sato	48H 8-50	Cyclic	4.5	2430	-	0.0083	-
Seki	RA-00P	Pseudo Dyn.	0.0	1473	-	-	-
Seki	RA-15P	Pseudo Dyn.	3.4	1671	0.0009	0.0060	0.0097
Seki	RB-00P	Pseudo Dyn.	0.0	1264	-	-	-
Seki	RB-15P	Pseudo Dyn.	3.5	1464	0.0009	0.0053	0.0060
Seki	RC-00P	Pseudo Dyn.	0.0	1032	-	-	-
Seki	RC-15P	Pseudo Dyn.	3.5	1170	0.0009	0.0045	0.0096
Park	S4	Cyclic	7.3	2544.5	0.0039	0.0100	0.0136
Dabbagh	SW1	Cyclic	10.3	999.5	0.0041	0.0109	-
Dabbagh	SW2	Cyclic	10.3	1191	0.0059	0.0137	0.0145
Dabbagh	SW3	Cyclic	9.3	1098.5	0.0041	0.0111	0.0121
Dabbagh	SW4	Cyclic	0.0	718	0.0039	0.0092	0.0117
Dabbagh	SW5	Cyclic	10.7	1103.5	0.0042	0.0109	0.0118
Dabbagh	SW6	Cyclic	10.7	1121	0.0056	0.0140	-
Ryo/Hirosawa	30	Cyclic	0.0	829	0.0009	0.0030	-
Ryo/Hirosawa	31	Cyclic	0.0	534	0.0010	0.0038	-
Sugano/Hirosawa	70	Cyclic	0.0	707	0.0010	0.0030	0.0044

Researcher	ID	Loading Type	P/f'_cA_g (%)	V_{peak} (kN)	R_{cr}	R_{peak}	R_u
Sugano/Hirosawa	71	Cyclic	0.0	729	0.0008	0.0032	0.0045
Endo	W7101	Cyclic	5.3	625	0.0016	0.0086	0.0191
Endo	W7102	Cyclic	5.6	522	0.0011	0.0072	0.0143
Endo	W7103	Cyclic	5.3	508	0.0015	0.0061	0.0098
Endo	W7402	Cyclic	6.0	529	0.0012	0.0073	0.0149
Endo	W7404	Cyclic	5.8	541	0.0008	0.0101	0.0221
Endo	W7501	Cyclic	5.1	635	-	-	-
Endo	W7503	Cyclic	6.4	639	0.0011	0.0075	0.0116
Endo	W7601	Cyclic	6.9	797	-	-	-
Endo	W7602	Cyclic	6.1	826	-	-	-
Endo	W7603	Cyclic	5.1	1008	-	-	-
Endo	W7604	Cyclic	4.0	493	-	-	-
Endo	W7605	Cyclic	4.5	622	0.0015	0.0126	0.0206
Endo	W7606	Cyclic	4.7	884	0.0015	0.0050	0.0102
NUPEC	U-1	Dynamic	3.9	1628	0.0014	0.0054	-
NUPEC	U-2	Dynamic	3.9	1618	0.0012	0.0057	-
Xiang Dong	FSW-4	Cyclic	9.3	606	0.0011	0.0050	0.0083
Xiang Dong	FSW-5	Cyclic	4.1	632	0.0014	0.0112	0.0146
Xiang Dong	FSW-6	Cyclic	1.5	453	0.0013	0.0142	0.0166
Xiang Dong	FSW-7	Cyclic	4.4	702	0.0013	0.0091	0.0148
Xiang Dong	FSW-8	Cyclic	4.8	553	0.0009	0.0061	0.0081
Xiang Dong	FSW-9	Cyclic	4.6	737	0.0016	0.0130	0.0156
Xiang Dong	FSW-10	Cyclic	8.2	825	0.0017	0.0069	0.0085
Xiang Dong	FSW-12	Cyclic	8.1	677	0.0014	0.0045	0.0058
Xiang Dong	FSW-13	Cyclic	1.3	474	0.0014	0.0098	0.0126
Chiba	CW-0.6-1.2-20	Cyclic	5.8	1658	-	-	-
Chiba	CW-0.6-0.6-20	Cyclic	6.6	1179	-	-	-
Chiba	CW-0.6-0.8-20	Cyclic	4.9	1475	-	-	-
Chiba	CW-0.6-1.6-20	Cyclic	5.8	1677	-	-	-
Chiba	CW-0.6-2.0-20	Cyclic	5.7	1823	-	-	-
Chiba	CW-0.6-1.2-40	Cyclic	12.3	1515	-	-	-
Chiba	CW-0.4-1.2-20	Cyclic	5.9	1617	-	-	-
Chiba	CW-0.8-1.2-20	Cyclic	5.9	1343	-	-	-
Yagishita	CW-0.6-0.6-20a	Cyclic	6.7	1246	-	-	-
Yagishita	CW-0.6-0.8-20a	Cyclic	6.6	1307	-	-	-
Yagishita	CW-0.6-1.2-0	Cyclic	0.0	1146	-	-	-
Fukuzawa	CW-0.6-0-20	Cyclic	5.6	1193	-	-	-
Fukuzawa	CW-0.6-0.3-20	Cyclic	5.6	1283	-	-	-
Fukuzawa	CW-0.6-2.4-20	Cyclic	5.8	2003	-	-	-

Researcher	ID	Loading Type	P/f'_cA_g (%)	V_{peak} (kN)	R_{cr}	R_{peak}	R_u
Fukuzawa	CW-0.6-2.8-20	Cyclic	6.2	1732	-	-	-
Fukuzawa	CW-0.6-0-0	Cyclic	0.0	744	-	-	-
Fukuzawa	CW-0.6-0-40	Cyclic	12.4	1421	-	-	-
Fukuzawa	CW-0.6-0.6-0	Cyclic	0.0	1151	-	-	-
Fukuzawa	CW-0.6-0.6-40	Cyclic	11.5	1698	-	-	-
Fukuzawa	CW-0.4-0.6-20	Cyclic	5.8	1871	-	-	-
Fukuzawa	CW-0.8-0.6-20	Cyclic	5.8	1275	-	-	-
Fukuzawa	CW-0.4-2.0-20	Cyclic	5.8	2081	-	-	-
Fukuzawa	CW-0.8-2.0-20	Cyclic	5.7	1656	-	-	-
Hatori	CW-0.6-2-0	Cyclic	0.0	1712	-	-	-
Hatori	CW-0.6-2-40	Cyclic	11.6	2035	-	-	-
Hatori	CW-0.6-2-20B	Cyclic	5.5	1775	-	-	-
Hatori	CW-0.6-0.6-20L	Cyclic	7.8	1276	-	-	-
Hatori	CW-0.6-1.2-20L	Cyclic	7.6	1390	-	-	-
Hatori	CW-0.6-2-20L	Cyclic	7.8	1491	-	-	-
Taga	No 1	Cyclic	7.2	1088	-	-	-
Taga	No 2	Cyclic	5.1	1334	-	-	-
Taga	No 3	Cyclic	3.4	1461	-	-	-
Taga	No 4	Cyclic	5.4	1236	-	-	-
Taga	No 5	Cyclic	7.6	1137	-	-	-
Taga	No 6	Cyclic	5.3	1461	-	-	-
Taga	No 7	Cyclic	3.4	1677	-	-	-

- Corresponding drift ratio value could not be obtained from the reported data.

APPENDIX B OPENSEES HYSTERETIC MODEL INPUT FILE EXAMPLE

```
# ================================================================
# Squat RC Shear Walls Hysteretic Behavior Modeling
# Carlos M. Adorno (carlos.adorno@upr.edu)
# University of Puerto Rico at Mayaguez

# ==================== DESCRIPTION ==============================
# Date: NOV 3, 2013 #
# Wall's behavior modeled as a single truss element with unit length and unit area

#_____________   <----> Q
#  L=1,A=1  _O_

# Hysteretic behavior at the uniaxial material: Hysteretic Material
# Refer to Hysteretic Material at oppensees wiki for full explanation of the material model & parameters
# Model subjected to reverse Cyclic Loading - using procedure: procRCycDAns.tcl (By: N. Mitra)
# File Name: RCyclicHyst.tcl
# Experimental Test: SW1 (NEES/Buffalo)
# Units: lb, in      (Other units can be used)

# ======================= DATA DIRECTORY ========================
wipe;                    # removes all constructed objects

set dataDir DataOut_SW1;       # set up name of output data directory
file mkdir $dataDir;          # create data directory

#========================== BACKBONE ============================
# Positive envelope Load vs Drift
set Qcr 181.1;                    # Cracking Shear
set Drifcr 0.00193;       # Cracking Drift
set Qy 256;                       # Yielding Shear
set Drify 0.0134;             # Yielding Drift
set Qcap 171.28;           # Capping Shear
set Drifcap 0.0252;       # Capping Drift

# Negative envelope Load vs Drift
set Qcrn -179;       # Cracking Shear - neg. branch
set Drifcrn -0.000926; # Cracking Drift - neg. branch
set Qyn -250;            # Yielding Shear - neg. branch
set Drifyn -0.0128;          # Yielding Drift - neg. branch
set Qcapn -242;         # Capping Shear - neg. branch
```

```
set Drifcapn -0.0173;     # Capping Drift - neg. branch

# Hysteretic Behavior Parameters
set pinchX 0.6;                 # pinching factor for strain (or deformation) during reloading
set pinchY 0.15;                # pinching factor for stress (or force) during reloading
set damage1 0.01;               # damage due to ductility: D1(mu-1)
set damage2 0;              # damage due to energy: D2(Eii/Eult)
set beta 0.3;               # power used to determine the degraded unloading stiffness based on
ductility
puts "OK hyst param read"


# ================ END OF INPUT DATA (Exept displacement peaks)=============

# -------------------------------- MODEL SET UP --------------------------------
model BasicBuilder -ndm 2 -ndf 2;  # define spatial dimension of model and number of DOF per
node

# add nodes - command: node nodeId xCrd yCrd
node 1 0.0 0.0;  # start node

node 2 1.0 0.0;  # end node

#*** keep the follwoing procedure on the same directory of the model ***#

#source procRCycDAns.tcl;      # procedure to apply the reversed cyclic pushover

#------------------------ UNIAXIAL MATERIAL GENERATION -------------------------
set matID 1; # material ID: assigns a tag number to the material behavior

# add the material to domain
uniaxialMaterial Hysteretic $matID $Qcr $Drifcr $Qy $Drify $Qcap $Drifcap $Qcrn $Drifcrn
$Qyn $Drifyn $Qcapn $Drifcapn $pinchX $pinchY $damage1 $damage2 $beta;

puts "OK material created"
#-------------------------- TRUSS ELEMENT GENERATION ---------------------------
# Element Conectivity
# add truss elements - command: element truss trussID node1 node2 A matID

element truss 1 1 2 1.0 1;

#------------------------------ Boundary Conditions ----------------------------
fix 1 1 1;    # command: fix nodeID xResrnt? yRestrnt? (1=fixed; 0=free)

fix 2 0 1;
```

```
#-------------------------------------------------------------------------------

#============================ RECORDERS ============================
recorder Node -file $dataDir/DFree.out -node 2 -dof 1 disp;       # records displacement (Drift) at free node into an output file (DFree.out) in the specified directory
recorder Node -file $dataDir/RBase.out -node 1 -dof 1 reaction;    # records reaction force (Shear) at fixed node into an output file (RBase.out) in the specified directory

#----------------- BUILD THE COMPONENTS FOR THE ANALYSIS OBJECT -----------------

system ProfileSPD;              # type of linear system of equations

constraints Plain;              # constraint handler

test NormDispIncr 1.0e-6 10;     # convergence test - test NormDispIncr $tol (convergence tolerance) $iter (max. number of iterations)

algorithm Newton;               # solution algorithm

numberer RCM;                   # DOF numbering protocol

#--------------------------- REVERSED CYCLIC LOADING ---------------------------
# characteristics of cyclic analysis

#======== PARAMETERS FOR THE STATIC REVERSED-CYCLIC LOAD ==========

#set peakpts [list 0.0001 0.000365 0.0005965 0.0009915 0.001405 0.001655 0.002265 0.003225 0.00454 0.007585 0.01075 0.020 0.029]; # vector of displacement-cycle peaks, in terms of storey drift ratio

#set increments 10;   # number of increments


set IDctrlNode 2;
set IDctrlDOF 1;

set nodeTag 2;       # node of displacement read for displacement control

set dofTag 1;        # degree of freedom of displacement read for displacement control

set iDmax "0.000611 0.000421 0.000623 0.000421 0.00121 0.00101 0.0013 0.00105 0.0018 0.00173 0.00185 0.00178 0.00244 0.0024 0.0025 0.00245 0.00334 0.0032 0.00344 0.00318 0.00432 0.00396 0.00435 0.00392 0.00656 0.0061 0.0065 0.0061 0.0086 0.0085 0.00875 0.0085 0.0134 0.0128 0.0136 0.0128 0.0212 0.0173 0.0252 0.0173";                    # vector of displacement-cycle peaks, in terms of storey drift ratio
```

```
set Dincr [expr 0.0001];                    # displacement increment for pushover. you want this to be very small, but not too small to slow down the analysis
set Fact 1;                                 # scale drift ratio
set CycleType HalfCycle;                    # you can do Full / Push / Half cycles with the proc
set Ncycles 1;                              # specify the number of cycles at each peak



#  ---------------------------------    perform Static Pushover Analysis
# ----------- set up analysis parameters

source LibAnalysisStaticParameters.tcl;                                 # constraintsHandler,DOFnumberer,system-ofequations,convergenceTest,solutionAlgorithm,integrator
set fmt1 "%s Pushover analysis: CtrlNode %.3i, dof %.1i, Disp=%.4f %s";     # format for screen/file output of DONE/PROBLEM analysis
set LunitTXT "mm";

# create load pattern for lateral pushover load



set iPushNode "2";                          # define nodes where lateral load is applied in static lateral analysis
pattern Plain 100 Linear {;                 # define load pattern -- generalized
        foreach PushNode $iPushNode {
                load $PushNode 1 0.0
        }
}

# ----------- set up analysis parameters
source LibAnalysisStaticParameters.tcl;     # constraintsHandler,DOFnumberer,system-ofequations,convergenceTest,solutionAlgorithm,integrator

#  ---------------------------------    perform Static Cyclic Displacements Analysis


source GeneratePeaksA.tcl

set fmt1 "%s Cyclic analysis: CtrlNode %.3i, dof %.1i, Disp=%.4f %s";     # format for screen/file output of DONE/PROBLEM analysis

foreach Dmax $iDmax {
        set iDstep [GeneratePeaksA $Dmax $Dincr $CycleType $Fact];     # this proc is defined above
        for {set i 1} {$i <= $Ncycles} {incr i 1} {
```

```
		set zeroD 0
		set D0 0.0
		foreach Dstep $iDstep {
			set D1 $Dstep
			set Dincr [expr $D1 - $D0]
			integrator DisplacementControl  $IDctrlNode $IDctrlDOF $Dincr
			analysis Static
			# ---------------------------------first analyze command----------------------
			set ok [analyze 1]
			# ---------------------------------if convergence failure----------------------
			if {$ok != 0} {
				# if analysis fails, we try some other stuff
				# performance is slower inside this loop	global
maxNumIterStatic;	# max no. of iterations performed before "failure to converge" is ret'd
				if {$ok != 0} {
					puts "Trying Newton with Initial Tangent .."
					test NormDispIncr   $Tol 2000 0
					algorithm Newton -initial
					set ok [analyze 1]
					test $testTypeStatic $TolStatic	$maxNumIterStatic	0
					algorithm $algorithmTypeStatic
				}
				if {$ok != 0} {
					puts "Trying Broyden .."
					algorithm Broyden 8
					set ok [analyze 1 ]
					algorithm $algorithmTypeStatic
				}
				if {$ok != 0} {
					puts "Trying NewtonWithLineSearch .."
					algorithm NewtonLineSearch 0.8
					set ok [analyze 1]
					algorithm $algorithmTypeStatic
				}
				if {$ok != 0} {
					set putout [format $fmt1 "PROBLEM" $IDctrlNode
$IDctrlDOF [nodeDisp $IDctrlNode $IDctrlDOF] $LunitTXT]
					puts $putout
					return -1
				}; # end if
			}; # end if
			# ------------------------------------------------------------------------------
			set D0 $D1;			# move to next step
		}; # end Dstep
	};		# end i
};	# end of iDmaxCycl
```

```
# ---------------------------------------------------------------------------------------------------
if {$ok != 0 } {
        puts [format $fmt1 "PROBLEM" $IDctrlNode $IDctrlDOF [nodeDisp $IDctrlNode
$IDctrlDOF] $LunitTXT]
} else {
        puts [format $fmt1 "DONE"  $IDctrlNode $IDctrlDOF [nodeDisp $IDctrlNode
$IDctrlDOF] $LunitTXT]
}
print node;     # print the results at nodes

print node;     # print the results at nodes
```

APPENDIX C OPENSEES FLEXURE-SHEAR INTERACTION MODEL INPUT FILE EXAMPLE

```
# file to analyze a RC wall using the flexure-shear interaction element
# this file is intended to model an individual wall with rectangular cross section and uniformly distributed vertical and horizontal reinforcement

wipe;                                   # clear memory of all past model definitions
model BasicBuilder -ndm 2 -ndf 3;  # Define the model builder, ndm=#dimension, ndf=#dofs
set dataDir wall_SW1;                           # set up name of data directory (can remove this)
file mkdir $dataDir;                    # create data directory
#set GMdir "../GMfiles/";

# units psi, in (this can be changed while maintaining consistent units)

# Analysis parameters----------------------------------------------------------------------

set tolAx 1.0e-5; set iterAx 100;
set tolLatNew .00035; set iterLatNew 8000;
set tolLatIni 1.0e-3; set iterLatIni 1000;
set dUi 0.001; # Displacement increment
set maxU 2.3; # Max. Displacement


#Nodes-----------------------------------------------------------------------------------------------------
#Define nodal coordinates
#set n 7

set y1 0; set y2 16.11; set y3 32.22; set y4 48.33; set y5 64.44;
set y6 80.55; set y7 96.66; set y8 112.8;

#Define nodes by assigning defined coordinates
node 1 0 $y1 0; node 3 0 $y2 0; node 4 0 $y3 0; node 5 0 $y4 0;
node 6 0 $y5 0; node 7 0 $y6 0; node 8 0 $y7 0; node 2 0 $y8 0;

#Define fixed base boundary condition
fix 1 1 1 1;

print node;

# Set up parameters that are particular to the model for displacement control

set IDctrlNode 2;          # node where displacement is read for displacement control
```

```
set IDctrlDOF 1;          # degree of freedom of displacement read for displacement control


#concrete parameters for Concrete 06 uniaxial model----------------------------------------------------


# Unconfined concrete
set fc -3600; set eo -0.003; set nc 2; set k 1; set fcr 450; set alphaC 0.32; set ecr 0.00008; set b 4;
set alphaT 0.08;


#steel parameters for Steel 02 uniaxial model-----------------------------------------------------------
#steel02($Fy $E          $b $R0 $CR1 $CR2 $a1 $a2 $a3 $a4)

# Vertical steel web

set fyv 67300; set E 29000000; set bs 0.018; set Ro 15; set cR1 0.925; set cR2 0.15; set a1 18.5;
set a2 0.0015; set a3 0; set a4 1.0;

# Vertical steel boundary element

#set fyvb 413.9; set Eb 200000; set bsb 0.016; set Rob 15; set cR1b 0.925; set cR2b 0.15; set a1b
18.5; set a2b 0.0015;

# Horizontal steel

set fyh 67300; set Eh 29000000; set bsh 0.018; set Roh 15; set cR1h 0.925; set cR2h 0.15; set
a1h 18.5; set a2h 0.0015; set a3h 0; set a4h 1.0;

#concrete (confined and unconfined)---------------------------------------------------------------------
#uniaxialMaterial Concrete06 $matTag $fc $e0 $n $k $alpha1 $fcr $ecr $b $alpha2

#uniaxialMaterial Concrete06 1 $fcc $ecc $ncc $kcc $alphaC $fcrc $ecr $b $alphaT;

uniaxialMaterial Concrete06 2 $fc $eo $nc $k $alphaC $fcr $ecr $b $alphaT;


#Steel (vertical and horizontal)------------------------------------------------------------------------
#web steel
uniaxialMaterial Steel02 1002 $fyv $E $bs $Ro $cR1 $cR2 $a1 $a2 $a3 $a4;
#boundary element steel
#uniaxialMaterial Steel02 1003 $fyvb $Eb $bsb $Rob $cR1b $cR2b $a1b $a2b;
#horiz. steel
uniaxialMaterial Steel02 1004 $fyh $Eh $bsh $Roh $cR1h $cR2h $a1h $a2h $a3h $a4h;
```

```
# Define cross-section-------------------------------------------------------------------------------------

set t1 8; set NStrip1 1; # thickness 1

set t2 8; set NStrip2 18; # thickness 2

set t3 8; set NStrip3 1; # thickness 3

geomTransf LinearInt 1

set np 1; # int. points

set C 0.4; # center of rotation

# Section definition ---------------------------------------------------------------------------------------

#section FiberInt $secTag -NStrip $nStrip1 $thick1 $nStrip2 $thick2 $nStrip3 $thick3
{fiber...Hfiber ...}

#fiber $yLoc $zLoc $A $matTag

#coordinates for each strip

set yLoc 3.43; set yLoc1 10.28; set yLoc2 17.13; set yLoc3 23.98; set yLoc4 30.84;
set yLoc5 37.69; set yLoc6 44.54; set yLoc7 51.40; set yLoc8 55.66; set yLoc9 58.25
set zLoc 0;

# Tributary areas for each strip

set Au1 54.42; set Au2 13.41; set Au3 27.6
set As1 0.4
set Ah 0.8;

#---------

section FiberInt 2 -NStrip $NStrip1 $t1 $NStrip2 $t2 $NStrip3 $t3 {

#vertical fibers

        fiber -$yLoc9 $zLoc $Au3 2; fiber -$yLoc9 $zLoc $As1 1002;

        fiber -$yLoc8 $zLoc $Au2 2;

        fiber -$yLoc7 $zLoc $Au1 2; fiber -$yLoc7 $zLoc $As1 1002;

        fiber -$yLoc6 $zLoc $Au1 2; fiber -$yLoc6 $zLoc $As1 1002;
```

```
        fiber -$yLoc5 $zLoc $Au1 2; fiber -$yLoc5 $zLoc $As1 1002;
        fiber -$yLoc4 $zLoc $Au1 2; fiber -$yLoc4 $zLoc $As1 1002;
         fiber -$yLoc3 $zLoc $Au1 2; fiber -$yLoc3 $zLoc $As1 1002;
        fiber -$yLoc2 $zLoc $Au1 2; fiber -$yLoc2 $zLoc $As1 1002;
        fiber -$yLoc1 $zLoc $Au1 2; fiber -$yLoc1 $zLoc $As1 1002;
        fiber -$yLoc $zLoc $Au1 2; fiber -$yLoc $zLoc $As1 1002;
        fiber $yLoc $zLoc $Au1 2; fiber $yLoc $zLoc $As1 1002;
         fiber $yLoc1 $zLoc $Au1 2; fiber $yLoc1 $zLoc $As1 1002;
         fiber $yLoc2 $zLoc $Au1 2; fiber $yLoc2 $zLoc $As1 1002;
        fiber $yLoc3 $zLoc $Au1 2; fiber $yLoc3 $zLoc $As1 1002;
        fiber $yLoc4 $zLoc $Au1 2; fiber $yLoc4 $zLoc $As1 1002;
        fiber $yLoc5 $zLoc $Au1 2; fiber $yLoc5 $zLoc $As1 1002;
        fiber $yLoc6 $zLoc $Au1 2; fiber $yLoc6 $zLoc $As1 1002;
        fiber $yLoc7 $zLoc $Au1 2; fiber $yLoc7 $zLoc $As1 1002;
        fiber $yLoc8 $zLoc $Au2 2;
        fiber $yLoc9 $zLoc $Au3 2; fiber $yLoc9 $zLoc $As1 1002;
#horiz. reinf.
   Hfiber 0 $zLoc $Ah 1004;
}

# Element definition----------------------------------------------------------------------------
#element dispBeamColumnInt $eleTag $iNode $jNode $numIntgrPts $secTag $transfTag $cRot
element dispBeamColumnInt 1 1 3 $np 2 1 $C
element dispBeamColumnInt 2 3 4 $np 2 1 $C
```

```
element dispBeamColumnInt 3 4 5 $np 2 1 $C

element dispBeamColumnInt 4 5 6 $np 2 1 $C

element dispBeamColumnInt 5 6 7 $np 2 1 $C

element dispBeamColumnInt 6 7 8 $np 2 1 $C

element dispBeamColumnInt 7 8 2 $np 2 1 $C


print element;

# Create a recorder to monitor nodal displacement and element forces---------------------------------

recorder Node -file $dataDir/nodeTop.out -time  -node 2 -dof 1 2 3 disp;

recorder Element -file $dataDir/elesX.out -time -ele 1 globalForce;


# recorder for element1 section1 steel stress/strain and section force-def.-----------------------------

recorder Element -file $dataDir/Sect_FandD.out -ele 1 section 1 forceAndDeformation

recorder Element -file $dataDir/Sect_FandD2.out -ele 1 section 2 forceAndDeformation

recorder Element -file $dataDir/Sect_eX.out -ele 1 section 1 eX

recorder Element -file $dataDir/Sect_eY.out -ele 1 section 1 eY

recorder Element -file $dataDir/Sect_sXsteel.out -ele 1 section 1 sX

recorder Element -file $dataDir/Sect_sYsteel.out -ele 1 section 1 sY


recorder Element -file $dataDir/Sect_e1.out -ele 1 section 1 e1

recorder Element -file $dataDir/Sect_e2.out -ele 1 section 1 e2

recorder Element -file $dataDir/Sect_s1conc.out -ele 1 section 1 s1

recorder Element -file $dataDir/Sect_s2conc.out -ele 1 section 1 s2

recorder Element -file Element1.out -time -ele 1  section 1 fiber 0 0 stressStrain
```

```
# Set axial load-----------------------------------------------------------------------------------------

set PCol 0;

pattern Plain 1 Constant {
  load 2 0 -$PCol 0;
}

# Gravity-analysis parameters -- load-controlled static analysis

initialize; integrator LoadControl 0;

system SparseGeneral -piv; test NormUnbalance $tolAx $iterAx 0;

numberer Plain; constraints Plain;

algorithm ModifiedNewton -initial; analysis Static;


# perform the gravity load analysis,

analyze [expr 1]


loadConst -time 0.0


# ---------------------------------- maintain constant gravity loads and reset time to zero

puts "Model Built"


# create load pattern for lateral pushover load

pattern Plain 200 Linear {;                     # define load pattern -- generalized
        load 2 100 0.0 0.0 ;            # define lateral load in static lateral analysis
}

test NormDispIncr $tolLatNew $iterLatNew;

algorithm Newton -initial

analysis Static
```

```
set dU $dUi;
set numSteps [expr int($maxU/$dU)];
integrator DisplacementControl 2 1 $dU 1 $dU $dU

#source cycle2.tcl
#### end

set ok [analyze $numSteps]; set jump 1;
if {$ok != 0} {
set currentDisp [nodeDisp 2 1]
set ok 0
while {abs($currentDisp) < abs($maxU)} {
set ok [analyze 1]
puts "\n Trying.. $currentDisp\n"
# if the analysis fails try initial tangent iteration
if {$ok != 0} {
puts "\n regular newton failed .. try an initial stiffness"
test NormDispIncr $tolLatIni $iterLatIni 0;
algorithm ModifiedNewton -initial ;
set ok [analyze 1]
puts "\n Trying.. $currentDisp\n"
if {$ok == 0} {
puts " that worked .. back to regular newton \n"
set jump 1
```

```
integrator DisplacementControl 2 1 $dU 1
} else {
puts "\n that didn't worked .. Try next point\n"
set jump [expr $jump+1];
integrator DisplacementControl 2 1 [expr $dU*$jump] 1
}
test NormDispIncr $tolLatNew $iterLatNew
algorithm Newton

} else {set jump 1
integrator DisplacementControl 2 1 $dU 1
}
set currentDisp [expr $currentDisp+$dU]
}
}
#### end
```

APPENDIX D OPENSEES MOMENT-CURVATURE CROSS SECTION ANALYSIS INPUT FILE EXAMPLE

```
# Wall Specimen SW1 (NEEShub Project 676)
# Input File to create rectangular RC fiber section
# Downloaded from OpenSees Examples Manual/Example 2 (Example2.1.tcl &
MomentCurvature.tcl)
# Modified to model RC Wall cross section by Carlos M. Adorno

# units: Kip, in (MPa, mm & kN may be used...just be consistent)

# Remove existing model
wipe

# Create ModelBuilder (with two-dimensions and 3 DOF/node)
# --------------------
model basic -ndm 2 -ndf 3

# Define materials for nonlinear columns
# ------------------------------------------
# CONCRETE                tag  f'c     ec      ecu     Ec
# Core concrete (lightly confined)
uniaxialMaterial Concrete04  1  -3.6  -0.002  -0.0056   3420
# Cover concrete (unconfined)
uniaxialMaterial Concrete04  2  -3.6  -0.002   -0.0056   3420

# STEEL
# Reinforcing Steel Material
# Define model parameters

set fy   67.3;     # Yield stress
set fu   102.7;    # Ultimate stress
set Es   29000;    # Initial Young's modulus
set Esh  1362;     # Tangent at initial strain hardening
set esh  0.0113;   # Strain corresponding to initial strain hardening
set eult 0.07;     # Strain at peak stress

# Define material
# uniaxialMaterial ReinforcingSteel $matTag $fy $fu $Es $Esh $esh $eult

uniaxialMaterial ReinforcingSteel 101 $fy $fu $Es $Esh $esh $eult;

# Define cross-section for nonlinear columns
```

```
# ----------------------------------------

# set some paramaters
set tw     8;          # wall thickness
set lw     120;        # wall length
set cover  1.5;     # concrete clear cover
set As     0.20;     # area of no. 4 bars

# some variables derived from the parameters
set y1 [expr $lw/2.0]
set z1 [expr $tw/2.0]

section Fiber 1 {

   # Create the concrete core fibers
   # patch rect $matTag $numSubdivY $numSubdivZ $yI $zI $yJ $zJ
   patch rect 1 120 1 [expr $cover-$y1] [expr $cover-$z1] [expr $y1-$cover] [expr $z1-$cover]

   # Create the concrete cover fibers (bottom,top,right, left)
   patch rect 2 120 1  [expr $cover-$y1] [expr $z1-$cover] [expr $y1-$cover] $z1
   patch rect 2 120 1  [expr $cover-$y1] [expr -$z1] [expr $y1-$cover] [expr $cover-$z1]
   patch rect 2  2 1  [expr -$y1] [expr -$z1] [expr $cover-$y1]  $z1
   patch rect 2  2 1  [expr $y1-$cover] [expr -$z1] $y1 $z1

   # Create the reinforcing fibers (bottom, top)
   # layer straight $matTag $numFiber $areaFiber $yStart $zStart $yEnd $zEnd
   layer straight 101 17 $As [expr $cover-$y1] [expr $cover-$z1] [expr $y1-$cover] [expr
$cover-$z1]
   layer straight 101 17 $As [expr $cover-$y1] [expr $z1-$cover] [expr $y1-$cover] [expr $z1-
$cover]
}

# Estimate yield curvature
# (Assuming no axial load and only top and bottom steel)
set d [expr $lw-$cover]          ;# d -- from cover to rebar
set epsy [expr $fy/$Es]          ;# steel yield strain
# Yield furvature for walls (Paulay & Priestley Seismic Design of RC & Masonry Buildings pp.
405)
set Ky [expr 0.0033/$lw]
#set Ky [expr $epsy/(0.7*$d)] # For other sections (OpenSees Example)

# Print estimate to standard output
puts "Estimated yield curvature: $Ky"

# Set axial load
set P 0
```

```
set mu 100;              # Target ductility for analysis
set numIncr 1000;        # Number of analysis increments

# Call the section analysis procedure
source MomentCurvature.tcl
MomentCurvature 1 $P [expr $Ky*$mu] $numIncr
```